

ISI

bilimi ve tekniđi
dergisi

Journal of Thermal Science and Technology

2022 Cilt/Volume 42 Sayı/Number 2
ISSN 1300-3615

Türk Isı Bilimi ve Tekniđi Derneđi tarafından yılda iki kez
Nisan ve Ekim aylarında yayınlanır.

*A publication of the Turkish Society for Thermal Sciences and
Technology, published twice a year, in April and October.*

TIBTD Adına Yayın Sahibi Sorumlu Yayımcı/Publisher:
Prof. Dr. Nuri YÜCEL, Gazi Üniversitesi

Sorumlu Yazı İşleri Müdürü-Editör/Editor-in-Chief:
Prof. Dr. Selin ARADAĞ ÇELEBİOĞLU
TED Üniversitesi Makine Mühendisliđi Bölümü,
submit@tibtd.org.tr

Yayın Türü: Yaygın, süreli

Editörler Kurulu/Editorial Board:

Prof. Dr. Murat KÖKSAL, Hacettepe Üniversitesi
Doç. Dr. Özgür EKİCİ, Hacettepe Üniversitesi
Doç. Dr. Barbaros ÇETİN, İhsan Doğramacı Bilkent
Üniversitesi
Doç. Dr. Özgür BAYER, Orta Dođu Teknik Üniversitesi

Dil Editörleri (Language Editors):

Prof. Dr. Zafer DURSUNKAYA, Orta Dođu Teknik
Üniversitesi (İngilizce/English)
Prof. Dr. Haşmet TÜRKOĞLU, Çankaya Üniversitesi
(Türkçe/ Turkish)

Baskı/Printed at: KALKAN Matbaacılık San. Tic. Ltd.
Büyük Sanayi 1. Cadde, Alibey İş Hamı No: 99/32 İskitler,
ANKARA 312 342 16 56

TIBTD

Türk Isı Bilimi ve Tekniđi Derneđi: Dernek ve bu dergi,
Türkiye'de ısı bilimi ve tekniđini geliştirmek amacıyla 1976
yılında Prof. Dr. Yalçın A. GÖĞÜŞ tarafından kurulmuştur.

Turkish Society of Thermal Sciences and Technology: The
association and the journal was founded by Prof. Dr. Yalçın A.
GÖĞÜŞ in 1976 to improve thermal sciences and technology
in Turkey.

Adresi/Address: TIBTD, Mühendislik Fakültesi, Zemin Kat
No.22 Gazi Üniversitesi, 06570 ANKARA

http://www.tibtd.org.tr, ibtd@tibtd.org.tr

Üyelik aidatları için: İş Bankası Maltepe Şubesi Hesap No:
42120867567, IBAN: TR08 0006 4000 0014 2120 8675 67

Yönetim Kurulu/Executive Board:

Prof. Dr. Nuri YÜCEL (Başkan), Prof. Dr. İlhami HORUZ
(Bşk. Yrd.), Prof. Dr. Selin ARADAĞ ÇELEBİOĞLU
(Editör), Doç. Dr. Mustafa Zeki YILMAZOĞLU (Genel Sek.),
Dr. Duygu UYSAL (Muhasip Üye), Prof. Dr. Oğuz TURGUT,
Doç. Dr. Ülkü Ece AYLI

İÇİNDEKİLER / CONTENTS

Savfa / Page

Analysis and assessment of daily and seasonal photovoltaic heat island effect on Sekbandemirli rural region by local weather data records	157
<i>Yerel meteorolojik veri kayıtları ile Sekbandemirli kırsal bölgesinde günlük ve mevsimsel fotovoltaiik ısı adasının incelenmesi ve değerlendirilmesi</i> Emre DEMİREZEN, Talat ÖZDEN and Bülent G. AKINOĞLU	
Nationwide mapping of optimum wall insulation thicknesses: A stochastic approach	169
<i>Optimum duvar yalıtımı kalınlıklarının ülke çapında haritalanması: Stokastik yaklaşım</i> Semih CAGLAYAN, Beliz OZORHON and Levent KURNAZ	
Theoretical and experimental investigation of V-Corrugated solar air heater for space heating	203
<i>V-Kat levhalı güneş enerjili hava ısıtıcının ortam ısıtması için teorik ve deneysel incelemesi</i> Murat ÖZDENEFİ and Khaled ALTEER	
Physics informed neural networks for two dimensional incompressible thermal convection problems	221
<i>Sıkıştırılmaz ısı taşınım problemlerinin fizik öğrenen yapay sinir ağları ile çözümü</i> Atakan AYGUN and Ali KARAKUS	
Cooling performance of thermoelectric cooler modules: Experimental and numerical methods	233
<i>Termoelektrik soğutma modüllerinin soğutma performansı: Deneysel ve sayısal yöntemler</i> İlhan KAHRAMAN and Naim DEREBAŞI	
Finding conditions in reprocessing of glass wool waste as a heat insulator	245
<i>Camyünü atığının ısı yalıtkan olarak yeniden proses edilmesinin koşullarının bulunması</i> Saharat CHUNTHUM, Anchasa PRAMUANJAROENKIJ, Siritluk PHANKHOKSOONG, Rungsima CHOLLAKUP and Sadık KAKAÇ	
Himmetođlu ve Seytömer bitümlü şeyleri ile plastik şehir atıklarının kabarcıklı akışkan yataklı reaktörde gazlaştırılması	257
<i>Gasification of Himmetođlu and Seytömer oil shales with plastic wastes in a bubbling fluidized bed reactor</i> Duygu UYSAL, Hazal ÖZTAN, Ahmed Abdullah GAFUR ve Özkan Murat DOĞAN	
Analysis of heat transfer enhancement in tubes with capsule dimpled surfaces and Al2O3-water nanofluid	269
<i>Boru yüzeyindeki kapsül tipi kabartmanın ve Al2O3-Su nanoakışkanın ısı transferine etkisinin sayısal analizi</i> Ekin ÖZGİRĞİN YAPICI, Mahmoud Awani A. Haj İBRAHİM and Haşmet TÜRKOĞLU	

Amaç/Objective

Isı bilimi ve tekniđinin geliştirilmesini teşvik etmek, ısı bilimi ve tekniđi
alanında özgün, teorik, sayısal ve deneysel çalışmaların yayınlanmasına
olanak sağlamaktır.

*To contribute to the improvement of thermal sciences and technology and
publication of original, theoretical, numerical and experimental studies in
thermal sciences and technology.*

İçerik/Content

Isı bilimi ve tekniđi alanındaki özgün ve derleme makaleler.

Original and review articles in thermal sciences and technology.

Deđerlendirme/Evaluation

Dergi hakemli bir dergi olup, her bir makale konusunda uzman en az iki
hakem tarafından değerlendirilir.

Each article published in this journal is evaluated by at least two referees.

Science Citation Index Expanded (SCIE), Engineering Index (EI), EBSCO ve Mühendislik ve Temel
Bilimler Veri Tabanı (TÜBİTAK-ULAKBİM) tarafından taranmaktadır.

*Indexed by Science Citation Index Expanded (SCIE), Engineering Index (EI), EBSCO and
Engineering and Natural Sciences Data Base (TÜBİTAK-ULAKBİM).*

Isı Bilimi ve Tekniđi Derneđi kurucusu Prof. Dr. Yalçın Gögüş'ün anısına...



Prof. Dr. Yalçın GÖĞÜŞ
22.6.1934-13.09.2022

1961-1970'de ODTÜ'de yoğun öğrenci olaylarının olduđu bir dönemde, Almanya Münih Teknik Üniversitesi Termodinamik A1 Enstitüsünden, Prof. Grigul, Prof. Mayinger'i davet ettim. Termodinamik A1 Enstitüsü'nün dünyaca meşhur olduğunu biliyordum. Tanınmış bilim adamı Prof. Schmidt de aynı A1 Enstitüsünde idi.

Prof. Schmidt ile doktora yapan Yalçın Gögüş bölüme bir dilekçe göndererek, öğretim üyesi olarak katılmak istediğinde çok sevindim. Yalçın bey doktorasını tamamlamış, yazma döneminde idi. Çok sevindim, Ankara'ya geldi, beraber konuştuk. Dekanımız Rahmetli Prof. Mustafa Parlar'a durumu bildirdim. O zamanlar, yeni bir öğretim üyesi alınırken, öğretim üyelerinden bir komite kurulur, mülakat ve İngilizce imtihanı yapılırdı. Dekanım Parlar'a, bu genci doğrudan tayin etmek istediğimi bildirdim, kabul ettiler. Bölümde Termodinamik dersini Yalçın Bey'le birlikte bir dönem de birlikte verdik.

Makine Bölümünde, TÜBİTAK Isı Tekniđi Araştırma Ünitesini kurmuştum. Yalçın Bey, bu Üniteye, sebze ve meyvelerin soğutma konularında, pratik uygulamalı çok değerli projeler yürütüyor, sürekli yayınlar yapıyordu. Bu arada, doktorasını yazma işlemlerini tamamladı, Almanya'ya giderek, Dr. Yalçın Gögüş olarak döndü.

Yalçın, daima yeni fikirler ile gelirdi. Birgün, Yalçın bana gelerek, "Türk Isı Bilimi ve Tekniđi Derneđi" kuralım dedi. "Güzel olur fakat beni biliyorsun çok meşgulüm, sen işlemleri tamamlarsan gerisi kolay" dedim, ilk başkanı da sen olursun dedim. Yalçın gerekli işlemleri tamamladı ve 1976 yılında Yalçın bey, Türk Isı Bilimi ve Tekniđi Derneđi'ni kurdu ve ilk başkanı olarak görev yaptı.

Bu dernek, değerli faaliyetleri, şimdi Gazi Üniversitesinde Prof. Dr. Nuri Yücel Beyin başkanlığında yürütülmektedir.

Prof. Dr. Yalçın Gögüş, Makine Bölümünün en değerli ve faal üyelerinden birisi olarak, bölümde MS ve Dr. tezleri yürüttü, Bölüm Başkanlığı yaptı. Sonra faaliyetlerini, ODTÜ Havacılık ve Uzay Mühendisliği bölümünde devam ettirdi.

2022'de, bu bölümde yapılan bir merasimle ebediyete yolcu ettik. Mekanı cennet olsun, nur içinde yatsın benim sevgili arkadaşım!

Prof. Dr. Sadık KAKAÇ
Ekim 2022



ANALYSIS AND ASSESSMENT OF DAILY AND SEASONAL PHOTOVOLTAIC HEAT ISLAND EFFECT ON SEKBANDEMIRLI RURAL REGION BY LOCAL WEATHER DATA RECORDS

Emre DEMIREZEN^{b,d,*}, Talat OZDEN^{c,d,**} and Bulent G. AKINOGLU^{a,b,d,***}

^a Middle East Technical University - Physics Department, Ankara, Turkey

^b Middle East Technical University - Earth System Science Department, Ankara, Turkey

^c Gumushane University - Department of Electrical and Electronics Engineering, Gumushane, Turkey

^d ODTÜ Center for Solar Energy Research and Applications (ODTÜ-GÜNAM), Ankara, Turkey

*demre@metu.edu.tr, ORCID: 0000-0001-8417-104X

**tozden@metu.edu.tr, ORCID: 0000-0002-0781-2904

***bulo@metu.edu.tr, ORCID: 0000-0003-1987-6937

(Geliş Tarihi: 22.12.2021, Kabul Tarihi: 19.07.2022)

Abstract: Photovoltaic Power Plants have a considerable share among solar energy conversion technologies toward environmentally sustainable and economically feasible electricity production. However, when a rural region's land surface formed by natural soil types is covered by a Photovoltaic Power Plant (PVPP)'s dark-colored solar modules in large numbers, an artificial albedo (reflectivity) change is expected on that surface. Because of the heat exchange between these modules and the air surrounding them due to albedo alteration, the region's natural weather conditions may experience Photovoltaic Heat Island Effect (PVHIE) as a result of external and time-dependent air temperature oscillations caused by the warming-cooling cycles of solar modules. To observe and analyze a possible PVHIE trend, it has been conducting a field study project since October 2017 for a PVPP near the Sekbandemirli rural region in the Kutahya city of Turkey. The weather data, including air temperature and wind (direction and speed) at every 10-minute and hourly intervals, are collected by the three weather monitoring stations installed at the specific locations inside and outside the PVPP field. The plant's hourly average power output and module temperature data can also be monitored. After conducting statistical, correlational, and graphical analyses, the results show some temporal PVHI formations at the PVPP field center daily and on a seasonal basis. The plant center's air temperature tends to be warmer (up to the 6°C difference) during daytimes and colder (up to the (-3)°C difference) during nighttimes.

Keywords: Heat island effect, Air temperature, Photovoltaic power plant, Weather station, Wind direction, Wind speed

YEREL METEOROLOJİK VERİ KAYITLARI İLE SEKBANDEMİRLİ KIRSAL BÖLGESİNDE GÜNLÜK VE MEVSİMSSEL FOTOVOLTAİK ISI ADASININ İNCELENMESİ VE DEĞERLENDİRİLMESİ

Özet: Fotovoltaik enerji santralleri, çevresel açıdan sürdürülebilir ve ekonomik olarak uygulanabilir elektrik üretimine yönelik güneş enerjisi dönüşüm teknolojileri arasında önemli bir paya sahiptir. Ancak, kırsal bir bölgenin doğal toprak türlerinin oluşturduğu arazi yüzeyi, bir fotovoltaik enerji santralinin büyük sayılardaki koyu renkli güneş modülleri ile kaplandığında, bu yüzeyde yapay bir albedo (yansıtma) değişimi beklenir. Albedo değişimi nedeniyle bu modüller ve onları çevreleyen hava arasındaki ısı alışverişine ve ısınma-soğuma döngülerine bağlı olarak oluşan harici ve zamana bağlı hava sıcaklığı salınımları sonucunda, bölgenin doğal hava koşulları "Fotovoltaik Isı Adası Etkisi"ne maruz kalabilir. Olası bir fotovoltaik ısı adası etkisi eğilimini gözlemlemek ve analiz etmek için, Türkiye'nin Kütahya ilinin Sekbandemirli kırsal bölgesi yakınındaki bir fotovoltaik enerji santrali için Ekim 2017'den itibaren bir saha çalışması projesi yürütülmektedir. Her 10 dakikalık ve saatlik aralıklarla hava sıcaklığı ve rüzgar (yön ve hız) dahil olmak üzere hava durumu verileri, santral alanının içindeki ve dışındaki belirli konumlara kurulu üç meteorolojik izleme istasyonu tarafından toplanmaktadır. Santralin saatlik ortalama güç çıkışı ve modül sıcaklık verileri de izlenebilmektedir. İstatistiksel, korelasyonel ve grafiksel analizler yapıldıktan sonra sonuçlar, fotovoltaik enerji santrali sahasının merkezinde günlük ve mevsimsel olarak bazı geçici fotovoltaik ısı adası oluşumlarını göstermektedir. Santral merkezinin hava sıcaklığı, gündüzleri daha sıcak (6°C farka kadar) ve geceleri daha soğuk ((-3)°C farka kadar) olma eğilimindedir.

Anahtar Kelimeler: Isı adası etkisi, Hava sıcaklığı, Fotovoltaik enerji santrali, Meteorolojik istasyon, Rüzgar yönü, Rüzgar hızı

NOMENCLATURE

°C	degree Celsius
ΔT	Temperature Difference
ANOVA	One-Way Analysis of Variance
avg	Average
BLUHI	Boundary Layer Urban Heat Island
CLUHI	Canopy Layer Urban Heat Island
HSD	Honest Significant Difference
m/s	meter/second
NE	North East
P	Hourly Average PVPP Power Output
PV	Photovoltaic
PVHI	Photovoltaic Heat Island
PVHIE	Photovoltaic Heat Island Effect
PVPP	Photovoltaic Power Plant
T_m	Module Temperature
T_{m_avg}	Hourly Average Module Temperature
T_{amb_avg}	Hourly Average Ambient Temperature
UHI	Urban Heat Island
UHIE	Urban Heat Island Effect
W/m^2	Watt/square-meter
WS_i	i^{th} number Weather Station ($i=1,2,3$)
WS_{Ti}	Temperature measured/recorded by i^{th} number weather station
WS_{Ti_avg}	Hourly Average temperature measured/recorded by i^{th} number weather station
WS_{WDi}	Wind Direction measured/recorded by i^{th} number weather station
WS_{wsi}	Wind Speed measured/recorded by i^{th} number weather station

INTRODUCTION

Large-scale use of rural land areas requires utility-scale solar energy systems referring to the immense power plants based on Solar Photovoltaic and Concentrated Solar technologies. While the recent R&D efforts improve the efficiency of cells, modules, and other solar energy devices, and solar electricity becomes more affordable, the construction of these plants is also expanded over cultivated/uncultivated or vacant lands. In this expansion process, the influence of microclimatic factors and determining the optimal installation sites should also be considered (e.g., for the "agrivoltaic systems" which meet the energy demand of agricultural production (Adeh et al., 2018; Adeh et al., 2019; Chamara and Beneragama, 2020; Mokarram et al., 2020). Nevertheless, the alteration of PVPP installations in land use brings an environmental problem into the agenda regarding the energy transfer between those land surfaces and the overlying atmosphere. Because of the changes in the balance between the incoming (shortwave) solar and outgoing

(longwave) terrestrial radiation, a possible HIE can be observable in the regions enclosing a solar photovoltaic power plant site.

HIE is usually defined with prefixes, which specify the type/source of the effect, and the most discussed one is Urban Heat Island Effect (UHIE). Including some researches for different world cities and analysis/modeling methods, UHIs have generally been studied according to the artificially-induced air temperature rises caused by the high-density buildings and low-density green spaces, lack of trees and ponds, vehicle traffic and roads, GHG emissions, etc. of metropolitan areas. Deilami et al. (2018) presented a comprehensive systematic review of UHIE methodology and Spatio-temporal factors. Spatial variability is found in Hardin et al. (2018)'s research: The daytime and nighttime temperatures were monitored for four U.S. cities by utilizing weather stations to understand the UHI intensity and regional air temperature variability under the local weather conditions.

Some UHI-related modeling studies are introduced by Dorer et al. (2013); Mirzaei (2015); Xu. et al. (2017). Dorer et al. (2013) examined UHI according to heat exchange and building energy demand depending on urban microclimate and urban fabric design, including city building geometries and street canyons. Mirzaei (2015) categorized 33 UHI studies by considering their purpose, location, methodology, and significant finding. Xu. et al. (2017) simulated high-rise buildings with stack-effect of split-type air-conditioners and the solar radiation-induced thermal environment around these buildings. Dwivedi and Khire (2014) compile UHI measurement methods and techniques in their work.

In the literature, there is also a variety of location-based UHI analyses made, such as for Ankara (Turkey) by Yuksel and Yilmaz (2008); for Istanbul (Turkey) by Kuscu and Sengezer (2012); for Cyprus by Hadjimitsis et al. (2013); for Chicago (U.S.) by Coseo and Larsen (2014); for Adana (Turkey) by Yilmaz (2015); for Nagpur (India) by Kotharkar and Surawar (2016); for Konya (Turkey) by Canan (2017); for Kendari City (Indonesia) by Aris et al. (2019). In these studies, different methodologies were utilized to understand the formation type, intensity, sources, and factors of daily/seasonal urban heat island effect, such as Landsat satellite images, land surface temperature analysis, meteorological weather stations traverse surveying, etc. The high absorptance and low reflectance of incoming solar radiation on the urban fabric during daytime are followed by the high thermal emittance (longwave InfraRed (IR) radiation) of extra heat during nighttime. Thus, daily UHIE (plus seasonally influenced) cycles can be detectable. Table 1 shows the basic features of

the main UHI formations, Atmospheric and Surface. Here, it is essential to note that the atmospheric UHI observations are made for the canopy (CLUHI) and boundary (BLUHI) layers of the atmosphere. At the same time, Surface UHI (SUHI) is linked to the surface temperature changes along with the urban fabric.

Table 1. Essential Features of UHI formations. (US EPA (2014); Dwivedi and Khire (2014); Voogt (2008))

Feature	Surface UHI	Atmospheric UHI
Time of day and season	Presence: All times of the day and night Intensity: During the day and in the summer	Presence: Small or absent during the day Intensity: At night, before dawn, and in the winter
Temperature Variation	Day: 10 – 15 °C Night: 5 – 10 °C	Day: -1 – 3 °C Night: 7 – 12 °C
Identification method / instrument	Remote Sensing (3D, 2D, ground): • Satellites • Aircrafts • Some ground systems	Fixed weather monitoring stations: • Ground-mounted versions for CLUHI • Tower-mounted versions for BLUHI Mobile traverses: • Automobiles for CLUHI • Aircraft for BLUHI Vertical sensing: • SODAR (Sonic Detection and Ranging) for BLUHI Tethered balloons for BLUHI
Depiction	Thermal imaging	Isotherm mapping, Temperature graphs

As a similar and ensuing issue with fewer studies, PVHIE has been discussed in the literature for the last ten years. Nemet (2009) presents a substitution effect between fossil fuels and the two PV installation scenarios in terms of albedo change and radiative forcing. Turney and Fthenakis (2011) and Hernandez et al. (2014) give a place for this drawback of land use within their articles concerning the environmental impacts of utility-scale solar energy. Armstrong et al. (2014), Barron-Gafford et al. (2016), and Barron-Gafford et al. (2019) demonstrated the ground-vegetation-air energy fluxes before- and after the mounting of a PV module. A few studies associate their field data and simulation/modeling works with PVHIE positively and negatively (Millstein and Menon, 2011; Fthenakis and Yu, 2013; Masson et al., 2014). As shown in Figure 1, heat release from a PV module surface depends on three physical processes: Radiation,

convection, and conduction. These processes are linked to several structural module properties such as solar cells' efficiency (commercially % 10-25 in general) and their packing density, electrical operating point, module heat capacity, and anti-reflective coatings (ARCs) as well.

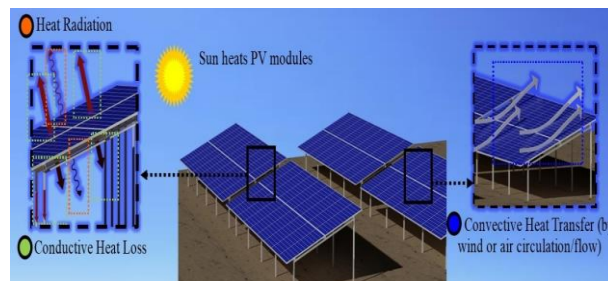


Figure 1. Heat Release Processes between PV Module Arrays and Surrounding Air (Demirezen et al., 2022)

In addition to the PVHIE researches above, some studies on thermal modeling (Lobera and Valkealahti, 2013; Siddiqui and Arif, 2013; Tuncel et al., 2018), degradation and reliability (Saadsaoud et al., 2017; Ozden and Akinoglu, 2018), and shading effect (Kiris et al., 2016) analyze PV module temperature and efficiency/performance according to weather/climatic and environmental conditions.

To make the contributions listed below to the previous PVHIE-related studies, it has been conducting the research projects of this field study since October 2017 for a photovoltaic power plant near the Sekbandemirli Village and Rural Region in the Kutahya city of Turkey:

- The first field study of Turkey related to this issue
- A comprehensive PVHIE analysis made by the combination of different methods/techniques (statistical, graphical, and correlational)
- Daily and seasonal assessments made thanks to 2-year field data-collection
- A simulation-based analysis planned for the next stage of the study by using a microclimate and heat island simulation software, ENVI-met
- A beneficial resource for the academicians, researchers, policy-makers, and stakeholders working on PVPP projects

FIELD STUDY AND METHODOLOGY

Sekbandemirli Village (39.52°N; 29.34°E) is a rural settlement area 16 km away from Tavsanli, one of the Kutahya city's districts in Turkey. As a geographic transition location between Turkey's three regions, its seasonal weather conditions are under Central Anatolia, Aegean, and Marmara climates. Sekbandemirli has mostly mild average temperatures and wind speeds from the category "calm" to "moderate

breeze" (Beaufort scale) throughout the year. The village is surrounded by grasslands and shrublands partly met some steppe fields.

In 2017, Sekbandemirli PVPP (2.5 MW) was constructed on an adjacent uncultivated area (44000 m²) of the village with the installations of mono-crystalline and poly-crystalline solar modules having the conversion efficiencies of 18.4 % and 16.6 %, respectively (Figure 3). The front edge of the PVPP's module arrays is 0.5 m above ground, whereas this height is 1.9 m for their rear edge. The solar module tilt angle is 20°.

There are two web interfaces used to monitor the study's field data: The first one, PlantMet (<http://web.plantmet.com.tr>), is an agricultural and meteorological data monitoring system for the measurements of the weather stations WS₁ and WS₂ (every 10-minute and hourly intervals). The second one, SunnyPortal (www.sunnyportal.com), is to track WS₃ (hourly intervals), the PVPP's power output, and the module temperature. Both numerical values and graphical demonstrations can be viewed for the selected dates or date intervals on these interfaces. The methodology diagram of the study is given in Figure 2.

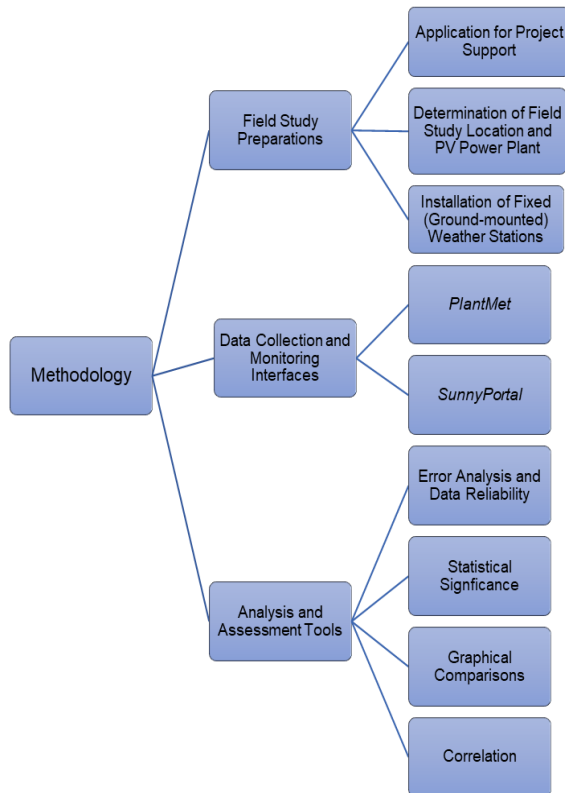
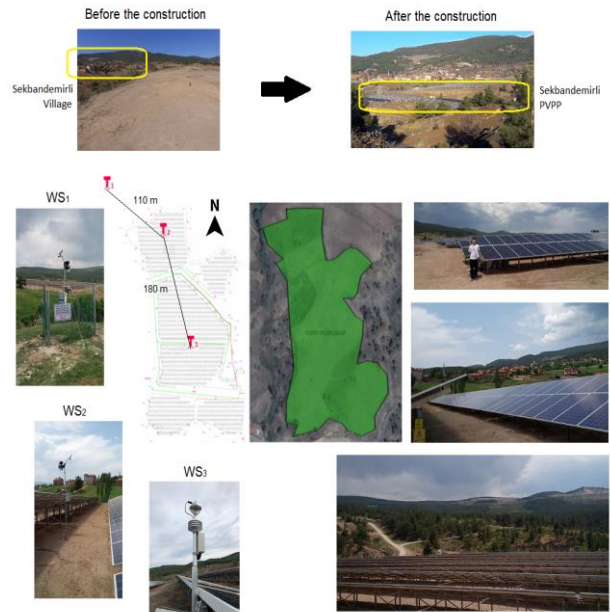


Figure 2. Methodology Diagram of the Study

In summary, the PVHI formations in the Canopy Layer were observed in the PVPP field and its close surroundings, and it was planned to use "fixed (ground-mounted) weather monitoring stations" for those

observations. The brand/model and features of these weather stations used are given in the following subsection. In addition, the interfaces where both the meteorological data collected via these weather stations and the PV module temperature and PVPP electrical power output data collected from the PVPP field are monitored on the web will be explained.



(a)



(b)

Figure 3. Site Plan (a) and Google Earth View (b) of the Sekbandemirli rural region and PVPP (Red drawings (a) and yellow-colored coordinates (b) show the weather station (WS) locations)

DATA COLLECTION AND MONITORING

The analysis methods, correlation results, and graphical comparisons of 24-month data collected from November 2018 to October 2020 via the three weather stations (WS_{1,2,3}) are explained in the following

sections. This 24-month data includes the main parameters below for PVHIE observation:

- hourly average (hourly averages are calculated from the 10-minute averages between the hours XX:00 – XX:50) air temperature (°C; from outside to the center of the PVPP field as WS_{T1,T2,T3} at 2 m above ground)
- photovoltaic module surface temperature (°C; T_{m_avg})
- average wind speed (m/s; WS_{WS1,WS2} at 2.5 m above ground; WS₃ doesn't have wind speed sensor)
- wind direction (degrees; WS_{WD1,WD2} at 2.5 m above ground; WS₃ doesn't have wind direction sensor)

The weather measurements below are also collected as supportive data:

- incoming solar radiation (W/m²; WS₁, WS₂, WS₃)
- relative humidity (%; WS_{RH1}, WS_{RH2}; WS₃ doesn't have relative humidity sensor)
- rainfall amount (mm; WS_{RA1}, WS_{RA2}; WS₃ doesn't have rainfall amount sensor)
- rainfall speed (mm/h; WS_{RS1}, WS_{RS2}; WS₃ doesn't have rainfall speed sensor)
- barometric pressure (mbar; WS_{BP1}, WS_{BP2}; WS₃ doesn't have barometric pressure sensor)

Each weather data specified above is grouped as the monthly data sets. Microsoft Office Excel 2019 and its Data Analysis ToolPak were used for the data filtering, the calculations of the results given in the next section, and chart illustrations.

Because WS₃ doesn't have a solar radiation sensor, WS₂'s incoming solar radiation measurements are required to separate the daytime and nighttime measurements from the daily data inside the PVPP field:

- a daytime value when "not zero"
- a nighttime value when "zero"

The statistical and graphical comparisons, correlation results, and further work will be explained in the following sections.

RESULTS

Error Analysis and Data Reliability

The sensor accuracy of weather station measurements (from their technical specification documents) and the confidence intervals calculated from the error analysis of each weather parameter's cumulative data are given in Table 2 (the Microsoft Excel 2019 functions used to calculate the numerical results on the table are specified for each category).

If the confidence level is smaller than sensor accuracy or equals it, this contributes to the usability of the relevant parameter measurements as reliable data. It should also be considered that the weather stations had sometimes failed to send field data (null values) due to some technical problems. As shown in Table 2, the confidence intervals of all the weather parameters are smaller than the accuracy of the WS sensors taking measurements. So, the data reliability is ensured for all the parameters.

Table 2. Confidence Intervals and Sensor Accuracy

	WS _{T1}	WS _{T2}	WS _{T3}	T _{m_avg}	WS _{WS1}	WS _{WS2}	WS _{WD1}	WS _{WD2}
Standard Deviation ^a	8.4	8.5	9.5	14.1	1.1	1.1	98.2	90.8
Standard Error ^b	0.1	0.1	0.1	0.1	0.0	0.0	0.6	0.6
Tcrit ^c	2.0	2.0	2.0	2.0	2.0	2.0	2.0	2.0
Confidence Interval (% 95) ^d	± 0.1°C	± 0.1°C	± 0.2°C	± 0.2°C	0.0 m/s	0.0 m/s	± 1.2°	± 1.1°
Sensor Accuracy ^e	± 0.3°C	± 0.3°C	± 0.3°C	± 0.3°C	± 0.9 m/s	± 0.9 m/s	± 3°	± 3°

a: SUBTOTAL (STDEV.P; Summation of the hourly averages of all the 24 month-data)

b: Standard Deviation / (SQRT (SUBTOTAL (COUNT; Summation of the hourly averages of all the 24 month-data)))

c: TINV(0,05; (SUBTOTAL (COUNT; Summation of the hourly averages of all the 24 month-data) - 1))

d: Tcrit * Standard Error

e: Technical specification documents of the weather stations:

- WS1 and WS2: Davis / Vantage Pro2™
- WS3: PV-met / 150
- PV module temperature sensor connected to WS3: PV-met / A2101

Statistical Significance between Weather Stations

In the first publication of the study (Demirezen et al., 2018), two statistical methods were used to compare the first 8-month (10-minute intervals) data sets of WS₁ and WS₂. The first one, One-Way Analysis of Variance (ANOVA), shows if there are statistically significant differences between the means of three or more independent groups (here, weather stations) or not. Following the results of One-Way ANOVA, the second method is a Post Hoc Test named Tukey's Honest Significant Difference (HSD) particularly shows which of these groups differ from each other. The nearby Tavsanlı WS's data from the Turkish State Meteorological Service (<https://www.mgm.gov.tr>) was provided to meet the requirement of a third WS to perform these methods. Among four weather parameters (air temperature, relative humidity, barometric pressure, and wind speed), the only insignificance between WS₁ and WS₂ was found for air temperature. That is to say; any distinct PVHI formations had not been observed yet around the location of the Sekbandemirli PVPP field surrounding WS₁ or WS₂ (Figure 4).

After the WS₃'s installation, both these methods were applied to make the comparisons again, and this time, the 24-month (hourly intervals) data sets of three WSs were used. Firstly, the ANOVA results are given in

Table 3. The measurements of three WSs differ significantly on air temperature concerning the two conditions of ANOVA:

$$p\text{-value} = 0.00 < \alpha = 0.05 \text{ (Significance level)} \quad (1)$$

$$F\text{-value} = 47.20 > F_{\text{critical}} = 3.00$$

Table 3. One-Way ANOVA Results

Groups	Data Count	Sum	Average (avg)	Variance
WS ₁	16524	221030.80	13.4	76.89
WS ₂	16899	223615.85	13.2	78.08
WS ₃	14210	201377.55	14.2	90.60

Source of Variation	Sum of Squares (S.S.)	Degrees of Freedom (df)	Mean Square (M.S.)	F-value	Fcritical	p-value
Between Groups	7683.87	2	3841.93	47.20	3.00	0.00
Within Groups	3877165.28	47630	81.40			
Total	3884849.14	47632				

The parameters below are used to find the HSD value (Equation (3)) and which of the weather stations differ from each other by Tukey's HSD test:

- MS_{within} (from Table 3);
- n (data number for the station having fewer measurements than the other two from Table 3);
- q (from Table 4) values

Table 4. Q Scores for Tukey's Method

(k: number of independent groups; df (within): degrees of freedom; α : significance level (0,05))

k	2	3	4	5	6	7	8	9	10
1	18.0	27.0	32.8	37.1	40.4	43.1	45.4	47.4	49.1
2	6.08	8.33	9.80	10.88	11.73	12.43	13.03	13.54	13.99
3	4.50	5.91	6.82	7.50	8.04	8.48	8.85	9.18	9.46
4	3.93	5.04	5.76	6.29	6.71	7.05	7.35	7.60	7.83
5	3.64	4.60	5.22	5.67	6.03	6.33	6.58	6.80	6.99
6	3.46	4.34	4.90	5.30	5.63	5.90	6.12	6.32	6.49
7	3.34	4.16	4.68	5.06	5.36	5.61	5.82	6.00	6.16
8	3.26	4.04	4.53	4.89	5.17	5.40	5.60	5.77	5.92
9	3.20	3.95	4.41	4.76	5.02	5.24	5.43	5.59	5.74
10	3.15	3.88	4.33	4.65	4.91	5.12	5.30	5.46	5.60
11	3.11	3.82	4.26	4.57	4.82	5.03	5.20	5.35	5.49
12	3.08	3.77	4.20	4.51	4.75	4.95	5.12	5.27	5.39
13	3.06	3.73	4.15	4.45	4.69	4.88	5.05	5.19	5.32
14	3.03	3.70	4.11	4.41	4.64	4.83	4.99	5.13	5.25
15	3.01	3.67	4.08	4.37	4.59	4.78	4.94	5.08	5.20
16	3.00	3.65	4.05	4.33	4.56	4.74	4.90	5.03	5.15
17	2.98	3.63	4.02	4.30	4.52	4.70	4.86	4.99	5.11
18	2.97	3.61	4.00	4.28	4.49	4.67	4.82	4.96	5.07
19	2.96	3.59	3.98	4.25	4.47	4.65	4.79	4.92	5.04
20	2.95	3.58	3.96	4.23	4.45	4.62	4.77	4.90	5.01
24	2.92	3.53	3.90	4.17	4.37	4.54	4.68	4.81	4.92
30	2.89	3.49	3.85	4.10	4.30	4.46	4.60	4.72	4.82
40	2.86	3.44	3.79	4.04	4.23	4.39	4.52	4.63	4.73
60	2.83	3.40	3.74	3.98	4.16	4.31	4.44	4.55	4.65
120	2.80	3.36	3.68	3.92	4.10	4.24	4.36	4.47	4.56
∞	2.77	3.31	3.63	3.86	4.03	4.17	4.29	4.39	4.47

If the differences (absolute values) between the averages (Table 3) are bigger than the HSD value, the air temperature measurements of those two weather stations are significantly different from each other. As a result of the comparisons in the equations (4,5,6), the PVPP field's center might be a possible PVHIE source.

$$HSD = q \sqrt{(MS_{\text{within}}/n)} = 3.31 \sqrt{(81,40/14210)} = 0.3 \quad (3)$$

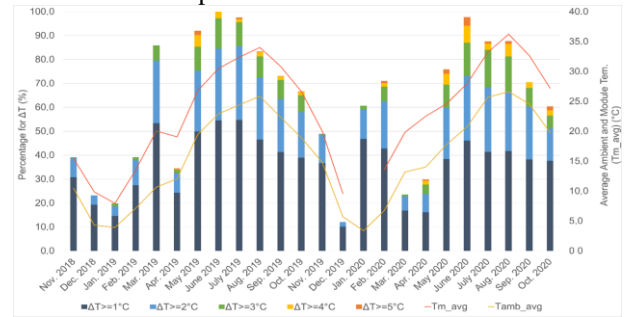
$$WS_{T2_avg} - WS_{T1_avg} = 0.2 < 0.3 \text{ (Not signif. diff.)} \quad (4)$$

$$WS_{T1_avg} - WS_{T3_avg} = 0.8 > 0.3 \text{ (Signif. different)} \quad (5)$$

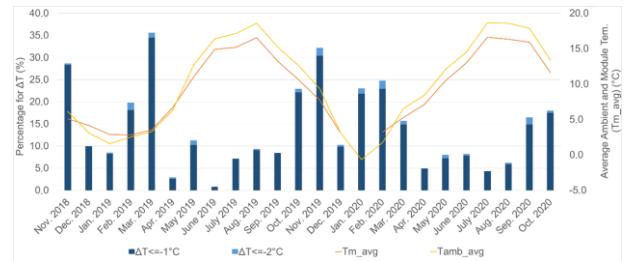
$$WS_{T2_avg} - WS_{T3_avg} = 0.9 > 0.3 \text{ (Signif. different)} \quad (6)$$

Graphical Comparisons

In the previous section, the occurrence of some temporal PVHIs caused by the PVPP is inferred regarding the WS₃'s data and statistical analyses. This inference is supported by the graphical comparisons of daytime (Figure 4a) and nighttime (Figure 4b) air temperature differences with quantitative data presented below. Among all the 24-month collected data, ΔT percentages correspond to the distribution of ΔT values bigger than 1°C or smaller than -1°C. The T_{m_avg} (hourly average module temperature) and T_{amb_avg} (hourly average air (ambient) temperature) curves were added to the comparisons.



(a)



(b)

Figure 4. Monthly ΔT Percentages for Daytimes (a) and Nighttimes (b) with T_{m_avg} and T_{amb_avg} curves

In the daytimes of each of the 24 months, PVHIE can be more or less observable at the PVPP field center, where up to 6°C higher air temperatures were found in Figure 4a. The T_{m_avg} and T_{amb_avg} curves also have a strong relationship with the PVHI formations. Because the T_{m_avg} curve always shows a trendline in the upper position of the T_{amb_avg} curve along the 24 months, the heat exchange (Figure 1) from the solar modules to the overlying atmosphere causes these daytime seasonal positive formations, and they can be observable. Besides, a negative but less effective PVHIE with up to 3°C air temperature differences ($WS_{T1} > WS_{T3}$) is more prominent in autumn and winter nights and less detectable in spring and summer nights (Figure 4b) due to the cooling process of the PV modules. Although the T_{m_avg} curve is above the T_{amb_avg} curve along all the seasons except winter, a distinct relation can't be

defined for the nighttime exchanges between each other and this negative PVHIE. The trend curves of monthly maximum daytime (Figure 5a) and minimum nighttime (Figure 5b) air temperatures measured by the WSs support the daily and seasonal PVHIE findings above.

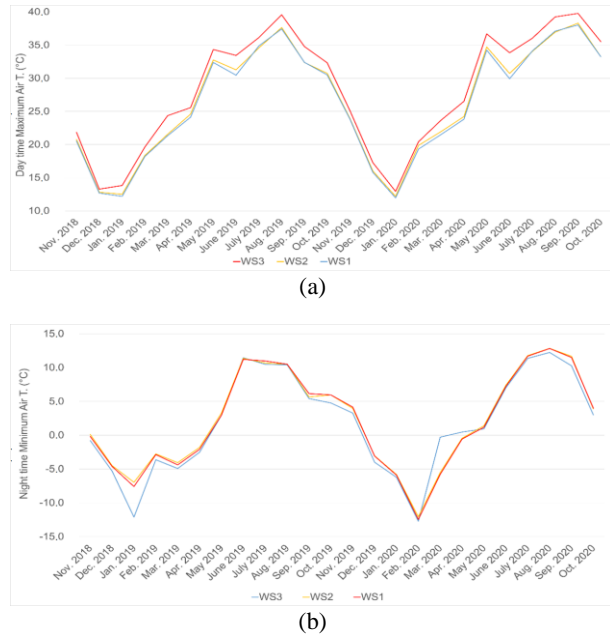


Figure 5. Monthly Daytime Maximum (a) and Nighttime Minimum (b) Air Temperature Changes

A graphical illustration of the Sekbandemirli rural region and the measured air temperatures on weather station locations for a day hour of November 2019 and a night hour of August 2019 are given in Figure 6. a PVHI occurrence can be understood towards the field center on November 24 at noon (Figure 6a). An inverse effect resulting in a colder PVPP field center on August 13 at 02:00 is illustrated, too (Figure 6b).

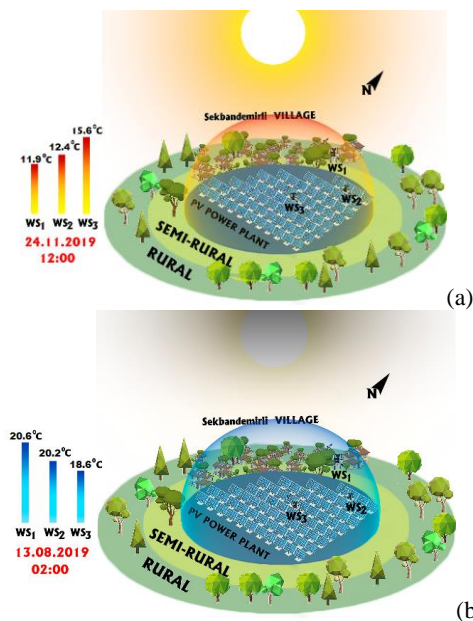


Figure 6. PVHI occurrences on a 2019 November day (a) and a 2019 August night (b) in Sekbandemirli Region

Correlation Results

Table 5. Pearson (a) and Spearman (b) Correlation Results for $\Delta T-T_{m_avg}$ and $\Delta T-P$ (closer to +1, the stronger positive linear relationship; closer to -1, the stronger negative linear relationship) (The correlation coefficients couldn't be given for Jan. 2020 due to a technical problem for the T_{m_avg} data records)

	$\Delta T-T_{m_avg}$		$\Delta T-P$		$\Delta T-T_{m_avg}$		$\Delta T-P$
	Day	Night	Day		Day	Night	Day
Nov. 2018	0.82	0.11	0.88	Nov. 2019	0.81	-0.11	0.88
Dec. 2018	0.79	-0.04	0.86	Dec. 2019	0.64	-0.04	0.67
Jan. 2019	0.67	0.21	0.62	Jan. 2020	n/a	n/a	0.76
Feb. 2019	0.67	-0.17	0.70	Feb. 2020	0.56	0.21	0.50
March 2019	0.72	0.03	0.69	March 2020	0.75	-0.28	0.79
April 2019	0.48	0.37	0.31	April 2020	0.58	0.59	0.38
May 2019	0.52	0.44	0.34	May 2020	0.49	0.40	0.31
June 2019	0.61	0.54	0.40	June 2020	0.55	0.69	0.33
July 2019	0.55	0.71	0.35	July 2020	0.51	0.70	0.25
Aug. 2019	0.55	0.65	0.32	Aug. 2020	0.51	0.83	0.24
Sept. 2019	0.58	0.68	0.31	Sept. 2020	0.54	0.71	0.32
Oct. 2019	0.57	0.63	0.33	Oct. 2020	0.53	0.57	0.32

(a)

	$\Delta T-T_{m_avg}$		$\Delta T-P$		$\Delta T-T_{m_avg}$		$\Delta T-P$
	Day	Night	Day		Day	Night	Day
Nov. 2018	0.78	0.10	0.91	Nov. 2019	0.82	-0.06	0.91
Dec. 2018	0.73	-0.05	0.86	Dec. 2019	0.70	0.07	0.81
Jan. 2019	0.49	0.13	0.65	Jan. 2020	n/a	n/a	0.78
Feb. 2019	0.69	-0.24	0.76	Feb. 2020	0.52	0.14	0.50
March 2019	0.74	0.07	0.72	March 2020	0.76	-0.29	0.85
April 2019	0.60	0.13	0.46	April 2020	0.66	0.52	0.47
May 2019	0.61	0.36	0.44	May 2020	0.59	0.25	0.47
June 2019	0.65	0.41	0.49	June 2020	0.64	0.56	0.47
July 2019	0.54	0.60	0.38	July 2020	0.52	0.63	0.27
Aug. 2019	0.51	0.58	0.31	Aug. 2020	0.48	0.73	0.24
Sept. 2019	0.57	0.62	0.34	Sept. 2020	0.54	0.62	0.37
Oct. 2019	0.58	0.61	0.38	Oct. 2020	0.58	0.41	0.47

(b)

In terms of linear (Table 5a) and monotonic (Table 5b) relation strength between the air temperature difference ΔT ($WS_{T3}-WS_{T1}$), hourly average PVPP power output (P), and hourly average module temperature (T_{m_avg}); Pearson and Spearman correlation coefficients were calculated for daytimes and nighttimes between November 2018 and October 2020. Here, ΔT is introduced as the primary indicator of a PVHI.

Local Winds and PVHIE

Utilizing the 10-minute average wind speed and direction data of WS₂'s measurements from October 2017 to August 2020, the wind roses for the Sekbandemirli PVPP field were depicted in Figure 7a, considering the maximum speed (up to 8 m/s) and prevailing speed intervals (0-2 and 2-8 m/s) of the region's local winds. They show that the prevailing winds over the PVPP field blow from the North-East (NE) between the speed intervals as follows (according to the Beaufort scale): 0-2 m/s: from "calm air" to "light breeze", 2-8 m/s: from "light breeze" to "moderate breeze".

To understand if these prevailing winds interact with the PVPP's South-facing modules (Figure 7b) and alter the daytime positive PVHIE trend, Figure 8 shows the daytime ΔT results associated with the daytime wind direction data (24-month), and the correlation coefficients between the hourly average wind speed measurements and ΔT are given in Table 6.

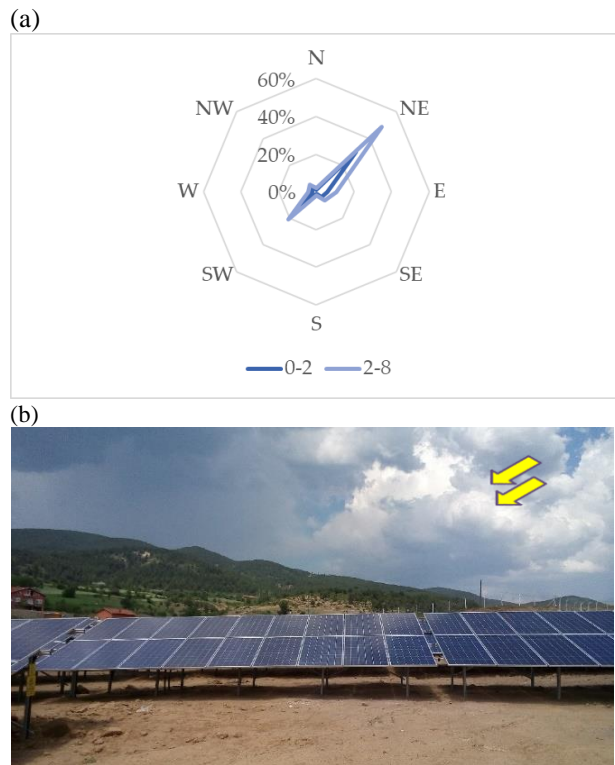


Figure 7. Sekbandemirli Region's Wind Rose (a) and Sekbandemirli PVPP's South-Facing Solar Modules (b) (Yellow arrows show the prevailing wind direction as NE)

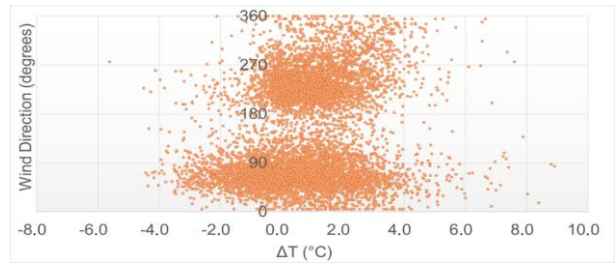


Figure 8. ΔT associated with Wind Direction data (24-month)

Table 6. Pearson (a) and Spearman (b) Correlation Results for ΔT - Hourly Average Wind Speed (closer to +1, the stronger positive linear relationship; closer to -1, the stronger negative linear relationship) (The correlation coefficients couldn't be given for Jan. 2020 due to a technical problem for the T_{m_avg} data records)

	ΔT -WS ₂ -HAWs		ΔT -WS ₂ -HAWs	
	Day		Day	
Nov. 2018	0.03	Nov. 2019	0.02	
Dec. 2018	0.06	Dec. 2019	-0.18	
Jan. 2019	0.12	Jan. 2020	0.13	
Feb. 2019	-0.06	Feb. 2020	-0.09	
Mar. 2019	-0.04	Mar. 2020	-0.10	
April 2019	0.29	April 2020	0.03	
May 2019	0.12	May 2020	0.00	
June 2019	0.37	June 2020	0.21	
July 2019	0.34	July 2020	0.22	
Aug. 2019	0.27	Aug. 2020	0.25	
Sept. 2019	0.12	Sept. 2020	0.25	
Oct. 2019	-0.18	Oct. 2020	-0.09	

(a)

	ΔT -WS ₂ -HAWs		ΔT -WS ₂ -HAWs	
	Day		Day	
Nov. 2018	0.09	Nov. 2019	0.03	
Dec. 2018	0.07	Dec. 2019	-0.21	
Jan. 2019	0.17	Jan. 2020	0.15	
Feb. 2019	0.00	Feb. 2020	-0.01	
Mar. 2019	-0.06	Mar. 2020	-0.08	
April 2019	0.35	April 2020	0.05	
May 2019	0.15	May 2020	0.02	
June 2019	0.41	June 2020	0.25	
July 2019	0.34	July 2020	0.18	
Aug. 2019	0.27	Aug. 2020	0.24	
Sept. 2019	0.09	Sept. 2020	0.27	
Oct. 2019	-0.16	Oct. 2020	-0.07	

(b)

DISCUSSION

As seen from the Sekbandemirli Site Plan (Figure 3), by comparing the northern sub-field (WS₂'s location) and the North-East part outside the PVPP field (WS₁'s location), the PV module arrays are denser at the center of the PVPP field center where WS₃ is installed. As a result, stronger heat dissipation and interaction between the PV modules and their close/surrounding environment might occur at the field center. Thus, significant air temperature differences between WS_{T3} and the other weather stations are detectable (see the "Statistical Significance between Weather Stations" section). Thus, the center of the PVPP field and the PV module arrays here might be a possible heat island source.

As given in the graphical comparisons of the study, the inferences from Figures 4a and 4b are made as follows:

- Figure 4a shows that the overall percentage of positive PVHI formation numbers at the field center gets higher during daytime in the summer months by varying between 0-3°C for 24 months (up to 6°C for some formation intensities). The term “positive” indicates that the PVPP field center is warmer than outside the field. The T_{amb_avg} and T_{m_avg} curves are directly proportional to the heights of the columns over 24 months. The PV module arrays warm faster than the air surrounding them, so the T_{m_avg} curve is at an upper position. When the distance between these curves increases in the summer months, the daytime positive PVHI formations are stronger. Figure 5a, the monthly daytime maximum air temperature changes measured by the weather stations, supports these findings when the WS curves are compared.

- As shown in Figure 4b, the overall percentage of negative PVHI formation numbers at the field center gets higher towards the autumn and winter months by varying between 0-3°C for 24 months. The term “negative” indicates that the PVPP field center is colder than outside the field. The T_{amb_avg} and T_{m_avg} curves are inversely proportional to the heights of the columns. The PV module arrays cool faster than the air surrounding them on spring and summer nights inferred from the figure; the T_{m_avg} curve is at a lower position. In the winter months, the air in the Sekbandemirli region cools faster than the PV module arrays. Therefore, T_{m_avg} is at an upper position during these months. In Figure 4b, there is not a significant relationship between the curves and PVHI formation intensity (percentage columns). As a supportive graph for Figure 4b, the monthly nighttime minimum air temperature changes measured by the weather stations are given in Figure 5b. WS_3 recorded mostly lower temperatures than WS_1 and WS_2 .

The study’s correlation results (Pearson and Spearman) are shown in Table 5a and 5b. During daytimes, the relation strength between ΔT (PVHI formation intensity) and T_{m_avg} tends to be getting weaker from autumn-winter to summer months, getting stronger from summer to winter months. ΔT and P also have similar correlations. Conversely, between these seasons, the ΔT - T_{m_avg} relation strength follows an inverse trend for nighttimes. Because of no electricity production during nighttimes, Table 5a and 5b do not include a nighttime ΔT - P correlation column.

In Figure 8, the PVHI formations are apparent with more data points when the wind blows from the directions between 0-90 and 180-270 degrees. Because the prevailing wind direction as NE (45 degrees) has many data points to indicate a PVHI occurrence in Figure 8, it can be concluded that their blowing angle is not convenient to reduce the positive PVHIE at the PVPP’s field center. These local, prevailing winds mostly blow towards the upper right corner of the PV

modules, not their surface, where a natural cooling effect can be provided). Although a slight increase in the correlation strength is observed during the summer months, the inconvenience explained above can also be mentioned by presenting the low or small correlation coefficients between the hourly average wind speed measurements and ΔT for most of the year (Table 6).

As for the third stage, it is planned to support the study with a microclimate and heat island simulation software, *ENVI-met* (<https://www.envi-met.com>) (Huttner, 2012; Ambrosini et al., 2014; Sodoudi et al., 2014), which provides a detailed simulation work/analysis by considering measured weather parameters and land cover change on a geographical location. Thus, this extra analysis will develop the current methodology and findings and contribute to the related studies on PVHIE.

CONCLUSIONS

The ground-based PVPP installations alter land surface albedo (reflectivity) due to their dark-colored solar PV modules (and their heat radiation while operating), and thus, Photovoltaic Heat Island (PVHI) formations might be observable as an atmospheric environmental impact. Although Urban Heat Island Effect is commonly and comprehensively studied in the literature, fewer studies investigate this effect caused by PVPPs. This paper presents our project’s two consecutive stages showing the progressive structure of its findings.

Following the error analysis for data reliability and the statistical analysis for measurement significance, 25-month data of the second stage show daily (day-night) PVHIs occurring at the PVPP’s center with up to 6°C higher air temperatures than the ones measured outside the PVPP field for daytimes. Some inverse (negative) but less-effective PV heat islands are also formed with up to 3°C higher air temperatures outside the field during nighttimes. Monthly maximum air temperatures for daytimes and monthly minimum air temperatures for nighttimes support these results. A graphical illustration of the Sekbandemirli rural region and the measured air temperatures on the weather station locations for a day hour of November 2019 and a night hour of August 2019 is also given in the Results section.

These PVHI formations have specific formation frequencies on a monthly (seasonal) basis. Although solar PV module temperature and power output can be mentioned as the essential determinants or indicators for PVHIE, their correlation weakens from winter to summer and strengthens from summer to winter for daytimes; and vice versa for nighttimes. Simultaneous monitoring of solar module and air (ambient) temperatures should be considered to understand the

PVHI formation mechanism by radiative and convective heat transfer (Figure 1). It should also be noted that the PV module types, which are commercially preferable for land/ground-based PVPP installations, have low heat capacity/high emissivity values taking a significant role in these formations.

As for geographical location choice and sunshine duration analysis, it is also important to investigate a PVPP field's local wind speed and direction before PV module placement and orientation. Wind has capable of reducing HIE by natural convective cooling. On the other hand, having the prevailing wind direction (North-East), the Sekbandemirli PVPP field can't benefit from the region's local winds: They blow onto the solar modules from an inconvenient angle, and thus, they can't cool them during daytimes. Another supportive finding for this inference is that there is a low or no correlation between wind speed and PVHI formation almost all year round.

ACKNOWLEDGMENTS

The authors would like to thank Middle East Technical University for financial supports (Project Numbers: BAP-07-02-2017-006 & TEZ-D-105-2020-10169) in the implementation of the study's research projects; Mr. Tolga Eryasar and Mr. Oguz Aydin for their technical assistance; Mr. Ahmet Hamdi Aksoy and Mr. Hakan Akinoglu for their contributions to the study's illustrations.

REFERENCES

Ambrosini, D., Galli, G., Mancini, B., Nardi, I., Sfarra, S., 2014, Evaluating Mitigation Effects of Urban Heat Islands in a Historical Small Center with the ENVI-Met® Climate Model. *Sustainability*, 6(10), 7013-7029, doi: 10.3390/su6107013

Aris, A., Syaf, H., Yusuf, D. N., Nurgiantoro, 2019, Analysis of urban heat island intensity using multi temporal landsat data; case study of Kendari City, Indonesia, Paper presented at *Geomatics International Conference 2019*, Surabaya, Indonesia

Armstrong, A., Waldron, S., Whitaker, J., Ostle, N., 2014, Wind farm and solar park effects on plant-soil carbon cycling: Uncertain impacts of changes in ground-level microclimate, *Global Change Biology*, 20(6), 1699-1706. doi: 10.1111/gcb.12437

Barron-Gafford, G. A., Minor, R. L., Allen, N. A., Cronin, A. D., Brooks, A. E., Pavao-Zuckerman, M. A., 2016, The Photovoltaic Heat Island Effect: Larger solar power plants increase local temperatures, *Scientific Reports*, 6(1), doi: 10.1038/srep35070

Barron-Gafford, G. A., Pavao-Zuckerman, M.A., Minor, R.L. et al., 2019, Agrivoltaics provide mutual benefits across the food–energy–water nexus in drylands, *Nat Sustain* 2, 2, 848–855, doi: 10.1038/s41893-019-0364-5

Canan, F., 2017, Kent Geometrisine Bağlı Olarak Kentsel Isı Adası Etkisinin Belirlenmesi: Konya Örneği, *Journal of the Faculty of Engineering and Architecture (Çukurova University)*, 32(3), 69-80, doi: 10.21605/cukurovaummfd.357202

Chamara, R., Beneragama, C., 2020, Agrivoltaic systems and its potential to optimize agricultural land use for energy production in Sri Lanka: A Review, *Journal of Solar Energy Research (JSER)*, 5(2), 417-431, doi: 10.22059/JSER.2020.302720.1154

Coseo, P., Larsen, L., 2014, How factors of land use/land cover, building configuration, and adjacent heat sources and sinks explain Urban Heat Islands in Chicago, *Landscape and Urban Planning*, 125, 117–129, doi: 10.1016/j.landurbplan.2014.02.019

Deilami, K., Kamruzzaman, Md., Liu, Y., 2018, Urban heat island effect: A systematic review of spatio-temporal factors, data, methods, and mitigation measures, *International Journal of Applied Earth Observation and Geoinformation*, 67, 30–42, doi: 10.1016/j.jag.2017.12.009

Demirezen, E., 2022, Monitoring, Analysis, and Simulation of Photovoltaic Heat Island Effect in Turkey: Sekbandemirli Solar Power Plant Field Study, (Doctoral dissertation), Turkey: *Middle East Technical University*.

Demirezen, E., Ozden, T., Akinoglu, B. G. (2018). Impacts of a Photovoltaic Power Plant for Possible Heat Island Effect Paper presented at the *1st International Conference on Photovoltaic Science and Technologies (PVCon2018)*, Ankara, Turkey. doi: 10.1109/PVCon.2018.8523937

Dorer, V., Allegrini, J., Orehounig, K., Moonen, P., Upadhyay, G., Kämpf, J., Carmeliet, J., 2013, Modelling the Urban Microclimate and Its Impact on the Energy Demand of Buildings and Building Clusters Paper presented at *13th Conference of International Building Performance Simulation Association*, Chambéry, France.

Duman, U., Yilmaz, O., 2008, Ankara Kentinde Kentsel Isı Adası Etkisinin Yaz Aylarında Uzaktan Algılama ve Meteorolojik Gözlemlere Dayalı Olarak Saptanması ve Değerlendirilmesi, *Journal of the Faculty of Engineering and Architecture of Gazi University*, 23(4), 937-952.

- Dwivedi, A., Khire, M. V., 2014, Measurement Technologies for Urban Heat Islands, *International Journal of Emerging Technology and Advanced Engineering*, 4(10), 539-545.
- Fthenakis, V., Yu, Y., 2013, Analysis of the potential for a heat island effect in large solar farms Paper presented at *IEEE 39th Photovoltaic Specialists Conference (PVSC)*, Florida, US.
doi: 10.1109/PVSC.2013.6745171
- Gokmen, N., Hu, W., Hou, P., Chen, Z., Sera, D., Spataru, S., 2016, Investigation of wind speed cooling effect on PV panels in windy locations, *Renewable Energy*, 90, 283-290, doi: 10.1016/j.renene.2016.01.017
- Hadjimitsis, D., Retalis, A., Michaelides, S., Tymvios, F., Paronis, D., Themistocleous, K., Agapiou, A., 2013, Satellite and Ground Measurements for Studying the Urban Heat Island Effect in Cyprus, *Remote Sensing of Environment - Integrated Approaches*, (pp. 1-24), Cyprus: IntechOpen. doi.org/10.5772/39313
- Hardin, A.W., Liu, Y., Cao, G., Vanos, J. K., 2018, Urban heat island intensity and spatial variability by synoptic weather type in the northeast U.S., *Urban Climate*, 24, 747-762, doi: 10.1016/j.uclim.2017.09.001
- Hassanpour Adeg, E., Selker, J., Higgins, C., 2018, Remarkable agrivoltaic influence on soil moisture, micrometeorology and water-use efficiency, *PLOS ONE*, 13(11), doi: 10.1371/journal.pone.0203256
- Hassanpour Adeg, E., Good, S., Calaf, M., Higgins, C., 2019, Solar PV Power Potential is Greatest Over Croplands, *Scientific Reports*, 9(11442), doi: 10.1038/s41598-019-47803-3
- Hernandez, R. R., Easter, S. B., Murphy-Mariscal, M. L., Maestre, F. T., Tavassoli, M., Allen, E. B., Barrows, C. W., Belnap, J., Ochoa-Hueso, R., Ravi, S., Allen, M. F., 2014, Environmental impacts of utility-scale solar energy, *Renewable and Sustainable Energy Reviews*, 29, 766-779, doi: 10.1016/j.rser.2013.08.041
- Homadi, A., 2016, Effect of Elevation and Wind Direction on Silicon Solar Panel Efficiency, *International Journal of Energy and Power Engineering*, 10, 1205-1212.
- Huttner, S., 2012, Further development and application of the 3D microclimate simulation ENVI-met, (Doctoral dissertation), Germany: *Johannes Gutenberg University of Mainz*.
- Kiris, B., Bingol, O., Senol, R., Altintas, A., 2016, Solar Array System Layout Optimization for Reducing Partial Shading Effect, *Special Issue of the 2nd International Conference on Computational and Experimental Science and Engineering (ICCESEN 2015)*, *Acta Physica Polonica A*, 130, doi: 10.12693/APhysPolA.130.55
- Kotharkar, R., Surawar, M., 2016, Land Use, Land Cover, and Population Density Impact on the Formation of Canopy Urban Heat Islands through Traverse Survey in the Nagpur Urban Area, *Journal of Urban Planning and Development*, 142(1), 1-13, doi: 10.1061/(ASCE)UP.1943-5444.0000277
- Lobera, D. T., Valkealahti, S., 2013, Dynamic thermal model of solar PV systems under varying climatic conditions, *Solar Energy*, 93, 183-194, doi: 10.1016/j.solener.2013.03.028
- Masson, V., Bonhomme, M., Salagnac, J. L., Briottet, X., Lemonsu, A., 2014, Solar panels reduce both global warming and urban heat island, *Frontiers in Environmental Science*, 2(14), doi: 10.3389/fenvs.2014.00014
- Millstein, V., Menon, S., 2011, Regional climate consequences of large-scale cool roof and photovoltaic array deployment, *Environmental Research Letters*, 6, doi: 10.1088/1748-9326/6/3/034001
- Mirzaei, P.A., 2015, Recent challenges in modeling of urban heat island, *Sustainable Cities and Society*, 19, 200-206, doi: 10.1016/j.scs.2015.04.001
- Mokarram, M., Mokarram, M., Khosravi, M., Saber, A., Rahideh, A., 2020, Determination of the optimal location for constructing solar photovoltaic farms based on multi-criteria decision system and Dempster-Shafer theory, *Scientific Reports*, 10(8200), doi: 10.1038/s41598-020-65165-z
- Nemet, G. F., 2009, Net Radiative Forcing from Widespread Deployment of Photovoltaics, *Environmental Science & Technology*, 43(6), 2173-2178, doi:10.1021/es801747c
- Ozden, T., Akinoglu, B. G., 2018, Preliminary investigations on two different procedures to calculate the efficiency and performance ratio of PV modules, *International Journal of Environmental Science and Technology*, 16(9), 5171-5176, doi: 10.1007/s13762-018-2003-5
- Saadsaoud, M., Ahmed, A. H., Er, Z., Rouabah, Z., 2017, Experimental Study of Degradation Modes and Their Effects on Reliability of Photovoltaic Modules after 12 Years of Field Operation in the Steppe Region, *Special Issue of the 3rd International Conference on Computational and Experimental Science and Engineering (ICCESEN 2016)*, *Acta Physica Polonica A*, 132, doi: 10.12693/APhysPolA.132.930

- Siddiqui, M. U., Arif, A. F. M., 2013, Electrical, thermal and structural performance of a cooled PV module: Transient analysis using a multiphysics model. *Applied Energy*, 112, 300-312, doi: 10.1016/j.apenergy.2013.06.030
- Simsek Kuscü, C., Sengezer, B., 2012, İstanbul Metropolitan Alanında Kentsel Isınmanın Azaltılmasında Yeşil Alanların Önemi, *Megaron*, 7(2), 116-128.
- Smets, A., Narayan, N., 2013, PV Systems: PV Modules II – Temperature dependency of PV output, *DelftX: ET3034TUx Solar Energy*, Delft University of Technology, https://www.youtube.com/watch?v=v8nbwvC8aBg&t=2s&ab_channel=3rabGeeks
- Sodoudi, S., Shahmohamadi, P., Vollack, K., Cubasch, U., Che-Ani, A., 2014, Mitigating the Urban Heat Island Effect in Megacity Tehran, *Advances in Meteorology*, 1-19, doi: 10.1155/2014/547974
- Tuncel, B., Ozden, T., Akinoglu, B. G., Balog, R. S., 2018, Thermal Modeling and Verification of PV Module Temperature and Energy Yield Using Outdoor Measurements for Ankara, Turkey Paper presented at the *1st International Conference on Photovoltaic Science and Technologies (PVCon2018)*, Ankara, Turkey, doi: 10.1109/PVCon.2018.8523953
- Turney, D., Fthenakis, V., 2011, Environmental impacts from the installation and operation of large-scale solar power plants, *Renewable and Sustainable Energy Reviews*, 15(6), 3261–3270, doi: 10.1016/j.rser.2011.04.023
- Voogt, J., 2008, How Researchers Measure Urban Heat Islands, *US Environmental Protection Agency*, https://19january2017snapshot.epa.gov/sites/production/files/2014-07/documents/epa_how_to_measure_a_uhi.pdf
- Wu, W., Yue, S., Zhou, X., Guo, M., Wang, J., Ren, L., Yuan, B., 2020, Observational Study on the Impact of Large-Scale Photovoltaic Development in Deserts on Local Air Temperature and Humidity, *Sustainability*, 12(3403), doi: 10.3390/su12083403
- Xu, M., Bruehlisauer, M., Berger, M., 2017, Development of a new urban heat island modeling tool: Kent Vale case study Paper presented at *International Conference on Computational Science (ICCS 2017)*, Zurich, Switzerland, doi: 10.1016/j.procs.2017.05.282
- Yılmaz, E., 2015, Landsat Görüntüleri ile Adana Yüzey Isı Adası, *Cografî Bilimler Dergisi (Ankara University)*, 13(2), 115-138. doi: 10.1501/Cogbil_0000000167
- 2014, Reducing Urban Heat Islands: Compendium of Strategies, *US Environmental Protection Agency (US EPA)*, <https://www.epa.gov/sites/production/files/2014-06/documents/basicscompendium.pdf>



NATIONWIDE MAPPING OF OPTIMUM WALL INSULATION THICKNESSES: A STOCHASTIC APPROACH

Semih CAGLAYAN*, Beliz OZORHON** and Levent KURNAZ***

* Sakarya University of Applied Sciences, Department of Civil Engineering, 54050 Sakarya, Turkey
semihcaglayan@subu.edu.tr, ORCID: 0000-0003-2052-0954

** Bogazici University, Department of Civil Engineering, 34342 Istanbul, Turkey
beliz.ozorhon@boun.edu.tr, ORCID: 0000-0002-4963-6937

*** Bogazici University, Department of Physics, 34342 Istanbul, Turkey
levent.kurnaz@boun.edu.tr, ORCID: 0000-0003-3050-9847

(Geliş Tarihi: 25.10.2021, Kabul Tarihi: 16.08.2022)

Abstract: Energy consumption in buildings accounts for a notable part of the primary energy consumption all over the world. The building industry also has a great potential to decrease the environmental impact by reducing greenhouse gas emissions. The national strategies of many developing countries are shaped by energy conservation issues. Improving energy efficiency and productivity is stated as one of the main elements of the Turkish national energy strategy. An efficient way to decrease energy consumption in buildings is to implement insulation on the building envelope. Identifying the optimum insulation thickness to be applied on the exterior walls is of prime importance. This study adapts a stochastic approach to determine optimum insulation thickness for 81 cities in Turkey. The stochastic approach, unlike the commonly used deterministic approach, incorporates the probabilistic nature of the process and presents the optimum insulation thickness as a probability distribution graph rather than a single value. For this purpose, a number of insulation thicknesses (1-20 cm) were regarded as the alternatives and the optimum alternative was determined based on life cycle costing analysis involving the cost of insulation application and annual energy savings. The average monthly temperature of each city and financial parameters such as the inflation and discount rates were considered as the stochastic elements. The results of the life cycle costing analysis were used to (i) identify the optimum thicknesses in each city as a probability distribution graph and (ii) generate an optimum insulation thickness map for Turkey.

Keywords: Stochastic analysis, Optimum insulation thickness, Wall insulation, Energy saving

OPTİMUM DUVAR YALITIMI KALINLIKLARININ ÜLKE ÇAPINDA HARİTALANMASI: STOKASTİK YAKLAŞIM

Özet: Binalarda enerji tüketimi tüm dünyadaki birincil enerji tüketiminin önemli bir kısmına karşılık gelmektedir. Bina sektörü ayrıca sera gazı salınımını düşürerek çevresel etkinin azaltılmasına yönelik büyük bir potansiyel teşkil etmektedir. Gelişmekte olan birçok ülkenin ulusal stratejileri enerjinin korunmasına ilişkin konularla şekillenmektedir. Enerji verimliliğinin ve üretkenliğin artırılması Türkiye ulusal enerji stratejisinin ana unsurlarından birisi olarak belirtilmiştir. Bina kılıfına yalıtım uygulamak binalarda enerji tüketimini azaltmak için etkili bir yoldur. Dış duvarlara uygulanacak olan optimum yalıtım kalınlığının belirlenmesi önem arz etmektedir. Bu çalışmada Türkiye'deki 81 ilin optimum yalıtım kalınlığını belirlemek amacıyla stokastik bir yaklaşım benimsenmiştir. Yaygın olarak kullanılan deterministik yaklaşımın aksine, stokastik yaklaşım sürecin olasılıksal doğasını bünyesinde barındırır ve optimum yalıtım kalınlığını tek bir değer yerine bir olasılık dağılım grafiği olarak sunar. Bu amaçla, birtakım yalıtım kalınlıkları (1-20 cm) alternatif olarak kabul edilmiş ve optimum alternatif yalıtım uygulamasının maliyeti ile yıllık enerji tasarruflarını dikkate alan bir yaşam dönemi maliyet analizi yapılarak belirlenmiştir. Şehirlerin aylık ortalama sıcaklıkları ve enflasyon ile iskonto oranları gibi finansal parametreler stokastik elemanlar olarak kabul edilmiştir. Yaşam dönemi maliyet analizinin sonuçları (i) her bir şehir için optimum yalıtım kalınlığını bir olasılık dağılım grafiği olarak elde etmek ve (ii) Türkiye için bir optimum yalıtım kalınlığı haritası oluşturmak amacıyla kullanılmıştır.

Anahtar Kelimeler: Stokastik analiz, Optimum yalıtım kalınlığı, Duvar yalıtımı, Enerji tasarrufu

INTRODUCTION

The energy crisis in 1973 caused conservation of energy to be considered as a national strategy especially in developing countries that import the majority of their energy needs from abroad. Global energy consumption is mainly formed by the building and construction industry, where energy consumption has been on the rise since the 1960s (Malecite et al., 2013). Energy consumed by the buildings corresponds to more than 40% of the primary energy consumption in the United States and European Union (Cao et al., 2016). The industry also has the greatest potential for decreasing the environmental impact as it is responsible for 10% of the global greenhouse gas emissions (IEO, 2013).

The economic and population growth in Turkey has accelerated the energy demand. The energy demand in Turkey has had the highest rate of growth among OECD (Organization for Economic Co-operation and Development) countries over the last 15 years. Turkey is also one of the biggest natural gas and electricity markets in its region. The national energy strategy of Turkey is mainly shaped by the increasing energy demand and dependency on imports. The main elements of the national energy strategy include (i) prioritization of energy supply security, (ii) having environmental concerns all along the energy chain, (iii) conducting R&D on energy technologies, and (iv) improving the energy efficiency and productivity (MFA, 2021).

A crucial component of Turkey's 2023 national strategy objectives is to promote energy efficiency. The objective is to reduce the energy consumed per national income, namely energy density, by 20% from 2011 to 2023 by conducting energy efficiency studies (MENR, 2021). Reducing heating energy consumption is known to be an effective way of increasing energy efficiency in residential buildings that can operate for 70 years (Zhan et al., 2018). Heating energy consumption can be reduced to a great extent by applying optimum insulation thickness to exterior walls. Applying such insulation to the exterior walls of existing buildings can provide a great amount of energy savings in Turkey, where the majority of the buildings are uninsulated (Kurekci, 2016).

Implementation of insulation material to the exterior walls of existing buildings requires an initial investment, but it helps the building to consume significantly less energy throughout its lifetime (Caglayan et al., 2020). While increasing the insulation thickness pushes up the investment cost, it leads to greater savings in energy. In this regard, it becomes crucial to identify the insulation thickness that is economically most feasible. The optimum insulation thickness can be expressed as the insulation thickness

that provides the greatest net benefit which is obtained by subtracting the cost from the savings.

The amounts of the investment cost and energy savings are the major determinants of the optimum insulation thickness. The investment cost is the cost of insulation application to the exterior walls. Expanded polystyrene, extruded polystyrene, and stone wool have frequently been selected as the insulation material in the literature. The savings are achieved by reducing the energy consumption in buildings. Electricity and natural gas have been mainly considered as the energy sources for cooling and heating, respectively. The optimization analyses have focused on certain cities representing different climate regions of Turkey.

The optimum insulation thickness has mostly been determined with the deterministic approach. Exact values have been assigned to key input parameters and the output (optimum insulation thickness) has been determined as a single value. The deterministic approach is useful if these parameters are subject to no random deviations and can be obtained without any ambiguity. Otherwise, it would be more appropriate to consider the stochastic approach where the output is presented as a probability distribution graph that describes the probability of obtaining various values.

This study adapted a stochastic approach to determine the optimum insulation thickness of a building prototype for 81 cities in Turkey. Within this context, a number of insulation thicknesses (1-20 cm) were regarded as the alternatives and the optimum alternative was determined for each city based on a life cycle costing analysis involving the insulation cost and annual energy savings. The results of the life cycle costing analysis were used to (i) identify the optimum thicknesses in each city as a probability distribution graph and (ii) generate an optimum insulation thickness map for Turkey. The average monthly temperature of each city and financial parameters such as the inflation and discount rates were considered as the stochastic elements for which historical data or future projections were obtained. The characteristics of the data (mean values, standard deviations) were identified and used for randomly generating the stochastic elements in the analysis.

The proposed study contributes to the body of knowledge in two ways: (i) achievement of reliable outputs by reflecting the uncertainty on the estimates and (ii) generation of an optimum insulation thickness map by repeating the analysis for each city in Turkey. The stochastic approach allows for random variation in stochastic elements and reflects it on the estimates. Presentation of an output as a probability distribution graph displays the most probable outcome, and more importantly, how much it can deviate. The latter implies the comprehensiveness of the study as the

analysis covers all the cities. Studies in the literature have made analysis for certain cities from different climate regions. Marking all the cities of the country provides the opportunity to draw an optimum insulation thickness map.

RESEARCH BACKGROUND

Determining the optimum insulation thickness has been an attractive academic topic both in the national and international areas. Several studies have been conducted in various countries to specify the optimum insulation thickness. Daouas et al. (2010) determined the optimum insulation thickness of building walls in Tunisia. The optimum insulation thickness was determined as 5.7 cm. Liu et al. (2015) identified the optimum insulation thicknesses for three cities in the hot summer and cold winter zones of China, which were Changsha, Chengdu, and Shaoguan. While the optimum insulation thicknesses for expanded polystyrene were found to change between 8.1 cm and 10.5 cm, the optimum thicknesses for extruded polystyrene varied between 5.3 cm and 6.9 cm. Baniassadi et al. (2016) determined the optimum insulation thickness for different climatic regions of Iran. The optimum thickness was found to be greater than 6.0 cm in cold regions. Nematchoua et al. (2017) calculated the optimum insulation thickness for two cities located in two different climate regions of Cameroon, namely Yaounde and Garoua. The optimum thicknesses were calculated as 8.0 cm and 11.0 cm for Yaounde and Garoua, respectively. Jraida et al. (2017) conducted a study to identify the optimum insulation thickness in six cities in six different climate zones of Morocco. Optimum insulation thicknesses for extruded polystyrene were determined as 2.3 cm, 3.7 cm, 5.2 cm, 7.7 cm, 4.1 cm, and 5.7 cm for Agadir, Tangier, Fez, Ifran, Marrakech, and Errachidia, respectively.

Numerous studies have also been conducted to identify the optimum insulation thickness for cities representing different climate regions of Turkey. A total of four different climate regions have been defined in the 2008 version of Turkish Standard 825 (TSI, 2008). Region 1 represents the hottest regions, while Region 4 comprises the coldest ones. Even though the number of climate regions was increased to five in the 2013 version, it was not published in the official gazette. The researchers have, therefore, considered and the discussion has focused on the climate regions defined in the 2008 version. Comakli and Yuksel (2003) identified the optimum insulation thickness for the coldest cities of Turkey. The optimum insulation thicknesses were observed as 8.5 cm, 10.4 cm, and 10.7 cm for Erzincan (Region 4), Erzurum (Region 4), and Kars (Region 4), respectively. Kaynakli (2008) determined the optimum insulation thickness for a prototype building in Bursa (Region 2) for different types of fuel. The optimum thicknesses were found to

be 5.3 cm, 10.5 cm, 11.2 cm, and 12.4 cm for natural gas, fuel oil, electricity, and LPG, respectively. Dombayci et al. (2017) calculated the optimum insulation thickness for a total of four cities representing the four climate regions of Turkey, namely Izmir (Region 1), Trabzon (Region 2), Ankara (Region 3), and Kars (Region 4). The optimum thicknesses for expanded polystyrene insulation were determined as 4.6 cm, 6.0 cm, 7.7 cm, and 10.7 cm for Izmir, Trabzon, Ankara, and Kars, respectively. Canbolat et al. (2018) determined the economic insulation thickness as 4.7 cm for Istanbul (Region 2). Akyuz et al. (2018) determined the optimum insulation thickness of the International Hasan Polatkan Airport terminal in Eskisehir (Region 3) for a number of insulation materials. The optimum thicknesses were found as 5.0 cm, 3.3 cm, 7.8 cm, and 9.7 cm for expanded polystyrene, extruded polystyrene, glass wool, and stone wool, respectively.

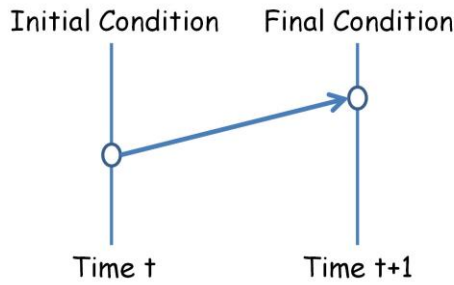
In previous studies, optimum insulation thicknesses have been determined for certain cities with a deterministic approach. The parameter values have been assumed deterministically and the results have revealed certain optimum insulation thickness values for the mentioned cities. The stochastic approach adapted in this study possessed a number of advantages over the deterministic approach. Generation of the stochastic elements based on historical data or future projections can provide more reliable outputs as the uncertainties are reflected on the estimates. The result is obtained as a probability distribution graph rather than a single value. In addition, repetition of the analysis for each city in Turkey offers the opportunity to generate an optimum insulation thickness map.

RESEARCH METHODOLOGY

This study adapts a stochastic model to determine optimum insulation thicknesses. A deterministic model represents a system where the relationships are fixed, implying that the probabilistic nature is ignored. For a set of given initial conditions, a deterministic model always performs the same way. On the other hand, a stochastic model is a mathematical representation of a system where a number of possible outputs can be generated by a given input. The randomness of the process makes the results obtained by the combination of independent factors slightly different (Leuenberger et al., 2018). The behaviours of the deterministic and stochastic models are illustrated in Figure 1 (adapted from Revelle et al., 2005).

A stochastic model possesses random variation in the inputs and forecasts the probability of various outputs. The uncertainty is built into the model through the inputs, where historical data is used to observe fluctuations. The probability distribution of the outputs reflects the random variation in the inputs and thus, the uncertainty is made explicit.

Deterministic Models



The outputs are fully determined by the parameter values and initial conditions

Stochastic Models

The inherent randomness results in generation of different outputs

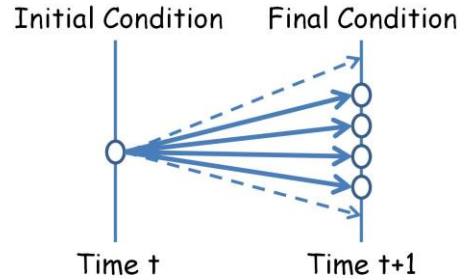


Figure 1. Deterministic vs. stochastic models

The methodology part of the research is composed of four main sections: (i) obtaining historical data and future projections for the stochastic elements, (ii) creating the building prototype, (iii) calculating annual energy requirements, and (iv) conducting life cycle costing analysis.

Obtaining Historical Data and Future Projections for the Stochastic Elements

In this study, the average monthly temperature of each city and financial parameters such as the inflation and discount rates were assumed as the stochastic elements. Inflation and discount rates are two financial parameters that influence the results of life cycle costing analysis to a great extent. These parameters have been subject to alteration in previous studies based on the time the study was conducted. Table 1 presents the inflation and discount rates used in 20 studies conducted in the last 15 years. According to the table, the inflation rate has varied between 0.00% and 11.75%, while the discount rate has ranged from 4.00% to 19.38%. Such a situation demonstrates the uncertainty within these parameters. Considering these parameters as stochastic elements and generating them based on the analysis of historical data can provide more reliable results.

Historical data was obtained for inflation and discount rates. The rate of increase in natural gas prices was considered as the inflation rate and data was acquired for the period from 01.05.2006 to 01.05.2020 from the official site of Istanbul Gaz Dagitim Sanayi ve Ticaret AS (IGDAS, 2021). The mean and standard deviation for the inflation rate were observed as 10.66% and 11.38%, respectively. The reason for such a great standard deviation might be the fact that energy prices are highly susceptible to economic and political issues. Historical data for discount rate was obtained from Interest Rate Statistics of the Central Bank of the Turkish Republic for the period from 01.01.2005 to

01.12.2019 (TCMB, 2021). The mean and standard deviation for the discount rate up to 1-year deposits were observed as 13.45% and 4.28%, respectively.

Table 1. Inflation and discount rates used in previous studies

No	Study	Inflation Rate	Discount Rate
1	Bolatturk (2006)	9.20%	17.89%
2	Dombayci et al. (2006)	0.00%	8.00%
3	Sisman et al. (2007)	9.32%	17.79%
4	Bolatturk (2008)	4.00%	5.00%
5	Ucar and Balo (2009)	5.00%	4.00%
6	Ozkan and Onan (2011)	9.67%	19.38%
7	Ekici et al. (2012)	5.00%	4.00%
8	Kaynakli (2013)	6.00%	9.00%
9	Kayfeci (2014)	5.00%	4.00%
10	Ozel et al. (2015)	8.39%	9.65%
11	Kurekci (2016)	7.91%	8.25%
12	Erturk (2016)	6.50%	13.00%
13	Kaya et al. (2016)	6.16%	13.75%
14	Kon and Yuksel (2016)	6.40%	9.00%
15	Aktemur and Atikol (2017)	8.53%	9.00%
16	Evin and Ucar (2019)	8.81%	9.00%
17	Aydin and Biyikoglu (2020)	10.35%	12.75%
18	Gulten (2020)	8.50%	10.00%
19	Aydin and Biyikoglu (2021)	10.35%	12.75%
20	Akan (2021)	11.75%	12.50%

Average monthly temperatures of each city were projected for the future period of 2021-2050 by using the supercomputers in the Center for Climate Change and Policy Studies (iklimBU) laboratory. Global Climate Models (GCMs), which project future climate conditions needed in studies examining the sectoral impacts of climate change, have low spatial resolution despite their high temporal resolution, which makes the outputs of these models inadequate in regional or local impact studies. This requirement leads researchers to downscaling approaches (i.e., dynamical, statistical, or hybrid) so that the outputs of these sophisticated tools can provide more reliable climate data at regional and local scales. Therefore, dynamical downscaling approach was applied to obtain high spatial resolution mean temperature data for Turkey, which has a high and complex topography. The dynamical downscaling approach is based on the principle of running a Regional Climate Model (RCM) that takes the lateral boundary conditions from a GCM.

MPI-ESM-MR and RegCM4.4 model pair, which have been tested in various studies (Akbas et al., 2020; An et al., 2018, 2020; Demircan et al., 2017; Demiroglu et al., 2016, 2021; Turp et al., 2014) were preferred. The outputs of MPI-ESM-MR (Giorgetta et al., 2013), one of the GCMs developed by the Max Planck Institute for Meteorology in Germany, were given as input to the Regional Climate Model Version 4.4 (RegCM4.4, Giorgi et al., 2012) developed by the Abdus Salam International Centre for Theoretical Physics (ICTP) in Italy. In other words, low spatial resolution (approximately 210 km x 210 km grid size) data of MPI-ESM-MR, one of the most widely used models in climate change studies (Demircan et al., 2017) and has a medium level of equilibrium climate sensitivity (Sherwood et al., 2014), was dynamically downscaled to higher spatial resolution (10 km x 10 km grid size) by using RegCM4.4. RegCM (Pal et al., 2007), which has been in use for more than three decades, is one of the most widely used RCMs because it is free, easy to access, user-friendly, practical, reliable, and has a globally wide user and developer network.

Future projection (2021-2050) was realized under the Representative Concentration Pathway (RCP) 8.5 emission scenario which is referred to the business-as-usual case. RCP8.5 (Riahi et al., 2007, 2011), the most pessimistic trajectory among the RCP scenarios, predicts that the atmospheric CO₂ concentration, which reached 420 ppm at the beginning of the 2020s, will reach approximately 541 ppm in the middle of the century and 936 ppm at the end of the century. Mean and standard deviation of the climate projections are presented in Appendix A, where the numbers in parenthesis represent the standard deviations.

Creating the Building Prototype

The building prototype represented a typical nine-story residential building with a length of 25 m, width of 20 m, and total height of 27 m. The window areas for the south, north, east, and west directions were determined as 150 m², 60 m², 120 m², and 60 m², respectively. Natural ventilation was assumed for air conditioning. Figure 2 and 3 present the cross-sectional details of the uninsulated and insulated building envelope, respectively. Ceiling and basement cross sections remained the same both in the insulated and uninsulated case. The only difference existed in the exterior walls (both infilled and reinforced concrete). An expanded polystyrene insulation material was added in the insulated case at varying thicknesses. which was the main subject of the study.

Calculating Annual Energy Requirements

A matlab code combining both the annual energy requirements and life cycle costing analysis was generated. The annual energy requirement of the building was calculated according to the method described by Turkish Standard (TS) 825 “thermal insulation requirements for buildings” published by the Turkish Standards Institute (TSI, 2008). The standard considers the building geometry and the climate region of the city. The cities are labelled by four climate regions, where the first region represents the warmest and the fourth region represents the coolest cities. The annual energy requirements are calculated not for each city, but for each climate region. In this study, however, the annual energy requirement was calculated for every single city based on the values generated in line with the climate simulations prepared according to the RCP8.5 scenario. With the exception of the climate conditions of the cities, the methodology shown in TS825 was strictly followed.

According to the methodology shown in TS825, the annual heating energy consumption (Q_{year}) is obtained by adding up the monthly heating energy requirements (Q_m).

$$Q_{year} = \sum Q_m \quad (1)$$

$$Q_m = \left[\begin{array}{l} H * (\theta_{in} - \theta_{out}) \\ -\eta * (\varphi_{in} + \varphi_s) \end{array} \right] * t \quad (2)$$

The specific loss (H) of the building is equal to the sum of the heat losses resulting from conduction and convection (H_{tr}) and ventilation (H_{ven}).

$$H = H_{tr} + H_{ven} \quad (3)$$

H_{tr} is equal to the sum of the products of area (A) and heat transfer coefficient (U) for the exterior wall (ew), glazing (gl), exterior door (ed), ceiling (ce), and floor (fl).

$$H_{tr} = \sum A * U = U_{ew} * A_{ew} + U_{gl} * A_{gl} + U_{ed} * A_{ed} + (0.8) * U_{ce} * A_{ce} + (0.5) * U_{fl} * A_{fl} \quad (4)$$

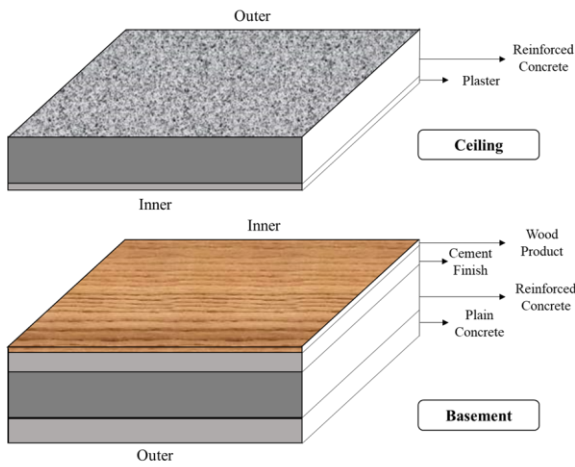


Figure 2. Cross sections of the uninsulated building envelope

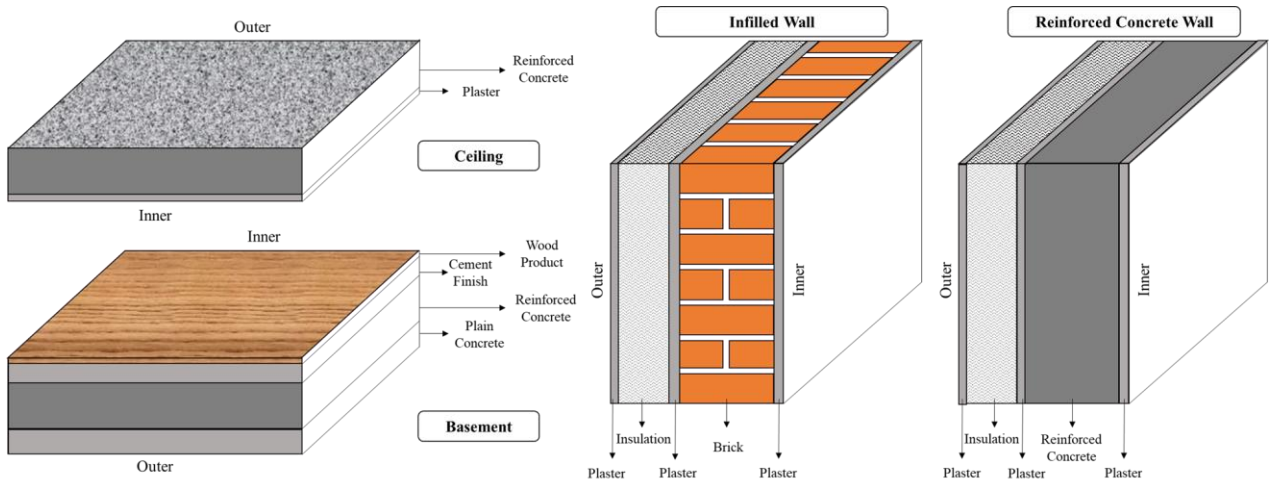


Figure 3. Cross sections of the insulated building envelope

A_n represents the building usage area and is determined by using the following equation:

$$A_n = (0.32) * V_{gross} \quad (7)$$

The monthly average solar energy gain (φ_s) is obtained as follows:

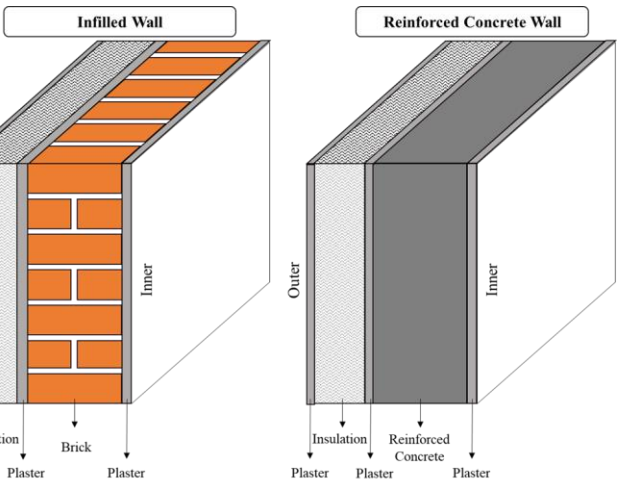
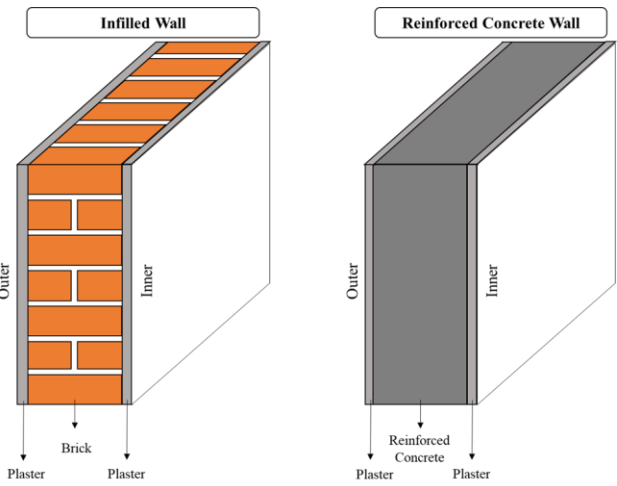
$$\varphi_{s,j} = \sum_k r_j * G_j * I_{j,k} * A_{gl,k} \quad (8)$$

r represents the monthly average shading factor of the transparent surfaces; $A_{gl,k}$ stands for the total glazing area in direction k ; and G is the solar energy

$$H_{ven} = (0.264) * n_a * V_{gross} \quad (5)$$

V_{gross} is the gross building volume. Air changing ratio (n_a) was considered as 0.8 for natural ventilation. The monthly average interior heat gain (φ_{in}) is obtained as in the following equation:

$$\varphi_{in} \leq 5 * A_n \quad (6)$$



permeation factor of the transparent elements. r was assumed as 0.8 for the detached building.

Monthly average solar radiation intensities ($I_{j,k}$) are presented in Table 2 (TSI, 2008). TS825 assumes similar solar radiation intensities for all the cities. However, solar radiation is affected from the geographic information of cities such as altitude, latitude, and longitude (Sahin et al., 2013). The assumption of similar solar radiation might result in higher heating energy requirement (due to insufficiently calculated solar heat gain) and thicker optimum insulation thickness in cities where solar

radiation is greater than the values indicated in the table.

Table 2. Monthly average solar radiation intensities (W/m²)

	Months											
	Jan	Feb	Mar	Apr	May	June	July	Aug	Sept	Oct	Nov	Dec
I _{south}	72	84	87	90	92	95	93	93	89	82	67	64
I _{north}	26	37	52	66	79	83	81	73	57	40	27	22
I _{east/ west}	43	57	77	90	114	122	118	106	81	59	41	37

The solar energy permeation factor (G) is obtained as follows:

$$G_j = F_w * g_{\perp} \quad (9)$$

The correction factor for windows (F_w) was assumed as 0.8 and the solar energy permeation factor (g_⊥) was considered as 0.75 for colourless glass. The monthly average usage factor of heat gain (η) is calculated as in the following equation:

$$\eta = 1 - e^{(-1/GLR)} \quad (10)$$

The gain/loss ratio (GLR) is determined by the following equation:

$$GLR = \frac{(\varphi_{in} + \varphi_s)}{H * (\theta_{in} - \theta_{out})} \quad (11)$$

If gain/loss ratio becomes equal to or greater than 2.5, no heat loss occurs in the corresponding month. Inserting the gain/loss ratio formula in equation 11 into equation 10;

$$\eta = 1 - e^{\left(\frac{H * (\theta_{out} - \theta_{in})}{(\varphi_{in} + \varphi_s)} \right)} \quad (12)$$

As suggested by the standard, the monthly average indoor temperature (θ_{in}) was considered as 19°C. The monthly average outdoor temperatures (θ_{out}) were considered as the stochastic elements and future projection for the period of 2021-205 is presented in Appendix A.

Calculating Life Cycle Costing Analysis

The life cycle costing analysis considered the insulation cost (IC) and operational saving (OS) achieved through insulation implementation. The operational saving was obtained by taking the difference between the annual energy requirement of the uninsulated and insulated case for each insulation thickness. The cost of energy was considered as 0.02 \$/kWh. The insulation cost was

determined by taking offers from insulation companies (material supply + installation) and taking their average. The cost of insulation implementation is summarized in Table 3. It could be noticed that even the thinnest insulation implementation had a certain total unit cost amount mainly due to the fixed amount of installation cost for each insulation thickness. Increasing the insulation thickness generated only incremental movements in the total unit cost.

Life cycle costing analysis was conducted for insulation alternatives (1 cm to 20 cm) in each city to determine the alternative resulting in the most desired economic outcome. The insulation alternative having the highest net saving (NS) value was regarded as the optimum insulation thickness. As the stochastic elements (average monthly temperature of each city, inflation rate, discount rate) were generated 1,000 times with the mentioned means and standard deviations, optimum insulation thicknesses were also determined 1,000 times. Net saving was calculated for each alternative as follows:

$$NS = OS * PWF - IC \quad (13)$$

The present worth of the operational savings was determined by multiplying the operational saving with the present worth factor (PWF), which was calculated as follows:

$$PWF = \frac{(1+i^*)^N - 1}{r * (1+i^*)^N} \quad (14)$$

The lifespan (N) was considered as 20 years and the interest rate adapted for inflation (i*) was determined by using the following equation:

$$i^* = \begin{cases} \frac{i-g}{1+g} & i > g \\ \frac{g-i}{1+i} & i < g \end{cases} \quad (15)$$

Inflation rate (g) and discount rate (i) were the stochastic elements generated based on historical data.

FINDINGS AND DISCUSSION

The histogram of the optimum insulation thicknesses represents the probability distribution graph and is shown in Appendix B. It could be noticed that the optimum insulation thicknesses showed great variation under different scenarios. In extreme cases, the optimum thickness moved up to 20 cm insulation in the coolest cities and became even 0 cm insulation (implying the uninsulated case) in the warmest cities. It was also noticed that insulation thicknesses from 1 to 3 cm were not selected as the optimum insulation thicknesses for any city under any scenario. Within this

range of thicknesses, the cost of insulation implementation was dominated by the relatively fixed amounts of installation and auxiliary items costs that overweighed the energy savings.

Figure 4 illustrates the histogram of optimum insulation thickness graphs for certain cities from four different climate regions, namely İzmir, Gaziantep, Ankara, and Kayseri. The most likely thicknesses were concentrated on 5-8 cm for İzmir, 6-10 cm for Gaziantep, 8-11 cm for Ankara, and 9-13 cm for Kayseri. For İzmir, the most frequently selected insulation thickness was 6 cm followed by 7 cm. The 6 cm insulation was selected in 218 of the 1,000 cases, corresponding to 21.8%.

The probabilities of optimum insulation thicknesses for each city are shown in percentages in Appendix C. Generation of the stochastic elements 1,000 times resulted in the determination of the optimum insulation thickness for 1,000 times in each city. A number in Table C1 and C2 represented the number of times (in percentages) the corresponding insulation thickness was selected as the optimum insulation thickness. To illustrate, it could be observed from the case of Afyonkarahisar that 9 cm insulation was selected as the optimum thickness 159 times in 1,000 trials, corresponding to 15.9% of the cases.

Table 3. Cost of insulation implementation

Insulation Thickness	Material Cost (\$/m ²)	Auxiliary Items Cost (\$/m ²)	Installation Cost (\$/m ²)	Total Unit Cost (\$/m ²)	Total Cost (\$)
1 cm	0.40	2.70	4.00	7.10	18.247
2 cm	0.80	2.84	4.00	7.64	19.635
3 cm	1.20	2.98	4.00	8.18	21.023
4 cm	1.60	3.12	4.00	8.72	22.410
5 cm	2.00	3.26	4.00	9.26	23.798
6 cm	2.40	3.40	4.00	9.80	25.186
7 cm	2.80	3.54	4.00	10.34	26.574
8 cm	3.20	3.68	4.00	10.88	27.962
9 cm	3.60	3.82	4.00	11.42	29.349
10 cm	4.00	3.96	4.00	11.96	30.737
11 cm	4.40	4.10	4.00	12.50	32.125
12 cm	4.80	4.24	4.00	13.04	33.513
13 cm	5.20	4.38	4.00	13.58	34.901
14 cm	5.60	4.52	4.00	14.12	36.288
15 cm	6.00	4.66	4.00	14.66	37.676
16 cm	6.40	4.80	4.00	15.20	39.064
17 cm	6.80	4.94	4.00	15.74	40.452
18 cm	7.20	5.08	4.00	16.28	41.840
19 cm	7.60	5.22	4.00	16.82	43.227
20 cm	8.00	5.36	4.00	17.36	44.615

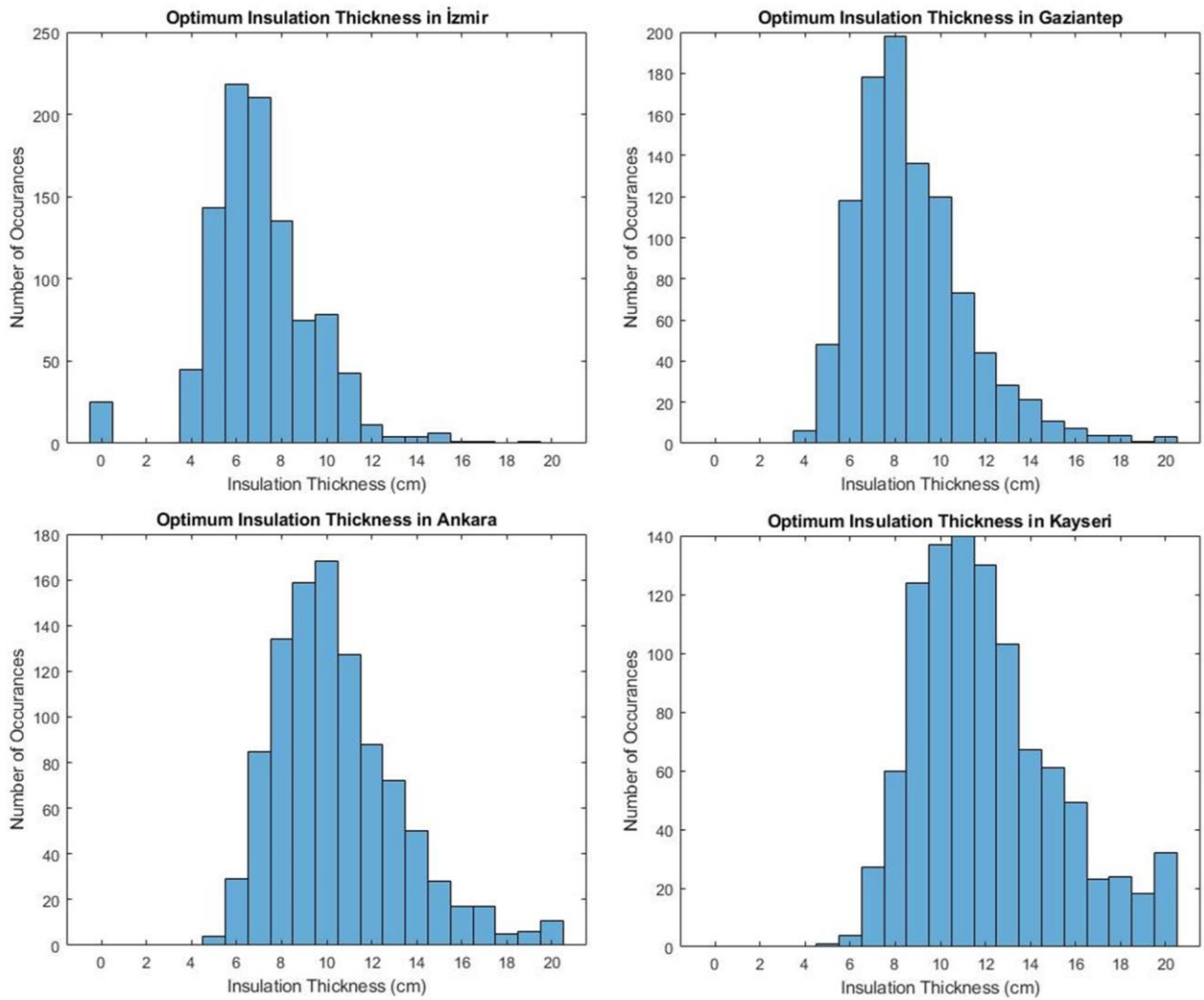


Figure 4. Optimum insulation thickness graphs for cities from four different climate regions

The expected value can be described as the weighted average of all possible values a discrete variable can take. In this case, the discrete variable was the insulation thickness and the weights were represented by the probabilities of being selected as the optimum. The expected value of optimum insulation thickness was calculated as:

$$E(X) = \sum_{i=0}^{20} x_i * p_i \quad (16)$$

$$= x_0 * p_0 + x_1 * p_1 + x_2 * p_2 + \dots + x_{20} * p_{20}$$

where $x_0, x_1, x_2, \dots, x_{20}$ represented the insulation thicknesses (from 0 to 20 cm) and $p_0, p_1, p_2, \dots, p_{20}$ were the corresponding probabilities (or the weights).

To illustrate, the expected value of the optimum insulation thickness for Van can be calculated as;

$$E(X) = 0*0 + 1*0 + 2*0 + 3*0 + 4*0 + 5*0 + 6*0 + 7*0.006 + 8*0.012 + 9*0.042 + 10*0.075 + 11*0.113 + 12*0.134 + 13*0.123 + 14*0.106 + 15*0.084 + 16*0.089 + 17*0.057 + 18*0.031 + 19*0.037 + 20*0.091 = 13.93 \text{ cm}$$

Table 4 summarizes the expected values of optimum insulation thicknesses calculated for 81 cities of Turkey. A great variation was observed among the expected values of different cities. The expected value varied between 6.73 cm (for Hatay) and 14.25 cm (for Ardahan) throughout Turkey. The expected value also showed great variation among the cities in the same climate region. The expected value in Region 1, Region 2, Region 3, and Region 4 ranged between 6.73-8.97 cm, 7.16-12.26 cm, 8.65-12.73 cm, and 10.95-14.25 cm, respectively. Such a finding also pointed out the discrepancies in the categorization. For example, even though Rize was located in Region 2, the expected value of Rize (12.26 cm) was greater than that of Kastamonu (10.95 cm) in Region 4. The reason behind such an inconsistency could be the changing climate conditions. The calculations in this study were based on the climate projections for the period 2021-2050 rather than historical records.

An optimum insulation thickness map was generated for Turkey (Figure 5). The cities were painted based on their expected values of optimum insulation thickness. A total of 9 different categories were painted in 9

different colours changing from white to black, where the darker colours represented greater thicknesses. The numbers in parentheses represented the number of cities falling into that category. Hatay was the only city with the lightest colour ($6 \text{ cm} \leq \text{thickness} < 7 \text{ cm}$), while Ardahan and Erzurum were painted with the darkest black ($14 \text{ cm} \leq \text{thickness} < 15 \text{ cm}$). The darker colours were observed mostly in the northeast of Turkey.

CONCLUSION

In this study, a stochastic approach was adapted to determine the optimum insulation thickness of a building prototype for 81 cities in Turkey. Stochastic elements were randomly generated based on the characteristics of historical data or future projections. The optimum insulation thickness of each city was obtained as a probability distribution graph indicating the most likely thicknesses. The expected value of each probability distribution graph was calculated and an optimum insulation thickness map was generated by categorizing the cities based on their expected values. The scientific contribution of the proposed study to the body of knowledge can be summarized as reliability and comprehensiveness.

The scientific value of the study stems mainly from the reliability of the adapted stochastic approach. Previous studies have adopted the deterministic approach to calculate the optimum thicknesses, which takes into consideration various assumptions for certain parameters. Since this approach incorporates uncertainties of these parameters, there might be a problem of consistency of the obtained results. As observed in the literature, varying values have been reported for the optimum insulation thicknesses in the studies done for the same cities. The stochastic approach, on the other hand, reflects these uncertainties on the estimates and is expected to provide more accurate results.

Another notable scientific value of the study is its comprehensiveness. The optimum insulation thickness graphs were drawn and the optimum insulation thickness map was generated for 81 cities in Turkey. In previous studies, optimum insulation thicknesses have frequently been determined for a couple of cities from certain climate regions. The results have been assumed to be valid and generalized for all the cities in the same climate region. Having identified the optimum insulation thickness for all the cities in this study provided the opportunity to check whether the optimum insulation thickness varied across the cities within the same climate region.

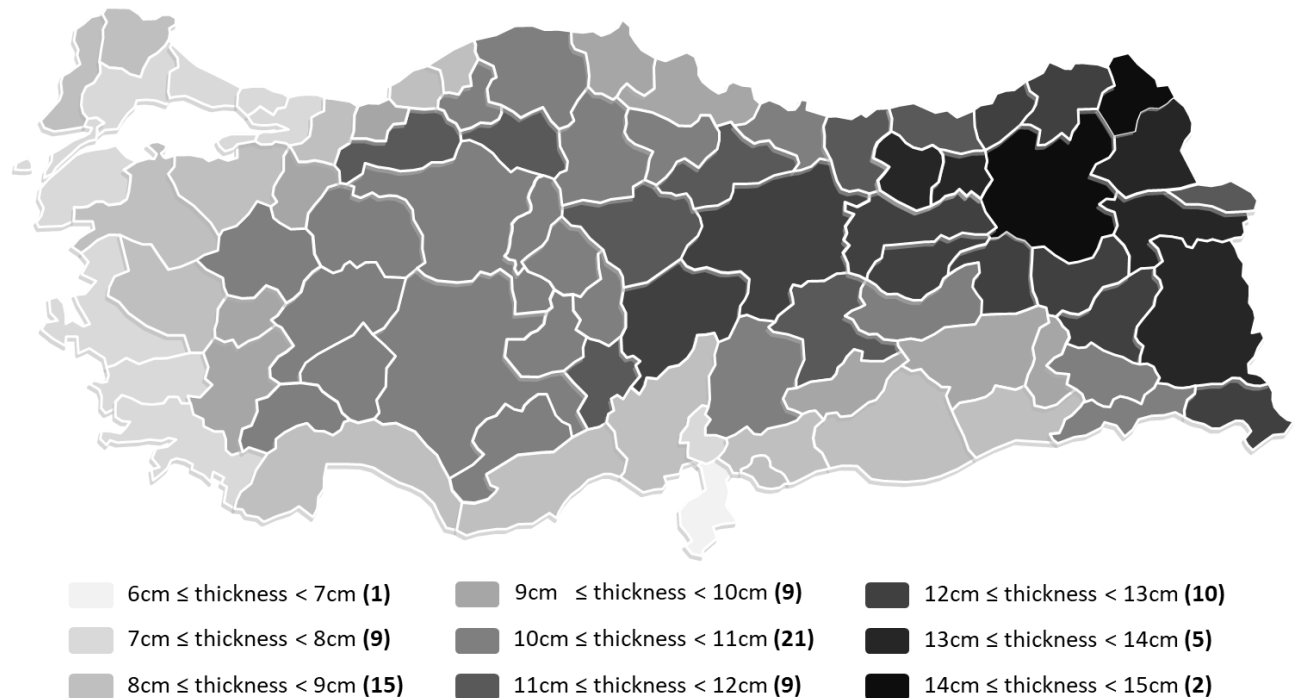
The identified optimum insulation thicknesses showed great variation across different parts of Turkey. The results revealed that the expected values varied from

6.73 cm (Hatay) to 14.25 cm (Ardahan) depending on the climate properties of the city. Accordingly, the optimum insulation thickness map listed the cities under 9 different categories. The results also emphasized the changing climate conditions as the expected value of a city in Region 2 (Rize: 12.26 cm) was observed to be greater than the expected value of a city in Region 4 (Kastamonu: 10.95 cm). The study had a number of limitations. Firstly, the climate feature obtained for the city center was assumed to be valid for the whole city. The climate features might show variation across different parts of certain cities. Another limitation is that the method presented in TS825 focuses solely on heating and ignores cooling energies. Incorporation of cooling energies into annual energy requirements might result in slightly greater optimum insulation thicknesses in cities that belong to the climate Region 1. It should also be noted that historical data for the inflation rate was obtained from one of the distributors of natural gas (due to the availability of data) and the rate of increase in natural gas prices was determined accordingly. Collecting product-based data rather than energy cost-based data might lead to variation in results. Moreover, the assumption for the cost of natural gas reflects the situation when the analysis was conducted. The price might be subjected to variation as the energy prices are highly vulnerable to the changes in both local and global conditions.

The optimum insulation thickness map obtained as a result of this study is expected to benefit several organizations to improve the energy efficiency of buildings in Turkey. Relevant bodies may adopt the map to revise the current regulation and the recommended thickness; sector professionals may consider the thickness values proposed in this study in their practices; and investors may evaluate their insulation decisions from a financial point of view. A further study should incorporate the cooling calculations in the energy efficiency analysis. Moreover, similar studies can be conducted in other countries based on their own national standards to promote energy efficiency countrywide. Achieving the national strategic objectives requires collaborative studies on energy efficiency. Academic studies should be encouraged and supported by public bodies, non-governmental organizations, and private sector associations. The outcomes of the studies should be interpreted to create social awareness.

Table 4. Expected value of optimum insulation thickness for 81 cities

Province	Climate Region	Expected Value (cm)	Province	Climate Region	Expected Value (cm)	Province	Climate Region	Expected Value (cm)
Adana	1	8.86	Edirne	2	8.07	Malatya	3	11.22
Adıyaman	2	9.59	Elazığ	3	10.87	Manisa	2	8.27
Afyonkarahisar	3	10.59	Erzincan	4	12.95	Mardin	2	8.66
Ağrı	4	13.61	Erzurum	4	14.01	Mersin	1	8.97
Aksaray	3	10.29	Eskişehir	3	10.15	Muğla	2	7.18
Amasya	2	10.51	Gaziantep	2	8.71	Muş	4	12.70
Ankara	3	10.47	Giresun	2	11.77	Nevşehir	3	10.68
Antalya	1	8.59	Gümüşhane	4	13.61	Niğde	3	11.69
Ardahan	4	14.25	Hakkari	4	12.97	Ordu	2	10.28
Artvin	3	12.57	Hatay	1	6.73	Osmaniye	1	7.65
Aydın	1	7.61	İğdir	3	11.99	Rize	2	12.26
Balıkesir	2	8.23	Isparta	3	10.84	Sakarya	2	8.47
Bartın	2	8.92	İstanbul	2	7.16	Samsun	2	9.28
Batman	2	9.49	İzmir	1	7.06	Şanlıurfa	2	8.18
Bayburt	4	13.75	Kahramanmaraş	2	10.95	Siirt	2	10.63
Bilecik	3	9.65	Karabük	3	10.54	Sinop	2	9.72
Bingöl	3	12.73	Karaman	3	10.97	Sivas	4	12.63
Bitlis	4	12.54	Kars	4	13.77	Şırnak	2	10.42
Bolu	3	11.38	Kastamonu	4	10.95	Tekirdağ	2	7.79
Burdur	3	10.17	Kayseri	4	12.07	Tokat	3	11.16
Bursa	2	8.76	Kilis	2	8.30	Trabzon	2	11.14
Çanakkale	2	7.48	Kırıkkale	3	10.42	Tunceli	3	12.11
Çankırı	3	11.29	Kırklareli	3	8.65	Uşak	3	9.59
Çorum	3	10.81	Kırşehir	3	10.44	Van	4	13.93
Denizli	2	9.63	Kocaeli	2	7.77	Yalova	2	7.37
Diyarbakır	2	9.58	Konya	3	10.40	Yozgat	4	11.10
Düzce	2	9.47	Kütahya	3	10.76	Zonguldak	2	8.75

**Figure 5.** Map of optimum insulation thicknesses

ACKNOWLEDGMENTS

This work was produced based on a research project funded by the Bogazici University Research Fund (BAP) under grant number 16782. The authors would like to thank researchers Dr. Tufan Turp and Dr. Nazan An from iklimBU for data sharing.

REFERENCES

- Akan, A. E., 2021, Determination and modeling of optimum insulation thickness for thermal insulation of buildings in all city centers of Turkey, *International Journal of Thermophysics*, 42 (4), 1-34.
- Akbas, A., Freer, J., Ozdemir, H., Bates, P. D., and Turp, M. T., 2020, What about reservoirs? Questioning anthropogenic and climatic interferences on water availability, *Hydrological Processes*, 34 (26), 5441-5455.
- Aktemur, C. and Atikol, U., 2017, Optimum insulation thickness for the exterior walls of buildings in Turkey based on different materials, energy sources and climate regions, *International Journal of Engineering Technologies IJET*, 3 (2), 72-82.
- Akyuz, M. K., Altuntas, O., Sogut, M. Z., Karakoc, T. H., and Kurama, S., 2018, Determination of optimum insulation thickness for building's walls with respect to different insulation materials: a case study of International Hasan Polatkan Airport terminal, *International Journal of Sustainable Aviation*, 4 (2), 147-161.
- An, N., Turp, M. T., Akbaş, A., Öztürk, Ö., and Kurnaz, M. L., 2018, Türkiye'nin değişen ikliminde ısıtma ve soğutma gün derecelerinin gelecek projeksiyonları [Future projections of heating and cooling degree days in a changing climate of Turkey], *Marmara Journal of Pure and Applied Sciences*, 30 (3), 227-240.
- An, N., Turp, M. T., Türkeş, M., and Kurnaz, M. L., 2020, Mid-term impact of climate change on hazelnut yield, *Agriculture*, 10 (5), 159.
- Aydin, N. and Biyikoglu, A., 2020, The effect of cooling load on optimum insulation thickness in residential buildings, *Journal of Thermal Science and Technology*, 40 (2), 281-291.
- Aydin, N. and Biyikoglu, A., 2021, Determination of optimum insulation thickness by life cycle cost analysis for residential buildings in Turkey, *Science and Technology for the Built Environment*, 27 (1), 2-13.
- Baniassadi, A., Sajadi, B., Amidpour, M., and Noori, N., 2016, Economic optimization of PCM and insulation layer thickness in residential buildings, *Sustainable Energy Technologies and Assessments*, 14, 92-99.
- Bolatturk, A., 2006, Determination of optimum insulation thickness for building walls with respect to various fuels and climate zones in Turkey, *Applied Thermal Engineering*, 26 (11-12), 1301-1309.
- Bolatturk, A., 2008, Optimum insulation thicknesses for building walls with respect to cooling and heating degree-hours in the warmest zone of Turkey, *Building and Environment*, 43 (6), 1055-1064.
- Canbolat, A. S., Bademlioglu, A. H., and Kaynakli, O., 2018, Determination of proper insulation thickness for building walls regarding economic consideration, *International Research Journal of Advanced Engineering and Science*, 4, 173-176.
- Caglayan, S., Ozorhon, B., Ozcan-Deniz, G., and Yigit, S., 2020, A lifecycle costing approach to determine the optimum insulation thickness of existing buildings, *Journal of Thermal Science and Technology*, 40 (1), 1-14.
- Cao, X., Dai, X., and Liu, J., 2016, Building energy-consumption status worldwide and the state-of-the-art technologies for zero-energy buildings during the past decade, *Energy and Buildings*, 128, 198-213.
- Comakli, K. and Yuksel, B., 2003, Optimum insulation thickness of external walls for energy saving, *Applied Thermal Engineering*, 23 (4), 473-479.
- Daouas, N., Hassen, Z., and Aissia, H. B., 2010, Analytical periodic solution for the study of thermal performance and optimum insulation thickness of building walls in Tunisia, *Applied Thermal Engineering*, 30 (4), 319-326.
- Demircan, M., Gürkan, H., Eskioğlu, O., Arabaci, H., and Coşkun, M., 2017, Climate change projections for Turkey: Three models and two scenarios, *Turkish Journal of Water Science and Management*, 1 (1), 22-43.
- Demiroglu, O. C., Turp, M. T., Ozturk, T., and Kurnaz, M. L., 2016, Impact of climate change on natural snow reliability, snowmaking capacities, and wind conditions of ski resorts in Northeast Turkey: A dynamical downscaling approach, *Atmosphere*, 7 (4), 52.
- Demiroglu, O. C., Turp, M. T., Kurnaz, M. L., and Abegg, B., 2021, The Ski Climate Index (SCI): fuzzification and a regional climate modeling application for Turkey, *International Journal of Biometeorology*, 65 (5), 763-777.

- Dombayci, O. A., Atalay, O., Acar, S. G., Ulu, E. Y., and Ozturk, H. K., 2017, Thermoeconomic method for determination of optimum insulation thickness of external walls for the houses: Case study for Turkey, *Sustainable Energy Technologies and Assessments*, 22, 1-8.
- Dombayci, O. A., Golcu, M., and Pancar, Y., 2006, Optimization of insulation thickness for external walls using different energy-sources, *Applied Energy*, 83 (9), 921-928.
- Ekici, B. B., Gulden, A. A., and Aksoy, U. T., 2012, A study on the optimum insulation thicknesses of various types of external walls with respect to different materials, fuels and climate zones in Turkey, *Applied Energy*, 92, 211-217.
- Erturk, M., 2016, Optimum insulation thicknesses of pipes with respect to different insulation materials, fuels and climate zones in Turkey, *Energy*, 113, 991-1003.
- Evin, D. and Ucar, A., 2019, Energy impact and eco-efficiency of the envelope insulation in residential buildings in Turkey, *Applied Thermal Engineering*, 154, 573-584.
- Giorgetta, M. A., Jungclaus, J., Reick, C. H., Legutke, S., Bader, J., Böttinger, M., ..., and Stevens, B., 2013, Climate and carbon cycle changes from 1850 to 2100 in MPI-ESM simulations for the Coupled Model Intercomparison Project phase 5, *Journal of Advances in Modeling Earth Systems*, 5 (3), 572-597.
- Giorgi, F., Coppola, E., Solmon, F., Mariotti, L., Sylla, M. B., Bi, X., ..., and Brankovic, C., 2012, RegCM4: model description and preliminary tests over multiple CORDEX domains, *Climate Research*, 52, 7-29.
- Gulden, A., 2020, Determination of optimum insulation thickness using the entransy based thermoeconomic and environmental analysis: A case study for Turkey, *Energy Sources, Part A: Recovery, Utilization, and Environmental Effects*, 42 (2), 219-232.
- IEO (International Energy Outlook), 2013, *Technical Report*, Energy Information Administration, Washington, United States.
- IGDAS, 2021, Istanbul Gaz Dagitim Sanayi ve Ticaret A.S., *Retailing Price*, <https://www.igdastanbul.com>.
- Jraida, K., Farchi, A., Mounir, B., and Mounir, I., 2017, A study on the optimum insulation thicknesses of building walls with respect to different zones in Morocco, *International Journal of Ambient Energy*, 38 (6), 550-555.
- Kaya, M., Firat, I., and Comakli, O., 2016, Economic analysis of effect on energy saving of thermal insulation at buildings in Erzincan Province, *Journal of Thermal Science and Technology*, 36 (1), 47-55.
- Kayfeci, M., 2014, Determination of energy saving and optimum insulation thicknesses of the heating piping systems for different insulation materials, *Energy and Buildings*, 69, 278-284.
- Kaynakli, O., 2008, A study on residential heating energy requirement and optimum insulation thickness, *Renewable Energy*, 33 (6), 1164-1172.
- Kaynakli, O., 2013, Optimum thermal insulation thicknesses and payback periods for building walls in Turkey, *Journal of Thermal Science and Technology*, 33 (2), 45-55.
- Kon, O. and Yuksel, B., 2016, Optimum insulation thickness calculated by measuring of roof, floor and exterior walls in buildings used for different purposes, *Journal of Thermal Science and Technology*, 36 (1), 17-27.
- Kurekci, N. A., 2016, Determination of optimum insulation thickness for building walls by using heating and cooling degree-day values of all Turkey's provincial centers, *Energy and Buildings*, 118, 197-213.
- Leuenberger, M., Parente, J., Tonini, M., Pereira, M. G., and Kanevski, M., 2018, Wildfire susceptibility mapping: Deterministic vs. stochastic approaches, *Environmental Modelling & Software*, 101, 194-203.
- Liu, X., Chen, Y., Ge, H., Fazio, P., Chen, G., and Guo, X., 2015, Determination of optimum insulation thickness for building walls with moisture transfer in hot summer and cold winter zone of China, *Energy and Buildings*, 109, 361-368.
- Maleviti, E., Wehrmeyer, W., and Mulugetta, Y., 2013, An Empirical Assessment to Express the Variability of Buildings' Energy Consumption, *International Journal of Energy Optimization and Engineering (IJEEO)*, 2 (3), 55-67.
- MENR (Republic of Turkey Ministry of Energy and Natural Resources), 2020, *Energy Efficiency*, <http://www.enerji.gov.tr/en-US/Pages/Energy-Efficiency>.
- MFA (Republic of Turkey Ministry of Foreign Affairs), 2021, *Turkey's Energy Profile and Strategy*, <http://www.mfa.gov.tr/turkeys-energy-strategy.en.mfa>.
- Nematchoua, M. K., Ricciardi, P., Reiter, S., and Yvon, A., 2017, A comparative study on optimum insulation

- thickness of walls and energy savings in equatorial and tropical climate, *International Journal of Sustainable Built Environment*, 6 (1), 170-182.
- Ozkan, D. B. and Onan, C., 2011, Optimization of insulation thickness for different glazing areas in buildings for various climatic regions in Turkey, *Applied Energy*, 88 (4), 1331-1342.
- Ozel, G., Acikkalp, E., Gorgun, B., Yamik, H., and Caner, N., 2015, Optimum insulation thickness determination using the environmental and life cycle cost analyses based entransy approach, *Sustainable Energy Technologies and Assessments*, 11, 87-91.
- Revelle, C. S., Whitlatch, E. E., and Wright, J. R., 2005, *Civil and Environmental Systems Engineering*, Prentice Hall PTR, New Jersey.
- Riahi, K., Grübler, A., and Nakicenovic, N., 2007, Scenarios of long-term socio-economic and environmental development under climate stabilization, *Technological Forecasting and Social Change*, 74 (7), 887-935.
- Riahi, K., Rao, S., Krey, V., Cho, C., Chirkov, V., Fischer, G., ..., and Rafaj, P., 2011, RCP 8.5 - A scenario of comparatively high greenhouse gas emissions, *Climatic Change*, 109 (1), 33-57.
- Sahin, M., Kaya, Y., and Uyar, M., 2013, Comparison of ANN and MLR models for estimating solar radiation in Turkey using NOAA/AVHRR data, *Advances in Space Research*, 51 (5), 891-904.
- Sherwood, S. C., Bony, S., and Dufresne, J. L., 2014, Spread in model climate sensitivity traced to atmospheric convective mixing, *Nature*, 505 (7481), 37-42.
- Sisman, N., Kahya, E., Aras, N., and Aras, H., 2007, Determination of optimum insulation thicknesses of the external walls and roof (ceiling) for Turkey's different degree-day regions, *Energy Policy*, 35 (10), 5151-5155.
- TCMB (Central Bank of Turkish Republic Interest Rate Statistics), 2021, *Interest Rate Statistics*, <https://www.tcmb.gov.tr/wps/wcm/connect/EN/TCMB+EN/Main+Menu/Statistics/Interest+Rate+Statistics>.
- TSI (Turkish Standard Institution), 2008, *TS 825: Thermal insulation requirements for buildings*, TSI, Ankara, Turkey.
- Turp, M. T., Öztürk, T., Türkeş, M., and Kurnaz, M. L., 2014, RegCM4.3.5 bölgesel iklim modelini kullanarak Türkiye ve çevresi bölgelerinin yakın gelecekteki hava sıcaklığı ve yağış klimatolojileri için öngörülen değişikliklerin incelenmesi [Investigation of projected changes for near future air temperature and precipitation climatology of Turkey and surrounding regions by using the regional climate model RegCM4.3.5], *Aegean Geographical Journal*, 23 (1), 1-24.
- Ucar, A. and Balo, F., 2009, Effect of fuel type on the optimum thickness of selected insulation materials for the four different climatic regions of Turkey, *Applied Energy*, 86 (5), 730-736.
- Zhan, J., Liu, W., Wu, F., Li, Z., and Wang, C., 2018, Life cycle energy consumption and greenhouse gas emissions of urban residential buildings in Guangzhou city, *Journal of Cleaner Production*, 194, 318-326.

APPENDIX A: MEAN AND STANDARD DEVIATION OF THE CLIMATE PROJECTION

Table A1. Mean and standard deviation of the climate projection for Adana-Düzce (°C)

Province	Jan.	Febr.	Mar.	Apr.	May	June	July	Aug.	Sept.	Oct.	Nov.	Dec.
Adana	3.32 (2.62)	4.64 (3.11)	8.05 (3.31)	12.88 (3.72)	18.08 (4.18)	22.67 (3.31)	25.35 (2.24)	25.97 (2.90)	22.20 (3.34)	16.30 (3.72)	9.89 (2.94)	4.64 (2.95)
Adıyaman	1.43 (2.61)	2.98 (3.20)	6.79 (3.59)	12.53 (4.19)	18.91 (4.28)	24.33 (3.42)	27.46 (2.59)	27.44 (3.04)	23.06 (3.62)	16.10 (4.11)	8.56 (3.17)	2.85 (3.03)
Afyonkarahisar	0.89 (2.97)	1.92 (3.37)	4.83 (3.54)	9.41 (3.90)	14.98 (4.22)	19.70 (3.62)	22.54 (2.71)	22.79 (3.09)	18.16 (3.71)	11.87 (4.02)	6.46 (3.04)	2.03 (3.26)
Ağrı	-5.58 (3.42)	-4.48 (4.06)	-0.93 (3.93)	4.36 (3.56)	10.19 (3.55)	15.33 (3.32)	19.09 (3.21)	18.92 (3.15)	14.24 (3.43)	7.69 (3.73)	1.49 (3.04)	-3.85 (3.62)
Aksaray	1.11 (2.99)	2.40 (3.48)	5.82 (3.84)	10.94 (4.18)	16.42 (4.28)	21.10 (3.64)	23.90 (2.85)	24.21 (3.25)	19.66 (3.90)	13.27 (4.29)	7.21 (3.28)	2.24 (3.31)
Amasya	1.56 (2.99)	2.65 (3.58)	5.80 (3.91)	10.43 (4.10)	15.26 (4.17)	19.12 (3.75)	21.05 (3.25)	21.77 (3.74)	17.82 (4.28)	12.52 (4.19)	7.39 (3.17)	2.79 (3.21)
Ankara	0.86 (2.93)	1.96 (3.40)	5.08 (3.62)	9.76 (3.89)	15.12 (4.19)	19.84 (3.70)	22.57 (2.87)	23.00 (3.29)	18.34 (3.94)	12.05 (4.21)	6.49 (3.04)	2.00 (3.16)
Antalya	4.75 (2.46)	5.57 (2.69)	8.01 (2.99)	12.30 (3.62)	17.61 (4.14)	22.06 (3.53)	25.06 (2.43)	25.19 (2.73)	21.14 (3.19)	15.47 (3.41)	10.22 (2.66)	6.05 (2.68)
Ardahan	-6.49 (3.42)	-5.58 (4.12)	-2.38 (4.13)	2.57 (3.81)	7.98 (3.75)	12.41 (3.58)	15.51 (3.64)	15.95 (3.63)	11.63 (3.89)	5.99 (3.96)	0.49 (3.19)	-4.78 (3.69)
Artvin	-2.71 (3.24)	-1.78 (3.95)	1.26 (4.10)	6.06 (4.01)	11.21 (3.90)	14.89 (3.78)	17.19 (3.70)	17.94 (4.10)	14.27 (4.32)	9.20 (4.22)	3.97 (3.26)	-1.15 (3.51)
Aydın	6.57 (2.87)	7.36 (2.96)	9.68 (3.05)	13.84 (3.59)	19.44 (4.20)	24.76 (3.77)	27.93 (2.81)	27.84 (2.95)	23.26 (3.53)	17.15 (3.52)	11.93 (2.96)	7.71 (3.22)
Balıkesir	5.37 (3.02)	6.19 (3.20)	8.54 (3.19)	12.59 (3.47)	18.01 (3.97)	22.63 (3.46)	25.09 (2.81)	25.29 (3.01)	20.89 (3.70)	15.31 (3.53)	10.72 (2.93)	6.67 (3.25)
Bartın	4.43 (3.03)	5.25 (3.53)	7.87 (3.94)	12.04 (4.06)	16.79 (4.25)	20.70 (3.78)	22.56 (3.49)	23.13 (3.81)	19.05 (4.11)	14.35 (3.88)	10.17 (3.12)	5.78 (3.20)
Batman	1.22 (2.61)	2.88 (3.27)	6.83 (3.65)	12.68 (4.08)	19.29 (3.90)	25.20 (3.05)	28.54 (2.20)	28.25 (2.48)	23.67 (3.10)	16.46 (3.85)	8.66 (3.15)	2.66 (3.05)
Bayburt	-5.75 (3.27)	-4.61 (3.93)	-1.30 (4.00)	3.69 (3.71)	9.22 (3.89)	13.95 (3.76)	16.90 (3.61)	17.16 (3.81)	12.92 (4.03)	7.08 (3.99)	1.38 (3.17)	-4.18 (3.66)
Bilecik	2.94 (3.19)	3.92 (3.65)	6.78 (3.88)	11.13 (4.05)	16.38 (4.35)	20.55 (3.77)	22.80 (3.13)	23.16 (3.57)	18.78 (4.10)	13.27 (4.10)	8.62 (3.19)	4.22 (3.35)
Bingöl	-4.30 (3.10)	-3.01 (3.72)	0.59 (3.80)	5.98 (3.66)	12.03 (3.82)	17.97 (3.42)	21.76 (2.63)	21.61 (2.87)	16.78 (3.39)	9.89 (3.81)	3.14 (3.17)	-2.70 (3.53)
Bitlis	-3.36 (2.83)	-2.25 (3.39)	0.96 (3.44)	5.84 (3.44)	11.52 (3.46)	16.93 (2.98)	20.42 (2.39)	20.17 (2.52)	15.83 (3.00)	9.43 (3.45)	3.21 (2.83)	-1.85 (3.14)
Bolu	-0.12 (3.15)	0.84 (3.60)	3.79 (3.89)	8.22 (4.01)	13.38 (4.27)	17.82 (3.87)	20.12 (3.34)	20.73 (3.82)	16.36 (4.32)	10.80 (4.24)	5.81 (3.20)	1.20 (3.33)
Burdur	1.64 (2.79)	2.66 (3.02)	5.40 (3.32)	10.08 (3.84)	15.77 (4.21)	20.56 (3.60)	23.70 (2.50)	23.70 (2.89)	19.01 (3.43)	12.71 (3.75)	7.20 (2.93)	2.81 (3.08)
Bursa	4.68 (3.00)	5.53 (3.38)	8.12 (3.61)	12.28 (3.85)	17.56 (4.19)	21.82 (3.62)	24.05 (3.02)	24.37 (3.33)	19.99 (3.91)	14.66 (3.76)	10.18 (2.98)	5.99 (3.17)
Çanakkale	7.01 (3.27)	7.72 (3.21)	9.69 (2.89)	13.38 (2.92)	18.39 (3.41)	22.92 (3.08)	25.47 (2.54)	25.63 (2.61)	21.54 (3.22)	16.43 (3.05)	12.22 (2.98)	8.52 (3.40)
Çankırı	-0.32 (3.04)	0.68 (3.52)	3.83 (3.82)	8.44 (3.96)	13.55 (4.14)	17.99 (3.76)	20.42 (3.16)	21.02 (3.57)	16.53 (4.18)	10.78 (4.18)	5.47 (3.10)	0.94 (3.19)
Çorum	0.89 (2.92)	2.02 (3.47)	5.25 (3.81)	9.94 (4.03)	15.02 (4.20)	19.29 (3.79)	21.56 (3.17)	22.19 (3.61)	17.89 (4.19)	12.08 (4.25)	6.65 (3.13)	2.10 (3.14)
Denizli	2.80 (2.94)	3.83 (3.17)	6.60 (3.49)	11.22 (3.98)	17.01 (4.35)	22.07 (3.67)	25.16 (2.66)	25.21 (3.01)	20.49 (3.58)	14.08 (3.89)	8.46 (3.09)	3.97 (3.20)
Diyarbakır	1.13 (2.62)	2.75 (3.22)	6.65 (3.56)	12.61 (3.99)	19.26 (4.03)	25.29 (3.20)	28.71 (2.27)	28.40 (2.61)	23.67 (3.22)	16.31 (3.90)	8.51 (3.10)	2.57 (3.03)
Düzce	3.68 (3.12)	4.59 (3.61)	7.30 (4.02)	11.47 (4.13)	16.22 (4.33)	19.99 (3.78)	21.87 (3.37)	22.37 (3.77)	18.38 (4.09)	13.65 (3.97)	9.48 (3.24)	5.00 (3.29)

Table A2. Mean and standard deviation of the climate projection for Edirne-Kütahya (°C)

Province	Jan.	Febr.	Mar.	Apr.	May	June	July	Aug.	Sept.	Oct.	Nov.	Dec.
Edirne	5.25 (4.31)	6.73 (3.85)	9.34 (3.17)	13.48 (2.89)	18.74 (3.46)	23.67 (3.31)	26.24 (2.79)	26.24 (2.86)	21.75 (3.62)	15.87 (3.62)	10.97 (3.82)	6.76 (4.27)
Elazığ	-1.04 (2.84)	0.35 (3.39)	4.06 (3.60)	9.67 (3.81)	15.86 (4.01)	21.69 (3.51)	25.27 (2.62)	25.05 (2.93)	20.29 (3.53)	13.20 (3.98)	6.12 (2.99)	0.47 (3.23)
Erzincan	-4.77 (3.18)	-3.57 (3.82)	-0.11 (3.87)	5.10 (3.73)	10.83 (3.93)	15.88 (3.69)	19.17 (3.33)	19.31 (3.53)	14.83 (3.94)	8.52 (3.99)	2.43 (3.12)	-3.20 (3.58)
Erzurum	-6.17 (3.32)	-5.07 (4.02)	-1.65 (3.99)	3.44 (3.64)	9.05 (3.66)	13.98 (3.44)	17.30 (3.22)	17.41 (3.33)	12.95 (3.61)	6.86 (3.80)	0.97 (3.14)	-4.51 (3.65)
Eskişehir	1.61 (3.09)	2.68 (3.56)	5.72 (3.76)	10.32 (4.01)	15.79 (4.30)	20.43 (3.69)	23.01 (2.88)	23.39 (3.30)	18.77 (3.93)	12.61 (4.18)	7.27 (3.18)	2.76 (3.33)
Gaziantep	3.23 (2.60)	4.80 (3.05)	8.48 (3.43)	14.06 (4.10)	20.16 (4.32)	25.30 (3.28)	28.01 (2.47)	28.35 (2.94)	24.23 (3.39)	17.45 (3.92)	9.96 (3.04)	4.46 (3.01)
Giresun	-1.09 (3.06)	-0.10 (3.70)	2.91 (3.95)	7.62 (4.00)	12.43 (4.04)	16.02 (3.73)	17.91 (3.44)	18.61 (4.00)	15.19 (4.31)	10.46 (4.09)	5.49 (3.25)	0.35 (3.41)
Gümüşhane	-4.88 (3.24)	-3.80 (3.89)	-0.58 (3.97)	4.35 (3.81)	9.76 (3.97)	13.95 (3.79)	16.47 (3.65)	16.93 (3.98)	13.02 (4.25)	7.54 (4.06)	2.05 (3.21)	-3.34 (3.60)
Hakkari	-5.05 (3.37)	-3.67 (3.89)	0.09 (3.92)	5.53 (3.78)	11.29 (3.49)	16.84 (3.04)	20.62 (2.71)	20.40 (2.62)	15.96 (3.18)	9.10 (3.59)	2.42 (3.24)	-3.29 (3.68)
Hatay	7.08 (2.53)	8.30 (2.83)	11.32 (2.97)	15.62 (3.58)	20.04 (4.11)	23.98 (3.15)	25.92 (2.31)	27.08 (3.06)	24.21 (3.16)	19.29 (3.49)	13.17 (2.78)	8.15 (2.87)
İğdır	-2.39 (3.17)	-1.19 (3.82)	2.52 (3.79)	8.20 (3.81)	14.01 (3.65)	18.47 (3.52)	21.98 (3.90)	22.03 (3.52)	17.53 (3.84)	10.82 (4.05)	4.22 (3.04)	-0.86 (3.30)
Isparta	0.81 (2.77)	1.74 (3.06)	4.43 (3.26)	8.87 (3.75)	14.32 (4.13)	18.87 (3.55)	21.82 (2.56)	21.98 (2.95)	17.53 (3.49)	11.45 (3.82)	6.21 (2.86)	1.95 (3.02)
İstanbul	7.36 (3.09)	7.97 (3.01)	10.02 (2.87)	13.57 (2.93)	18.22 (3.29)	22.24 (2.83)	24.38 (2.38)	24.81 (2.54)	21.22 (2.87)	16.70 (2.92)	12.73 (2.93)	8.66 (3.35)
İzmir	7.63 (2.87)	8.28 (2.90)	10.26 (2.75)	13.96 (3.08)	19.23 (3.84)	24.46 (3.58)	27.44 (2.71)	27.51 (2.86)	23.11 (3.43)	17.41 (3.28)	12.77 (2.81)	8.88 (3.16)
Kahramanmaraş	-0.88 (2.97)	0.46 (3.51)	4.09 (3.63)	9.33 (3.91)	15.03 (4.17)	20.03 (3.42)	23.13 (2.49)	23.35 (3.01)	19.07 (3.58)	12.59 (3.91)	6.02 (3.04)	0.59 (3.30)
Karabük	1.31 (3.17)	2.26 (3.69)	5.18 (4.08)	9.59 (4.18)	14.53 (4.33)	18.79 (3.92)	20.83 (3.53)	21.51 (3.98)	17.17 (4.44)	12.01 (4.25)	7.26 (3.32)	2.64 (3.37)
Karaman	0.13 (3.17)	1.33 (3.59)	4.62 (3.86)	9.76 (4.15)	15.21 (4.21)	19.77 (3.50)	22.89 (2.55)	22.99 (2.90)	18.48 (3.56)	12.14 (3.97)	6.29 (3.21)	1.45 (3.43)
Kars	-5.72 (3.40)	-4.69 (4.05)	-1.28 (3.90)	3.98 (3.56)	9.70 (3.55)	14.28 (3.32)	17.61 (3.43)	17.72 (3.29)	13.21 (3.62)	7.00 (3.73)	1.13 (2.99)	-3.98 (3.56)
Kastamonu	0.89 (3.07)	1.79 (3.61)	4.70 (4.03)	9.05 (4.08)	13.85 (4.16)	17.83 (3.75)	19.74 (3.35)	20.49 (3.81)	16.38 (4.29)	11.49 (4.11)	6.81 (3.21)	2.24 (3.25)
Kayseri	-2.07 (3.25)	-0.89 (3.80)	2.63 (3.90)	7.76 (4.07)	13.18 (4.22)	17.83 (3.73)	20.80 (3.14)	21.22 (3.47)	16.86 (4.07)	10.58 (4.20)	4.59 (3.26)	-0.70 (3.58)
Kilis	4.03 (2.54)	5.59 (3.01)	9.22 (3.47)	14.68 (4.23)	20.56 (4.51)	25.55 (3.42)	28.04 (2.66)	28.61 (3.13)	24.71 (3.50)	18.17 (3.96)	10.77 (3.10)	5.23 (2.97)
Kırıkkale	1.43 (2.91)	2.60 (3.44)	5.82 (3.73)	10.67 (4.02)	15.97 (4.24)	20.55 (3.76)	23.18 (2.96)	23.63 (3.35)	19.00 (3.97)	12.70 (4.23)	7.02 (3.13)	2.49 (3.17)
Kırklareli	4.07 (4.04)	5.55 (3.74)	8.25 (3.27)	12.46 (3.11)	17.63 (3.60)	22.19 (3.36)	24.45 (2.90)	24.54 (3.04)	20.29 (3.58)	14.72 (3.59)	9.89 (3.71)	5.49 (4.07)
Kırşehir	0.65 (2.98)	1.85 (3.52)	5.22 (3.81)	10.16 (4.12)	15.58 (4.35)	20.18 (3.81)	22.84 (3.08)	23.30 (3.49)	18.74 (4.11)	12.42 (4.39)	6.52 (3.22)	1.76 (3.27)
Kocaeli	6.69 (2.81)	7.28 (3.11)	9.48 (3.32)	13.25 (3.46)	17.96 (3.72)	21.84 (3.21)	23.83 (2.73)	24.27 (2.96)	20.44 (3.31)	15.87 (3.20)	11.99 (2.77)	8.04 (2.94)
Konya	0.98 (3.03)	2.16 (3.43)	5.31 (3.71)	10.28 (4.02)	15.71 (4.14)	20.24 (3.54)	23.12 (2.67)	23.35 (3.02)	18.76 (3.69)	12.44 (4.05)	6.77 (3.14)	2.12 (3.31)
Kütahya	1.00 (3.10)	2.04 (3.48)	4.86 (3.61)	9.20 (3.92)	14.75 (4.37)	19.58 (3.76)	22.22 (2.97)	22.56 (3.43)	17.97 (4.01)	11.86 (4.11)	6.71 (3.12)	2.25 (3.37)

Table A3. Mean and standard deviation of the climate projection for Malatya-Zonguldak (°C)

Province	Jan.	Febr.	Mar.	Apr.	May	June	July	Aug.	Sept.	Oct.	Nov.	Dec.
Malatya	-1.61 (2.99)	-0.28 (3.51)	3.40 (3.66)	8.93 (3.89)	14.82 (4.06)	20.12 (3.60)	23.52 (2.90)	23.49 (3.18)	18.91 (3.79)	12.08 (4.05)	5.31 (3.03)	-0.15 (3.33)
Manisa	5.03 (2.97)	5.99 (3.13)	8.54 (3.24)	12.88 (3.72)	18.76 (4.35)	24.09 (3.79)	26.97 (2.86)	27.09 (3.22)	22.24 (3.86)	15.87 (3.87)	10.50 (3.04)	6.18 (3.29)
Mardin	2.58 (2.50)	4.43 (3.11)	8.56 (3.70)	14.71 (4.36)	21.53 (4.05)	27.36 (3.00)	30.43 (2.16)	30.24 (2.48)	25.74 (3.11)	18.37 (3.86)	10.09 (3.25)	3.94 (2.92)
Mersin	3.44 (2.57)	4.58 (2.99)	7.68 (3.36)	12.55 (3.88)	17.79 (4.25)	22.24 (3.43)	25.07 (2.37)	25.47 (2.89)	21.48 (3.30)	15.66 (3.61)	9.54 (2.88)	4.76 (2.83)
Muğla	7.35 (2.39)	7.95 (2.50)	9.94 (2.69)	13.69 (3.32)	18.82 (4.06)	23.69 (3.67)	26.90 (2.69)	26.81 (2.71)	22.87 (3.18)	17.35 (3.09)	12.54 (2.61)	8.62 (2.65)
Muş	-4.21 (3.26)	-2.93 (3.84)	0.66 (3.70)	6.03 (3.47)	12.28 (3.67)	18.08 (3.24)	21.77 (2.56)	21.44 (2.73)	16.57 (3.21)	9.67 (3.63)	3.08 (2.95)	-2.51 (3.52)
Nevşehir	0.27 (3.12)	1.49 (3.70)	4.99 (3.97)	10.09 (4.28)	15.54 (4.40)	20.18 (3.83)	22.91 (3.15)	23.34 (3.52)	18.87 (4.18)	12.56 (4.41)	6.49 (3.35)	1.45 (3.45)
Niğde	-1.83 (3.30)	-0.60 (3.80)	2.87 (3.95)	8.03 (4.20)	13.49 (4.28)	18.19 (3.66)	21.32 (2.89)	21.60 (3.20)	17.21 (3.84)	10.91 (4.14)	4.80 (3.33)	-0.44 (3.60)
Ordu	1.89 (3.04)	2.82 (3.72)	5.69 (4.05)	10.12 (4.14)	14.50 (4.11)	17.72 (3.63)	19.27 (3.24)	20.12 (3.89)	16.93 (4.26)	12.67 (4.06)	8.16 (3.33)	3.26 (3.34)
Osmaniye	5.33 (2.50)	6.87 (3.05)	10.29 (3.36)	15.03 (3.91)	19.99 (4.38)	24.18 (3.39)	26.25 (2.61)	27.26 (3.25)	24.00 (3.47)	18.58 (3.84)	12.06 (3.06)	6.57 (2.89)
Rize	-1.36 (3.23)	-0.39 (3.96)	2.55 (4.29)	7.21 (4.22)	11.93 (4.07)	15.15 (3.90)	16.80 (3.70)	17.69 (4.28)	14.60 (4.55)	10.18 (4.38)	5.31 (3.50)	0.14 (3.59)
Sakarya	5.08 (3.05)	5.94 (3.48)	8.55 (3.75)	12.64 (3.87)	17.46 (4.11)	21.17 (3.54)	23.06 (3.05)	23.46 (3.40)	19.52 (3.73)	14.72 (3.66)	10.63 (3.04)	6.35 (3.19)
Samsun	4.12 (2.96)	5.00 (3.56)	7.72 (3.84)	11.91 (3.90)	16.31 (3.92)	19.80 (3.39)	21.54 (2.96)	22.35 (3.45)	18.74 (3.87)	14.27 (3.78)	9.83 (3.09)	5.38 (3.09)
Şanlıurfa	3.59 (2.44)	5.35 (2.99)	9.31 (3.57)	15.31 (4.26)	21.91 (4.16)	27.45 (3.17)	30.33 (2.34)	30.36 (2.76)	25.98 (3.32)	18.79 (3.88)	10.79 (3.16)	4.87 (2.84)
Siirt	-0.68 (2.82)	0.86 (3.45)	4.69 (3.74)	10.29 (4.04)	16.65 (3.86)	22.53 (3.04)	25.96 (2.19)	25.72 (2.45)	21.15 (3.04)	14.16 (3.73)	6.73 (3.21)	0.86 (3.30)
Sinop	3.02 (2.95)	3.90 (3.53)	6.61 (3.88)	10.86 (3.97)	15.37 (3.99)	19.04 (3.51)	20.81 (3.13)	21.62 (3.59)	17.77 (4.00)	13.21 (3.87)	8.74 (3.09)	4.30 (3.07)
Sivas	-2.96 (3.22)	-1.83 (3.78)	1.58 (3.87)	6.73 (3.95)	12.07 (4.06)	16.43 (3.77)	19.15 (3.45)	19.61 (3.79)	15.44 (4.28)	9.46 (4.13)	3.74 (3.17)	-1.51 (3.50)
Şırnak	-0.93 (2.91)	0.71 (3.51)	4.69 (3.82)	10.43 (4.16)	16.91 (3.85)	22.78 (2.98)	26.24 (2.17)	26.02 (2.36)	21.46 (3.01)	14.31 (3.69)	6.68 (3.29)	0.68 (3.36)
Tekirdağ	5.73 (3.95)	6.95 (3.63)	9.38 (3.10)	13.38 (2.99)	18.50 (3.44)	23.02 (3.11)	25.45 (2.59)	25.58 (2.72)	21.42 (3.37)	16.04 (3.42)	11.41 (3.61)	7.13 (4.11)
Tokat	0.12 (3.15)	1.20 (3.77)	4.49 (4.11)	9.31 (4.26)	14.21 (4.29)	17.90 (3.97)	19.76 (3.59)	20.52 (4.13)	16.85 (4.62)	11.62 (4.37)	6.41 (3.33)	1.46 (3.43)
Trabzon	0.66 (3.10)	1.62 (3.83)	4.45 (4.19)	9.04 (4.27)	13.60 (4.25)	16.79 (3.94)	18.28 (3.55)	19.20 (4.23)	16.12 (4.56)	11.84 (4.32)	7.19 (3.43)	2.13 (3.45)
Tunceli	-3.28 (2.93)	-2.03 (3.53)	1.48 (3.69)	6.79 (3.68)	12.64 (3.86)	18.18 (3.55)	21.78 (2.93)	21.77 (3.18)	17.19 (3.64)	10.53 (3.93)	3.90 (3.07)	-1.74 (3.39)
Uşak	2.65 (2.91)	3.73 (3.19)	6.53 (3.42)	11.04 (3.94)	16.96 (4.47)	22.25 (3.79)	25.24 (2.85)	25.41 (3.27)	20.55 (3.83)	13.95 (4.09)	8.32 (3.06)	3.80 (3.20)
Van	-6.13 (3.31)	-5.03 (3.86)	-1.67 (3.80)	3.42 (3.45)	8.94 (3.30)	14.32 (2.94)	18.02 (2.59)	17.65 (2.56)	13.17 (2.95)	6.82 (3.35)	0.82 (2.97)	-4.41 (3.55)
Yalova	6.93 (2.72)	7.55 (3.10)	9.85 (3.41)	13.80 (3.60)	18.83 (3.91)	22.96 (3.41)	25.07 (2.89)	25.38 (3.08)	21.14 (3.53)	16.24 (3.28)	12.17 (2.71)	8.34 (2.82)
Yozgat	-0.32 (3.08)	0.83 (3.64)	4.28 (3.92)	9.20 (4.14)	14.50 (4.33)	18.87 (3.91)	21.31 (3.38)	21.90 (3.80)	17.64 (4.37)	11.58 (4.40)	5.85 (3.23)	0.93 (3.38)
Zonguldak	4.79 (3.07)	5.61 (3.56)	8.23 (3.97)	12.39 (4.08)	17.11 (4.27)	20.87 (3.71)	22.67 (3.34)	23.17 (3.69)	19.18 (3.99)	14.54 (3.84)	10.45 (3.13)	6.11 (3.22)

APPENDIX B: HISTOGRAM OF THE OPTIMUM INSULATION THICKNESSES

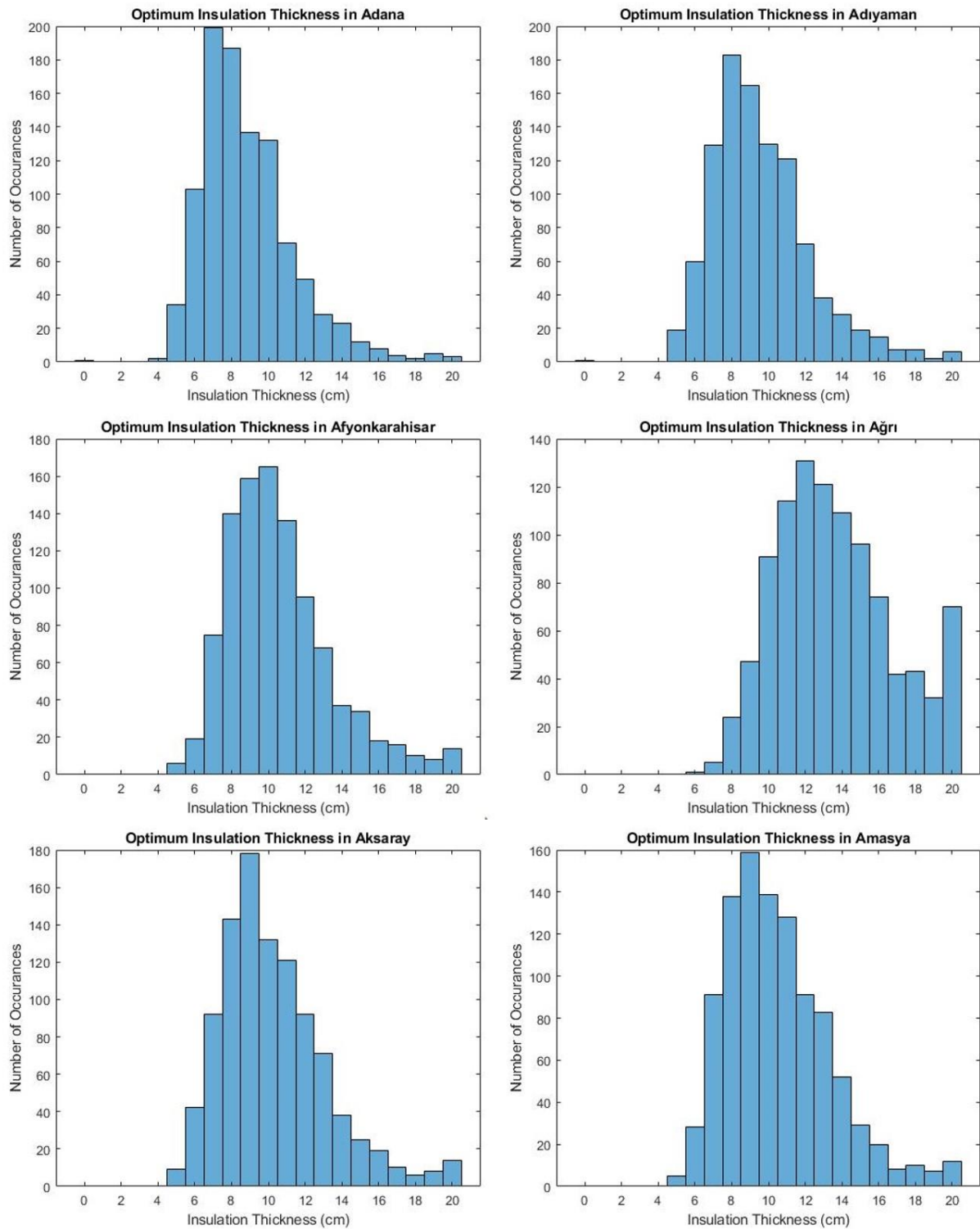


Figure B1. Optimum insulation thickness in Adana-Amasya

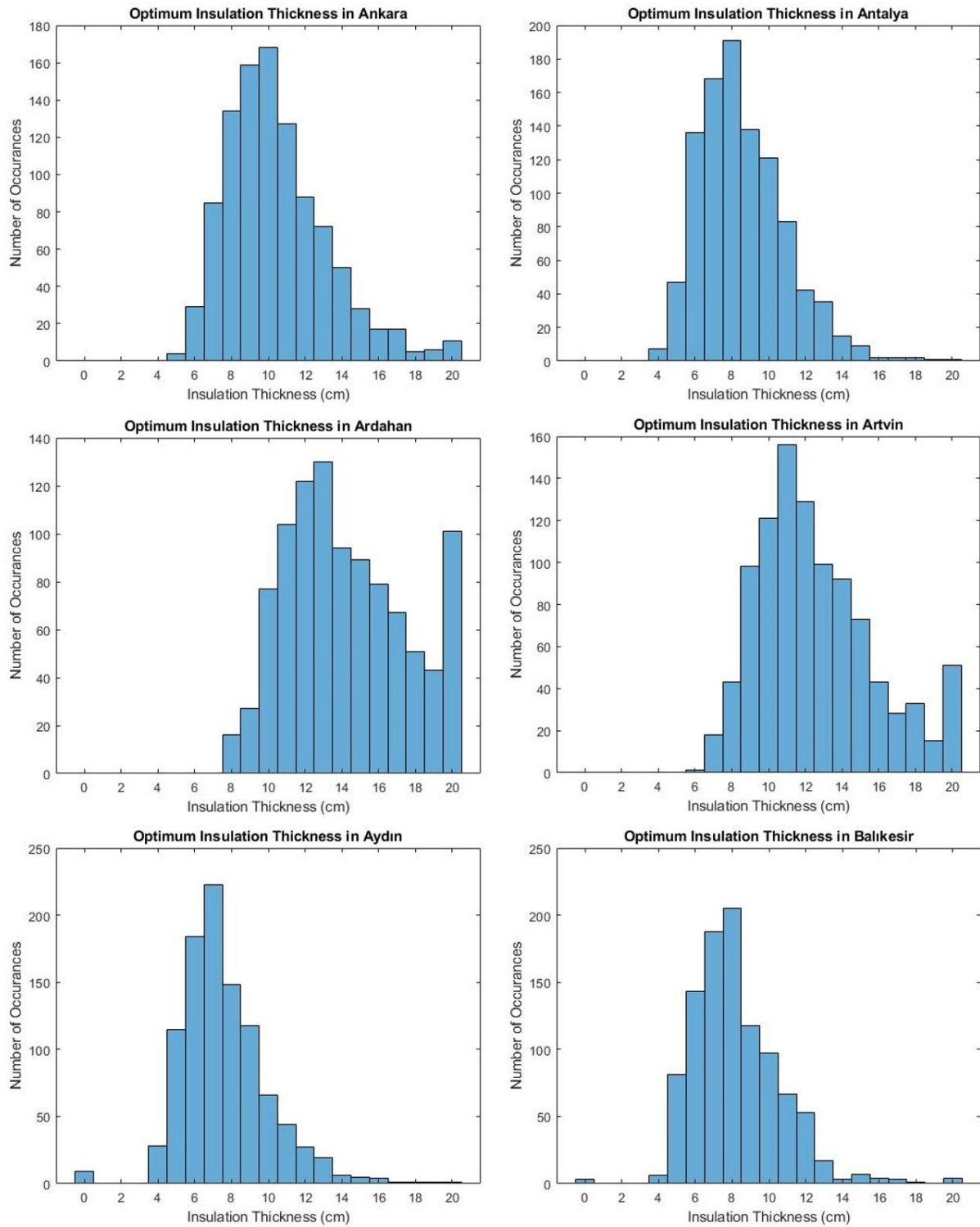


Figure B2. Optimum insulation thickness in Ankara-Balıkesir

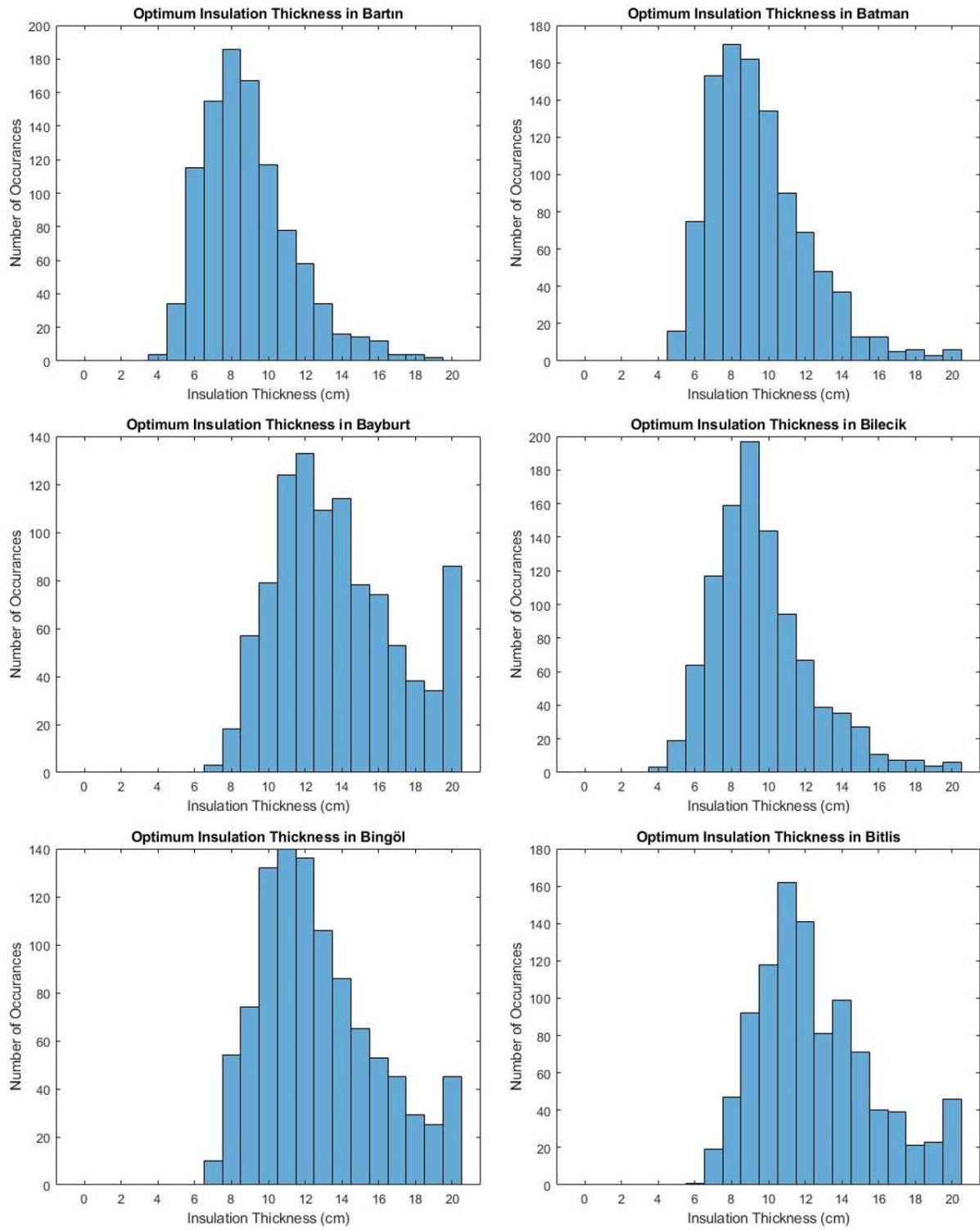


Figure B3. Optimum insulation thickness in Bartın-Bitlis

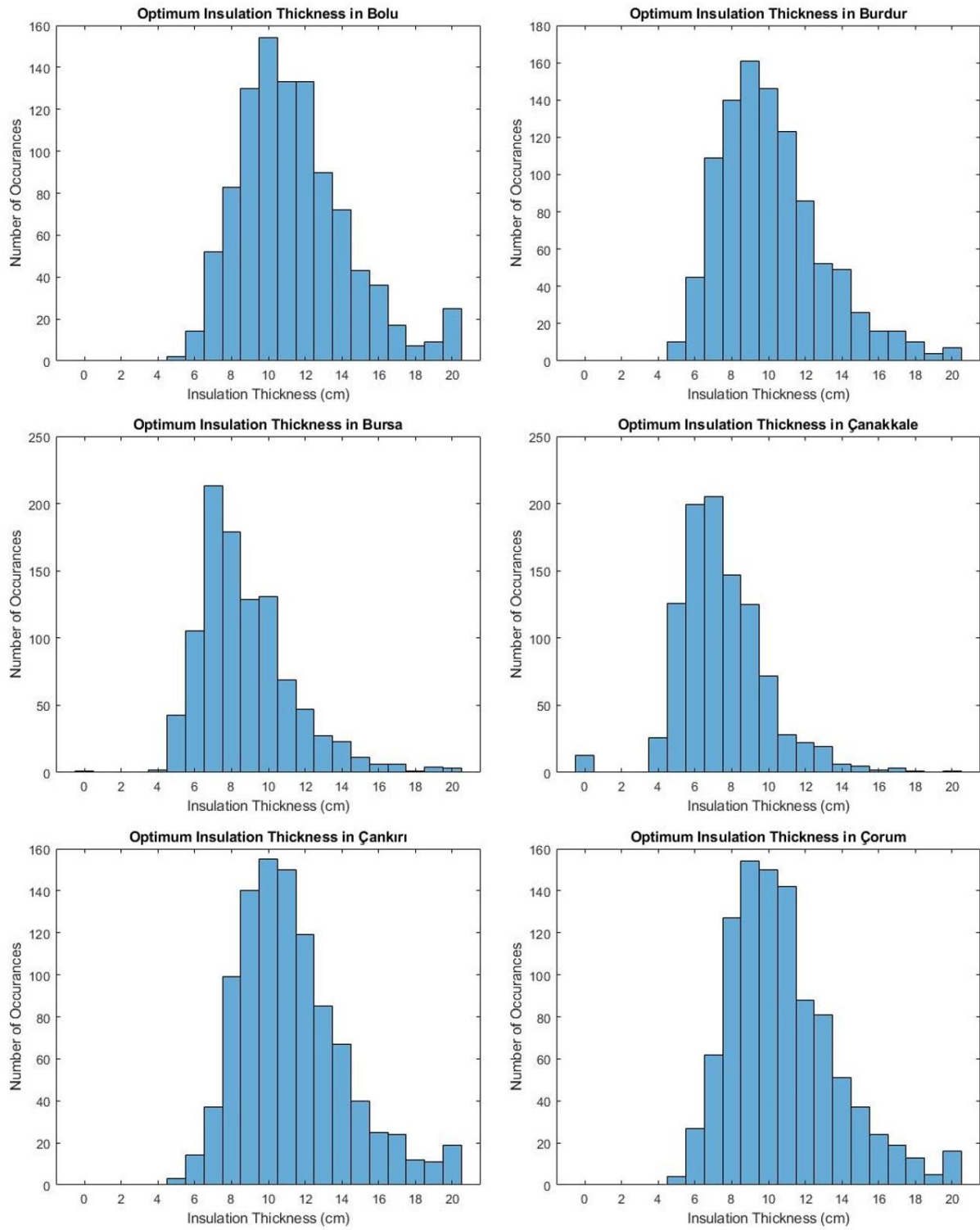


Figure B4. Optimum insulation thickness in Bolu-Çorum

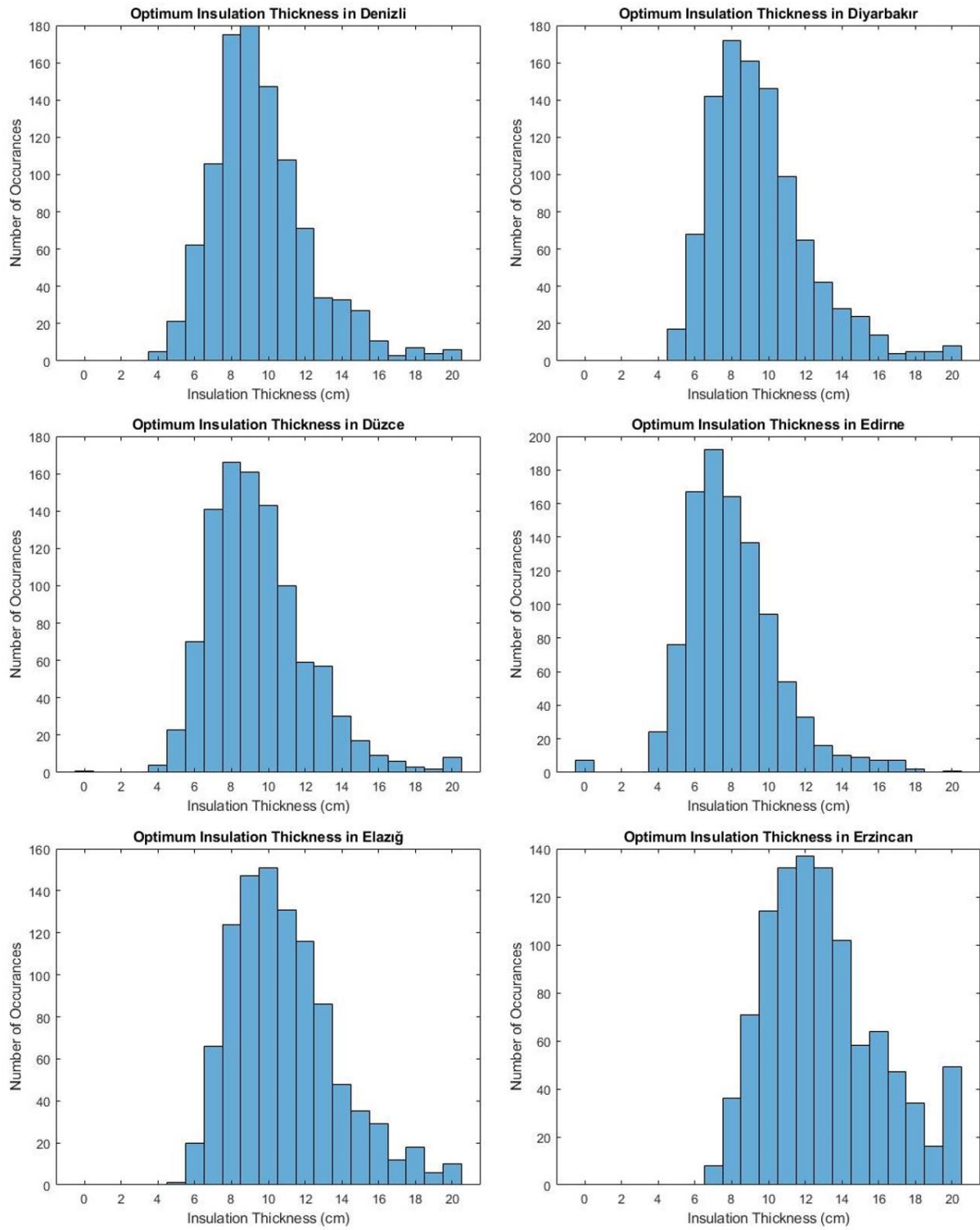


Figure B5. Optimum insulation thickness in Denizli-Erzincan

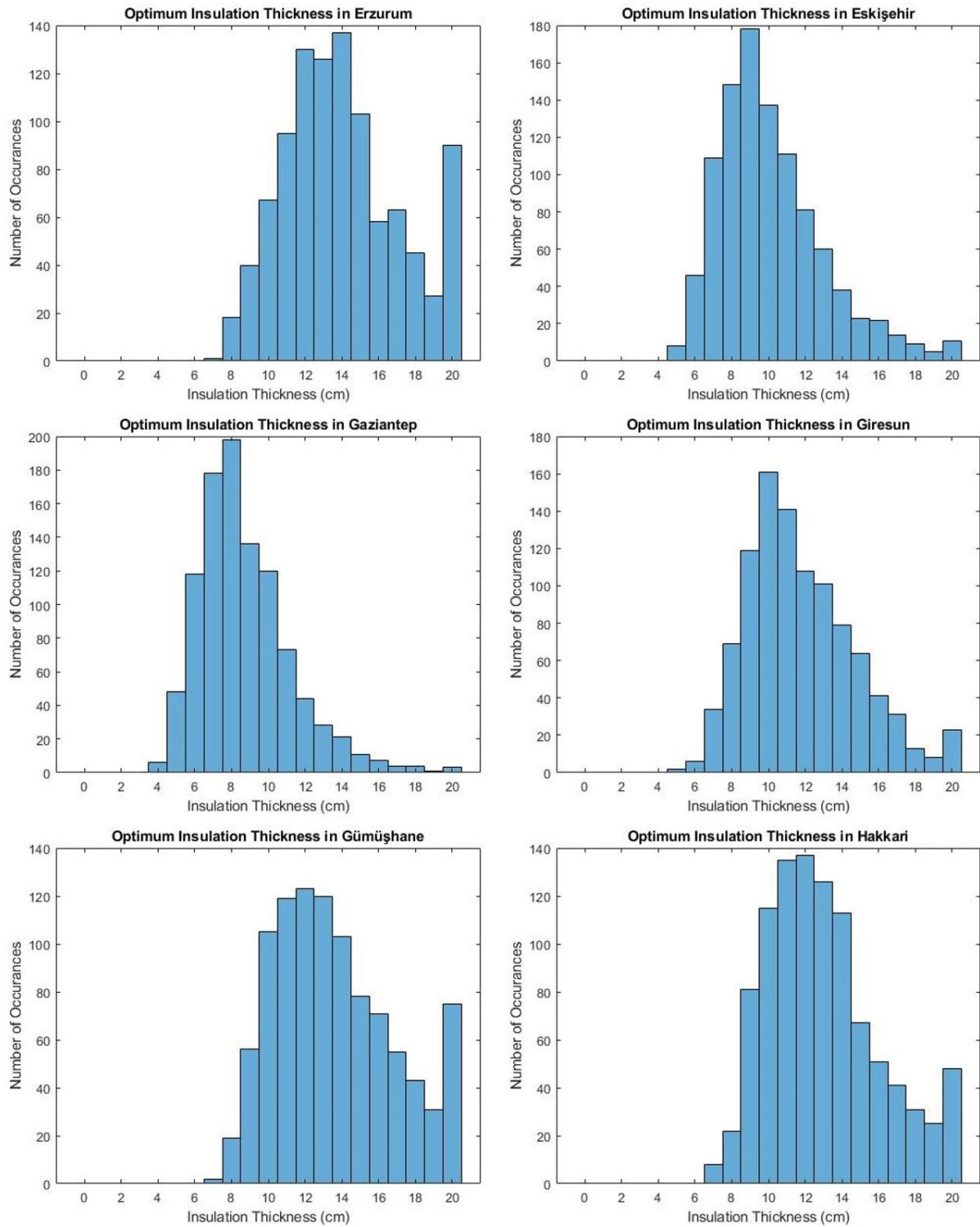


Figure B6. Optimum insulation thickness in Erzurum-Hakkari

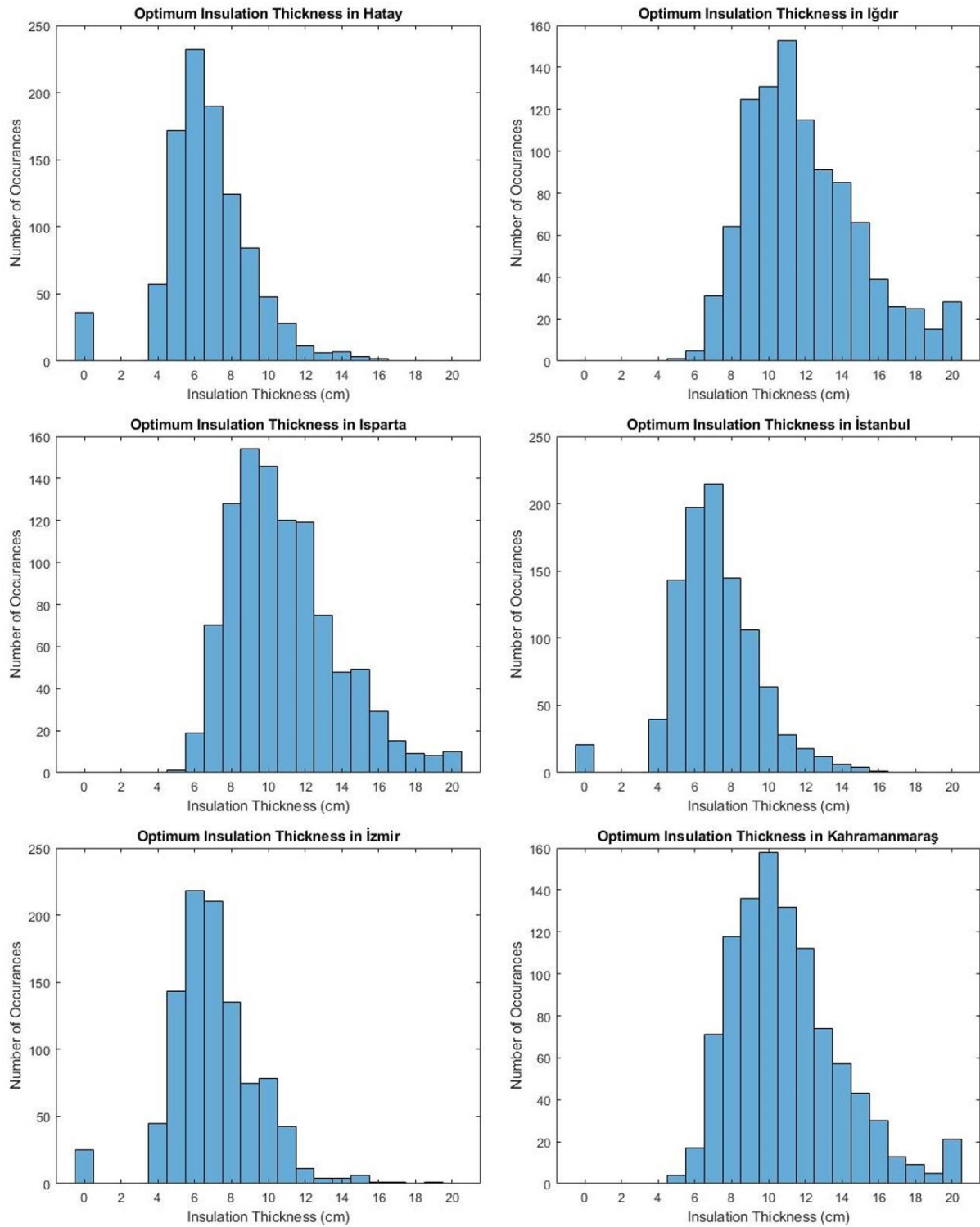


Figure B7. Optimum insulation thickness in Hatay-Kahramanmaraş

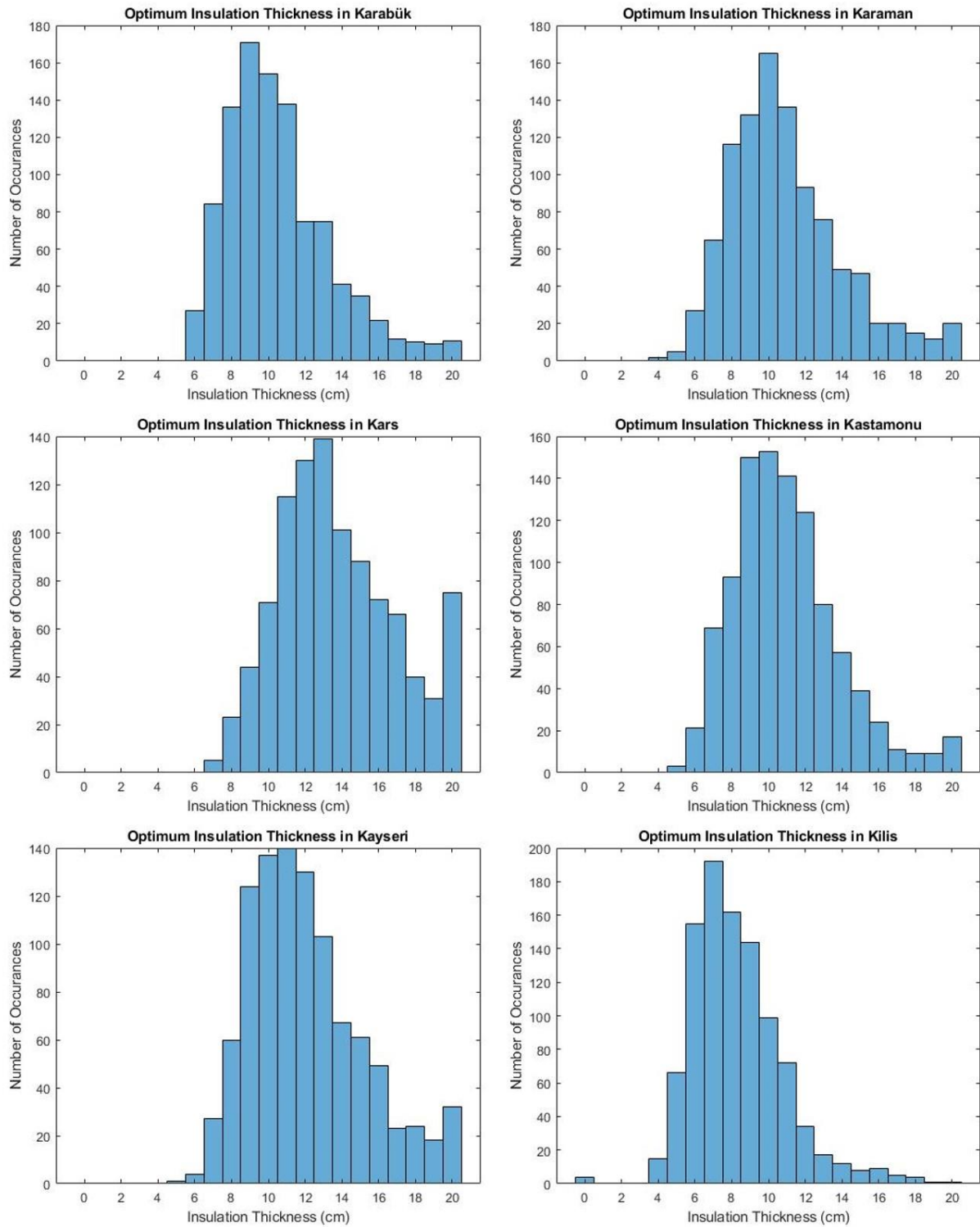


Figure B8. Optimum insulation thickness in Karabük-Kilis

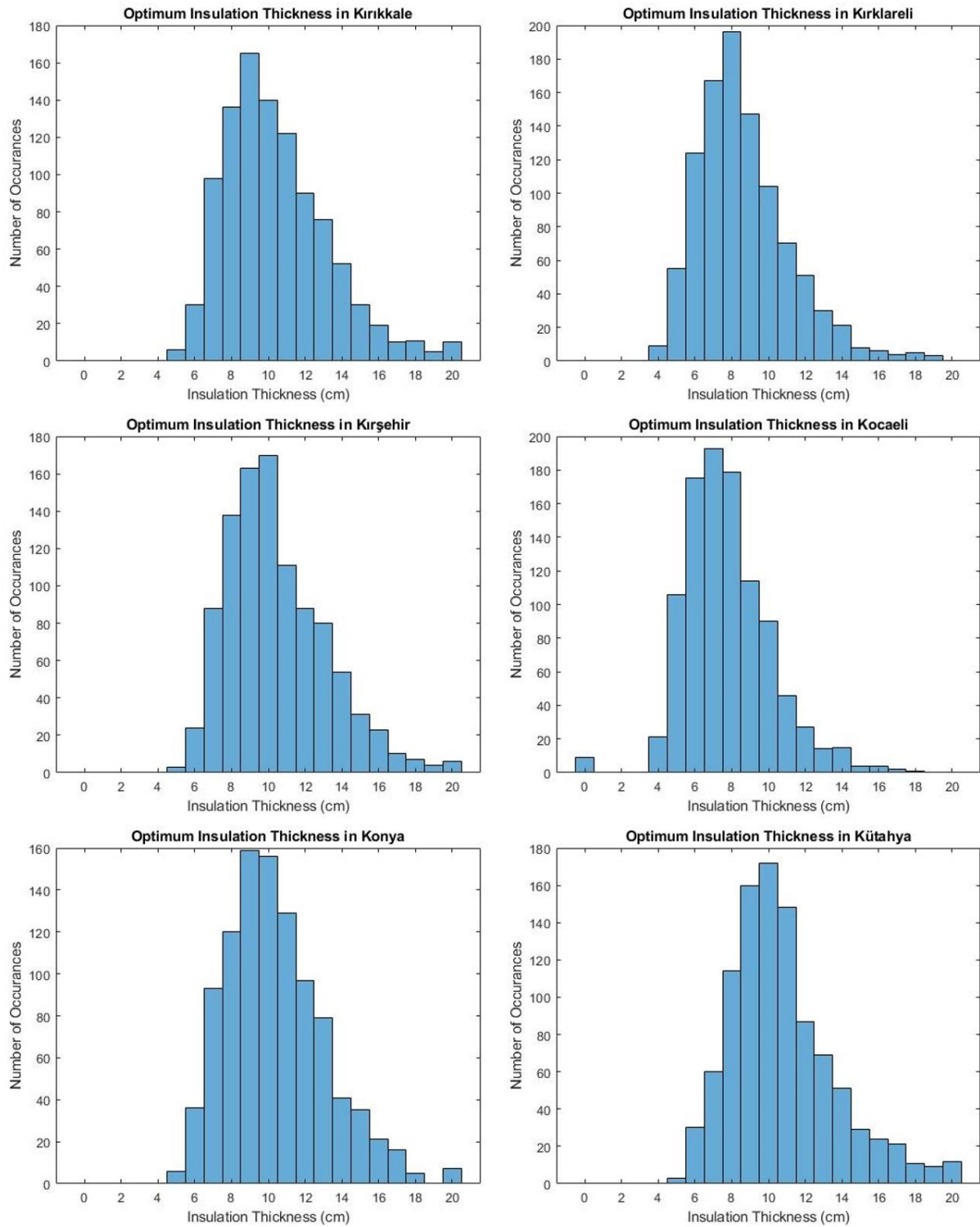


Figure B9. Optimum insulation thickness in Kırkkale-Kütahya

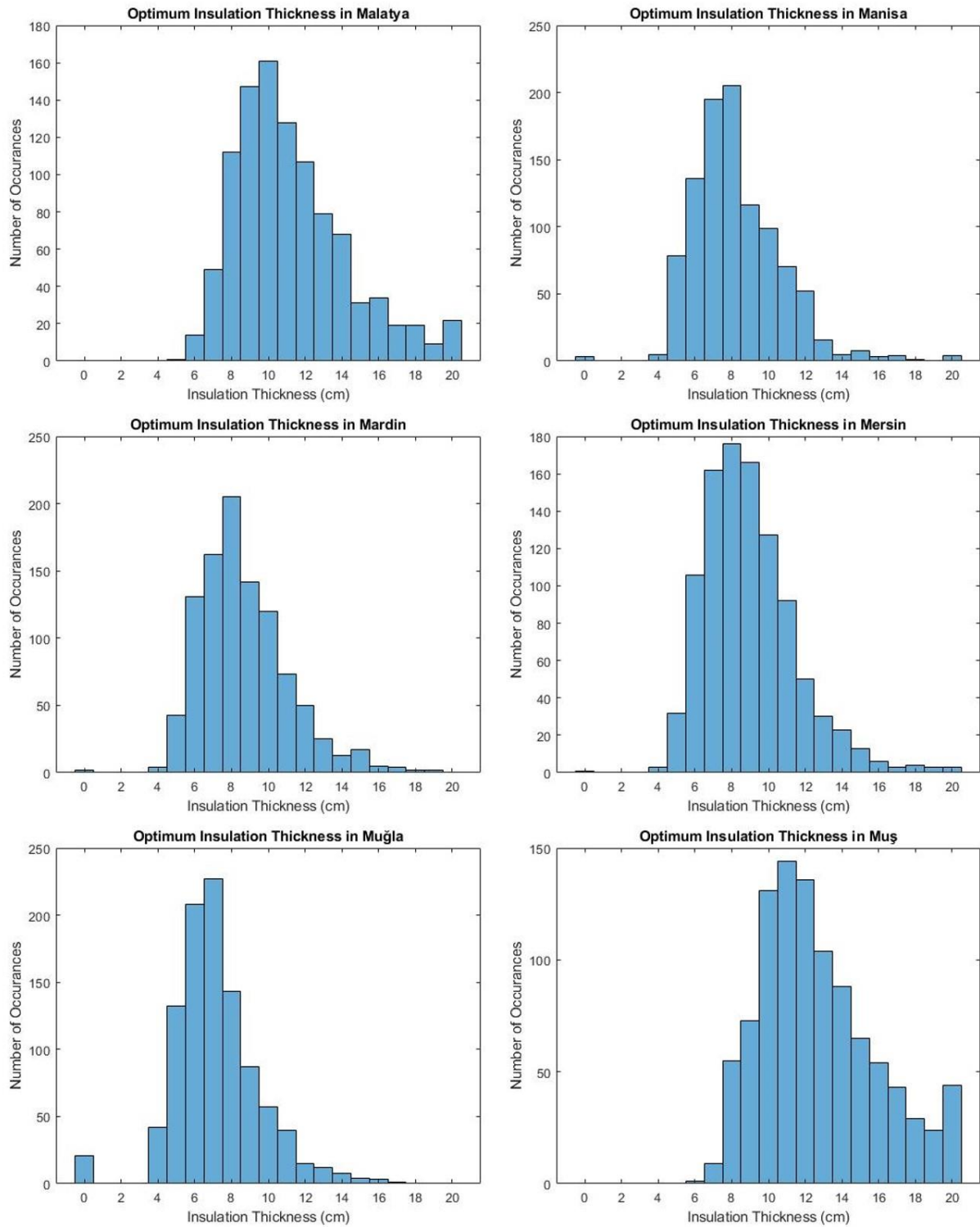


Figure B10. Optimum insulation thickness in Malatya-Muş

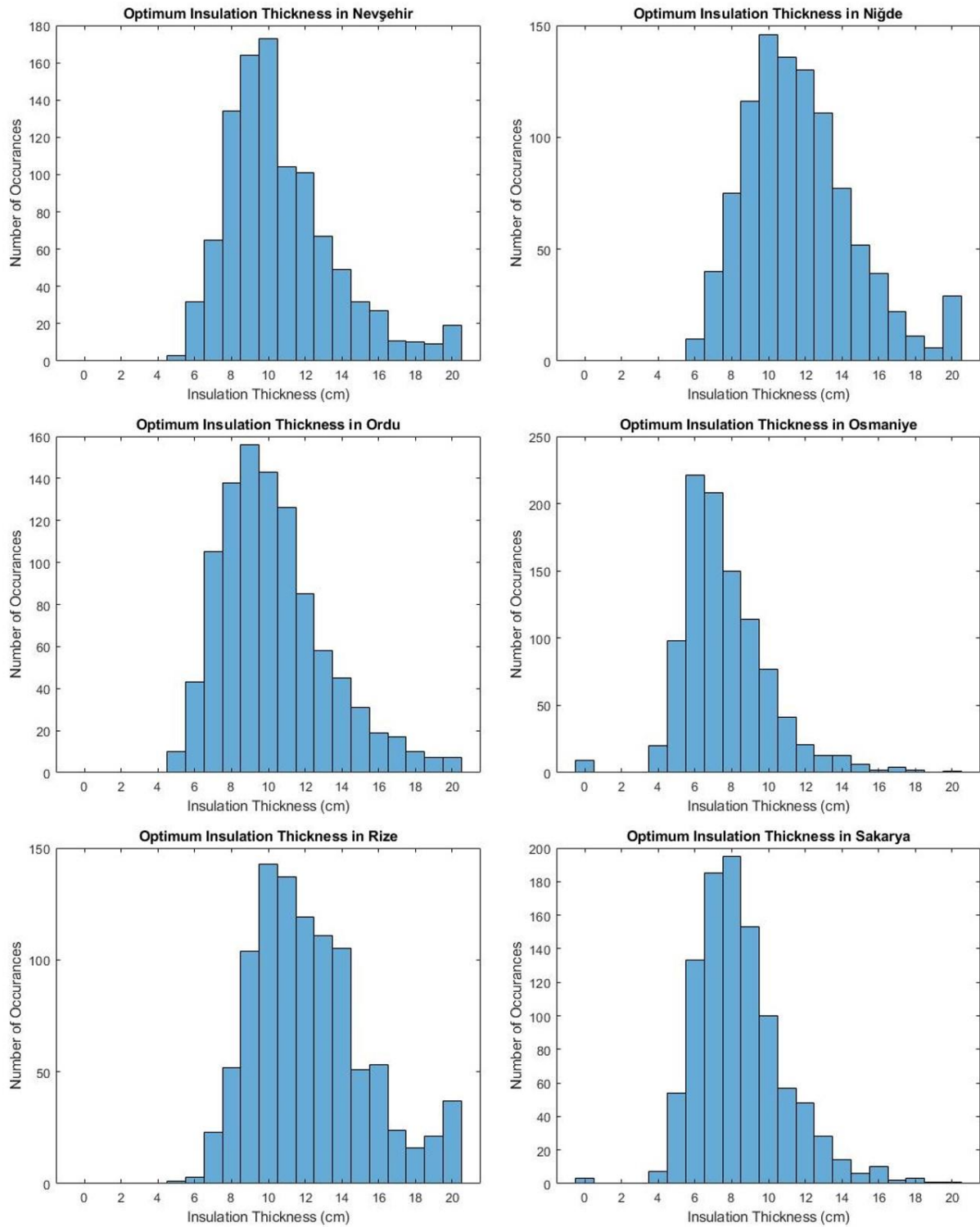


Figure B11. Optimum insulation thickness in Nevşehir-Sakarya

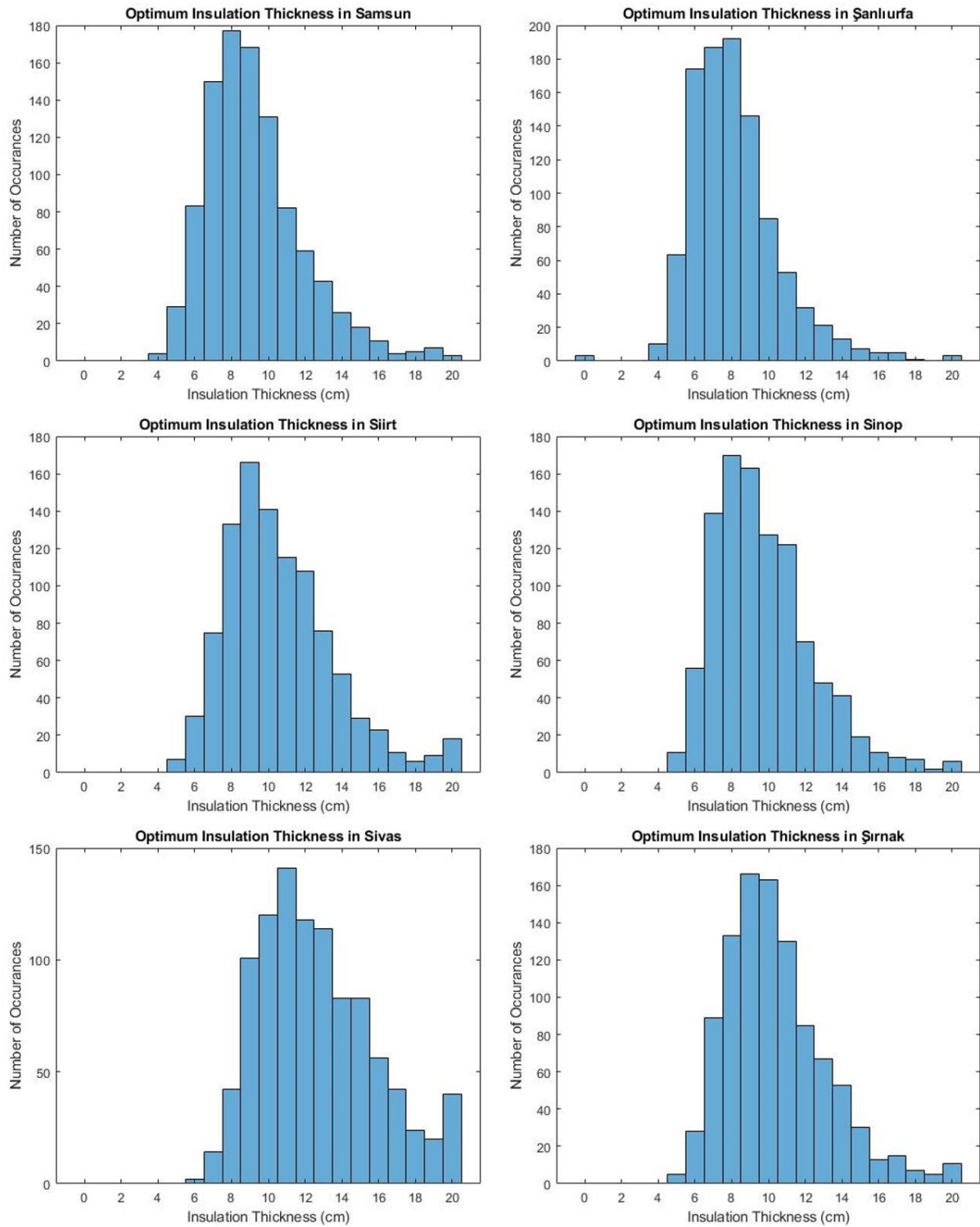


Figure B12. Optimum insulation thickness in Samsun-Şırnak

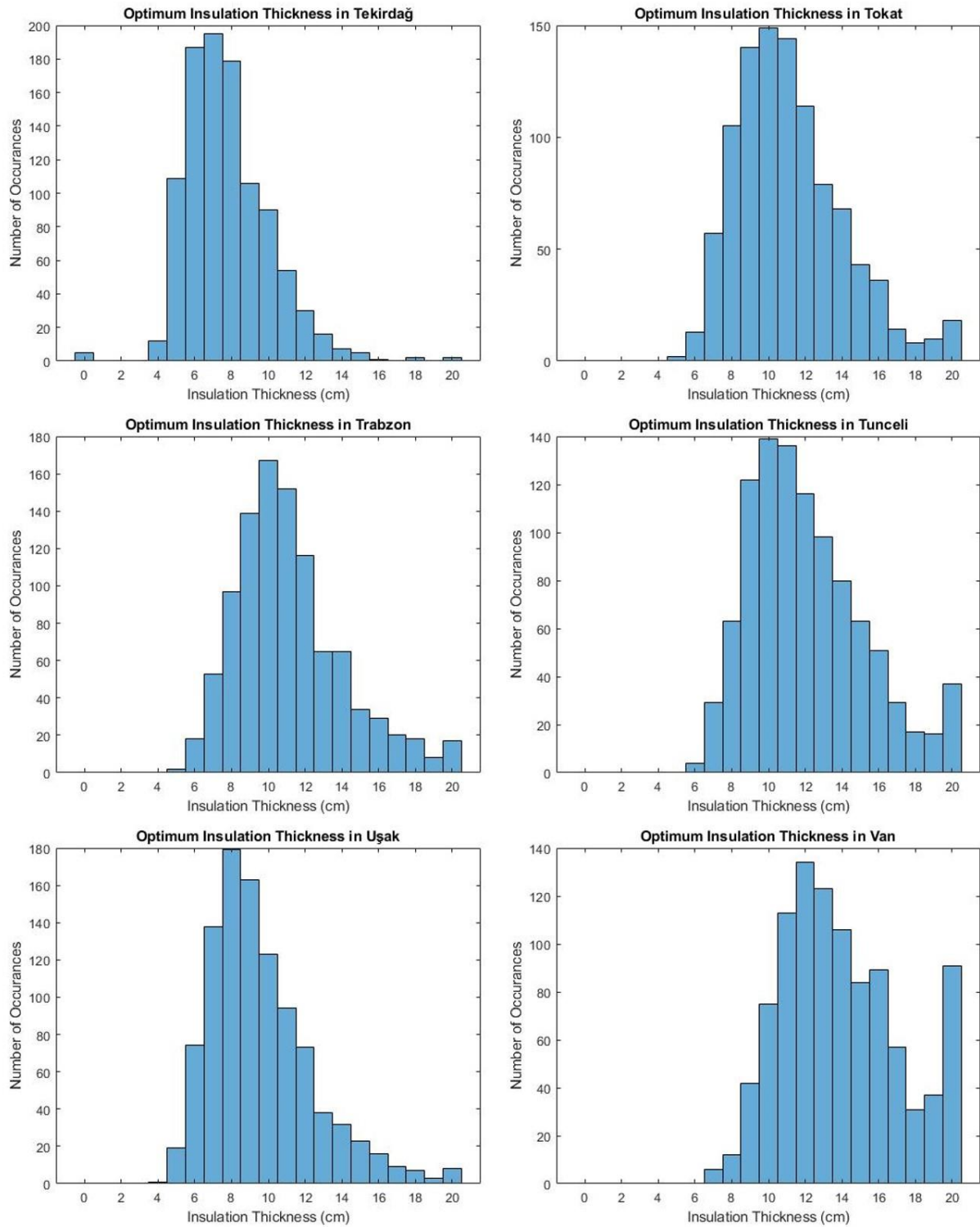


Figure B13. Optimum insulation thickness in Tekirdağ-Van

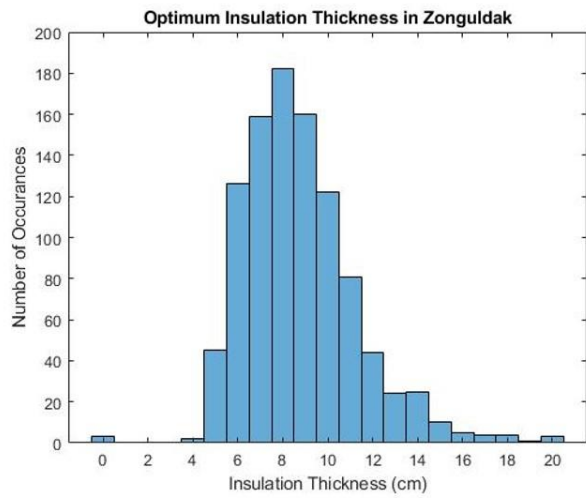
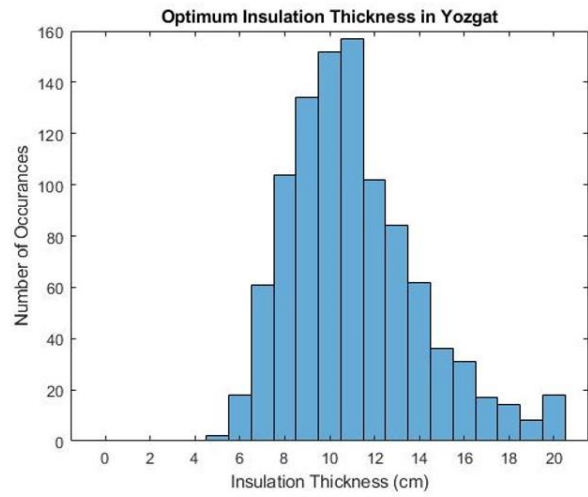
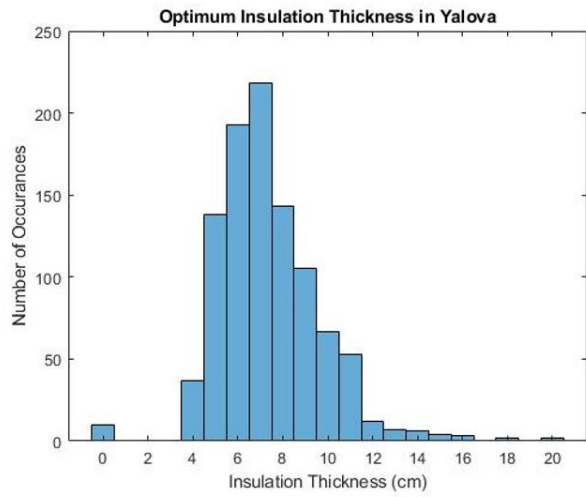


Figure B14. Optimum insulation thickness in Yalova-Zonguldak

APPENDIX C: PROBABILITIES OF OPTIMUM INSULATION THICKNESSES

Table C1. Probabilities of optimum insulation thicknesses in Adana-İstanbul

Province	Probability of Optimum Insulation Thickness (%)																				
	0	1	2	3	4	5	6	7	8	9	10	11	12	13	14	15	16	17	18	19	20
Adana	0.1	0.0	0.0	0.0	0.2	3.4	10.3	19.9	18.7	13.7	13.2	7.1	4.9	2.8	2.3	1.2	0.8	0.4	0.2	0.5	0.3
Adıyaman	0.1	0.0	0.0	0.0	0.0	1.9	6.0	12.9	18.3	16.5	13.0	12.1	7.0	3.8	2.8	1.9	1.5	0.7	0.7	0.2	0.6
Afyonkarahisar	0.0	0.0	0.0	0.0	0.0	0.6	1.9	7.5	14.0	15.9	16.5	13.6	9.5	6.8	3.7	3.4	1.8	1.6	1.0	0.8	1.4
Ağrı	0.0	0.0	0.0	0.0	0.0	0.0	0.1	0.5	2.4	4.7	9.1	11.4	13.1	12.1	10.9	9.6	7.4	4.2	4.3	3.2	7.0
Aksaray	0.0	0.0	0.0	0.0	0.0	0.9	4.2	9.2	14.3	17.8	13.2	12.1	9.2	7.1	3.8	2.5	1.9	1.0	0.6	0.8	1.4
Amasya	0.0	0.0	0.0	0.0	0.0	0.5	2.8	9.1	13.8	15.9	13.9	12.8	9.1	8.3	5.2	2.9	2.0	0.8	1.0	0.7	1.2
Ankara	0.0	0.0	0.0	0.0	0.0	0.4	2.9	8.5	13.4	15.9	16.8	12.7	8.8	7.2	5.0	2.8	1.7	1.7	0.5	0.6	1.1
Antalya	0.0	0.0	0.0	0.0	0.7	4.7	13.6	16.8	19.1	13.8	12.1	8.3	4.2	3.5	1.5	0.9	0.2	0.2	0.2	0.1	0.1
Ardahan	0.0	0.0	0.0	0.0	0.0	0.0	0.0	0.0	1.6	2.7	7.7	10.4	12.2	13.0	9.4	8.9	7.9	6.7	5.1	4.3	10.1
Artvin	0.0	0.0	0.0	0.0	0.0	0.0	0.1	1.8	4.3	9.8	12.1	15.6	12.9	9.9	9.2	7.3	4.3	2.8	3.3	1.5	5.1
Aydın	0.9	0.0	0.0	0.0	2.8	11.5	18.4	22.3	14.8	11.8	6.6	4.4	2.7	1.9	0.6	0.5	0.4	0.1	0.1	0.1	0.1
Balıkesir	0.3	0.0	0.0	0.0	0.6	8.1	14.3	18.8	20.5	11.8	9.7	6.7	5.3	1.7	0.3	0.7	0.4	0.3	0.1	0.0	0.4
Bartın	0.0	0.0	0.0	0.0	0.4	3.4	11.5	15.5	18.6	16.7	11.7	7.8	5.8	3.4	1.6	1.4	1.2	0.4	0.4	0.2	0.0
Batman	0.0	0.0	0.0	0.0	0.0	1.6	7.5	15.3	17.0	16.2	13.4	9.0	6.9	4.8	3.7	1.3	1.3	0.5	0.6	0.3	0.6
Bayburt	0.0	0.0	0.0	0.0	0.0	0.0	0.0	0.3	1.8	5.7	7.9	12.4	13.3	10.9	11.4	7.8	7.4	5.3	3.8	3.4	8.6
Bilecik	0.0	0.0	0.0	0.0	0.3	1.9	6.4	11.7	15.9	19.7	14.4	9.4	6.7	3.9	3.5	2.7	1.1	0.7	0.7	0.4	0.6
Bingöl	0.0	0.0	0.0	0.0	0.0	0.0	0.0	1.0	5.4	7.4	13.2	14.0	13.6	10.6	8.6	6.5	5.3	4.5	2.9	2.5	4.5
Bitlis	0.0	0.0	0.0	0.0	0.0	0.0	0.1	1.9	4.7	9.2	11.8	16.2	14.1	8.1	9.9	7.1	4.0	3.9	2.1	2.3	4.6
Bolu	0.0	0.0	0.0	0.0	0.0	0.2	1.4	5.2	8.3	13.0	15.4	13.3	13.3	9.0	7.2	4.3	3.6	1.7	0.7	0.9	2.5
Burdur	0.0	0.0	0.0	0.0	0.0	1.0	4.5	10.9	14.0	16.1	14.6	12.3	8.6	5.2	4.9	2.6	1.6	1.6	1.0	0.4	0.7
Bursa	0.1	0.0	0.0	0.0	0.2	4.3	10.5	21.3	17.9	12.9	13.1	6.9	4.7	2.7	2.3	1.1	0.6	0.6	0.1	0.4	0.3
Çanakkale	1.3	0.0	0.0	0.0	2.6	12.6	19.9	20.5	14.7	12.5	7.2	2.8	2.2	1.9	0.6	0.5	0.2	0.3	0.1	0.0	0.1
Çankırı	0.0	0.0	0.0	0.0	0.0	0.3	1.4	3.7	9.9	14.0	15.5	15.0	11.9	8.5	6.7	4.0	2.5	2.4	1.2	1.1	1.9
Çorum	0.0	0.0	0.0	0.0	0.0	0.4	2.7	6.2	12.7	15.4	15.0	14.2	8.8	8.1	5.1	3.7	2.4	1.9	1.3	0.5	1.6
Denizli	0.0	0.0	0.0	0.0	0.5	2.1	6.2	10.6	17.5	18.0	14.7	10.8	7.1	3.4	3.3	2.7	1.1	0.3	0.7	0.4	0.6
Diyarbakır	0.0	0.0	0.0	0.0	0.0	1.7	6.8	14.2	17.2	16.1	14.6	9.9	6.5	4.2	2.8	2.4	1.4	0.4	0.5	0.5	0.8
Düzce	0.1	0.0	0.0	0.0	0.4	2.3	7.0	14.1	16.6	16.1	14.3	10.0	5.9	5.7	3.0	1.7	0.9	0.6	0.3	0.2	0.8
Edirne	0.7	0.0	0.0	0.0	2.4	7.6	16.7	19.2	16.4	13.7	9.4	5.4	3.3	1.6	1.0	0.9	0.7	0.7	0.2	0.0	0.1
Elazığ	0.0	0.0	0.0	0.0	0.0	0.1	2.0	6.6	12.4	14.7	15.1	13.1	11.6	8.6	4.8	3.5	2.9	1.2	1.8	0.6	1.0
Erzincan	0.0	0.0	0.0	0.0	0.0	0.0	0.0	0.8	3.6	7.1	11.4	13.2	13.7	13.2	10.2	5.8	6.4	4.7	3.4	1.6	4.9
Erzurum	0.0	0.0	0.0	0.0	0.0	0.0	0.0	0.1	1.8	4.0	6.7	9.5	13.0	12.6	13.7	10.3	5.8	6.3	4.5	2.7	9.0
Eskişehir	0.0	0.0	0.0	0.0	0.0	0.8	4.6	10.9	14.8	17.8	13.7	11.1	8.1	6.0	3.8	2.3	2.2	1.4	0.9	0.5	1.1
Gaziantep	0.0	0.0	0.0	0.0	0.6	4.8	11.8	17.8	19.8	13.6	12.0	7.3	4.4	2.8	2.1	1.1	0.7	0.4	0.4	0.1	0.3
Giresun	0.0	0.0	0.0	0.0	0.0	0.2	0.6	3.4	6.9	11.9	16.1	14.1	10.8	10.1	7.9	6.4	4.1	3.1	1.3	0.8	2.3
Gümüşhane	0.0	0.0	0.0	0.0	0.0	0.0	0.0	0.2	1.9	5.6	10.5	11.9	12.3	12.0	10.3	7.8	7.1	5.5	4.3	3.1	7.5
Hakkari	0.0	0.0	0.0	0.0	0.0	0.0	0.0	0.8	2.2	8.1	11.5	13.5	13.7	12.6	11.3	6.7	5.1	4.1	3.1	2.5	4.8
Hatay	3.6	0.0	0.0	0.0	5.7	17.2	23.2	19.0	12.4	8.4	4.8	2.8	1.1	0.6	0.7	0.3	0.2	0.0	0.0	0.0	0.0
İğdir	0.0	0.0	0.0	0.0	0.0	0.1	0.5	3.1	6.4	12.5	13.1	15.3	11.5	9.1	8.5	6.6	3.9	2.6	2.5	1.5	2.8
Isparta	0.0	0.0	0.0	0.0	0.0	0.1	1.9	7.0	12.8	15.4	14.6	12.0	11.9	7.5	4.8	4.9	2.9	1.5	0.9	0.8	1.0
İstanbul	2.1	0.0	0.0	0.0	4.0	14.3	19.7	21.5	14.5	10.6	6.4	2.8	1.8	1.2	0.6	0.4	0.1	0.0	0.0	0.0	0.0

Table C2. Probabilities of optimum insulation thicknesses in İzmir-Zonguldak

Province	Probability of Optimum Insulation Thickness (%)																				
	0	1	2	3	4	5	6	7	8	9	10	11	12	13	14	15	16	17	18	19	20
İzmir	2.5	0.0	0.0	0.0	4.5	14.3	21.8	21.0	13.5	7.5	7.8	4.3	1.1	0.4	0.4	0.6	0.1	0.1	0.0	0.1	0.0
Kahramanmaraş	0.0	0.0	0.0	0.0	0.0	0.4	1.7	7.1	11.8	13.6	15.8	13.2	11.2	7.4	5.7	4.3	3.0	1.3	0.9	0.5	2.1
Karabük	0.0	0.0	0.0	0.0	0.0	0.0	2.7	8.4	13.6	17.1	15.4	13.8	7.5	7.5	4.1	3.5	2.2	1.2	1.0	0.9	1.1
Karaman	0.0	0.0	0.0	0.0	0.2	0.5	2.7	6.5	11.6	13.2	16.5	13.6	9.3	7.6	4.9	4.7	2.0	2.0	1.5	1.2	2.0
Kars	0.0	0.0	0.0	0.0	0.0	0.0	0.0	0.5	2.3	4.4	7.1	11.5	13.0	13.9	10.1	8.8	7.2	6.6	4.0	3.1	7.5
Kastamonu	0.0	0.0	0.0	0.0	0.0	0.3	2.1	6.9	9.3	15.0	15.3	14.1	12.4	8.0	5.7	3.9	2.4	1.1	0.9	0.9	1.7
Kayseri	0.0	0.0	0.0	0.0	0.0	0.1	0.4	2.7	6.0	12.4	13.7	14.0	13.0	10.3	6.7	6.1	4.9	2.3	2.4	1.8	3.2
Kilis	0.4	0.0	0.0	0.0	1.5	6.6	15.5	19.2	16.2	14.4	9.9	7.2	3.4	1.7	1.2	0.8	0.9	0.5	0.4	0.1	0.1
Kırıkkale	0.0	0.0	0.0	0.0	0.0	0.6	3.0	9.8	13.6	16.5	14.0	12.2	9.0	7.6	5.2	3.0	1.9	1.0	1.1	0.5	1.0
Kırklareli	0.0	0.0	0.0	0.0	0.9	5.5	12.4	16.7	19.6	14.7	10.4	7.0	5.1	3.0	2.1	0.8	0.6	0.4	0.5	0.3	0.0
Kırşehir	0.0	0.0	0.0	0.0	0.0	0.3	2.4	8.8	13.8	16.3	17.0	11.1	8.8	8.0	5.4	3.1	2.3	1.0	0.7	0.4	0.6
Kocaeli	0.9	0.0	0.0	0.0	2.1	10.6	17.5	19.3	17.9	11.4	9.0	4.6	2.7	1.4	1.5	0.4	0.4	0.2	0.1	0.0	0.0
Konya	0.0	0.0	0.0	0.0	0.0	0.6	3.6	9.3	12.0	15.9	15.6	12.9	9.7	7.9	4.1	3.5	2.1	1.6	0.5	0.0	0.7
Kütahya	0.0	0.0	0.0	0.0	0.0	0.3	3.0	6.0	11.4	16.0	17.2	14.8	8.7	6.9	5.1	2.9	2.4	2.1	1.1	0.9	1.2
Malatya	0.0	0.0	0.0	0.0	0.0	0.1	1.4	4.9	11.2	14.7	16.1	12.8	10.7	7.9	6.8	3.1	3.4	1.9	1.9	0.9	2.2
Manisa	0.3	0.0	0.0	0.0	0.5	7.8	13.6	19.5	20.5	11.6	9.9	7.0	5.2	1.6	0.5	0.8	0.3	0.4	0.1	0.0	0.4
Mardin	0.2	0.0	0.0	0.0	0.4	4.3	13.1	16.2	20.5	14.2	12.0	7.3	5.0	2.5	1.3	1.7	0.5	0.4	0.2	0.2	0.0
Mersin	0.1	0.0	0.0	0.0	0.3	3.2	10.6	16.2	17.6	16.6	12.7	9.2	5.0	3.0	2.3	1.3	0.6	0.3	0.4	0.3	0.3
Muğla	2.1	0.0	0.0	0.0	4.2	13.2	20.8	22.7	14.3	8.7	5.7	4.0	1.5	1.2	0.8	0.4	0.3	0.1	0.0	0.0	0.0
Muş	0.0	0.0	0.0	0.0	0.0	0.0	0.1	0.9	5.5	7.3	13.1	14.4	13.6	10.4	8.8	6.5	5.4	4.3	2.9	2.4	4.4
Nevşehir	0.0	0.0	0.0	0.0	0.0	0.3	3.2	6.5	13.4	16.4	17.3	10.4	10.1	6.7	4.9	3.2	2.7	1.1	1.0	0.9	1.9
Niğde	0.0	0.0	0.0	0.0	0.0	0.0	1.0	4.0	7.5	11.6	14.6	13.6	13.0	11.1	7.7	5.2	3.9	2.2	1.1	0.6	2.9
Ordu	0.0	0.0	0.0	0.0	0.0	1.0	4.3	10.5	13.8	15.6	14.3	12.6	8.5	5.8	4.5	3.1	1.9	1.7	1.0	0.7	0.7
Osmaniye	0.9	0.0	0.0	0.0	2.0	9.8	22.1	20.8	15.0	11.4	7.7	4.1	2.1	1.3	1.3	0.6	0.2	0.4	0.2	0.0	0.1
Rize	0.0	0.0	0.0	0.0	0.0	0.1	0.3	2.3	5.2	10.4	14.3	13.7	11.9	11.1	10.5	5.1	5.3	2.4	1.6	2.1	3.7
Sakarya	0.3	0.0	0.0	0.0	0.7	5.4	13.3	18.5	19.5	15.3	10.0	5.7	4.8	2.8	1.4	0.6	1.0	0.2	0.3	0.1	0.1
Samsun	0.0	0.0	0.0	0.0	0.4	2.9	8.3	15.0	17.7	16.8	13.1	8.2	5.9	4.3	2.6	1.8	1.1	0.4	0.5	0.7	0.3
Şanlıurfa	0.3	0.0	0.0	0.0	1.0	6.3	17.4	18.7	19.2	14.6	8.5	5.3	3.2	2.1	1.3	0.7	0.5	0.5	0.1	0.0	0.3
Siirt	0.0	0.0	0.0	0.0	0.0	0.7	3.0	7.5	13.3	16.6	14.1	11.5	10.8	7.6	5.3	2.9	2.3	1.1	0.6	0.9	1.8
Sinop	0.0	0.0	0.0	0.0	0.0	1.1	5.6	13.9	17.0	16.3	12.7	12.2	7.0	4.8	4.1	1.9	1.1	0.8	0.7	0.2	0.6
Sivas	0.0	0.0	0.0	0.0	0.0	0.0	0.2	1.4	4.2	10.1	12.0	14.1	11.8	11.4	8.3	8.3	5.6	4.2	2.4	2.0	4.0
Şırnak	0.0	0.0	0.0	0.0	0.0	0.5	2.8	8.9	13.3	16.6	16.3	13.0	8.5	6.7	5.3	3.0	1.3	1.5	0.7	0.5	1.1
Tekirdağ	0.5	0.0	0.0	0.0	1.2	10.9	18.7	19.5	17.9	10.6	9.0	5.4	3.0	1.6	0.7	0.5	0.1	0.0	0.2	0.0	0.2
Tokat	0.0	0.0	0.0	0.0	0.0	0.2	1.3	5.7	10.5	14.0	14.9	14.4	11.4	7.9	6.8	4.3	3.6	1.4	0.8	1.0	1.8
Trabzon	0.0	0.0	0.0	0.0	0.0	0.2	1.8	5.3	9.7	13.9	16.7	15.2	11.6	6.5	6.5	3.4	2.9	2.0	1.8	0.8	1.7
Tunceli	0.0	0.0	0.0	0.0	0.0	0.0	0.4	2.9	6.3	12.2	13.9	13.6	11.6	9.8	8.0	6.3	5.1	2.9	1.7	1.6	3.7
Uşak	0.0	0.0	0.0	0.0	0.1	1.9	7.4	13.8	17.9	16.3	12.3	9.4	7.3	3.8	3.2	2.3	1.6	0.9	0.7	0.3	0.8
Van	0.0	0.0	0.0	0.0	0.0	0.0	0.0	0.6	1.2	4.2	7.5	11.3	13.4	12.3	10.6	8.4	8.9	5.7	3.1	3.7	9.1
Yalova	1.0	0.0	0.0	0.0	3.7	13.8	19.3	21.8	14.3	10.5	6.7	5.3	1.2	0.7	0.6	0.4	0.3	0.0	0.2	0.0	0.2
Yozgat	0.0	0.0	0.0	0.0	0.0	0.2	1.8	6.1	10.4	13.4	15.2	15.7	10.2	8.4	6.2	3.6	3.1	1.7	1.4	0.8	1.8
Zonguldak	0.3	0.0	0.0	0.0	0.2	4.5	12.6	15.9	18.2	16.0	12.2	8.1	4.4	2.4	2.5	1.0	0.5	0.4	0.4	0.1	0.3



THEORETICAL AND EXPERIMENTAL INVESTIGATION OF V-CORRUGATED SOLAR AIR HEATER FOR SPACE HEATING

Murat ÖZDENEFE* and Khaled ALTEER **

* Eastern Mediterranean University, Department of Mechanical Engineering

Gazimağusa, North Cyprus via Mersin 10, Turkey

murat.ozdeneffe@emu.edu.tr, ORCID: 0000-0002-8905-0885

** Vocational Technical Institute, Technical Affairs, and Equipment Unit

AL-smalia st, Algarabolli, Tripoli, Libya

alteer22111@gmail.com, ORCID: 0000-0001-6379-8054

(Geliş Tarihi: 05.02.2022, Kabul Tarihi: 23.08.2022)

Abstract: This work is an effort to investigate the thermal performance of a V-Corrugated Solar Air Heater (SAH), which is intended for supplying heating to an office space having a floor area of 84 m². Thermal performance investigation has been carried out both theoretically and experimentally. V-Corrugated SAHs have not been investigated for space heating in offices, hence this study aims to contribute by proposing and promoting them for this purpose. The load of the office space has been evaluated by the Energy Plus building simulation program as 4546 W. Thermal performance of the SAH is investigated by solving the governing equations with developed MATLAB code and concurrently by carrying out real-time monitoring of the operating parameters (e.g. component temperatures, air speed, etc.) of the SAH. It is aimed to obtain the temperature of each component of the SAH, useful heat output, thermal efficiency, number of SAHs and the corresponding area that is necessary to meet the heating load. It is found that 9 SAHs with 16 m² are required to supply the target load for the experimental case and 6 SAHs with 10 m² for the theoretical case.

Keywords: V-Corrugated solar air heater, Thermal performance, Heating load simulation, Energy Plus

V-KAT LEVHALI GÜNEŞ ENERJİLİ HAVA ISITICISININ ORTAM ISITMASI İÇİN TEORİK VE DENEYSSEL İNCELEMESİ

Özet: Bu çalışma, 84 m² alana sahip bir ofise ısıtma sağlamak için tasarlanan V-Kat levhalı güneş enerjili hava ısıtıcısının ısı performansını incelemektedir. Hava ısıtıcısının ısı performansı hem teorik hem de deneysel olarak incelenmiştir. V-Kat levhalı güneş enerjili hava ısıtıcıları daha önce ofislere ısıtma sağlamak için çalışılmamıştır. Dolayısıyla bu çalışma bu sistemleri bu amaç için inceleyerek literatüre katkı sunmayı hedeflemektedir. Ofisin ısıtma yükü, Energy Plus bina simülasyon yazılımı ile 4546 W olarak hesaplanmıştır. Hava ısıtıcısının ısı performansı, hava ısıtıcısı enerji denklemlerinin geliştirilen MATLAB kodu kullanılarak çözülmesi ile ve aynı zamanda hava ısıtıcısı işletme değişkenlerinin (örn. bileşen sıcaklıkları, hava hızı vb.) ölçülmesi ile incelenmiştir. Hava ısıtıcısının her bir bileşeninin sıcaklığı, faydalı ısı üretimi, ısı verim, ısıtma yükünü karşılamak için gerekli olan hava ısıtıcısı sayısı ve karşılık gelen alan elde edilmesi amaçlanmaktadır. Deneysel incelemenin sonucunda ısıtma yükünü karşılamak için 16 m² lik 9 adet hava ısıtıcısı gerekirken, teorik incelemede yükü karşılamak için 10 m² lik 6 adet hava ısıtıcısının gerekli olduğu sonucu ortaya çıkmıştır.

Anahtar Kelimeler: V-Kat levhalı güneş enerjili hava ısıtıcısı, Isıl performans, Isıtma yükü simülasyonu, Energy Plus

NOMENCLATURE

		A2	Cross-sectional area-lower channel [m ²]
		Cp	Specific heat of air [J/kg.K]
Aa	Absorber surface area [m ²]	Dh	Hydraulic diameter [m]
Ah	SAH Area [m ²]	G	Solar irradiance [W/m ²]
A1	Cross-sectional area-upper channel [m ²]	H	Thickness [m]

h	Heat transfer coefficient [W/m ² .K]
k	Thermal conductivity [W/m .K]
L	Length of SAH [m]
\dot{m}	mass flow rate [kg/s]
N	Number of SAH
Nu	Nusselt number [=hL/k]
Pr	Prandtl number
Qu	Total useful heat [W]
Q _{htg}	Heating load of the office space [W]
qu1	Useful heat from upper channel [W]
qu2	Useful heat from lower channel [W]
R	Back elements resistance [m.K/W]
Ra	Rayleigh number [=gβPr(T ₁ -T ₂)L ³ /ν ²]
Re	Reynolds number [=VρD/μ]
T	Temperature [K]
V	Velocity/Wind speed [m/s]

Greek letters

α	Absorptance
τ	Transmittance
σ	Stefan Boltzmann constant [W/m ² . K ⁴]
β	Thermal expansion coefficient [1/K]
ε	Emissivity
ν	Dynamic viscosity [m ² /s]
θ	Tilt angle [°]
η	Thermal efficiency
μ	Dynamic viscosity [kg/m·s]
ρ	Density [kg/m ³]

Subscripts:

1	Upper channel
2	Lower channel
a	Ambient air
ap	Absorber plate
bp/b	Back plate
c	Convection
Exp	Experimental
f1	Air flow in upper channel
f2	Air flow in lower channel
g1	Upper glass cover
g2	Lower glass cover
i & o	Inlet & Outlet
ins	Insulation
pc	Protective cover
r	Radiation
s	Sky
Sim	Simulation
w	wind

INTRODUCTION

Solar energy collectors are devices that convert solar radiation to useful thermal energy by absorbing the incident radiation, transforming it to heat, and transferring the heat to the working fluid (water, oil, air, etc.). Solar air heaters (SAHs) are solar energy collectors employing air as the working fluid. Unlike solar water heaters (working fluid is water) where the conduits are pipes, SAHs utilize ducts for transporting the working fluid i.e., air (Duffie John A. et al., 2020; Kalogirou, 2004).

A generic SAH consists of a transparent cover system, an absorber plate, and insulated air ducts/channels. The cover system is at the top, whereas the absorber plate commonly is above the air ducts/channels. A portion of the incident radiation on the cover system is transmitted and falls on the absorber plate where it is absorbed. The remaining on the other hand is reflected. The air which flows either naturally by buoyancy force (passive SAH) or by an external force (active SAH with a fan) exchanges heat with the absorber plate by convection and can be used for different purposes such as space heating or drying of crops. Thermal performance of SAHs depends on many variables such as dimensions of SAH, absorber plate type and material, amount of solar radiation, the geometry of the air ducts and the amount of air flow, etc.

Motivation

Although SAHs are simple and cheap, their real-life applications for space heating are not very common. Indeed, they possess a vast potential for space heating in locations with moderate climates having abundant solar radiation. For instance, the Mediterranean region could be ideal for employing SAHs for space heating.

Buildings are responsible for one-third of the world's end use energy consumption. This makes them the second largest energy-consuming sector after industrial sector. They also account for 30% of global CO₂ emissions. Within the buildings, space heating end-use has the largest contribution to CO₂ emissions accounting for 60% (International Energy Agency, 2021).

It is apparent, that renewable technologies if employed for space heating can have an appreciable effect on end-use energy reduction and CO₂ mitigation. SAHs which currently have no widespread real-life applications can be considered one of those renewable technologies which are simple and inexpensive that can have a considerable

effect on reducing energy consumption and CO₂ emissions, particularly in locations where the climate is mild.

North Cyprus is an ideal place to be considered for space heating with SAHs, since the island has mild weather (Mediterranean Climate) with a yearly average temperature of 19 °C and average daily solar radiation of 17.5 MJ/m² (4.86 kWh/m²) through the year. During winter the coldest month is January with daytime temperatures in the range of 9-12 °C and daily mean solar radiation of 9.0 MJ/m² (2.50 kWh/m²) (North Cyprus Meteorological Office, 2022).

Commercial buildings in North Cyprus accounted for 36% of the total electricity consumption in 2021 (kib-tek, 2021). These buildings are mainly offices, and they heavily rely on electricity-powered heat pumps for space heating during winter. Considering that electricity production in North Cyprus relies on fuel oil-driven power plants, facilitating the real-life applications of SAHs for space heating would have a significant impact on reducing energy and greenhouse gas emissions.

Hence, the principal motivation of the current work is to propose and promote the SAHs, particularly the V-Corrugated absorber plate type, through investigating its thermal performance for office heating applications under North Cyprus weather conditions.

Literature Review

There has been extensive research on the SAHs. Numerous models have been developed for examining their performance and many configurations have been tested for different applications some of which are presented below.

Yıldırım and Solmuş (2014) numerically investigated a double glass double pass SAH. The authors aimed to find the duct depth and air flow rate that would give the maximum thermohydraulic efficiency. They revealed that the maximum thermohydraulic efficiency occurred as 67% with a duct depth of 4 cm and an air flow rate of 0.11 kg/s. The authors also found that the daily mean thermal efficiency of the SAH decreases with increasing air duct depth.

Al-Kayiem and Yassen (2015) compared the theoretically evaluated Nusselt numbers (Nu) with those obtained experimentally for a flat plate glass covered SAH for different tilt angles under natural convection

conditions. The authors found that some theoretical models overestimate, whereas some others underestimate the Nu. They also revealed that the optimum tilt angle is about 50° for obtaining the highest Nusselt number.

Bayrak and Oztop (2015) experimentally tested flat plate SAHs which are incorporated with Aluminum foam obstacles with different arrangements. The authors revealed that the SAH with 6 mm thick Aluminum foam obstacles having staggered arrangement has the highest efficiency as 77%.

Gawande et al. (2016) investigated the effect of L-shaped roughness elements which are introduced reversely on the absorber plate of a SAH. The authors performed CFD simulations (with ANSYS Fluent) and compared their results with experimental measurements. They found that introducing the roughness elements substantially affects the heat transfer characteristics. They also revealed that optimum heat transfer enhancement is with a thermo-hydraulic performance parameter of 1.90 and the CFD simulations are agreeing with experimental results.

Gilani et al. (2017) experimentally examined the Nu number enhancement of natural convection SAHs by installing conical-shaped turbulators. The authors observed that the staggered arranged turbulators with a height of 4 mm and a pitch of 16 mm increased the Nu number the most.

Gao et al. (2000) solved the governing equations (continuity, momentum and energy) in order to investigate the parameters effecting natural convection in a sine wave absorber plate cross corrugated SAH. They found that the channel height to the amplitude of the sine wave shaped absorber plate ratio and one-fourth of the sine wave shaped absorber plate wavelength to the amplitude of the sine wave shaped absorber plate should be greater than 2 and 1 respectively, whereas the tilt angle should be less than 40° to suppress the natural convection heat loss.

El-Sebaili et al. (2011) theoretically and experimentally investigated the double-pass finned-absorber plate and double-pass V-Corrugated absorber plate SAHs. The authors observed that the double-pass V-Corrugated absorber plate SAH exit air temperature and efficiency are 2.1-9.7% and 9.3-11.9% greater than the double-pass finned-absorber plate SAH's exit air temperature and efficiency. The authors also found that both solar air heater's efficiencies are increasing up to a mass flow rate

of 0.04 kg/s which beyond this value efficiency enhancement is insignificant.

Kumar A. et al. (2022) proposed a novel counter flow curved double-pass solar air heater (DPSAH). The authors performed CFD analysis and experimentally validate their results with those available in the literature. They also compared the results of smooth curved single pass, smooth curved parallel double-pass, smooth curved counter double-pass, roughened curved parallel double-pass, and roughened curved counter double-pass. The authors found that roughened curved counter double-pass has the best performance with a maximum of 23% increase in the thermal performance.

In another study, Jain and Jain (2004) investigated the performance of a multi-pass flat absorber plate SAH having a granite storage material attached to the back of the absorber plate which is intended for drying paddy crops. The authors solved the energy equations and calculated the temperatures of the air at different locations in the SAH as well as the paddy grain temperature. They have found that increasing the SAH length and breadth increases paddy grain temperature.

Another experimental drying application (for roselle) of a SAH is examined by Kareem et al. (2017) The authors investigated the drying performance of a multi-pass flat plate SAH integrated with granite for heat storage. Their design achieved a drying rate of $33.57 \text{ g (kg m}^2 \text{ h)}^{-1}$ with an efficiency of 64%. The systems' techno-economic appraisal resulted in a payback period of 2.14 years.

A more recent work regarding the use of the SAHs as a dryer is done by Çiftçi et al. (2021) The authors developed a vertical photovoltaic thermal (PVT) solar dryer and performed numerical and experimental investigation (for drying mint). They considered the system with and without fins. The authors revealed that the thermal efficiency of the system without fins and with fins could be as high as 54.86% and 58.16% respectively. They also found that waste exergy ratios of the system without fins and with fins are in the ranges of 0.47-0.58 and 0.43-0.56 respectively.

Fan et al. (2017) developed a dynamic model for a hybrid photovoltaic thermal collector solar air heater (PVT-SAH) which is equipped with longitudinal fins for evaluating system performance. The authors validated their model with an experimental study under real-life conditions. They measured the temperatures of the system components at various points and compared them

with those evaluated with the model and found that the root-mean-square deviation ranges from 0.3 to 1.3 °C.

In another study, Fan et al. (2019a) designed a model for a PV thermal solar air heater (PVT-SAH) system integrated with heat pipes whose SAH portion is a double pass type with longitudinal fins. The system is intended to generate high-temperature air. The authors evaluated the thermal efficiency of the proposed system as 69.2% and payback time in the range of 5.7 and 16.8 years (Fan et al., 2019a).

In a study subsequent to aforementioned one, Fan et al (2019b) employed the PVT-SAH for the regeneration process of a desiccant cooling system. The authors applied the developed system to a commercial building having offices for cooling which is in a hot and humid climate. The authors found that the COP of the system can be as high as 19.8 and a minimum area of 0.35 m² PVT-SAH is necessary per m² of the conditioned floor area to go above the typical COPs (2.6-3.0).

Agathokleous et al. (2019) developed a dynamic simulation model which was implemented through MATLAB for simulating the energy performance of building integrated, vertically installed multi-pass serpentine type flat plate SAH. The authors also investigated the thermal comfort of the occupants and performed an economic analysis of the system. The authors tested the prototype of the SAH and performed simulations of the proposed system for an office building with a 200 m² floor area for three different locations. The authors found that space heating savings could be as much as 3.4 MWh/y.

Prakash et al. (2022) investigated the energy and exergy performance of double pass hybrid SAH with sensible heat storage material (Metco and aluminum scrap mixture) which was placed underneath the backplate of the system. The authors tested the system for three different operation modes: natural convection mode, forced convection mode, and forced convection mode with a reflector. The forced convection mode with a reflector performed best with energy and exergy efficiencies of 86.19% and 17.617% respectively. The authors concluded that the system is suitable for space heating, desalination, drying, and other industrial and domestic applications.

Research Gap and Contribution of the Current Work

Although there has been broad research on SAHs, notable real-life applications of these systems to offices for space heating and performance testing are very few. It has been presented in the literature review that Fan et al. (2019b) and Agathokleous et al. (2019) developed, tested, and considered SAHs for offices. However, the system developed by Fan et al. is for producing heated air which is intended to be used in the regeneration process of a desiccant cooling system that supplies cooling to a commercial building. The work done by Agathokleous et al. on the other hand is intended for office heating, though the SAHs are building integrated, vertically installed and are multi-pass serpentine type.

To the best knowledge of the authors, real-life performance testing and application of a V-Corrugated SAH for space heating of offices do not exist. Hence, the current study will contribute to the literature by filling this gap. The objectives of the work can be summarized as (1) to evaluate the heating load of the selected office, (2) to model the V-Corrugated SAH for evaluating component temperatures, useful heat, efficiency, and area required to cover the load, (3) to experimentally test the SAH and compare the theoretical results with the test results.

Structure of the Paper

This work comprises five sections: Introduction, Methodology, Results & Discussion, Uncertainty Analysis and Conclusion. The Introduction section involves the motivation for the study, a review of the state of art of SAHs, and the contribution of the current work to the literature. The Methodology section elaborates on the materials and methods that are followed to realize the objectives of the study. First, the office space in consideration is described and subsequently its load evaluation is explained. Then the mathematical model of the V-Corrugated SAH is presented. Lastly Experimental procedure is elaborated. Results of the theoretical and experimental approach are presented and discussed in the Results & Discussion section. A brief uncertainty analysis is performed under the Uncertainty Analysis section. The Conclusion section at the end presents the principal findings of the study and concluding remarks.

METHODOLOGY

In this study, previously manufactured V-Corrugated SAH (Sahebari *et al.*, 2013) is retrofitted and installed to supply heat to an office space (Alteer, 2017). It is intended to evaluate the required number and area of SAHs that will cover the heating demand for a typical winter day. The performance of the system is investigated theoretically (through the solution of the mathematical model of the SAH by developed MATLAB code) and experimentally and the results are compared. Energy Plus software is utilized to estimate the heating load of the office space which is necessary for evaluating the required number and area of SAH.

The SAH employed in this study is a type with two glass covers and an absorber plate that is in V-Corrugated shape. The air flows through the series of channels having equilateral cross-section areas that are formed by the V-Corrugated absorber plate and the lower glass cover/back plate. Figure 1 illustrates the cross-section and the main components of the V-Corrugated SAH that is considered in this study. The principal advantages of the V corrugations are the increase in the absorber plate area and the enhancement of the convection heat transfer coefficient due to the corrugated shape which also positively affects the radiative characteristics of the absorber plate (Sparrow and Lin, 1962).

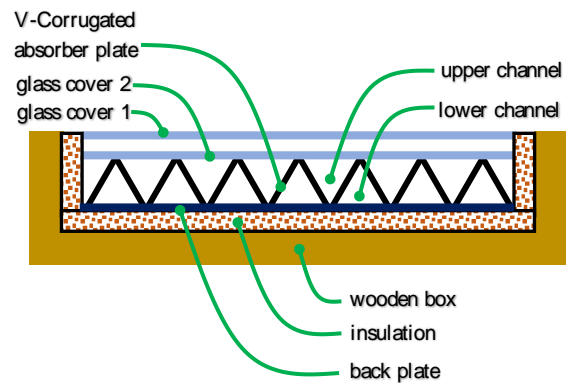


Figure 1. Cross section and the main components of the V-Corrugated SAH.

This work involves three principal segments: 1- load evaluation of the office space, 2- mathematical modelling and theoretical investigation of the SAH and 3- experimental investigation of the SAH.

The load of the office space is evaluated by Energy Plus program whereas the mathematical model of the SAH (energy balance equations of each component of SAH) is solved by the MATLAB program for associated

temperatures and useful heat output. Theoretically evaluated useful heat output (from MATLAB) is used together with the load of the office space to find the number of SAHs and area that are necessary to meet the heating demand of the space during a typical winter day. The SAH is also investigated experimentally. Temperature measurements of the SAH components together with the environmental variables (ambient temperature, solar radiation, and wind speed) have been taken and used to evaluate the actual useful heat output from the SAH.

The outputs of the MATLAB program have been compared with the experimental results to reveal the difference between the actual and model performance of the SAH. The methodology which has been followed in this work is schematically illustrated in Figure 2.

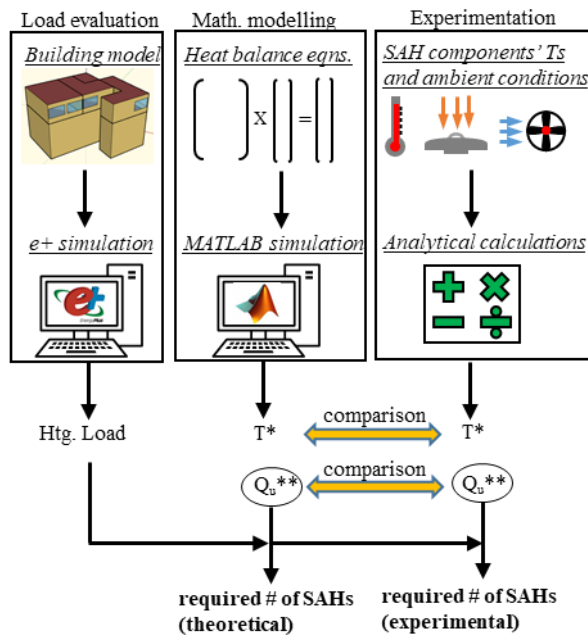


Figure 2. Methodology (*: SAH components' temperatures, **: Useful energy output from SAH).

Load Evaluation

The Energy Plus program is the tool employed for evaluating the heating load of the office space. The program is a dynamic energy and load simulation engine which is for energy appraisal and heating/cooling load calculations of buildings. It has been developed by the US Department of Energy and comes with components for constructing input files (IDF editor) and running processes (EP-launch). Energy Plus is made up from various modules which are designed for modeling and simulating applications such as pumping power calculations, conduction heat transfer evaluations

through building fabric, heating/cooling coil computations, etc. In addition to the modelling/simulation modules, there are other files and auxiliary programs that can be fed to and embedded into Energy Plus such as weather data files, example files generator and 3D ground heat transfer tool that enable a proper building energy simulation (U.S. Department of Energy, 2016a; 2016b; 2016c).

The office space that is intended to be served by the SAH is the Mechanical Engineering Department chairperson's office located at the top floor of the Mechanical Engineering Department building at the Eastern Mediterranean University campus in North Cyprus, Famagusta. The office space has a floor area of 84 m² and is made up from the construction materials that are widely used in North Cyprus. Figure 3 presents the plan of the office space, whereas Figure 4 shows the 3D model of the office space generated and to be exported to the Energy Plus program. The construction materials' properties that are entered into the program are given in Table 1 (ASHRAE, 2017; CIBSE, 2015; Turkish Standards Institute, 2008).

Indoor air temperature of 20°C is assumed for the space, whereas the outdoor conditions of the city of Larnaca (Lat. 34.9°, Lon. 33.6°) are employed for the load calculations since Famagusta's weather data does not exist in the Energy Plus. The meteorological conditions of Famagusta and Larnaca are very similar as two locations lie on the coast only about 50 km away from each other and have almost identical geographical features. The outdoor design temperature is 3.8°C.

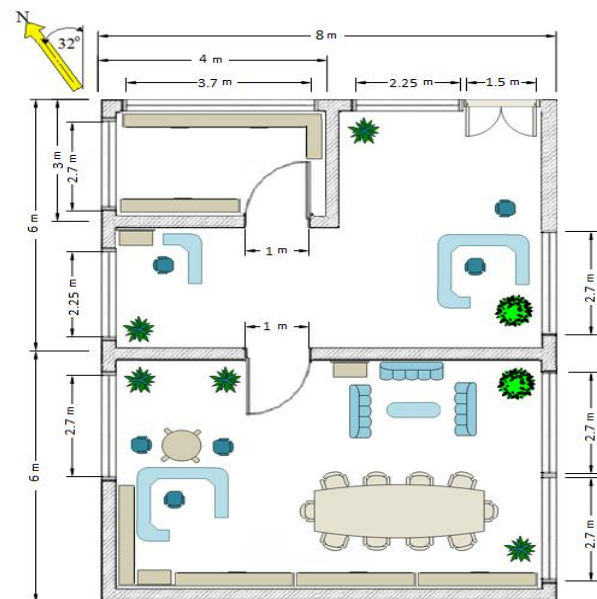


Figure 3. Office space to be served by SAH.

Table 1. Properties of the construction materials (ASHRAE, 2017; CIBSE, 2015; Turkish Standards Institute, 2008).

Struct.	Material & thickness	k (W/m.K)	ρ (kg/m ³)	c_p (J/kg.K)
Walls	Cement 2.5 cm	1.4	2100	650
	Brick 25 cm	0.4	700	840
	Cement 2.5 cm	1.4	2100	650
Floor	Marble 2 cm	2.9	2750	840
	Screed 1.5 cm	1.4	2100	650
	RC 20 cm	2.1	2400	840
	Cement 2.5 cm	1.4	2100	650
Roof	Screed 5 cm	1.4	2100	650
	RC 20 cm	2.1	2400	840
	Cement 2.5 cm	1.4	2100	650
Doors	Hardwood	0.17	700	1880
Windows' U values are 3.2 W/m ² .K RC: reinforced concrete				

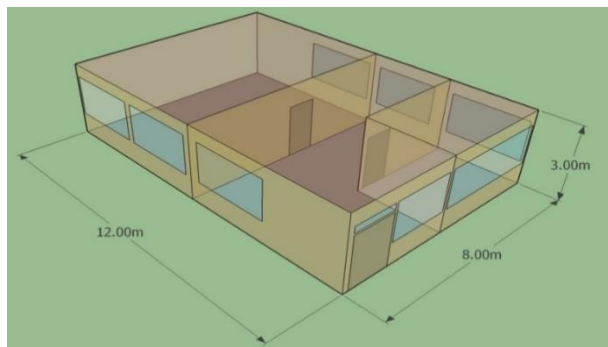


Figure 4. 3D model of the office space that is exported to Energy Plus for load evaluation.

Mathematical Model

As emphasized in the preceding sections it is intended to estimate the number and area of SAHs that is necessary to supply the amount of heat required to cover the load of the office space during a typical winter design day. To do that useful heat (Q_u) output from the SAH is to be evaluated theoretically. Q_u can be evaluated by multiplying the capacity rate of the air (mass flow rate times the specific heat of the air) with the inlet-outlet air

temperature difference through the SAH. Specific heat of air is known, and a mass flow rate can be set. However, the outlet air temperature of the SAH should be evaluated. This requires the calculation of temperatures of each constituent (e.g., glass, absorber plate, air layer, etc.) of the SAH. Associated temperatures of the SAH are obtained by deriving the energy balance equations (algebraic equations) for each component separately and forming a matrix to be solved for each component's as well as air layers' temperature simultaneously.

The components of the SAH are two flat transparent glasses i.e., glass 1 and glass 2, a V-Corrugated absorber plate, a flat back plate, and back elements (insulation, back wood, and galvanized steel protective cover). The list of these components from top to down and their dimensions are given in Table 2. The cross-section of the SAH is as shown in Figure 1 and the side and top views are as in Figure 5.

Table 2. SAH components and dimensions (from top to down).

Component	Material	Dimensions
Transparent cover 1 & 2	Glass	94 cm x 194 cm 0.4 cm thick
V- Corrug. absorber plate	Galvanized steel dyed in black	Corrug. angle 60° 0.2 cm thick
Back plate	Galvanized steel	97 cm x 197 cm 0.2 cm thick
Back insulation	Polystyrene	97 cm x 197 cm 2 cm thick
Back wood	Balsa wood	100 cm x 200 cm 4 cm thick
Protective cover	Galvanized steel	100 cm x 200 cm 0.2 cm thick

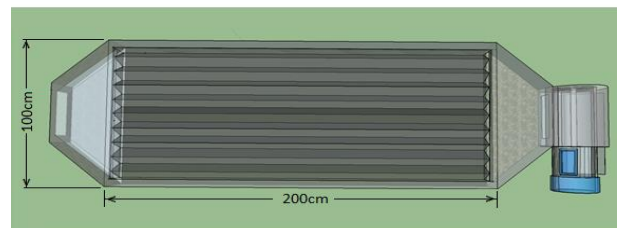
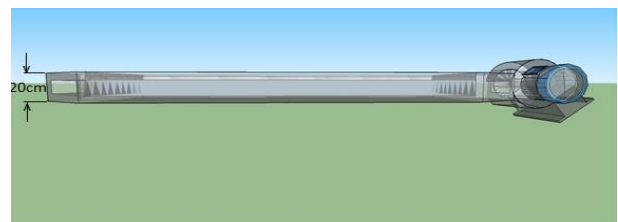


Figure 5. Side and top view of the SAH.

The equations of energy balance are constructed based on the thermal resistance network of the SAH which is

shown in Figure 6. Heat loss from the first cover occurs via forced convection (due to wind) and radiation to the ambient air and sky respectively. Thus, between the first cover and ambient air, there is forced convection resistance and there exists radiation resistance between the first cover and the sky. These two resistances are parallel to each other. Natural convection and radiation heat exchange take place across the second and first cover resulting in natural convection and radiation resistances in parallel. The absorbed radiation by the V-Corrugated absorber plate is distributed to the second glass cover and bottom plate by radiation and to the air flows in the upper and lower channels via forced convection. In addition, the flowing air in the upper and lower channels loses heat to the second glass cover and back plate respectively by forced convection. This results in a series of forced convection resistances connected to radiation resistance in parallel in the upper and lower channels. There exists heat loss across the back of the SAH which is via conduction through the back elements and convection from the outer surface. These are represented by a single resistance. The mathematical model of the SAH is based on the following assumptions (Lin *et al.*, 2006; Liu *et al.*, 2007):

- Steady-state conditions prevail
- Heat flow through the back elements is 1D
- The thermal inertia of SAH components is neglected
- Both air channels are free of leakage
- During operation, temperatures of each component are uniform
- The sky is considered as a blackbody for long wavelength radiation at an equivalent sky temperature
- Heat loss through the front and back side of the collector is to the same ambient temperature
- The shading generated by the V-Corrugated absorber plate, dirt, and dust on the glass covers are negligible
- Air temperature varies in the heat flux direction

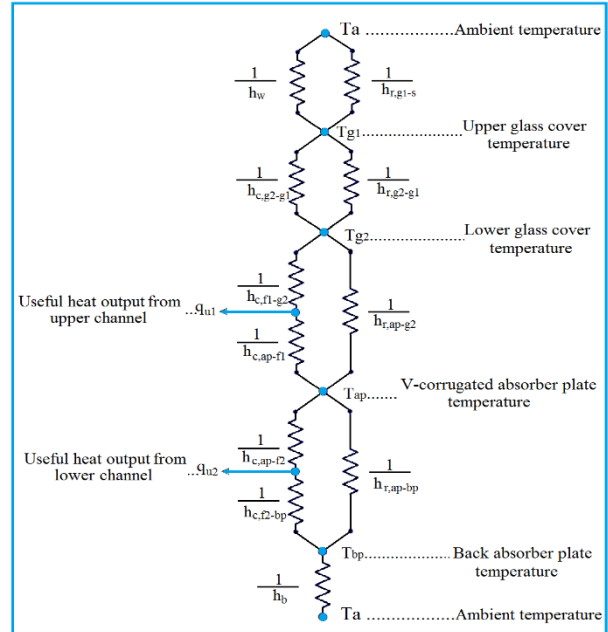


Figure 6. Thermal resistance network of the SAH.

The reasonings for the principal assumptions given above are elaborated as follows:

The mathematical model will be solved for each unknown parameter once at a time (once per hour) hence, assuming steady state is sufficient for the current study. In addition, the results would be presented hourly and within an hour in solar air heater applications, conditions can be presumed to be time-invariant. Since the considered SAH's back elements width (about 1 m) and length (about 2 m) are very large relative to the other dimension (thickness is about 0.062 m) and because the side wall areas of the SAH are very small it is reasonable to consider 1D heat transfer through the back elements. The thicknesses of the SAH components are very small (the thickest is the back wood with 0.04 m) hence the thermal storage of the components is neglected. Since the SAH's top and the bottom side is exposed to the same environment it is sufficient to assume that heat loss will be to the same temperature.

Equations (1) to (6) present energy balance equations for upper glass cover, lower glass cover, air in the upper channel, V-Corrugated absorber plate, air in the lower channel and back plate respectively (for description of abbreviations see the Symbols section) (Hedayatzadeh *et al.*, 2016; Lin *et al.*, 2006; Liu *et al.*, 2007):

$$\begin{aligned} \alpha_{g1}GA_h + (h_{r,g2-g1} + h_{c,g2-g1})(T_{g2} - T_{g1})A_h \\ = h_w(T_{g1} - T_a)A_h \\ + h_{r,g1-s}(T_{g1} - T_s)A_h \end{aligned} \quad (1)$$

$$\begin{aligned} \tau_{g1}\alpha_{g2}GA_h + h_{r,ap-g2}(T_{ap} - T_{g2})A_a \\ + h_{c,f1-g2}(T_{f1} - T_{g2})A_h \\ = (h_{r,g2-g1} + h_{c,g2-g1})(T_{g2} \\ - T_{g1})A_h \end{aligned} \quad (2)$$

$$\begin{aligned} h_{c,ap-f1}(T_{ap} - T_{f1})A_a \\ = \dot{q}_{u1} + h_{c,f1-g2}(T_{f1} \\ - T_{g2})A_h \end{aligned} \quad (3)$$

$$\begin{aligned} \tau_{g1}\tau_{g2}\alpha_{ap}GA_a = h_{r,ap-g2}(T_{ap} - T_{g2})A_a \\ + h_{c,ap-f1}(T_{ap} - T_{f1})A_a \\ + h_{c,ap-f2}(T_{ap} - T_{f2})A_a \\ + h_{r,pa-bp}(T_{ap} - T_{bp})A_a \end{aligned} \quad (4)$$

$$\begin{aligned} h_{c,ap-f2}(T_{ap} - T_{f2})A_a \\ = \dot{q}_{u2} \\ + h_{c,f2-bp}(T_{f2} - T_{bp})A_h \end{aligned} \quad (5)$$

$$\begin{aligned} h_{r,ap-bp}(T_{ap} - T_{bp}) + h_{c,f2-bp}(T_{f2} - T_{bp}) \\ = h_b(T_{bp} - T_a) \end{aligned} \quad (6)$$

Each of the above equations is arranged in the general form of the equation (7) where A, B, C, D, E, and F are factors in terms of convection and radiation coefficients, SAH and absorber plate area as well as air's capacity rate. Those equations can be written in the matrix multiplication form as $[A]x[T]=[B]$. $[A]$ is a matrix that is made up from the coefficients of the temperatures of the elements (glass 1, glass 2, air, etc.) of the SAH. $[T]$ is the column matrix which is made up from the temperature values of the elements of the SAH. $[B]$ is also a column matrix that is formulated by using the heat transfer coefficients, environmental parameters, and thermophysical properties of the elements. The resulting matrix multiplication form is shown in Figure 7.

$$\begin{aligned} T_{g1}A + T_{g2}B + T_{f1}C + T_{ap}D + T_{f2}E \\ + T_{bp}F = G \end{aligned} \quad (7)$$

$$\begin{bmatrix} (h_{r,g2-g1} + h_{c,g2-g1} + h_w + h_{r,g1-s}) & -(h_{r,g2-g1} + h_{c,g2-g1}) & 0 & 0 & 0 & 0 \\ -(h_{r,g2-g1} + h_{c,g2-g1})A_h & (h_{r,ap-g2}A_a + (h_{c,f1-g2} + h_{r,g2-g1} + h_{c,g2-g1})A_h) & -(h_{c,f1-g2})A_h & -(h_{r,ap-g2}A_a) & 0 & 0 \\ 0 & -(h_{c,f1-g2})A_h & h_{c,ap-f1}A_a + m c_p + h_{c,f1-g2}A_h & -(h_{c,ap-f1})A_a & 0 & 0 \\ 0 & -(h_{r,ap-g2})A_a & -(h_{c,ap-f1})A_a & (h_{r,ap-g2} + h_{c,ap-f1} + h_{c,ap-f2} + h_{r,ap-bp})A_a & -(h_{c,ap-f2})A_a & -(h_{r,ap-bp})A_a \\ 0 & 0 & 0 & -(h_{c,ap-f2})A_a & (h_{c,ap-f2}A_a + m c_p + h_{c,f2-bp}A_h) & -(h_{c,f2-bp})A_h \\ 0 & 0 & 0 & -(h_{r,ap-bp}) & -(h_{c,f2-bp}) & (h_b + h_{r,ap-bp} + h_{c,f2-bp}) \end{bmatrix} \begin{bmatrix} T_{g1} \\ T_{g2} \\ T_{f1} \\ T_{ap} \\ T_{f2} \\ T_{bp} \end{bmatrix} = \begin{bmatrix} (\alpha_{g1}G + h_w T_a + h_{r,g1-s} T_s) \\ (\tau_{g1}\alpha_{g2}GA_h) \\ (m c_p T_a) \\ (\tau_{g1}\tau_{g2}\alpha_{ap}GA_h) \\ (m c_p T_a) \\ (h_b T_{bp}) \end{bmatrix}$$

Figure 7. Matrix multiplication form of the energy balance equations.

Heat transfer coefficients associated with the SAH are elaborated below (Duffie *et al.*, 2020; Hedayatizadeh *et al.*, 2016; Lin *et al.*, 2006; Liu *et al.*, 2007).

Convection heat transfer coefficient between the glass cover 1 (upper glass cover) and the wind as well as radiation heat transfer coefficient between the glass cover 1 and sky is as follows (Duffie *et al.*, 2020):

$$h_w = 2.8 + 3V_w \quad (8)$$

$$h_{r,g1-s} = \sigma \varepsilon_{g1}(T_{g1} + T_s)(T_{g1}^2 + T_s^2) \quad (9)$$

The sky temperature (T_s) can be calculated by the expression given below (Hedayatizadeh *et al.*, 2016):

$$T_s = T_a - 6 \quad (10)$$

Natural convection and radiation heat transfer coefficients across glass cover 1 and glass cover 2 are expressed as (Duffie *et al.*, 2020):

$$h_{c,g2-g1} = Nu_{g1-g2} \frac{k}{L} \quad (11)$$

$$h_{r,g2-g1} = \frac{\sigma(T_{g1}^2 + T_{g2}^2)(T_{g1} + T_{g2})}{\frac{1}{\varepsilon_{g1}} + \frac{1}{\varepsilon_{g2}} - 1} \quad (12)$$

where Nu_{g1-g2} is the Nusselt number across the covers. Since the tilt angle of the SAH in the current work is 45° , the following equation applies to the Nusselt number. Note that the * indicates that only positive values in the brackets will be used (Duffie et al., 2020).

$$Nu_{g1-g2} = 1 + 1.44 \left[1 - \frac{1708}{Ra \cdot \cos \theta} \right]^* \left[1 - \frac{1708(\sin 1.8\theta)^{1.6}}{Ra \cdot \cos \theta} \right] + \left[\left(\frac{Ra \cdot \cos \theta}{5830} \right)^{\frac{1}{3}} - 1 \right]^* \quad (13)$$

Forced convection heat transfer coefficient between the air in the upper channel and the V-Corrugated absorber plate as well as the radiation heat transfer coefficient across the V-Corrugated absorber plate and the glass cover 2 (lower glass cover) is given below (Hedayatizadeh *et al.*, 2016):

$$h_{c,ap-f1} = Nu_{ap-f1} \frac{k_1}{D_h} \quad (14)$$

$$h_{r,ap-g2} = \frac{\sigma \varepsilon_{g2} \varepsilon_{ap} (T_{ap}^2 + T_{g2}^2) (T_{ap} + T_{g2})}{\varepsilon_{g2} + \varepsilon_{ap} - \varepsilon_{ap} \varepsilon_{g2}} \quad (15)$$

Nu_{ap-f1} is the Nusselt number in the upper channel and is given in the following equation. In the present work the Reynolds number (Re) of the flow in the upper channel is 8200 ($2800 < Re = 8208 < 10000$) hence the flow is transitional flow. Thus, the expression given below is for a transitional flow regime (Liu *et al.*, 2007).

$$Nu_{ap-f1} = 1.9 \times 10^{-6} Re_1^{1.79} + 225 \frac{H_1}{L} \quad (16)$$

The forced convection heat transfer coefficient between the air in the lower channel and the back plate as well as the radiation heat transfer coefficient across the V-Corrugated absorber plate and the back plate are analogous to equation 14 and 15.

In the preceding equations where properties of air i.e., density, thermal conductivity, and dynamic viscosity,

are necessary and following expressions can be used respectively (Lin et al., 2006):

$$\rho = 3.9147 - 0.016082T_f + 2.9013 \times 10^{-5}T_f^2 - 1.9407 \times 10^{-8} \times T_f^3 \quad (17)$$

$$k = (0.0015215 + 0.097459T_f - 3.3322 \times 10^{-5}T_f^2) \times 10^{-3} \quad (18)$$

$$\mu = (1.6157 + 0.06523T_f - 3.0297 \times 10^{-5}T_f^2) 10^{-6} \quad (19)$$

The overall heat transfer coefficient of the back elements is calculated by the following equation:

$$h_b = \left(\frac{H_{bp}}{k_{bp}} + \frac{H_{ins}}{k_{ins}} + \frac{H_{wood}}{k_{wood}} + \frac{H_{pc}}{k_{pc}} + \frac{1}{h_w} \right)^{-1} \quad (20)$$

A MATLAB code is constructed to calculate the required number and area of SAH to cover the heating load of the office space. The code solves the linear heat balance equations that are expressed in the form of $[A]x[T]=[B]$ by using the matrix inversion method. It evaluates the SAH components' temperatures simultaneously. Then the code calculates the exit temperature of the air from the upper and lower channels (T_{f1o} and T_{f2o}) of the SAH by inserting the evaluated upper and lower channel fluid temperature values (T_{f1} and T_{f2}) into the following equations. Note that it has been assumed that the air temperatures in the channels are the average of the inlet (ambient air temperature) and the outlet air temperatures:

$$T_{f1o} = 2T_{f1} - T_a \quad (21)$$

$$T_{f2o} = 2T_{f2} - T_a \quad (22)$$

Subsequently, the code evaluates the useful heat from the upper and lower air channels, total useful heat from the SAH and thermal efficiency respectively by the following equations:

$$q_{u1} = \dot{m}c_p(T_{f1o} - T_a)/2 \quad (23)$$

$$q_{u2} = \dot{m}c_p(T_{f2o} - T_a)/2 \quad (24)$$

$$Q_u = q_{u1} + q_{u2} \quad (25)$$

$$\eta = \frac{Q_u}{GA_h} \times 100 \quad (26)$$

Lastly, the number of collectors and total area required to cover the heating load of the office space are evaluated by the subsequent expressions:

$$N = \frac{Q_{htg}}{Q_u} \quad (27)$$

$$A_{total} = A_h N \quad (28)$$

Note that Q_{htg} is the heating load of the office space that is calculated by Energy Plus and required to be inputted into the MATLAB code. Also, it should be stated that the thermophysical properties of the SAH and measured parameters/operating parameters (wind speed, ambient temperature, global solar radiation, air mass flow rate through SAH), with assumed initial temperatures of each component (T_{g1} , T_{g2} , T_{f1} , T_{f2} , T_{ap} , T_{bp}) are introduced into the code to determine all the initial values of heat transfer coefficients. Accordingly, the code obtains new temperature values for the new iteration, and this continues until the preset condition is satisfied. The flowchart illustrating the workflow of the MATLAB code is shown in Figure 8.

Table 3 on the other hand presents the thermophysical properties of the SAH that are entered into the MATLAB code.

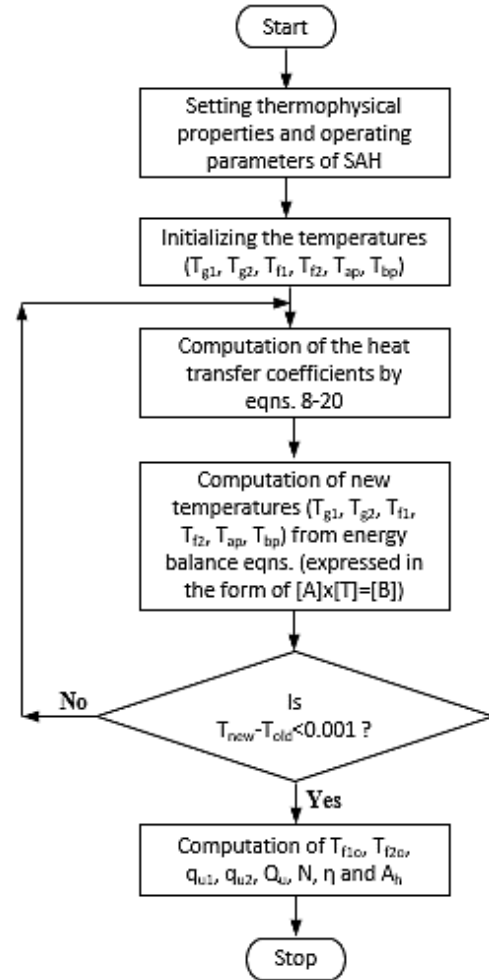


Figure 8. Workflow of the MATLAB code.

Table 3: Measured and thermophysical parameters required for the MATLAB code.

Item:	SAH width	SAH length	g1 to g2 distance
Value:	0.9 m	1.94 m	0.01 m
Item:	Height of the air channels	Back plate thickness	Insulation thickness
Value:	0.1 m	0.002 m	0.02 m
Item:	Back wood thickness	Protective cover thickness	Back plate k
Value:	0.04 m	0.002 m	80 W/m.K
Item:	Back wood k	Insulation k	Protective cover k
Value:	0.1 W/m.K	0.045 W/m.K	80 W/m.K
Item:	α_{ap}	α_{g1} & α_{g2}	τ_{g1} & τ_{g2}
Value:	0.9	0.06	0.9
Item:	ε_{g1} & ε_{g2}	ε_{ap} & ε_{bp}	Tilt angle
Value:	0.9	0.9	45°
Item:	Cp air		
Value:	1000 J/kg.K		

Experimental Procedure

Comparing the outputs of the MATLAB code for the various parameters (T_{g1} , T_{g2} , T_{f1} , T_{f2} , T_{ap} , T_{bp}) and the monitored values of the same parameters is one of the aims of this work. In this section, the experimental procedure is explained for monitoring the parameters that are used for comparison.

Various stages during the manufacturing of the V-Corrugated SAH (Sahebari *et al.*, 2013) are presented in Figure 9. As explained in the preceding section main components of the SAH are: two transparent glass covers, a V-Corrugated sheet metal absorber plate that is formed with groove angles of 60° , back absorber plate, polystyrene insulation, back wood, and protective cover. Air through the channels of the SAH is mobilized by an electric fan (type: OBR 200 M-2K) which is illustrated in Figure 10. The mass flow rate of the air is set by an electric resistor tool, which controls the input voltage in the range of 60 – 220 V.



Figure 9. Various stages of SAH manufacturing (Sahebari *et al.*, 2013).



Figure 10. Motor and fan of the SAH.

For recording the temperatures of each component of the SAH, ambient temperature, wind speed and air velocity from the SAH channels, the handheld data loggers Pasco Xplore GLX are used. These data loggers can be used with various sensors e.g., anemometer, temperature sensors, etc. Anemometer sensor (range: 0.5-29 m/s, accuracy: \pm (3% of reading+ 0.2 m/s)) is employed for wind speed and air velocity measurements, whereas temperature sensors (range: from -30°C to 105°C , accuracy: $\pm 0.5^\circ\text{C}$) are used to measure ambient air temperature and temperatures of the SAH components. A pyranometer mounted on the SAH (linearity: $\pm 0.5\%$ from 0 to 2800 W/m^2) together with a data acquisition system, Omega OMB-DAQ-3000 is utilized to measure and log the global solar radiation incident on the SAH. The data acquisition system is connected to a desktop computer by a USB wire. The software package of the Data acquisition system is installed on this computer. Figure 11 shows the measuring/monitoring equipment

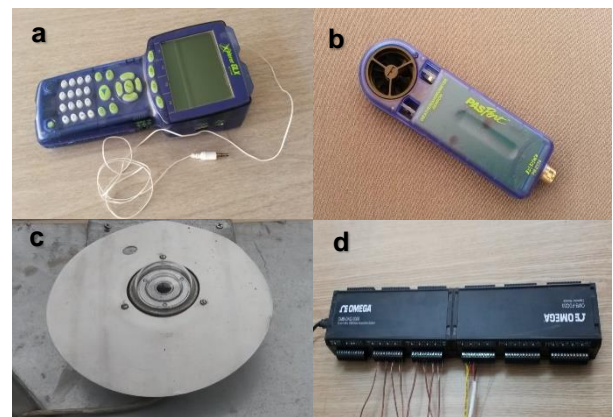


Figure 11. Measuring/monitoring equipment (a: handheld data logger and temperature sensor, b: anemometer, c: pyranometer and d: data acquisition system)

The SAH is tested at Famagusta, N. Cyprus (35.1°N and 33.9°E). The surface azimuth of the collector is set as 0° thus; the collector is towards the south. The tilt angle of the collector is 45° . Figure 12 and Figure 13 illustrates the schematic and real view of the experimental setup. The measured wind speed is a required parameter in the MATLAB code for evaluating the convection heat transfer coefficient (see equation (8)) from the top and back of the SAH. Also, global solar radiation and air mass flow rate measurements are required parameters in the code for evaluating useful heat output. Equations (23), (24), (25), and (26) that are given in the preceding section are used to determine the useful heat from the upper air channel, the useful heat from the lower air channel, the total useful heat, and the thermal efficiency of the SAH experimentally.

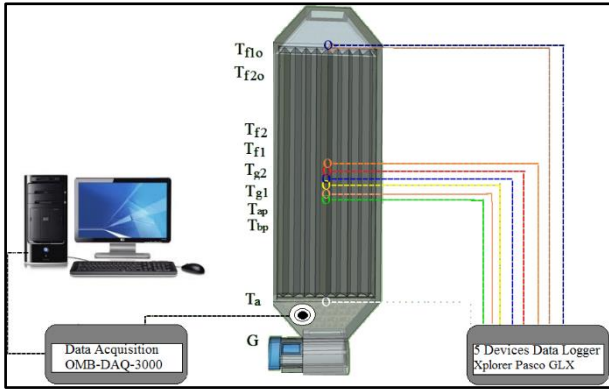


Figure 12. Schematic layout of the experimental setup.



Figure 13. View of the experimental setup.

RESULTS AND DISCUSSION

The office space that is intended to be served by the SAH has been modeled and simulated by Energy Plus software to calculate the heating load. The simulation results revealed the space heating load as 4564 W.

To run the MATLAB code for evaluating the useful heat, thermal efficiency, etc. various environmental/operational parameters such as ambient/inlet air temperature (T_a), global solar radiation (G), wind speed (V_w), and air mass flow rate through the air duct are required to be inputted. These parameters have been monitored and recorded on 15th December throughout the times when the solar radiation is at its utmost level, from 11:00 until 14:30 for every 5 minutes (i.e. time step= 5 minutes). The mean of six values is evaluated for representing every half hour. Figure 14 presents the measured wind speed and global solar radiation incident on the SAH, whereas Figure 15 shows the measured ambient/inlet air temperature. The flow

rate of the air is set according to the motor rpm. The motor rpm is adjusted to result in an air velocity of 1.8 m/s which gives a flow rate of 0.2 kg/s. With this flow rate, Reynolds numbers in the upper and lower channels are 8208 and 7579 respectively corresponding to the transitional flow regime in both channels.

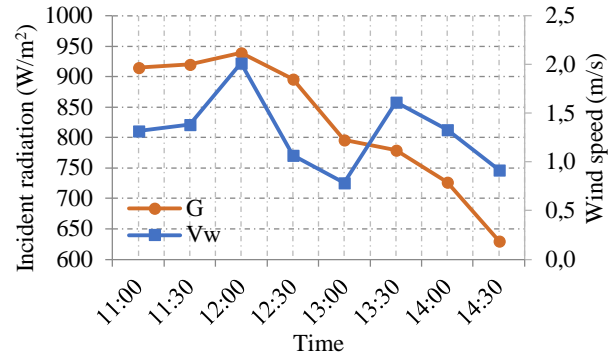


Figure 14. Measured wind speed and global solar radiation incident on SAH.

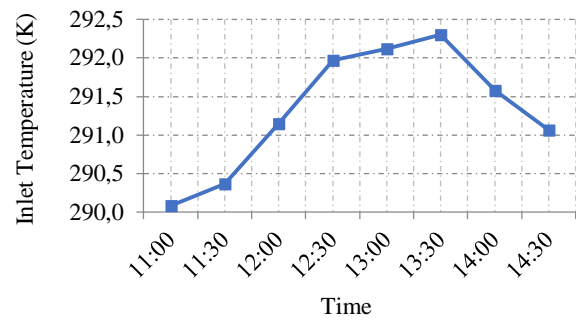


Figure 15. Measured ambient/inlet air temperature.

The temperature of the SAH elements; upper and lower glass cover, V-Corrugated absorber plate, and back plate are shown in Figure 16, Figure 17, Figure 18 and Figure 19 respectively.

When those figures are investigated, it is seen that the simulation results are having similar trends as the experimental ones. There is some discrepancy between the measured and simulated values. In some hours these discrepancies are very low whereas in some they are in significant order. The average of the differences of the simulated and monitored temperatures for upper glass cover, lower glass cover, V-Corrugated plate, and back plate are 1.4, 1.6, 2.8 and 2.0 K respectively.

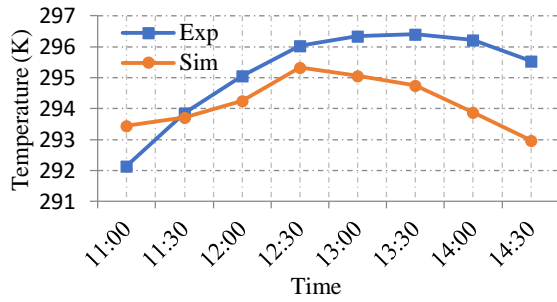


Figure 16. Upper glass cover temperatures.

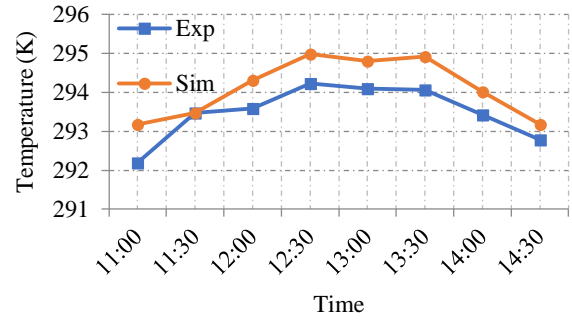


Figure 20. Air temperature at the middle of the upper channel.

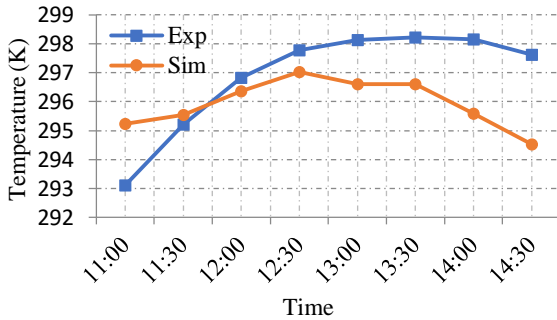


Figure 17. Lower glass cover temperatures.

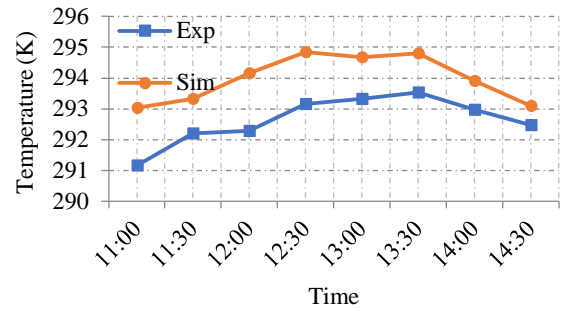


Figure 21. Air temperature at the middle of the lower channel.

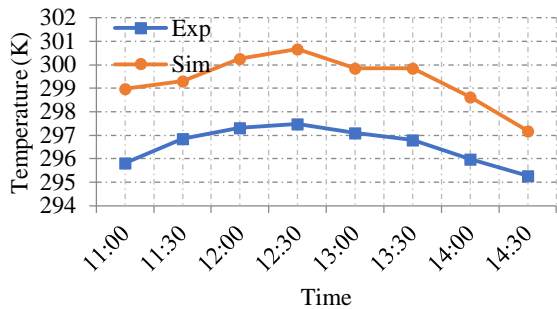


Figure 18. V-Corrugated absorber plate temperatures.

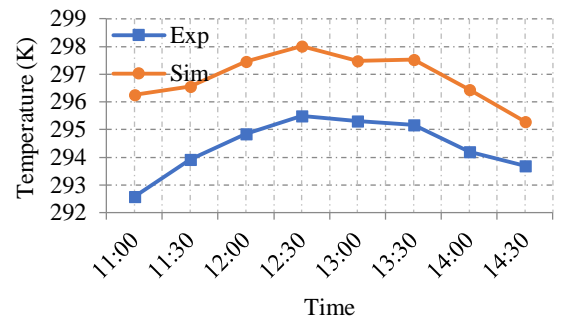


Figure 22. Air temperature at the exit of the upper channel.

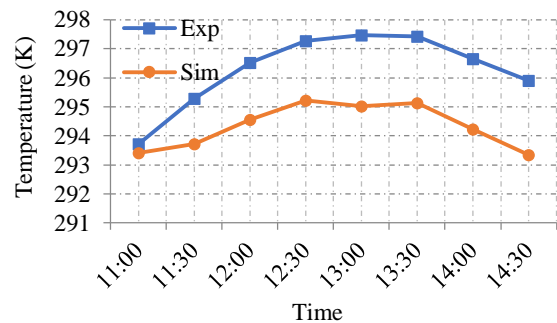


Figure 19. Back plate temperatures.

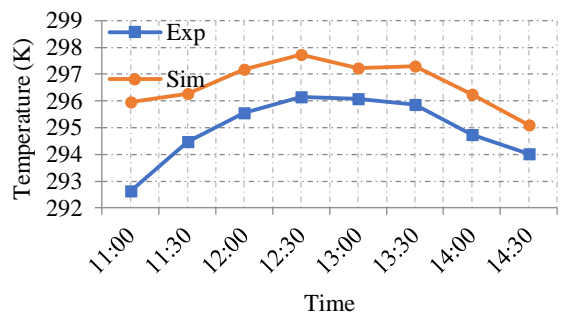


Figure 23. Air temperature at the exit of the lower channel.

Air temperatures in the SAH; air temperature in the middle of the upper and lower channels as well as the air temperatures at the exit of the upper and lower channels are given in Figure 20, Figure 21, Figure 22, and Figure 23 respectively.

Once the air temperatures at the middle and the exit of the upper and lower channels obtained from simulations and measurements are investigated, it is seen that the simulations and the measurements agree with some difference, however, the agreement is better than those for the SAH elements. The average of the differences between the measured and simulated values are 0.6, 1.3, 2.5, and 1.7 K for the air temperatures at the middle of

the upper channel, at the middle of the lower channel, at the exit of the upper channel, and at the exit of the lower channel respectively. The better agreement between the simulation results and the experimental measurements for the air temperatures than the SAH element temperatures is presumably due to the quick response of the air to the changes resulting in less effective dynamic behavior. It is expected to have some disagreement between the simulations and the measured values. First of all, the mathematical model that the MATLAB code is based on is not taking the thermal inertia and the dynamic behavior of the SAH into consideration (see the assumptions in the Mathematical model section). The response of the collector elements should be accounted to obtain more realistic results. In addition, the actual properties of the SAH components such as glass emissivity and transmissivity, absorber plate absorptivity, thermal conductivity, etc. are likely to have values that are different from those employed for MATLAB simulations. Although the values for these properties are found from reliable sources and catalogs, they may not match precisely with the actual values. Furthermore, the accuracies of the monitoring equipment are thought to influence the discrepancies.

Total useful heat output from the SAH and the thermal efficiency are shown in Figure 24 and Figure 25 respectively. The required number of SAHs and the area to meet the target heating load evaluated by the MATLAB code and the experimental analysis are shown in Table 4. Note that the values are given for every half hour. Number of SAH and corresponding area that is necessary to supply the load is taken as the max. number which resulted in 9 SAHs with 16 m² for the real case (experimental) and 6 SAHs with 10 m² for simulations.

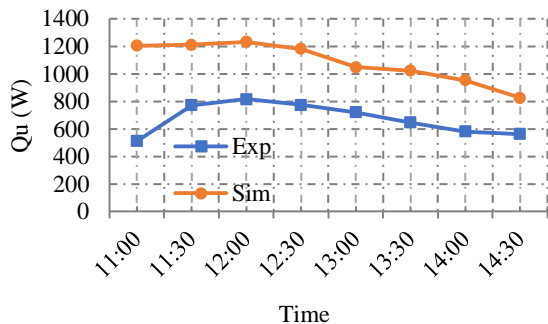


Figure 24. Useful heat from SAH.

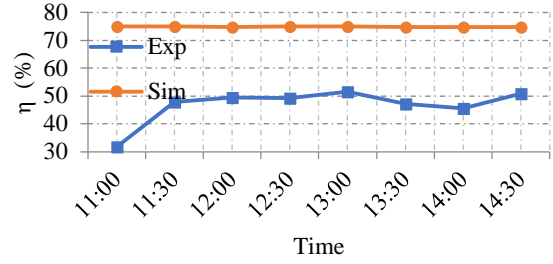


Figure 25. Thermal efficiency of the SAH.

Table 4: Required number of SAHs and area to meet the target heating load.

Time	# _{exp}	# _{sim}	Ah _{exp} (m ²)	Ah _{sim} (m ²)
11:00	8.9	3.8	15.6	6.6
11:30	5.9	3.8	10.4	6.6
12:00	5.6	3.7	9.8	6.5
12:30	5.9	3.9	10.3	6.8
13:00	6.3	4.4	11.1	7.6
13:30	7.1	4.5	12.4	7.8
14:00	7.8	4.8	13.8	8.4
14:30	8.1	5.5	14.2	9.7
Max.	≈ 9	≈ 6	≈ 16	≈ 10

UNCERTAINTY ANALYSIS

Comparison of the obtained results by simulations and measurements revealed that, there are discrepancies between them. As stated in the preceding section one of the reason for this difference is believed to be because of the accuracies of the employed equipment in the experimentation. In this section an uncertainty analysis of the experimental results (for useful heat) is performed based on the following expression (Holman, 2012):

$$\omega_R = \left[\left\{ \left(\frac{\partial R}{\partial x_1} \right)^2 \times (\omega_{x_1})^2 \right\} + \left\{ \left(\frac{\partial R}{\partial x_2} \right)^2 \times (\omega_{x_2})^2 \right\} + \dots + \left\{ \left(\frac{\partial R}{\partial x_n} \right)^2 \times (\omega_{x_n})^2 \right\} \right]^{0.5} \quad (29)$$

Where R is a function of variables of x_1, x_2, \dots, x_n , which its uncertainty is to be evaluated. $\omega_1, \omega_2, \dots, \omega_n$ are the associated uncertainties of the variables and ω_R is the overall uncertainty of the function.

In the context of this study R is the Qu which its uncertainty will be evaluated and is function of the following measured variables:

- air temperature at the exit and inlet of the SAH
- air speed in the SAH

Note that Q_u is evaluated by equation (25) which can be expanded as:

$$Q_u = \rho_1 A_1 V c_p (T_{f1o} - T_{f1i}) + \rho_2 A_2 V c_p (T_{f2o} - T_{f2i}) \quad (30)$$

It should be also noted that the air density is also function of temperature (see equation (17)).

Uncertainty of the Q_u is evaluated by applying equation (29) together with the uncertainties of the air temperature and air speed measuring equipment (± 0.5 °C and $\pm 3\%$ of reading + 0.2 m/s, see subsection “Experimental Procedure”) and it is found that the average of the uncertainty of the Q_u throughout the day is 25.6% (Alteer, 2017).

CONCLUSION

The principal aim of the present work is to investigate the performance of a V-Corrugated absorber plate SAH which is intended to be used in an office for space heating during a typical winter day in N. Cyprus. Although there are many studies on SAHs, space heating applications with them are few. Besides, to the knowledge of the authors, there are no V-Corrugated SAH applications for offices for space heating. Hence this study aims to contribute by proposing and promoting them for this purpose via thermal performance investigation. The performance of SAH is investigated theoretically and experimentally and the below outcomes are achieved:

The first phase of the work is to estimate the heating load of the office space in consideration by using Energy Plus software. The simulations gave the heating load as 4564 W.

The second outcome of this work is the number of SAHs and the area necessary to cover the load of the office space. This is achieved by evaluating the thermal performance of the SAH. Thermal performance is investigated theoretically and experimentally under the same environmental parameters that are obtained on 15th of December, from 11:00 until 14:30. The number of SAHs and the area that are necessary to cover the target heating load are found as 6 and 10 m² for the theoretical case. On the other hand, it is found from experimental investigation that, 9 SAHs with 16 m² are required. It is

seen that there is disagreement between the theoretical (simulations) and experimental results. The disagreement is thought to be generated by the following reasons:

1) In the experimental setup the exit air from the SAH is exposed directly to the ambient. This is likely to reduce the exit air temperature for the experimental case, causing discrepancy between the theoretical and experimental results.

2) Thermal properties of the materials that are employed for manufacturing the SAH should be investigated in detail thus reducing the possible mismatch between the actual properties and those used for the theoretical evaluations.

3) The accuracies of the employed measuring equipment may generate noteworthy uncertainties in the experimental results thus equipment having better accuracies can be used.

Consequently, 9 of the V-Corrugated SAHs can be coupled together for covering the heating demand of the considered office space. It is also recommended that the simulations for obtaining the required number of SAHs for covering the demand for the space should be used with care as they are resulting in larger useful heat which gives a smaller number of SAHs.

It is suggested that in any case an auxiliary heater should be employed for the days having not enough solar radiation.

ACKNOWLEDGMENTS

This work is produced from the Master of Science Thesis of Mr. Khaled Alteer, titled “Installation and Performance Testing of Solar Air Heater for Office Heating” which was presented in the Department of Mechanical Engineering of Eastern Mediterranean University in 2017 (Alteer, 2017).

The first author of the current work finds this opportunity to acknowledge the efforts of Mr. Khaled Alteer during his studies and would like to thank for his contribution to the current work.

REFERENCES

Agathokleous R., Barone G., Buonomano A., Forzano C., Kalogirou S. A. and Palombo A, 2019, Building Facade Integrated Solar Thermal Collectors For Air

Heating: Experimentation, Modelling and Applications, *Applied Energy*, 239, 658–679.

Al-Kayiem H. H. and Yassen T. A., 2015, On the Natural Convection Heat Transfer in a Rectangular Passage Solar Air Heater, *Solar Energy*, 112, 310–318.

Alteer K., 2017, *Installation and Performance Testing of Solar Air Heater for Office Heating*, M.Sc. Thesis Eastern Mediterranean University, Famagusta.

ASHRAE, 2017, *ASHRAE Fundamentals 2017*, (SI Edition), ASHRAE, Atlanta.

Bayrak F. and Oztop H. F., 2015, Experimental Analysis of Thermal Performance of Solar Air Collectors with Aluminum Foam Obstacles. *J. of Thermal Science and Technology*, 35, 11–20.

CIBSE, 2015, *Environmental design CIBSE Guide A*, (Eighth Edition), The Chartered Institution of Building Services Engineers, London.

Çiftçi E., Khanlari A., Sözen A., Aytaç İ. and Tuncer, A. D., 2021, Energy And Exergy Analysis Of A Photovoltaic Thermal (PVT) System Used In Solar Dryer: A Numerical and Experimental Investigation, *Renewable Energy*, 180, 410–423.

Duffie J. A., Beckman W. A. and Blair N., 2020. *Solar Engineering of Thermal Processes, Photovoltaics and Wind*, (5th ed.), Wiley, New Jersey.

El-Sebaï A. A., Aboul-Enein S., Ramadan M. R. I., Shalaby S. M. and Moharram B. M., 2011, Thermal Performance Investigation of Double Pass-Finned Plate Solar Air Heater, *Applied Energy*, 88(5), 1727–1739.

Fan W., Kokogiannakis G. and Ma Z., 2019a, Optimisation of Life Cycle Performance of a Double-Pass Photovoltaic Thermal-Solar Air Heater with Heat Pipes, *Renewable Energy*, 138, 90–105.

Fan W., Kokogiannakis G. and Ma Z., 2019b, Integrative Modelling and Optimisation of a Desiccant Cooling System Coupled with a Photovoltaic Thermal-Solar Air Heater, *Solar Energy*, 193, 929–947.

Fan W., Kokogiannakis G., Ma, Z. and Cooper P., 2017, Development of a Dynamic Model for a Hybrid Photovoltaic Thermal Collector – Solar Air Heater with Fins. *Renewable Energy*, 101, 816–834.

Gao W., Lin W., and Lu E., 2000, Numerical Study on Natural Convection Inside the Channel Between the Flat-Plate Cover and Sine-Wave Absorber of a Cross-Corrugated Solar Air Heater, *Energy Conversion and Management*, 41, 145–151.

Gawande V. B., Dhoble A. S., Zodpe, D. B. and Chamoli S., 2016. Experimental and CFD Investigation of Convection Heat Transfer in Solar Air Heater with Reverse L-Shaped Ribs. *Solar Energy*, 131, 275–295.

Gilani S. E., Al-Kayiem, H. H., Woldemicheal D. E., and Gilani S. I., 2017, Performance Enhancement of Free Convective Solar Air Heater by Pin Protrusions on the Absorber. *Solar Energy*, 151, 173–185.

Hedayatizadeh M., Sarhaddi F., Safavinejad A., Ranjbar F. and Chaji H., 2016, Exergy Loss-Based Efficiency Optimization of a Double-Pass/Glazed V-Corrugated Plate Solar Air Heater. *Energy*, 94, 799–810.

Holman J. P., 2012, *Experimental Methods for Engineers* (Eighth Edition), McGraw-Hill, New York.

Internet, 2021, International Energy Agency, *World Energy Outlook 2021*, www.iea.org/weo.

Jain D. and Jain R. K., 2004, Performance Evaluation of an Inclined Multi-Pass Solar Air Heater with In-Built Thermal Storage on Deep-Bed Drying Application. *Journal of Food Engineering*, 65(4), 497–509.

Kareem M. W., Habib K., Ruslan M. H. and Saha B. B., 2017, Thermal Performance Study of a Multi-Pass Solar Air Heating Collector System for Drying of Roselle (*Hibiscus Sabdariffa*). *Renewable Energy*, 113, 281–292.

Internet, 2021, kib-tek (*Kıbrıs Türk Elektrik Kurumu*), Production-Consumption Statistics, <https://www.kibtek.com/statistikler/>.

Kumar A., Singh A. P., Akshayveer and Singh O. P., 2022, Performance Characteristics of a New Curved Double-Pass Counter Flow Solar Air Heater. *Energy*, 239.

Lin W., Gao W. and Liu T., 2006, A Parametric Study on the Thermal Performance of Cross-Corrugated Solar Air Collectors. *Applied Thermal Engineering*, 26(10), 1043–1053.

- Liu T., Lin W., Gao W. and Xia, C., 2007, A Comparative Study of the Thermal Performances of Cross-Corrugated And V-Groove Solar Air Collectors, *International Journal of Green Energy*, 4(4), 427–451.
- Internet, 2022, North Cyprus Meteorological Office, *Cyprus Climate*. General Weather of North Cyprus, <http://kktcmeteor.org/meteorolojikbilgi/kibris-iklimi#>
- Prakash O., Kumar A., Samsher Dey K. and Aman A., 2022, Exergy and Energy Analysis of Sensible Heat Storage Based Double Pass Hybrid Solar Air Heater, *Sustainable Energy Technologies and Assessments*, 49.
- Sahebari R., Enesi V. and Tamer U., 2013, *Designing and Manufacturing of a Solar Air Heater*, B.Sc. Thesis, Eastern Mediterranean University, Famagusta.
- Sparrow E. M., and Lin S. H., 1962, Absorption of Thermal Radiation in A V-Groove Cavity, *International Journal of Heat and Mass Transfer*, 5(11), 1111–1115.
- Turkish Standards Institute, 2008, *TSE 825 Thermal Insulation Requirements for Buildings*. Turkish Standards Institute, Ankara.
- U.S. Department of Energy, 2016a, *EnergyPlus™ Version 8.6 Documentation Engineering Reference*, U.S. Department of Energy, Berkeley.
- U.S. Department of Energy, 2016b, *EnergyPlus™ Version 8.6 Documentation Getting Started*, U.S. Department of Energy, Berkeley.
- U.S. Department of Energy, 2016c, *EnergyPlus™ Version 8.6 Documentation Input Output Reference (Version 8.6)*, U.S. Department of Energy, Berkeley.
- Yildirim C., and Solmuş, İ., 2014, Investigaton of Double Pass Solar Air Collector Channel Depth on Thermohydraulic Efficiency. *J. of Thermal Science and Technology*, 34, 111–122.



PHYSICS INFORMED NEURAL NETWORKS FOR TWO DIMENSIONAL INCOMPRESSIBLE THERMAL CONVECTION PROBLEMS

Atakan AYGUN and Ali KARAKUS

Department of Mechanical Engineering, Middle East Technical University, 06800 Çankaya Ankara
atakana@metu.edu.tr, ORCID: 0000-0003-4399-1935
akarokus@metu.edu.tr, ORCID: 0000-0002-9659-6712

(Geliş Tarihi: 27.04.2021, Kabul Tarihi: 12.09.2022)

Abstract: Physics-informed neural networks (PINNs) have drawn attention in recent years in engineering problems due to their effectiveness and ability to tackle problems without generating complex meshes. PINNs use automatic differentiation to evaluate differential operators in conservation laws and hence do not need a discretization scheme. Using this ability, PINNs satisfy governing laws of physics in the loss function without any training data. In this work, we solve various incompressible thermal convection problems, and compare the results with numerical or analytical results. To evaluate the accuracy of the model we solve a channel problem with an analytical solution. The model is highly dependent on the weights of individual loss terms. Increasing the weight of boundary condition loss improves the accuracy if the flow inside the domain is not complicated. To assess the performance of different type of networks and ability to capture the Neumann boundary conditions, we solve a thermal convection problem in a closed enclosure in which the flow occurs due to the temperature gradients on the boundaries. The simple fully connected network performs well in thermal convection problems, and we do not need a Fourier mapping in the network since there is no multiscale behavior. Lastly, we consider steady and unsteady partially blocked channel problems resembling industrial applications to power electronics and show that the method can be applied to transient problems as well.

Keywords: physics-informed neural networks, machine learning, automatic differentiation, incompressible, heat transfer.

SIKIŞTIRILAMAZ ISIL TAŞINIM PROBLEMLERİNİN FİZİKLE ÖĞRENEN YAPAY SİNİR AĞLARI İLE ÇÖZÜMÜ

Öz: Fizikle öğrenen yapay sinir ağları (PINN'ler), etkinlikleri ve karmaşık ağlar oluşturmadan problemlerin üstesinden gelme yetenekleri nedeniyle son yıllarda mühendislik problemlerinde dikkat çekmiştir. PINN'ler, koruma yasalarında diferansiyel operatörleri değerlendirmek için otomatik türevlenmeyi kullanır ve bu nedenle bir ayrıklaştırma şemasına ihtiyaç duymaz. Bu yeteneği kullanarak, PINN'ler herhangi bir eğitim verisi olmadan kayıp fonksiyonunda geçerli fizik yasalarını karşılar. Bu çalışmada, gerçek uygulamalar ve karşılaştırılabilir sayısal veya analitik sonuçlara sahip problemler de dahil olmak üzere çeşitli sıkıştırılmaz ısı taşınım problemlerini çözüyoruz. Modelin performansını değerlendirmek için analitik çözümü olan bir kanal problemini çözüyoruz. Model, bireysel kayıp terimlerinin ağırlıklarına büyük ölçüde bağlıdır. Alan içindeki akış çok karmaşık değilse, sınır koşulu kaybının ağırlığının artırılması doğruluğu artırır. Farklı tipteki ağların performansını ve Neumann sınır koşullarını yakalama yeteneğini değerlendirmek için, sınırlardaki sıcaklık gradyanlarından dolayı akışın meydana geldiği kapalı bir muhafazada bir termal konveksiyon problemini çözüyoruz. Basit tam bağlantılı ağ, termal konveksiyon problemlerinde iyi performans gösterir ve çok ölçekli davranış olmadığından ağda Fourier dönüşümüne ihtiyacımız yoktur. Son olarak, endüstriyel uygulamaları güç elektroniğine benzeyen sabit ve kararsız kısmen bloke kanal problemlerini ele alıyoruz ve yöntemin geçici problemlere de uygulanabileceğini gösteriyoruz.

Anahtar Kelimeler: fizikle öğrenen yapay sinir ağları, makine öğrenmesi, otomatik türevlenme, sıkıştırılmaz, ısı transferi.

NOMENCLATURE

Abbreviations

Gr	Grashof Number $[= g\beta(T - T_r)L_r^3/\nu^2]$
Pr	Prandtl Number $[= \nu/\alpha]$
Ra	Rayleigh Number $[= GrPr]$
Re	Reynolds Number $[= U_r L_r/\nu]$
DGM	Deep Galerkin Method

DNS	Direct Numerical Simulation
FCN	Fully Connected Network
MLP	Multilayer Perceptron
NS	Navier-Stokes
NTK	Neural Tangent Kernel
PDE	Partial Differential Equation
PINN	Physics Informed Neural Network

Subscripts

u	Velocity Related Value
θ	Temperature Related Value
BC	Boundary Condition
D	Dirichlet Boundary
IC	Initial Condition
N	Neumann Boundary
R	Residual
r	Reference Value

Greek Symbols

α	Thermal Diffusivity [= m^2/s]
β	Expansion Coefficient [= $1/^\circ C$]
$\nabla \cdot$	Divergence Operator
∇	Gradient Operator
Δ	Laplace Operator
ν	Kinematic Viscosity [= m^2/s]
ω	Weight of loss terms
σ	Activation Function
θ	Non-dimensional Temperature

Symbols

s_u	Source Term of Momentum Equation
u	Velocity Vector
\mathcal{L}	Loss Term of a Neural Network
\mathcal{N}	Generalized Differential Operator
g_D	Dirichlet Boundary Condition
g_N	Neumann Boundary Condition
L_2	L_2 Vector Norm of Error
p	Non-dimensional Pressure
s_θ	Source Term of Energy Equation
t	Non-dimensional Time

INTRODUCTION

Thermal convection problems arise in many practical engineering applications, such as cooling electronic chips. This type of real-life analysis of fluid flow and heat transfer requires high degrees of freedom to minimize the numerical error. This can be achieved with high-quality mesh or high order discretizations. However, mesh generation is time consuming and requires expertise. Also, high order simulation tools for these types of problems are computationally demanding.

The incompressible thermal convection is studied in the literature with various numerical methods (Baïri et al., 2014). Tang and Tsang (1993) used a least squares finite element method based on a velocity, pressure, vorticity, temperature, and heat flux formulation for time dependent problems. Hossain et al. (2021) developed a spectral/hp element method for the Direct Numerical Simulation (DNS) of incompressible thermal convective flows by considering Boussinesq type thermal body-forcing with periodic boundary conditions and enforcing a constant volumetric flow rate. In Karakus (2022), the author presented a GPU accelerated nodal discontinuous Galerkin method on unstructured triangular meshes for solving problems on different convective regimes.

Apart from the conventional numerical methods such as finite difference, finite volume, and finite element methods, data-driven machine learning methods are used to solve the partial differential equations (PDE) (Willard et al., 2020). These regression methods offer effective and mesh free approaches (Karniadakis et al., 2021). Neural networks were first employed to solve the PDEs as in Lee and Kang (1990) and Lagaris et al. (1998), and in Raissi et al. (2017a) and Raissi et al. (2017b), the authors employed Gaussian processes regression to accurately predict the solution and provide the uncertainty in the model. Raissi et al. (2019) introduced the concept of physics-informed neural networks (PINNs) that use automatic differentiation (Baydin et al., 2017) to solve forward and inverse problems for several types of PDEs. PINNs do not require mesh generation. Instead, the PDEs and any other constraints can be directly enforced into the loss function of the neural network using automatic differentiation by forcing the prediction to the target value. The loss function includes zero residuals for conservation laws and satisfying the boundary/initial conditions.

To solve PDEs using PINNs, generally, fully connected networks are used. However, plain fully connected networks perform poorly for different types of problems. In the learning process, these networks have a learning bias toward low-frequency functions called spectral bias (Rahaman et al., 2019). This reduces the accuracy in which the target function exhibits high frequency or multi-scale behavior. To overcome this problem, Tancik et al. (2020) and Wang et al. (2021b) proposed Fourier feature mapping of the input vectors before feeding them into the network. The input coordinates \mathbf{v} is mapped with $\gamma(\mathbf{v}) = a_1 \cos(2\pi \mathbf{b}_1^T \mathbf{v}), a_1 \sin(2\pi \mathbf{b}_1^T \mathbf{v}), \dots, a_m \cos(2\pi \mathbf{b}_m^T \mathbf{v}), a_m \sin(2\pi \mathbf{b}_m^T \mathbf{v})$ and then passed into the multi-layer perceptron (MLP). This mapping transforms the Neural Tangent Kernel (NTK) (Jacot et al., 2018) into a stationary kernel and enables controlling the learning of the range of frequencies by modifying the frequency vectors \mathbf{b} in the mapping function. Tancik et al. (2020) show the performance of this method in many low-dimensional tasks in computer vision. Wang et al. (2021b) show its efficiency for challenging problems involving partial differential equations with multi-scale behavior where conventional PINN models might have issues, such as wave propagation and reaction-diffusion equations.

In another approach, Esmaeilzadeh et al. (2020) proposed a PDE constrained deep learning algorithm that reconstructs high-resolution solutions using the low resolution physical solutions in space and time, and solved the well-known Rayleigh-Bénard instability problem. This model is referred to as super resolution model and enables effectively scaling to large domains and having physically reasonable solutions by

regularizing the outputs with PDE constraints. The framework is named as MeshfreeFlowNet and consists of two subnetworks. The first network, called Context Generation Network, is a convolutional encoder that takes low resolution physical input and creates a Latent Context Grid. This grid contains latent context vectors along with the spatio-temporal coordinates, and these values are fed into another network called Continuous Decoding network modeled as an MLP. This framework allows the output to be continuous instead of a discrete output, removing the output resolution limitations. In addition, this continuous output allows us to effectively compute the output's gradients, enabling us to enforce the PDE-based constraints.

Due to the popular deep learning frameworks such as TensorFlow (Abadi et al., 2016) and PyTorch (Paszke et al., 2019), and their easy implementation, PINNs have become quite popular for solving PDEs. Moreover, some software libraries are designed explicitly for physics-informed machine learning, such as DeepXDE (Lu et al., 2021) and NeuralPDE (Zubov et al., 2021). It is used for solving incompressible and compressible Navier-Stokes equations (Rao et al., 2020; Jin et al., 2021; Cai et al., 2022), as well as in inverse heat transfer problems (Cai et al., 2021). To the best of our knowledge, solving forward thermal convection problems with PINNs, the effect of different neural networks on the accuracy, and the effect of the weights in the loss terms for different thermal convection regimes are not studied in detail.

In this work, we present the application of PINNs to coupled fluid flow and heat transfer problems in different thermal convection regimes. In particular, we examined the effectiveness of specific weights assigned to the different loss terms in the composite loss function. Changing these specific weights can increase the accuracy of the model according to the problem where boundary conditions or flow inside the computational domain dominates the residual. In addition, for thermal convection problems, different types of networks can be used instead of simple, fully connected networks. These various networks can change the convergence of the model.

The remainder of this paper is organized as follows. First, we present the mathematical formulation of incompressible Navier-Stokes equations coupled with the energy equation through Boussinesq approximation. Then we give brief information about the physics-informed neural networks and their loss functions, followed by the 2D numerical validation cases. The last section is about concluding remarks and future works.

FORMULATION

We consider a closed two-dimensional domain $\Omega \subset R^2$ and denote the boundary of Ω by $\partial\Omega$. Following the notation presented in Karakus et al. (2019b), we assume that $\partial\Omega$ can be partitioned into two non-overlapping regions denoted by $\partial\Omega_D$ and $\partial\Omega_N$ referring prescribed Dirichlet or Neumann boundary conditions, respectively. We are interested in the approximation of non-isothermal incompressible Navier-Stokes equations coupled by the energy equations through Boussinesq approximation which reads:

$$\nabla \cdot \mathbf{u} = 0, \quad (1.1)$$

$$\frac{\partial \mathbf{u}}{\partial t} + (\mathbf{u} \cdot \nabla) \mathbf{u} = -\nabla p + \frac{1}{Re} \Delta \mathbf{u} + \mathbf{s}_u, \quad (1.2)$$

$$\frac{\partial \theta}{\partial t} + (\mathbf{u} \cdot \nabla) \theta = \frac{1}{Re Pr} \Delta \theta + s_\theta, \quad (1.3)$$

in non-dimensional form and space-time slab $\Omega \times (0, \mathcal{T}]$ subject to the initial conditions

$$\mathbf{u} = \mathbf{u}_0, \theta = \theta_0 \text{ for } t = 0, \mathbf{x} \in \Omega, \quad (2)$$

and the boundary conditions

$$\mathbf{u} = \mathbf{g}_D \text{ on } x \in \partial\Omega_D^u, t \in (0, \mathcal{T}], \quad (3.1)$$

$$\frac{\partial \mathbf{u}}{\partial \mathbf{n}} = 0, p = 0 \text{ on } x \in \partial\Omega_N^u, t \in (0, \mathcal{T}], \quad (3.2)$$

$$\theta = g_D \text{ on } x \in \partial\Omega_D^\theta, t \in (0, \mathcal{T}], \quad (3.3)$$

$$\frac{\partial \theta}{\partial \mathbf{n}} = g_N \text{ on } x \in \partial\Omega_N^\theta, t \in (0, \mathcal{T}]. \quad (3.4)$$

Here u , p , and θ are non-dimensional velocity, static pressure, and temperature fields, respectively. In the equation, following parameters are used to get dimensionless quantities,

$$\begin{aligned} x &= \frac{x^*}{L_r}, t = \frac{t^*}{L_r/U_r}, \mathbf{u} = \frac{\mathbf{u}^*}{U_r}, p = \frac{p^*}{\rho_r U_r^2} \\ \rho &= \frac{\rho^*}{\rho_r}, \nu = \frac{\nu^*}{\nu_r}, \alpha = \frac{\alpha^*}{\alpha_r}, \theta = \frac{T - T_r}{T_s}, \end{aligned} \quad (4)$$

where superscript $*$ denotes the dimensional parameter, and the subscript r refers to the corresponding reference value i.e., reference length scale L_r , velocity U_r , density ρ_r , viscosity ν_r , thermal diffusivity α_r and temperature T_r . The non-dimensional Reynolds and Prandtl numbers are defined as $Re = U_r L_r / \nu_r$ and $Pr = \nu_r / \alpha_r$. $\mathbf{s}_u = (\mathbf{g}\beta(T - T_r)L_r/U_r)\theta$ is the forcing term for Navier-Stokes, where \mathbf{g} is the gravitational acceleration, β is the expansion coefficient. In free convection problems, the reference velocity is selected as $U_r = \mathbf{g}\beta(T - T_r)L_r$. $s_\theta = s_\theta(\theta, \nabla\theta, \mathbf{u})$ is the generic generation term for the energy equation written in terms of temperature. We would like to emphasize that superscripts u and θ in

boundary representation separate the Dirichlet and Neumann conditions on the physical boundary set for flow and heat transfer equations.

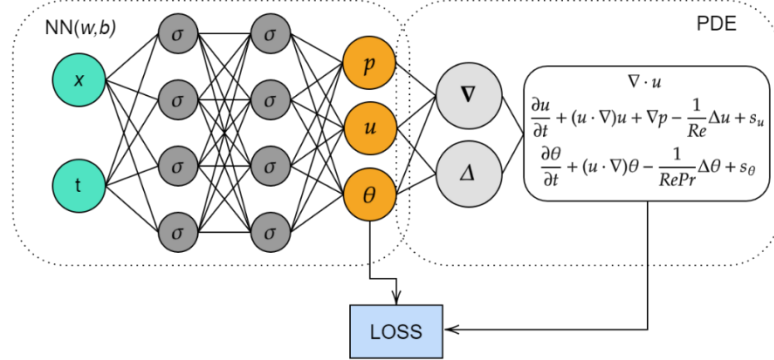


Figure 1. Schematic of a PINN framework

PHYSICS-INFORMED NEURAL NETWORKS

Consider a general partial differential equation expressed as:

$$\mathbf{u}_t + \mathcal{N}[\mathbf{u}] = 0, \quad \mathbf{x} \in \Omega, t \in [0, T] \quad (5.1)$$

$$\mathbf{u}(x, 0) = f(x), \quad \mathbf{x} \in \Omega \quad (5.2)$$

$$\mathbf{u}(x, t) = g(x, t), \quad \mathbf{x} \in \partial\Omega, t \in [0, T] \quad (5.3)$$

where \mathcal{N} is a generalized differential operator that can be linear or nonlinear, $x \in R^d$ and t are the spatial and temporal coordinates. Ω and $\partial\Omega$ represent the computational domain and the boundary, respectively. $u(x, t)$ is the general solution of the PDE with $f(x)$ is the initial condition and $g(x, t)$ is the boundary condition.

The solution $u(x, t)$ can be approximated by a fully connected network according to the framework of physics-informed neural networks (PINN) proposed by Raissi et al. (2019). This network takes the spatio-temporal coordinates (x, t) as input and outputs a solution $u_{NN}(x, t)$. Between these input and output layers, there exist multiple hidden layers. Each hidden layer takes input $X = [x_1, x_2, \dots, x_i]$ and outputs $Y = [y_1, y_2, \dots, y_j]$ through a nonlinear activation function $\sigma(\cdot)$ such as

$$y_j = \sigma(\omega_{i,j} + b_j), \quad (6)$$

where $\omega_{i,j}$ and b_j are trainable hyperparameters, weights and biases, respectively. These hyperparameters are tuned such that it minimizes a composite loss function in the form

$$\mathcal{L} = \omega_D \mathcal{L}_D + \omega_R \mathcal{L}_R + \omega_{BC} \mathcal{L}_{BC} + \omega_{IC} \mathcal{L}_{IC} \quad (7)$$

where

$$\mathcal{L}_D = \frac{1}{N_D} \sum_{i=1}^{N_D} |u(x^i, t^i) - u^i|^2 \quad (8.1)$$

$$\mathcal{L}_R = \frac{1}{N_R} \sum_{i=1}^{N_R} |u_t + \mathcal{N}[u(x^i, t^i)]|^2 \quad (8.2)$$

$$\mathcal{L}_{BC} = \frac{1}{N_{BC}} \sum_{i=1}^{N_{BC}} |u(x^i, t^i) - g(x^i, t^i)|^2 \quad (8.3)$$

$$\mathcal{L}_{IC} = \frac{1}{N_{IC}} \sum_{i=1}^{N_{IC}} |u(x^i, 0) - f(x^i)|^2 \quad (8.4)$$

\mathcal{L} is a loss term indicating the accuracy of the prediction if there are some data available in the domain, $\mathcal{L}_R, \mathcal{L}_{BC}$, and \mathcal{L}_{IC} represent the residual of the governing PDE, the boundary conditions, and the initial condition, respectively. N_D, N_R, N_{BC} , and N_{IC} are the number of data points for different terms, $\omega_D, \omega_R, \omega_{BC}$ and ω_{IC} are user specified weighting coefficients of each loss term. To calculate the residuals for \mathcal{L}_R , one needs to take the derivative of the output \mathbf{u} with respect to inputs (x, t) . In PINNs, this can be achieved by using automatic differentiation (Baydin et al., 2017). Automatic differentiation applies the chain rule repeatedly to the elementary functions and arithmetic operations to achieve the derivative of the overall composition. It plays a key role in the development of PINNs by enabling the computation of the residual of the governing differential equation (Raissi et al., 2019). Automatic differentiation is well implemented in most deep learning frameworks, such as TensorFlow (Abadi et al., 2016) and PyTorch (Paszke et al., 2019).

Figure 1 illustrates a schematic of the PINN framework in which the residuals of the coupled Navier-Stokes and energy equations are shown as the loss terms. This general schematic of the neural network takes the spatio-temporal coordinates as the input, and through the hidden layers, it outputs the pressure, velocity, and temperature fields. After this output, the framework calculates the

boundary losses from the boundary conditions and the data loss if there are any observations. In the next step, PINN uses automatic differentiation and calculates the residual inside the domain by enforcing the neural network output to the Navier-Stokes and energy equations. Also, if the boundary conditions are Neumann type, the neural network output can be differentiated to find the boundary loss. Then the overall loss can be calculated by adding the residual loss from the PDE, the boundary loss, and if there exist any available observations, the data loss. An optimization algorithm minimizes this combined loss function via changing the hyperparameters.

RESULTS

We have implemented our physics-informed neural network on top of the NVIDIA Modulus framework (Hennigh et al., 2021). We use the Adam optimizer (Kingma and Ba, 2017) to minimize the loss function defined in Equation 7 and use 8 hidden layers with 40 units for each test case where the neural network parameters are initialized using the Glorot scheme (Glorot and Bengio, 2010). We solve different 2D thermal convection tests to show the solutions by representing the velocity, pressure, and temperature fields.

Poiseuille Flow

In the first test case, we consider two-dimensional channel flow with a fully developed Poiseuille profile. The channel dimension is $[0,2] \times [-1,1]$. The upper and lower walls have a constant temperature of $\theta_L = 1$ and $\theta_U = 0$. No-slip boundary conditions are imposed for upper and lower walls. The fully developed solution of the velocity field with the linear temperature profile shown below is implemented as the boundary conditions of the inlet and the outlet. The flow conditions are stated as $Ra = 10^3$, $Pr = 0.71$, and $Re = 100$.

$$u = 1 - y^2, \quad v = 0,$$

$$p = \frac{Ra}{2PrRe^2} \left(y - \frac{y^2}{2} \right) - \frac{2x}{Re}, \quad \theta = \frac{1 - y}{2}.$$

We trained our framework with 250 samples inside the domain and 30 samples on each boundary with 10000 iterations for this case. The training points are sampled using Latin hypercube sampling, and the loss function for this problem contains only the Dirichlet boundary condition loss for the velocity and the temperature on the walls combined with the residual loss inside the domain. After training, we performed a prediction on a (251×251) grid and obtained the velocity, pressure, and temperature fields. The predicted fields can be seen in Figure 2. The accuracy of the PINN is highly dependent on the weights of the loss function. In this case, we tried different weights of the different terms of the loss function to match our solution with the exact solution. Especially for an accurate pressure field, we increased the weights of the boundary condition losses. The solution in Figure 2 is obtained with a boundary loss weight ω_{BC} which is eight times higher than the weight of the residual loss ω_R . Since the convective effects are not very dominant for this problem, boundary losses are dominant, so increasing the boundary loss weights increases the accuracy.

We test the performance of the PINNs with the addition of true observations at random points on the domain. We fused a different number of randomly sampled exact solutions inside the domain to the network and added a data loss term into the loss function. The training process is done with 250 points inside the domain and 30 boundary points on each boundary beside the true solution points. In Table 1, we can see the L_2 norm of the error of the predicted u velocity and temperature fields. The number of observations represents the addition of the true solutions, and increasing this number reduces the L_2 norm of the prediction of the velocity and the temperature from the true solution.

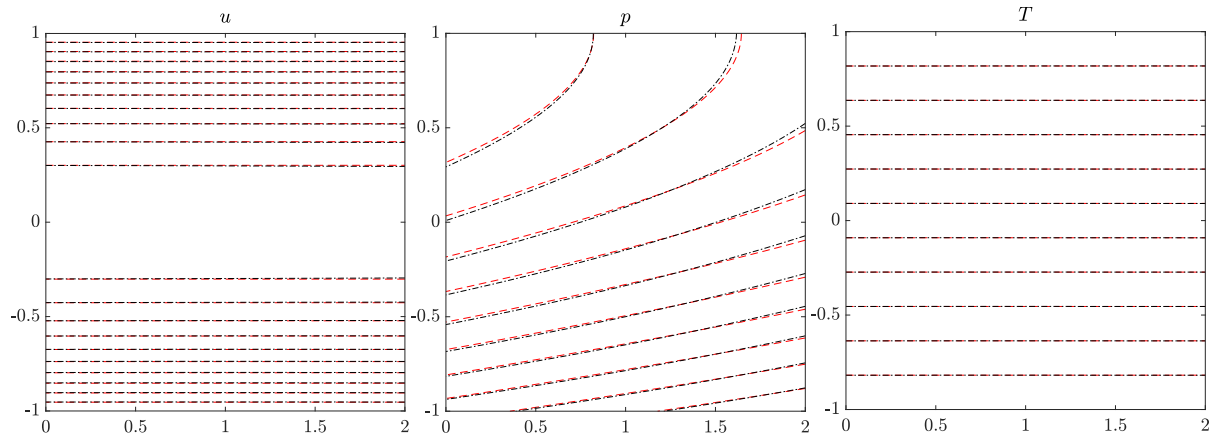


Figure 2. Prediction of Poiseuille flow with PINN. The u velocity, pressure and temperature fields are shown in order. Black contours show the exact solution and red dashed contours show the solution with PINN

Table 1. L_2 norm of the error of the predicted u velocity and the temperature fields

Number of observations	u	T
20	0.527	0.087
50	0.253	0.057
100	0.166	0.034
150	0.141	0.032

Differentially Heated Square Cavity

We focus on the natural convection problem on a two dimensional closed enclosure. The enclosure is a square cavity with its height denoted as $H = 1$, and width as $W = 1$. The boundary conditions of the cavity are simple no-slip walls, $u = 0, v = 0$, on all four walls. The thermal boundary conditions on the left and right walls are prescribed as

$$\theta_L = 1, \quad \theta_R = 0$$

and the upper and the lower walls are thermally insulated

$$\frac{\partial \theta}{\partial y} = 0, \quad \text{for } y = 0, y = H.$$

The flow conditions are $Pr = 0.71$, and three different Rayleigh numbers as $Ra = 10^3, 10^4, 10^5$.

For the PINN solution, we sampled 150 points on each boundary and 1000 collocation points inside the domain for the training process. Boundary points are used to minimize the loss of Dirichlet and Neumann boundary conditions, and collocation points are used to minimize the residual inside the domain. Automatic differentiation is used to calculate the derivatives on Neumann boundaries.

Table 2. Maximum and minimum velocities along the center lines of the square cavity for $Pr = 0.71$ and $Ra = 10^3, 10^4, 10^5$.

	$Ra = 10^3$		$Ra = 10^4$		$Ra = 10^5$	
	u_{max}	v_{max}	u_{max}	v_{max}	u_{max}	v_{max}
PINN	0.137	0.138	0.192	0.233	0.128	0.258
Karakus (2022)	0.137	0.139	0.192	0.233	0.129	0.257
Stokos et al. (2015)	0.137	0.139	0.192	0.233	0.130	0.256
De Vahl Davis (1983)	0.136	0.138	0.192	0.234	0.153	0.261

After the training process, prediction is performed on a (251×251) grid. In Table 2, we presented the maximum and minimum velocities on the horizontal and vertical centerlines after the prediction with PINN. For cases with different Ra numbers, our framework has values that are comparable with the ones in the literature. In Figure 3, the solution of PINN and its comparison with a high-fidelity solver through the temperature contours can be seen. Also, in Figure 4, the center line profiles of velocity and temperature for different Ra numbers are shown. These contours and profiles qualitatively match with the high order solutions (Karakus, 2022). To increase the accuracy, we changed the weights of different loss terms as Ra changes. In Table 3, we

presented the center line velocities for different Ra numbers and different weight ratios of the residual loss over the boundary loss where ω_R represents the weight of the residual loss, and ω_{BC} represents the weight of loss on the boundary conditions. We stopped changing weights when we matched the center line velocities with the reference solutions. As the Ra increases, the convective effect inside the domain becomes more dominant. Hence, we need to decrease the weight of the boundary losses and focus more on the residual inside the domain. We select the loss ratio according to Table 3 which minimizes the error both inside the domain and on the boundaries.

Table3. Maximum and minimum velocities along the centerlines with different weight ratio of residual loss and the boundary loss

ω_R/ω_{BC}	$Ra = 10^3$		$Ra = 10^4$		$Ra = 10^5$	
	u_{max}	v_{max}	u_{max}	v_{max}	u_{max}	v_{max}
0.5	0.137	0.138	0.190	0.231	0.137	0.273
1			0.192	0.233	0.128	0.258
2					0.132	0.261
4					0.130	0.261

We tested different types of neural network architectures and monitored the behavior of the total loss of the Adam optimizer for the cavity problem with $Ra = 10^3$ and presented in Figure 5. The plain fully connected network (FCN), a variation of the fully connected network named as Deep Galerkin Method (DGM) (Sirignano and Spiliopoulos, 2018), a Fourier network, and a modified Fourier network (Wang et al., 2021a), a modified highway network using Fourier features (Srivastava et al., 2015), and a multiplicative filter network (Fathony et al., 2021) are used. All of these architectures are readily available in NVIDIA Modulus framework. In all the tests, 8 layer networks are constructed with 40 units. Hyperbolic tangent is set as the activation function, and the learning rate is 10^{-3} . The architectures that use Fourier mapping converges later than the plain fully connected network since the problem does not have multi-scale behavior. For this simple problem, we do not

need a Fourier mapping; hence networks that are basically built on plain fully connected networks converge in fewer iterations.

Heated Block

In this section, we focus on an application of coupled heat transfer with a heat transfer in a partially blocked channel. The domain and the boundary conditions can be seen in Figure 6. The heated block represents an electronic part on a vertical electronic board (Habchi and Acharya, 1986). The top wall is adiabatic, and the bottom wall is at a prescribed temperature. A low temperature flow comes from the inlet and the outflow is a fully developed outlet meaning the changes in the x direction is zero. The Prandtl number is set to 0.7 for this problem and the Reynolds number is 37.8. The ratio of Gr/Re^2 is 1 and the forcing is on the x direction.

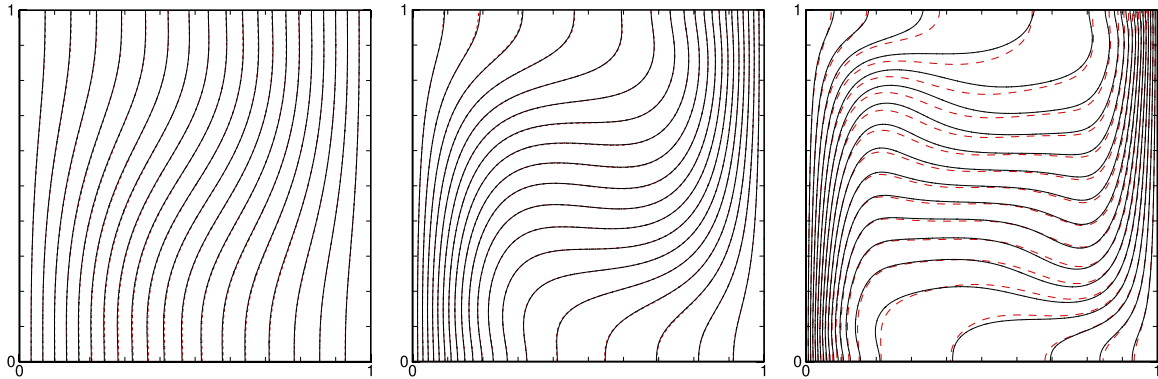


Figure 3: Temperature contours for the square cavity test. The high fidelity solution obtained with high fidelity discontinuous Galerkin solver between 1 and 0 with the increment of 0.05 for $Ra = 10^3, 10^4, 10^5$ from left to right shown with the black contours while the red contours are the solution with PINNs

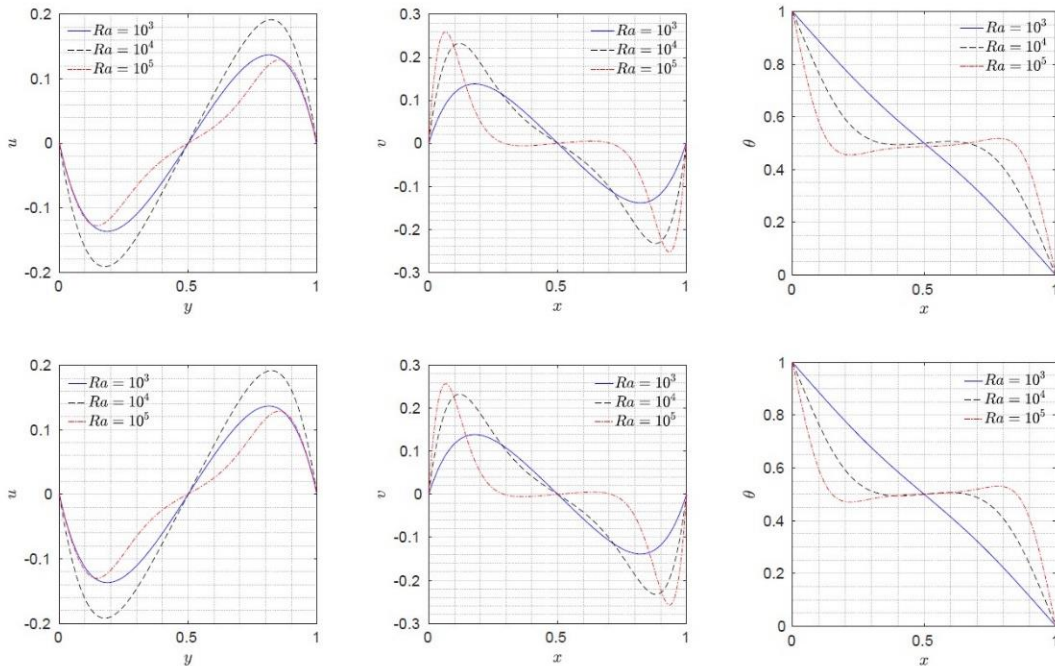


Figure 4. Velocity and temperature profiles along $y = 0.5$ and $x = 0.5$ lines for different Ra numbers. The first row shows the values obtained with the PINN, while the second row shows the values of high order discontinuous Galerkin solver.

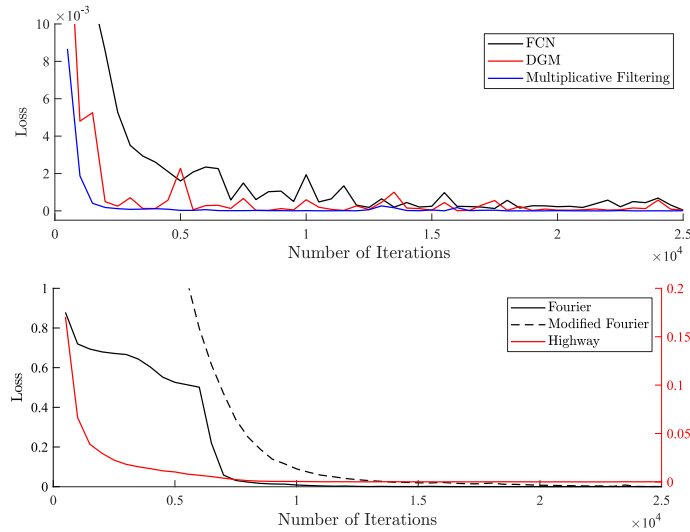


Figure 5. Behavior of the total loss on the square cavity problem with $Ra = 10^3$ with different types of neural network architectures

For training the network, we sampled 30 points on the inlet and the outlet, 210 points on the adiabatic wall, a total of 40 points on the heated block, a total of 180 points on the bottom wall, and 1400 points inside the domain. We used 25000 iterations for the Adam optimizer with the learning rate of 5×10^{-4} and obtained the solution presented in Figure 7. PINN solution well predicts the Neumann boundary conditions on the top wall and the fully developed outlet, and the no-slip Dirichlet velocity conditions

Multiple Heated Blocks

In this section, we focus on a similar problem in which multiple blocks are present. The problem is time dependent, and it is solved for a final time of 8 seconds. The geometric representation of the case is presented in Figure 8. The geometric parameters are given such that $H = 1, H/w = 2.5, L/w = 25, h/w = 0.5$, as presented in Wu and Perng (1999).

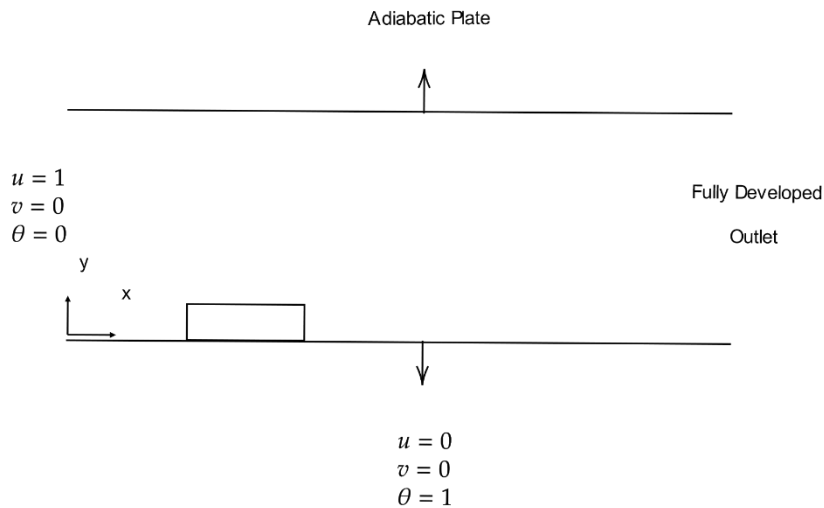


Figure 6. Schematic of the partially blocked channel

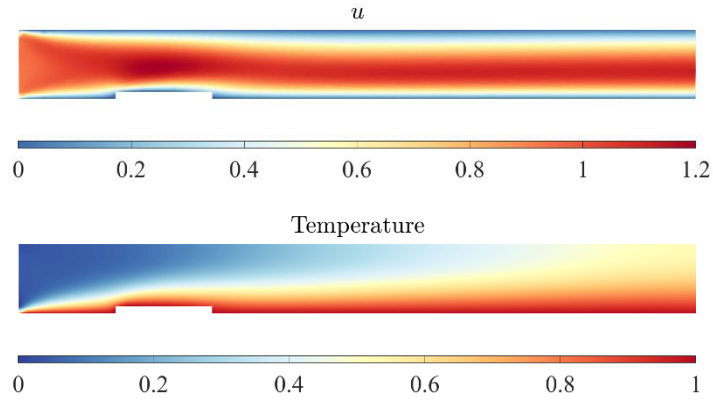


Figure 7. Velocity and temperature profiles for the heated block case. The figure on the top shows the velocity profile and the figure on the bottom shows the temperature field predicted by the PINN.

At time $t = 0$, the initial condition is $u = v = \theta = 0$ in the domain. There is a uniform inflow with $u = 1, v = 0$ with the temperature of $\theta = 0$. The upper and bottom walls have no-slip conditions as the velocity boundary condition and Neumann temperature boundary condition of $\partial\theta/\partial n = 0$. The blocks also have no-slip conditions and temperature boundary conditions of $\partial\theta/\partial n = -1$. Gravity is in the y direction, and flow parameters are given as $Re = 400, Pr = 0.7$, and $Gr/Re^2 = 0.5$.

In the training phase, 50 points on the inlet and the outlet are generated uniformly. 40 points on each block, 500

points on the top wall, and 450 points on the bottom wall are sampled. The problem is solved with a continuous time approach such that we treat time t as another variable as the spatial coordinates instead of approaching the time sequentially. Adam optimizer is used again to find the optimized hyperparameters with a learning rate of 5×10^{-4} . The solution at the final time $t = 8s$ is shown in Figure 9. The horizontal velocity and the temperature fields are plotted, and it can be seen that the PINN solution represents the flowfield well physically inside the domain and also satisfy the Dirichlet and Neumann boundary conditions.

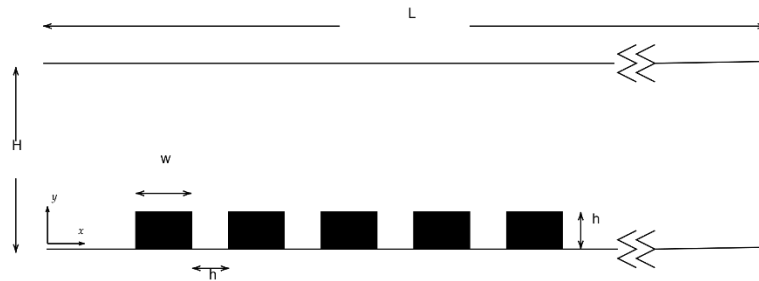


Figure 8. Geometric representation of the channel with multiple blocks

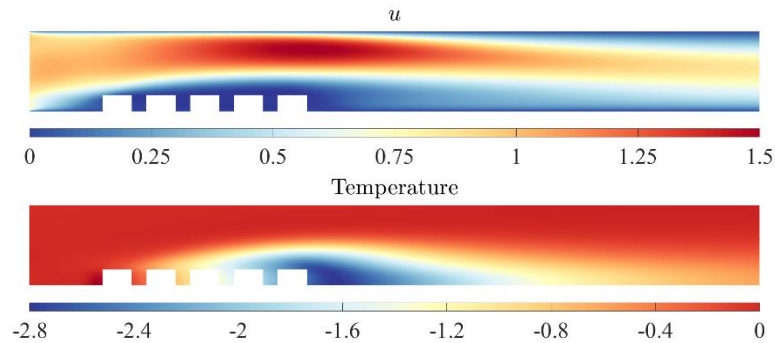


Figure 9. Velocity and temperature profiles for the multiple heated blocks case at time $t = 8s$. The figure on the top shows the velocity profile and the figure on the bottom shows the temperature field predicted by the PINN.

CONCLUSION

In this work, we solve two dimensional incompressible thermal convection problems with PINNs. The PINN solutions predict the flow and temperature fields well compared to the solution of high order solvers and analytical solutions in various problems. We show that adding observations into the flow field increases the accuracy of the prediction and the framework is very sensitive to the weights of the individual loss terms. In addition, different types of networks can be used to solve thermal convection problems instead of fully connected networks. However, since these types of problems do not have multiscale behavior, it is not necessary to use Fourier mapping. Furthermore, we consider two different channel problems with a partial blockage that resemble power electronics applications. The model can be implemented into time dependent problems by adding time as a continuous input variable. For future work, the time dependent problems can be implemented with time marching approaches such as Recurrent Neural Networks or Gated Response Units.

REFERENCES

- Abadi, M., Barham, P., Chen, J., Chen, Z., Davis, A., Dean, J., Devin, M., Ghemawat, S., Irving, G., Isard, M., Kudlur, M., Levenberg, J., Monga, R., Moore, S., Murray, D. G., Steiner, B., Tucker, P., Vasudevan, V., Warden, P., Wicke, M., Yu, Y., and Zheng, X., 2016, TensorFlow: A system for large-scale machine learning. *12th USENIX Symposium on Operating Systems Design and Implementation (OSDI 16)*, 265-283.
- Bairi, A., Zarco-Pernia, E., and De Maria, J.-M. G., 2014, A review on natural convection in enclosures for engineering applications. the particular case of the parallelogrammic diode cavity. *Applied Thermal Engineering*, 63(1), 304-322.
- Baydin, A. G., Pearlmutter, B. A., Radul, A. A., and Siskind, J. M., 2017, Automatic differentiation in machine learning: a survey. *The Journal of Machine Learning Research*, 18(1), 5595-5637.
- Cai, S., Mao, Z., Wang, Z., Yin, M., and Karniadakis, G. E., 2022, Physics-informed neural networks (PINNs) for fluid mechanics: a review. *Acta Mechanica Sinica*, 1-12.
- Cai, S., Wang, Z., Wang, S., Perdikaris, P., and Karniadakis, G., 2021, Physics-informed neural networks (PINNs) for heat transfer problems. *Journal of Heat Transfer*, 143(6).
- De Vahl Davis, G., 1983, Natural convection of air in a square cavity: A bench mark numerical solution. *International Journal for Numerical Methods in Fluids*, 3(3).
- Esmaeilzadeh, S., Azizzadenesheli, K., Kashinath, K., Mustafa, M., Tchelepi, H. A., Marcus, P., Prabhat, M., Anandkumar, A., et al., 2020, Meshfreeflownet: A physics-constrained deep continuous space-time super-resolution framework. *SC20: International Conference for High Performance Computing, Networking, Storage and Analysis*, IEEE, 1-15.
- Fathony, R., Sahu, A. K., Willmott, D., and Kolter, J. Z., 2020, Multiplicative filter networks. *In International Conference on Learning Representations*.
- Glorot, X. and Bengio, Y., 2010, Understanding the difficulty of training deep feedforward neural networks. *In Proceedings of the Thirteenth International Conference on Artificial Intelligence and Statistics*, 249-256.
- Habchi, S. and Acharya, S., 1986, Laminar mixed convection in a partially blocked, vertical channel. *International Journal of Heat and Mass Transfer*, 29(11), 1711-1722.
- Hennigh, O., Narasimhan, S., Nabian, M. A., Subramaniam, A., Tangsali, K., Fang, Z., Rietmann, M., Byeon, W., and Choudhry, S., 2021, Nvidia SimNet™: An ai-accelerated multi-physics simulation framework. *In International Conference on Computational Science*, 447-461.
- Hossain, M. Z., Cantwell, C. D., and Sherwin, S. J., 2021, A spectral/hp element method for thermal convection. *International Journal for Numerical Methods in Fluids*, 93(7), 2380-2395.
- Jacot, A., Gabriel, F., and Hongler, C., 2018, Neural tangent kernel: Convergence and generalization in neural networks. *Advances in neural information processing systems*, 31.
- Jin, X., Cai, S., Li, H., and Karniadakis, G. E., 2021, NSFnets (Navier-Stokes Flow nets): Physics-informed neural networks for the incompressible Navier-Stokes equations. *Journal of Computational Physics*, 426, 109951.
- Karakus, A., 2022, An accelerated nodal discontinuous Galerkin method for thermal convection on unstructured meshes: Formulation and Validation. *Journal of Thermal Science and Technology*, 42(1), 91-100.
- Karakus, A., Chalmers, N., Swirydowicz, K., and Warburton, T., 2019, A GPU accelerated discontinuous Galerkin incompressible flow solver. *Journal of Computational Physics*, 390, 380-404.

- Karniadakis, G. E., Kevrekidis, I. G., Lu, L., Perdikaris, P., Wang, S., and Yang, L., 2021, Physics-informed machine learning. *Nature Reviews Physics*, 3(6), 422-440.
- Kingma, D. P. and Ba, J., 2017, Adam: A method for stochastic optimization. *arXiv:1412.6980*.
- Lagaris, I., Likas, A., and Fotiadis, D., 1998, Artificial neural networks for solving ordinary and partial differential equations. *IEEE Transactions on Neural Networks*, 9(5), 987-1000.
- Lee, H. and Kang, I. S., 1990, Neural algorithm for solving differential equations. *Journal of Computational Physics*, 91(1), 110-131.
- Lu, L., Meng, X., Mao, Z., and Karniadakis, G. E., 2021 DeepXDE: A deep learning library for solving differential equations. *SIAM Review*, 63(1), 208-228.
- Paszke, A., Gross, S., Massa, F., Lerer, A., Bradbury, J., Chanan, G., Killeen, T., Lin, Z., Gimelshein, N., Antiga, L., Desmaison, A., Kopf, A., Yang, E., DeVito, Z., Raison, M., Tejani, A., Chilamkurthy, S., Steiner, B., Fang, L., Bai, J., and Chintala, S., 2019, PyTorch: An imperative style, high-performance deep learning library. *In Advances in Neural Information Processing Systems*, 32.
- Rahaman, N., Baratin, A., Arpit, D., Draxler, F., Lin, M., Hamprecht, F., Bengio, Y., and Courville, A., 2019, On the spectral bias of neural networks. *In International Conference on Machine Learning*, 5301-5310.
- Raissi, M., Perdikaris, P., and Karniadakis, G., 2019, Physics-informed neural networks: A deep learning framework for solving forward and inverse problems involving nonlinear partial differential equations. *Journal of Computational Physics*, 378, 686-707.
- Raissi, M., Perdikaris, P., and Karniadakis, G. E., 2017a, Inferring solutions of differential equations using noisy multi-fidelity data. *Journal of Computational Physics*, 335, 736-746.
- Raissi, M., Perdikaris, P., and Karniadakis, G. E., 2017b, Machine learning of linear differential equations using Gaussian processes. *Journal of Computational Physics*, 348, 683-693.
- Rao, C., Sun, H., and Liu, Y., 2020, Physics-informed deep learning for incompressible laminar flows. *Theoretical and Applied Mechanics Letters*, 10(3), 207-212.
- Sirignano, J. and Spiliopoulos, K., 2018, DGM: A deep learning algorithm for solving partial differential equations. *Journal of Computational Physics*, 375, 1339-1364.
- Srivastava, R. K., Greff, K., and Schmidhuber, J., 2015, Training very deep networks. *In Advances in Neural Information Processing Systems*, 28.
- Stokos, K., Vrahliotis, S., Pappou, T., and Tsangaris, S., 2015, Development and validation of an incompressible Navier-Stokes solver including convective heat transfer. *International Journal of Numerical Methods for Heat & Fluid Flow*, 25(4), 861-886.
- Tancik, M., Srinivasan, P., Mildenhall, B., Fridovich-Keil, S., Raghavan, N., Singhal, U., Ramamoorthi, R., Barron, J., and Ng, R., 2020, Fourier features let networks learn high frequency functions in low dimensional domains. *In Advances in Neural Information Processing Systems*, 33, 7537-7547.
- Tang, L. Q. and Tsang, T. T., 1993, A least-squares finite element method for time-dependent incompressible flows with thermal convection. *International Journal for Numerical Methods in Fluids*, 17(4), 271-289.
- Wang, S., Teng, Y., and Perdikaris, P., 2021a, Understanding and mitigating gradient flow pathologies in physics-informed neural networks. *SIAM Journal on Scientific Computing*, 43(5), A3055-A3081.
- Wang, S., Wang, H., and Perdikaris, P., 2021b, On the eigenvector bias of fourier feature networks: From regression to solving multi-scale pdes with physics-informed neural networks. *Computer Methods in Applied Mechanics and Engineering*, 384, 113938.
- Willard, J., Jia, X., Xu, S., Steinbach, M., and Kumar, V., 2020, Integrating physics-based modeling with machine learning: A survey. *arXiv:2003.04919*.
- Wu, H.-W. and Perng, S.-W., 1999, Effect of an oblique plate on the heat transfer enhancement of mixed convection over heated blocks in a horizontal channel. *International Journal of Heat and Mass Transfer*, 42(7), 1217-1235.
- Zubov, K., McCarthy, Z., Ma, Y., Calisto, F., Pagliarino, V., Azeglio, S., Bottero, L., Lujan, E., Sulzer, V., Bharambe, A., Vinchhi, N., Balakrishnan, K., Upadhyay, D., and Rackauckas, C., 2021, NeuralPDE: Automating physics-informed neural networks (PINNs) with error approximations. *arXiv:2107.09443*.



COOLING PERFORMANCE OF THERMOELECTRIC COOLER MODULES: EXPERIMENTAL AND NUMERICAL METHODS

İlhan KAHRAMAN* and Naim DEREBAŞI**

Bursa Uludag University, Department of Physics, 16059 Gorukle, Bursa, Turkey

*kahramanilhan85@gmail.com, ORCID: 0000-0003-0662-1636

**naim@uludag.edu.tr, ORCID: 0000-0003-2546-0022

(Geliş Tarihi: 06.04.2022, Kabul Tarihi: 16.09.2022)

Abstract: A novel pulse-driving method in which the pulse frequency modulation is was developed by optimising the input power owing to the duty cycle of rectangular wave to enhance the cooling efficiency and thermal stability of the thermoelectric module. The aim of this driving method is to have better control of the thermoelectric cooler module temperature and to improve its coefficient of performance. In this method, the average current and the peak of pulse drive are in the 50% duty cycle with the same magnitude and the performance of Peltier module driving with average dc is compared with the pulse driving. The measurement results show that the coefficient of performance of the thermoelectric module with the pulse-frequency modulation driving method increased up to 102% as compared to the constant dc driving method. An artificial neural network has been successfully used to analyse these experimentally collected data and predict the performance of the module. When the developed artificial neural network model was tested using untrained data, the average correlation of the model was 99% and the overall prediction error was 1.38%. An accurate and simple analytical equation based on the predicted and experimental results was determined using the MATLAB® Curve Fitting Toolbox. The average correlation of the analytical model was 0.99 and the root-mean-square error was 0.074.

Keywords: thermoelectric cooler module, cooling performance, drive method, artificial neural network.

TERMOELEKTRİK SOĞUTMA MODÜLLERİNİN SOĞUTMA PERFORMANSI: DENEYSEL VE SAYISAL YÖNTEMLER

Özet: Termoelektrik modülün ısısal kararlılığını ve soğutma verimini arttırmak için, atımlı frekans modülasyonunda yeni bir atımlı sürücü yöntemi dikdörtgen dalga olan girişin en uygun yapılması ile geliştirilmiştir. Bu sürücü yönteminin amacı termoelektrik soğutma modülünün sıcaklığını daha iyi kontrol etmek ve verimini arttırmaktır. Bu yöntemde, %50 çalışma periyodundaki ortalama akım ve sürücü atımın en büyük değeri aynı büyüklüktedir ve dc ile sürülen Peltier modülün performansı atımla sürülen ile karşılaştırılmıştır. Ölçme sonuçları, termoelektrik modülün verim katsayısının, atımlı frekans modülasyonu sürücü yöntemi ile sabit dc sürücü yöntemi karşılaştırıldığında %102'ye kadar arttığını göstermiştir. Yapay sinir ağları, alınan deneysel verileri çözümlmek ve modülün performansını tahmin etmek için başarı ile kullanılmıştır. Geliştirilen yapay sinir ağı modeli öğrenmede kullanılmayan verilerle denendiğinde, modülün ortalama uyumu %99 ve en büyük tahmin etme hatası %1.38 olmuştur. Deneysel ve tahmin verilerine bağlı olarak doğru ve basit bir analitik denklem MATLAB® eğri uyum programı kullanılarak belirlenmiştir. Analitik denklemin ortalama uyumu 0.99 ve etkin hatası 0.074 olmuştur.

Anahtar kelimeler: Termoelektrik soğutma modülü, Soğutma performansı, Sürücü yöntemi, Yapay sinir ağı.

NOMENCLATURE

CFC	ChloroFluoroCarbon	Z	Figure of merit
TEC	Thermoelectric cooler	P_{pc}	Pulse current power, W
COP	Coefficient of performance	I_{av}	Average current of the module, A
PWM	Pulse width modulation	N	Real number
PFM	Pulse frequency modulation	P_{dc}	dc power, W
Q_C	Endothermic quantity, heat dissipative, W	P_p	Power consumption, W
Q_J	Joule heat, W	RMS	Root mean square
Q_{hc}	Rate of heat conduction, W	f	frequency, Hz
α	Seebeck coefficient, V/K	m	Mass of aluminium heated block, kg
I	Direct current passing through the module, A	C	Specific heat coefficient, J/(kg K)
T_C	Cold side temperature of the module, K	ANN	Artificial neural network
ρ	Electrical resistivity, Ω m,	RAM	Read access memory
l	Length, m	T_h	Hot side temperature of the module, K
A	Cross sectional area, m^2 ,	t	time, s
Q_P	Electrical energy consumption, W	V	Voltage across the terminals of TEC module, V
k	thermal conductance, W/K	ΔT	Temperature difference, K
λ	Thermal conductivity, W/(m K)		
NTC	Negative Temperature Coefficient		

INTRODUCTION

In recent years, heat dissipation of electronic systems has grown rapidly with improving manufacturing technology. This growth has induced a serious electronic cooling problem. A conventional cooling system includes an evaporator, a compressor and a condenser and they are widely using for many purposes. However, energy costs and environmental regulations regarding the manufacture and release of chlorofluorocarbons (CFCs) are also increasing. These facts are encouraging manufacturers and their customers to seek alternative for conventional cooling technology (Derebasi *vd*, 2015).

Being no moving parts, environmentally friendly technology and requiring almost no maintenance, thermoelectric technology has become one of the most promising alternative methods to solve increasingly serious energy shortage and environmental pollution problems. Thermoelectric cooler (TEC) modules have been applied for electronic cooling in many industries such as medical instrument, aerospace, military, industrial products, offering the advantages of small size, quiet operation, long lasting time, ease of use and reliability (Sekiguchi *vd*, 2018).

The coefficient of performance (COP) for the thermoelectric technology is the ratio of output and input energy, which depends on the current through the module and the temperature difference between two sides of the thermoelectric module. The COP of thermoelectric module is smaller than the COP of conventional cooling system has. Therefore, much research has focused on the improvement of the COP of thermoelectric cooling systems by means of developing new materials for the TEC modules, optimization of module systems design, fabrication, improvement of the heat exchange efficiency and optimisation for geometrical dimensions of each p-

and n- types semiconductors of TEC (Derebasi *vd*, 2015, Sekiguchi *vd*, 2018, Twaha *vd*, 2016, Song *vd*, 2020, Derebasi *vd*, 2015). However, few studies have been carried out on the performance of cooling modules including the current driving method of them (Sekiguchi *vd*, 2018, Baubaris *vd*, 2017).

Peltier devices are thermoelectric conversion devices that consist of two types of electric conductors joined by a junction. Heat travels from one of the conductors to the other, when current is applied to the junction. Thermoelectric refrigeration is achieved, when a direct current is passed through one or more pairs of n- and p-type semiconductor materials, primarily comprised bismuth-tellurium alloys. In the cooling mode, direct current passes from the n- to p-type semiconductor materials, which are soldered in series to copper electrodes.

Peltier devices are used to cool electrical components, because they are capable of localised cooling. The refrigeration capability of a semiconductor material is dependent on the combined effect of the material's Seebeck voltage, electrical resistivity, and thermal conductivity over the operating temperature range between the cold and hot ends (Guclu and Cuce 2019).

One method of driving Peltier devices is on-off control in which constant dc current interrupted according to a set temperature. In this on-off control, the ripple component in the output voltage of power supply comprised a switching converter and the like increases the self-heating of the Peltier device. To resolve this, an extra electronic filter circuits are used to attenuate the ripple component.

Another method of driving Peltier devices is the Pulse Width Modulation (PWM) control in which repetitive

pulse current with a constant amplitude is controlled with a high precision. However, in the on-off and the PWM control, cooling efficiency decreases due to the self-heating of the Peltier device increasing as a result of the intermittent control of driving current (Sekiguchi *vd*, 2018). Moreover, the electromagnetic interference issues have raised considerable limitations on PWM applicability, especially high switching frequencies. Therefore, an extra electronic circuitry are necessary (Baubaris *vd*, 2017).

The use of Artificial Neural Networks (ANN) has grown in popularity during the last decade. The reason for this is that neural networks represent a novel and modern approach that can provide solutions to problems for which conventional mathematics, algorithms and methodologies are unable to find a satisfactory and acceptable solution. ANNs are inspired by the human brain functionality and structure, which can be imagined as a network that comprises of densely interconnected elements called neurons. Despite this fact, the ANNs' objective is not to model it.

Instead, their purpose is to be useful models that can be used for problem solving and knowledge engineering, in a way that resembles the human process for problem solving and knowledge acquisition. Both biological and artificial networks have the following main and important features: learning adaptation, generalization, massive parallelism, robustness, associative storage information and spatiotemporal information processing (Laidi and Hanini, 2013).

Furthermore, for the numerical analysis, the MATLAB® Curve Fitting Toolbox™ can be used to determine an accurate and simple analytical equation for the performance of TEC module corresponding to experimental and predicted data obtained.

Many researches have been carried out to control the temperature of TEC module using the on-off and PWM driving current methods. However, this research concentrates on the pulse frequency modulation (PFM) current driving method of TEC module to control its temperature and to improve its COP. An optimised PFM driving current is proposed and applied to the module to reduce the Joule heating and then to control the temperature of TEC module and improving the COP. Furthermore, the ANN has applied to the experimental data to estimate the performance of the TEC module and the MATLAB® Curve Fitting Toolbox™ was also used to define an accurate and simple analytical equation for the performance of TEC module corresponding to experimental and predicted data.

This investigation particularly highlights an optimised PFM driving method, which provides to control of temperature of TEC module and improve the COP. Moreover, an ANN model and an analytical equation were obtained to predict the performance of the TEC module corresponding to experimental data.

THEORY OF THERMOELECTRIC COOLING

A typical TEC module (Peltier module) consists of p- and n-types semiconductors connected electrically in series and thermally parallel sandwiched between two ceramics substrates [Fig. 1]. Whenever direct current passes through the circuit of thermoelectric heterogeneous conductors, it causes temperature differential between TEC module sides. As a result, one TEC face, which is called cold side, will be cooled while its opposite face, which is called hot side, is simultaneously heated. This phenomenon is known as the Peltier effect (Sulaiman *vd*, 2018, Rowe, 2006). The thermoelectric heat (Q_c) pumped by the Peltier effect at the cold end of a thermoelectric couple as shown in Fig. 2 is given by;

$$Q_c = \alpha I T_c \quad (1)$$

where α , I , and T_c are the Seebeck coefficient, which is dV/dT [V/K], the direct current in Ampere passing through the thermoelectric material and the cold-side temperature in Kelvin, respectively. Current flow generates Joule heat (Q_j) in the thermoelectric material, which goes equally to the cold and hot ends:

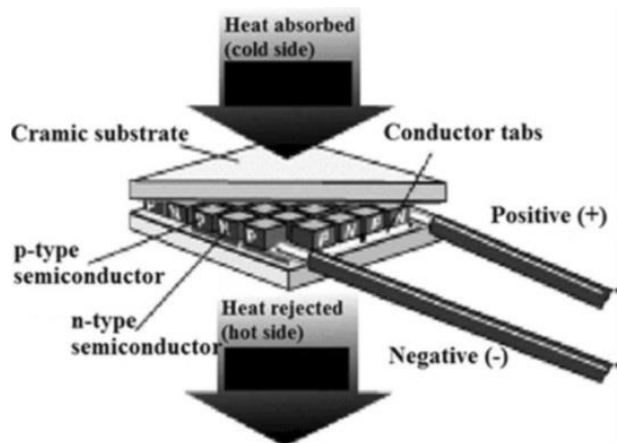


Figure 1. Typical TEC module.

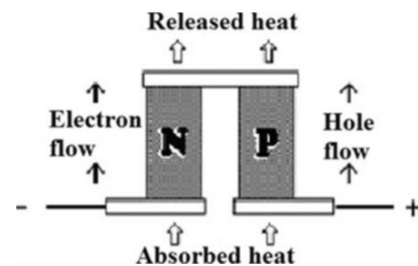


Figure 2. Thermoelectric heat pumping by the Peltier effect in a thermoelectric p-n couple.

$$Q_j = \frac{i^2 \rho l}{2A} \quad (2)$$

where ρ , l and A are the electrical resistivity [Ω m], length [m] and cross sectional area [m^2] of thermoelectric material. During operation, heat is conducted by electrons from the hot to the cold end through the thermoelectric material. The rate of heat conduction (Q_{hc}) is given by;

$$Q_{hc} = k(T_h - T_c) = k\Delta T \quad (3)$$

where k and ΔT are the thermal conductance [W/K] and the temperature difference [K] between the hot and cold sides of thermoelectric couple, respectively. k can be defined as;

$$k = \lambda \frac{A}{l} \quad (4)$$

where λ is the thermal conductivity in W/(m K), A is the cross sectional area and l is the length of the thermoelectric material. Combining Eqs. (1, 2, 3 and 4) into an energy balance at the end of the thermoelectric couple gives;

$$Q_c = \alpha IT_c - \frac{I^2 \rho l}{2A} - k\Delta T \quad (5)$$

The refrigeration capability of a semiconductor material is dependent on combined effect of the material's Seebeck voltage, electrical resistivity, and thermal conductivity over the operational temperature range between cold and hot ends (Derebasi *vd*, 2015, Sekiguchi *vd*, 2018, Rowe, 2006, Riffat and Ma, 2003).

The first term on the right hand side of Eq. (5) represents the Peltier effect, and is thought to generate heat flow proportional to the average current I . The second term represents the reduction in endothermic quantity due to the heat generation of the Peltier device itself and corresponds to the half of the Joule heating of the Peltier device. The last term describes the reverse heat flow from the high temperature part due to the low temperature part.

The electrical energy consumption (Q_p) [W] of a couple is given by;

$$Q_p = \frac{I^2 \rho l}{A} + \alpha I \Delta T \quad (6)$$

The electric power consumption of a thermoelectric couple is used to generate the Joule heat and overcome the Seebeck effect, which generates power due to the temperature difference between two junctions of the couple. The coefficient of performance (COP) of the thermoelectric couple for cooling is given by;

$$COP = \frac{Q_c}{Q_p} = \frac{\alpha IT_c - \frac{I^2 \rho l}{2A} - k\Delta T}{\frac{I^2 \rho l}{A} + \alpha I \Delta T} \quad (7)$$

The COP of a thermoelectric material is a combined effect of the material Seebeck coefficient, electrical resistivity, geometrical dimensions of thermoelectric material and thermal conductivity over the operational temperature range between the cold and hot ends. The performance of thermoelectric material is called as a figure of merit (Z) and expresses;

$$ZT = \frac{\alpha^2 A}{k \rho l} T = \frac{\alpha^2}{k R} T \quad (8)$$

Each of the n- and p-type semiconductor thermoelectric material properties varies as a function of temperature and therefore the figure of merit for each material is temperature dependent. Maximising the figure of merit is larger objective in the selection and optimising of thermoelectric materials and then it limits the temperature differential, whereas the geometrical dimensions for each n- and p-type of semiconductor material define the heat pumping capacity. The most widely used thermoelectric semiconductor material for cooling in the temperature range of 0-200 °C is the Bismuth-Telluride (Bi_2Te_3) due to its thermal properties at room temperature as compared to other thermoelectric materials (Bar-Cohen *vd*, 2005).

DRIVING METHOD

Analysing the pulse current driving with constant amplitude the reduction in pulse current power (P_{pc}) can be understood in the endothermic quantity due to the heat generation of the Peltier device itself during the pulse driving. The duty cycle (one period) of the pulse driving is based on the driving current waveform of the Peltier device shown in Fig. 3. The reduction in the endothermic quantity can be explained in terms of average current applied to the Peltier device (I_{av}) as;

$$\frac{P_{pc}}{N} = \frac{\rho l}{2A} N \left(\frac{I_{av}}{N} \right)^2 = \frac{\rho l}{2A} \frac{I_{av}^2}{N} \quad (9)$$

where N is a real number between zero and one.

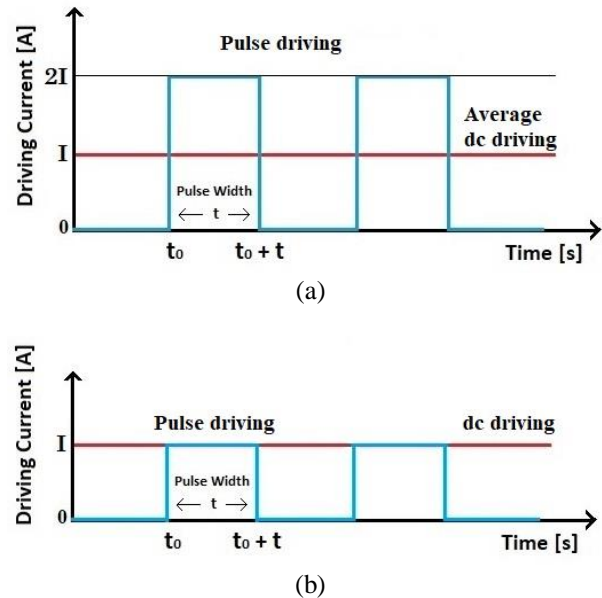


Figure 3. Driving current waveforms in different magnitudes, a) average and b) constant

The reduction in power using the PWM control is analysed in the endothermic quantity due to heat generation of the Peltier device itself during pulse driving with 50% duty cycle (Sekiguchi *vd*, 2018). In addition, it is compared to the same average current as dc to obtain the same Peltier effect. In this case, when the average

current is I , the peak of pulse drive must be $2I$ in the 50% duty cycle of PWM [Fig 3 (a)]. However, in this research, the average current and the peak of pulse drive are in the 50% duty cycle with the same magnitude and the performance of Peltier module driving with average dc is compared with pulse driving [Fig. 3 (b)].

Accordingly, it is clear that the reduction in driving power of endothermic quantity can be reduced N times regarding the driving direct current. The COP of the Peltier device (TEC module) can be expressed by;

$$COP = \frac{Q_c}{P_p} \quad (10)$$

where Q_c and P_p are the heat dissipation and power consumption of the Peltier device respectively. The heat dissipation can be calculated as;

$$Q_c = m C \Delta T \quad (11)$$

where m is the mass of heated side of the Peltier device [kg], C is the specific heat [J/(kg K)] and ΔT is the

temperature difference between hot and cold sides of Peltier device. The power consumption of the Peltier device can be calculated by input power as;

$$Q_p = IV \quad (12)$$

EXPERIMENTAL SET UP

The measurement system consists of 3 parts: driving of Peltier module, signal processing and temperature control. Fig. 4 shows a block diagram of the system. The Peltier module, type Z-MAX TEC1 – B12708AC, which has an aluminium layer on both sides is used. This Peltier module is a special production and has higher efficiency than the other modules. Aluminium layers on two surfaces of module were originally fitted to the module surface using thermal paste to have better heat transfer (Fig. 5). In addition, the module was also fitted to the heat sink using thermal paste. Thus, it is ease of fitting to the heat sink and minimises the heat losses between the module and heat sink.

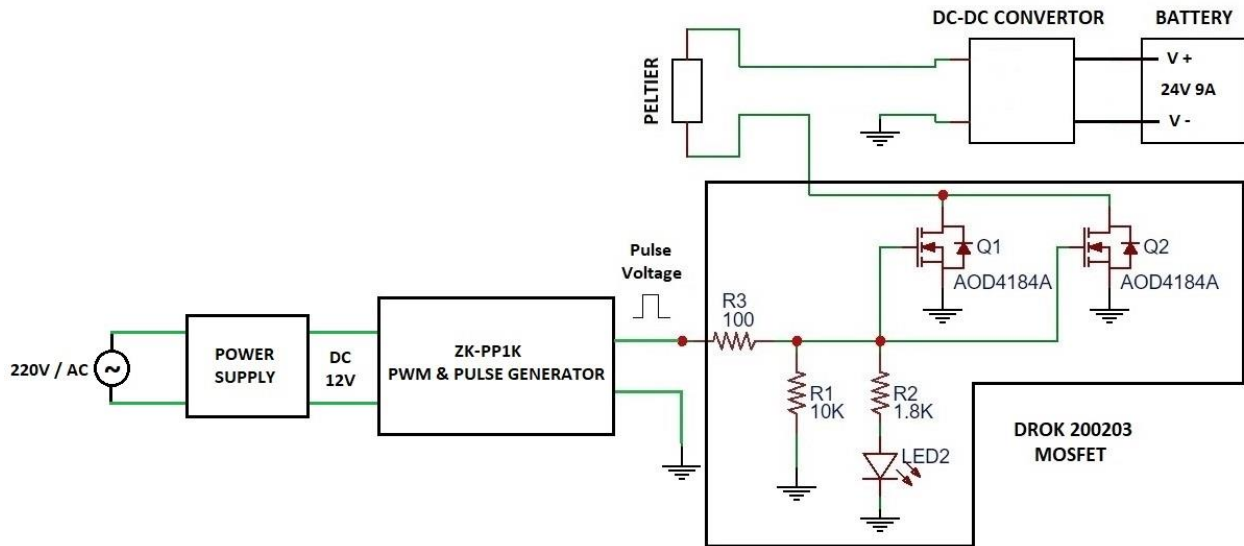


Figure 4. Block diagram of measurement system.

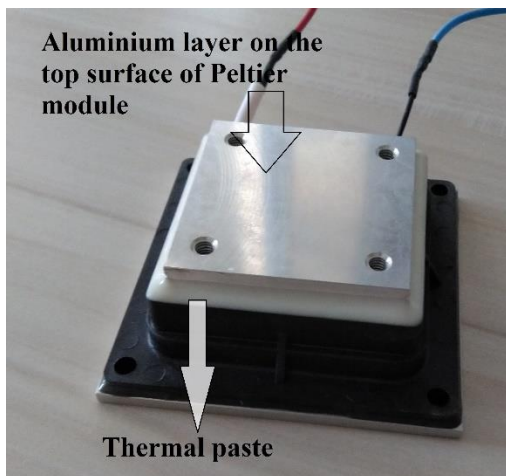


Figure 5. The Peltier module, type Z-MAX TEC1 – B12708AC.

The voltage across the module was measured by a digital multimeter, type AN8002. Table 1 shows the technical specifications of the Peltier TEC module used. Peltier TEC modules are very sensitive for the waveform of driving current and then, their performance can be affected, if the driving current waveform has any harmonic or noise. Two batteries, which are 12 V 9 A in power, are used as a power supply. They are connected in series to increase the output voltage and can be provided a continuous noiseless power to be able to tolerate the power loss of Peltier TEC module.

A DC-DC converter, [Fig. 4] type DPS5015, is connected to the batteries in series to limit the driving current of the Peltier module at varied current values in the range of 0.5 to 5 A.

In signal processing part, a signal generator, type ZK-PP1, produces a rectangular wave signal 0 – 5 V, 30 mA,

from 1 Hz to 150 kHz operating frequency. Its duty cycle can be arranged from 1% to 100%, but in this system, 50% duty cycle was chosen to drive the module at varied frequency. The output of rectangular wave generator is connected to the MOSFET transistors, type DROK 200203. They can be operated from 5 – 36 V up to 15 A current and 20 kHz frequency as an output. Since the tested Peltier module operates 12 V 6 A power. The MOSFET transistors are increased the peak of rectangular wave signal to this level of power.

In the temperature control part, two digital thermometers, type LT172N, measured the temperature on hot and cold sides of the Peltier device. The initial temperature was recorded as a room temperature by means of a digital thermometer, just before the tests were begun to keep the thermal stability of hot and cold surfaces of the module. The digital thermometers LT172N have $\pm 3\%$ sensitivity in full scale due to their temperature sensors used, which are the NTC thermistor, type GM-NTC-105C. The sensitivity of other measurement devices is less than ± 0.1 in full scale. Therefore, the maximum overall measurement error of the system is found to be about $\pm 3\%$. Fig. 6 and Fig. 7 show the general view of measurement system and Peltier device system respectively.

Table 1. Technical specifications of the Peltier module used.

Dimensions	W70xD70xH27 (mm)
Cooling performance	57.8 W
Rated voltage	DC ± 12 V
Rated current	6 A
Inner resistance	1.35 – 1.65 Ω

The system was tested using an aluminium mass, which has the mass of 0.193 kg and the specific heat coefficient of aluminium is 903 J/(kg K). The heat dissipation Q_c was calculated by Eq. (11) in the measured temperature range and power consumption of Peltier device Q_p was obtained by the recorded voltage across the module and current passing through the module. Then the COP was calculated by the ratio of Q_c/Q_p , which is given in Eq. (10).

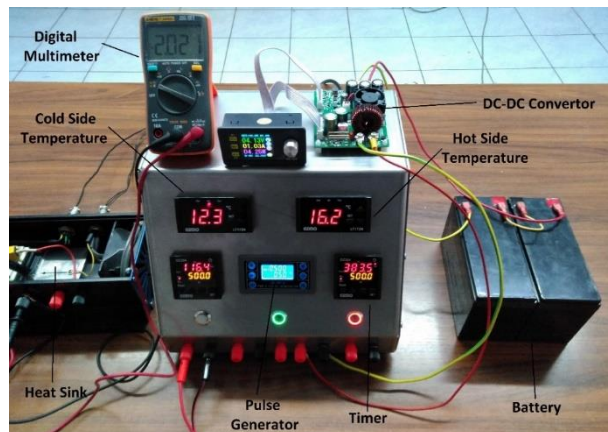


Figure 6. View of measurement system.

ARTIFICIAL NEURAL NETWORK MODEL

Neural networks represent a novel and modern approach that can provide solutions to problems, for which conventional mathematics, algorithms, and methodologies are unable to find a satisfactory and acceptable solution. ANNs are inspired by the functionality and structure of the human brain, which can be imagined as a network comprising densely interconnected elements called neurons (Graupe, 1997).

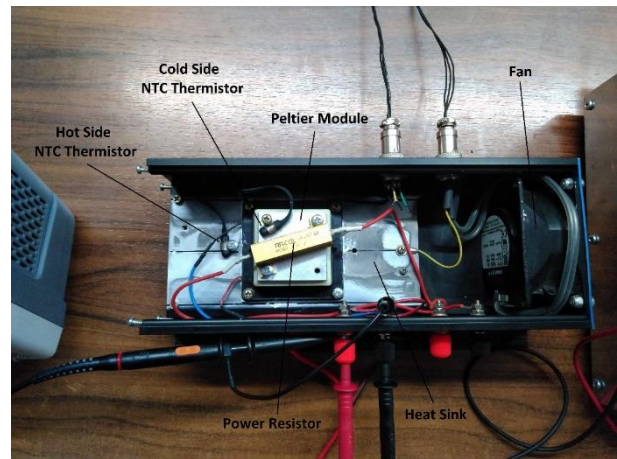


Figure 7. Peltier device system.

The most popular neural network is the multilayer perceptron, which is a feed-forward network; i.e., all signals flow in a single direction from the input to the output of the network. It consists of neurons organized in a number of layers that can be categorized into three parts: the first part is the input layer, which allows the network to communicate with the environment; the second part is commonly known as the hidden part, in which one or more layers of neurons exist depending on the problem's demands and requirements for generalization; and the third part is the output layer.

The artificial neurons are arranged in layers, wherein the input layer receives inputs from the real world and each successive layer receives weighted outputs from the preceding one as its input, thereby resulting in a feed-forward ANN, where each input is fed forward to the subsequent layer for treatment. The outputs of the last layer constitute the outputs to the real world.

The main problem with an ANN model has been to establish representative training data, particularly, when a large number of variables are considered as being in this study. Training data from the experimental work on TEC modules was obtained for dimensions with the length, width and height 70x70x27 mm. In the proposed neural network models, the input parameters were the cold side temperature (T_c), the hot side temperature (T_h), the temperature difference between cold and hot side of TEC module (ΔT), the driving current (I), voltage across the terminals of the TEC module (V), the driving time (t) and frequency (f), while the output parameter was the performance of TEC module (COP) (Fig. 8).

Qnet 2000[®], a commercial neural network package, was used for the prediction of the performance of TEC module, offering the advantage of rapid network development through flexible choices of algorithms, output functions, and other training parameters, thereby enhancing accuracy (Qnet2000). A total of 150 input vectors obtained from the TEC module for the COP, and it was available in the training set for a back-propagation neural network. The number of hidden layers and neurons in each layer were determined by trial and error to be optimal, including different transfer functions such as hyperbolic tangent, sigmoid, and hybrid. After the network had been trained, better results were obtained from the network formed by the hyperbolic tangent transfer function in the four hidden layers as well as in output layer for prediction of the COP. The hyperbolic tangent transfer function is

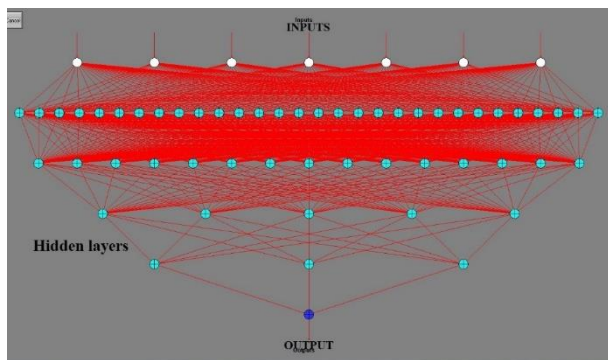


Figure 8. The developed ANN for performance of TEC module.

$$\tanh x = \frac{e^x - e^{-x}}{e^x + e^{-x}} \quad (13)$$

The networks included 7 input neurons, 1 output neuron, and four hidden layers with 53 neurons for the COP, with full connectivity between nodes [Fig. 8]. Back-propagation ANNs require that all training input data must be normalized to improve the training characteristics. Therefore, all data for the nodes in the input layer and training targets for the output layer were normalized between the limits of 0.15 and 0.85. In training of networks, a HP workstation, which had an Intel[®] core i7-720QM microprocessor, 1.6 GHz, 6 MB L3 cache, and 16 GB RAM, was used. The calculation time was about 10 hours for each trained network.

ANALYTICAL ANALYSIS WITH MATLAB[®]

The MATLAB[®] Curve Fitting Toolbox[™] was used to determine an accurate and simple analytical equation for the performance of TEC module corresponding to experimental and predicted data. It provides graphical tools and command-line functions for fitting curves to data. The toolbox performs exploratory data analysis, pre-processes and post-process data; compares candidate models and removes outliers and allows working an interactive environment with graphical user interface.

The regression analysis using the library of linear and nonlinear models provided can be conducted or specified own custom equations. The library provides optimized solver parameters and starting conditions to improve the quality of your fits. The toolbox also supports nonparametric modelling techniques, such as splines, interpolation, and smoothing. After loading some data, a fit can be created using a fit function, specifying variables and a model type including exponential, Fourier, Gaussian, polynomial, power, etc (MATLAB[®] R2018b).

RESULTS AND DISCUSSIONS

When the Peltier module is operated, it is heated up itself due to current passing through it and then, its resistance changes. The voltage across the module varies with temperature, because the current passing through the module keeps constant consistently. Fig. 9 shows the variation of module resistance with the temperature difference between the cold and hot sides of the TEC module under constant 1 A dc current and in 500 seconds test time.

The resistance of the module slightly increases with the temperature difference up to about 1 °C, whereas it keeps almost constant at higher temperature difference values above 1 °C. The maximum change was about 0.59 ohm with the temperature difference 8.2 °C.

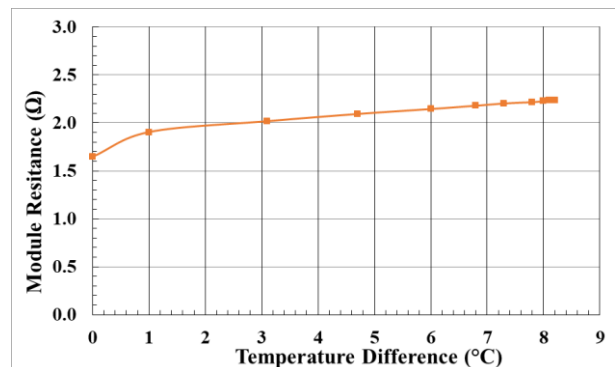


Figure 9. Variation of module resistance with temperature difference ΔT under constant dc current 1 A and in 500 seconds test time.

Fig. 10 shows the variation of module resistance with the driving current for the constant dc current and PFM. The module resistance slightly decreases with the driving current up to 2 A, while its maximum variation is about 0.06 ohm between 2 A and 6 A. The constant module resistance yields to the thermal stability of the module and then, it affects its efficiency.

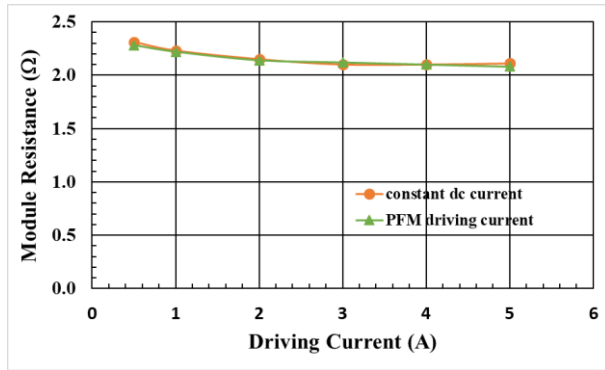


Figure 10. Variation of module resistance with driving current for constant dc current and PFM.

The aim of the research is to compare the performance of the module between the driving methods with constant dc current and optimised rectangular wave. The dc current value corresponding with the peak value of the rectangular waveform was chosen. Thus, the driving of the module with both methods was realised using the same system and conditions during the tests and they can be appropriately comparable. The measurements were

carried out using constant dc driving current values with 0.5, 1, 2, 3, 4 and 5 A and the obtained results were summarised in Table 2. The temperature difference (ΔT) increases with increasing dc current and voltage of the module, whereas the COP value decreases. The COP value was dramatically reduced after 1 A dc current.

The Peltier module was also derived by the rectangular wave (50% duty cycle) with frequency values at 50, 100, 200, 300, 400, 500 and 1000 Hz. The operating frequency was comparatively determined by means of the COP values among experimental data. Although they are very close to each other as shown in Table 3. The thermoelectric module has the best COP value at 500 Hz for the rectangular wave driving current.

Electromagnetic interference is a critical issue during experiments due to high frequency current pulses at Peltier modules. An appropriate shielding and smart control techniques are the tools for the employment of higher switching frequencies above 10 kHz (Baubaris *et al.*, 2017).

Table 2. Measurement results at varied constant dc driving current values in 500 s test time.

Dc current (A)	Cold side temperature (°C)	Hot side temperature (°C)	Room temperature (°C)	ΔT (°C)	Module Voltage (V)	Module Resistance (Ω)	COP
0.5	14.6	18.5	17.8	3.9	1.16	2.31	2.55
1	10.0	18.2	17.3	8.2	2.23	2.23	1.38
2	6.4	19.8	17.6	13.4	4.30	2.15	0.58
3	3.2	22.3	17.6	19.1	6.31	2.10	0.37
4	0.3	25.0	17.6	24.7	8.40	2.10	0.27
5	-0.9	27.9	17.6	28.8	10.57	2.11	0.20

Therefore, the electromagnetic interference issues, which emerged during experimental process, have raised considerable limitations on the PWM applicability. However, the electromagnetic interference can be ignored on the PFM applicability due to its low switching frequency. Moreover, the system does not require extra electronic circuit protection such as shielding, filtering, wire length and appropriate location of them.

When the COP value in the PFM driving method was compared with the COP value in the constant dc driving method has, it is almost double and shows that the PFM driving method improves the cooling efficiency by reducing the input power due to duty cycle in the Peltier device.

Table 3. Measurement results at varied frequency and 1 A constant current in 500 s test time.

Frequency (Hz)	Cold side temperature (°C)	Hot side temperature (°C)	Room temperature (°C)	ΔT (°C)	Module Voltage (V)	Module Resistance (Ω)	COP
50	14.5	21.9	20.4	7.4	2.26	2.26	2.46
100	14.3	21.8	20.4	7.5	2.26	2.26	2.48
200	14.2	21.5	20.3	7.3	2.26	2.26	2.42
300	14.1	21.5	20.0	7.4	2.26	2.26	2.45
400	14.3	21.8	20.0	7.5	2.27	2.27	2.48
500	13.7	21.2	20.0	7.5	2.26	2.26	2.49
1000	14.6	22.0	20.9	7.4	2.27	2.27	2.45

The experimental data driving the PFM method with 50% duty cycle during 500 s test time were summarised in Table 4. It is clear that the COP was improved by the PFM driving method. Improvement of COP was maximum at driving current 0.5 A with 102%, whereas it

was minimum at 5 A with 55% as compared to the constant dc driving current method.

Fig. 11 shows the variation of COP with the constant dc and pulse driving method and improvement % between

them. The percent COP improvement was dramatically fallen after 0.5 A driving current and it keeps almost constant until 4 A, finally, it was sharply dropped at 5 A again. The COP values at low driving current were found to be higher than the COP values at high driving current due the input power and the Joule heating. The variation of COP with the driving current is not linear; it seems, an exponential change exists, since the thermoelectric semiconductors have a non-linear property.

The ANN model was trained in the range of 0.5 – 5.0 A driving current and 100 – 500 Hz frequency up to 500 s operation time. The performance of the ANN model was statistically measured by the RMS error and average correlation. After the network was trained by 10 million-iteration number, the linear correlation coefficient and RMS errors were found to be 99.99% and 2.88% for the COP. Table 5 also shows the percent contribution of input nodes.

Table 4. Measurement results at rectangular wave driving current with 50% duty cycle in 500 s test time.

Current (A)	Cold side temperature (°C)	Hot side temperature (°C)	Room temperature (°C)	ΔT (°C)	Module Voltage (V)	Module Resistance (Ω)	COP	Improvement %
0.5	14.0	17.9	17.6	3.9	1.14	2.28	5.15	102
1	11.2	18.7	17.6	7.5	2.22	2.22	2.53	83
2	8.2	20.7	17.7	12.5	4.28	2.14	1.08	80
3	7.4	24.3	17.6	16.9	6.36	2.12	0.65	76
4	8.6	28.6	17.7	20.0	8.69	2.10	0.47	74
5	11.5	33.5	17.6	22.0	10.39	2.08	0.31	55

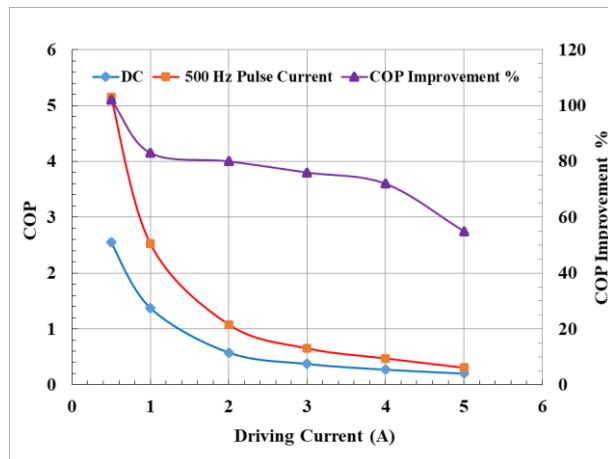


Figure 11. Variation of COP with constant dc and pulse driving current and improvement % of COP.

From Table 5, the frequency has a minimum contribution, while the temperature differentiation has the major contribution for the performance of the TEC module. It is clear that the temperature differentiation, voltage, cold and hot surface temperatures and current are very effective individually for estimation of the COP. The frequency makes a 0.54% contribution, which is significant among the input parameters, while the temperature differentiation also makes a major contribution about 28% to the prediction of the COP. The voltage across the module, current passing through the module and time 20.73%, 17.68% and 2.18% respectively also make significant contribution to the prediction of the COP. The cold and hot surfaces temperatures make 16.9% and 14.42% contributions, respectively.

A set of test data, different from the training data, was used to investigate the network performance. The average correlation and maximum error for prediction were found to be 99.99% and 1.38%, respectively, for the tested TEC module. The ANN model was assessed with

0.5 and 1 A current value and 100 and 500 Hz frequency at varied cold and hot surfaces temperatures, voltage and time, which were outside the range of the training dataset.

The results show that the developed ANN model has an acceptable prediction capability for the performance of TEC modules within the defined training dataset and good correlation with acceptable accuracy between measurement and predicted results (Fig. 12). Table 6 was summarised the measurement and predicted data for the tested sample. Therefore, the ANN model can be efficiently used to estimate for the performance of the TEC module.

Table 5. Contribution of input nodes to COP in the ANN model.

Input nodes	Contribution % for COP
I (A)	17.68
T_c (°C)	16.90
T_h (°C)	14.42
ΔT (°C)	27.97
V (V)	20.32
t (s)	2.18
f (Hz)	0.54

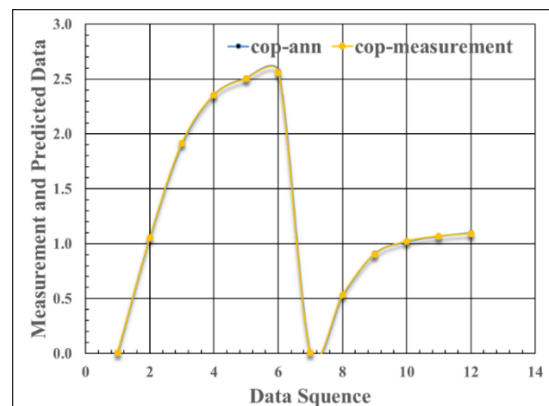


Figure 12. Correlation between measurement and predicted results.

The goodness of fit should be evaluated, after fitting data with one or more models using the MATLAB® Curve Fitting Toolbox™ is carried out. When several fits have executed by the goodness-of-fit statistics, to look for the smallest number of coefficients help to decide, which fit is the best. Exponentials are often used, when the rate of change of a quantity is proportional to the initial amount of the quantity. Thus, the best curve fit for the ANN data was found to be a two-term exponential model as given by;

$$f(x) = ae^{bx} + ce^{dx} \quad (14)$$

where the coefficients with 95% confidence bounds are $a= 1.725 \times 10^4$, $b= -0.2$, $c= -1.726 \times 10^4$ and $d= -0.2$ respectively. The RMS error was 0.074, whereas the correlation between the predicted from ANN and calculated from exponential model values was 0.99, which shows a good agreement between them (Fig. 13).

Table 6. Measurement and predicted data for the test sample.

Data no	COP	
	measurement	predicted
1	0.01	0.01
2	1.05	1.06
3	1.92	1.91
4	2.35	2.36
5	2.50	2.51
6	2.56	2.57
7	0.01	0.01
8	0.53	0.53
9	0.90	0.91
10	1.02	1.02
11	1.07	1.07
12	1.09	1.10

All values obtained from measurements, prediction with ANN, and analytical equation with curve fitting are in good agreement with the average correlation 99% and maximum RMS error 1.38. It is clear that both numerical models, which are the ANN and analytical equation, are working well and verifying the experimental results.

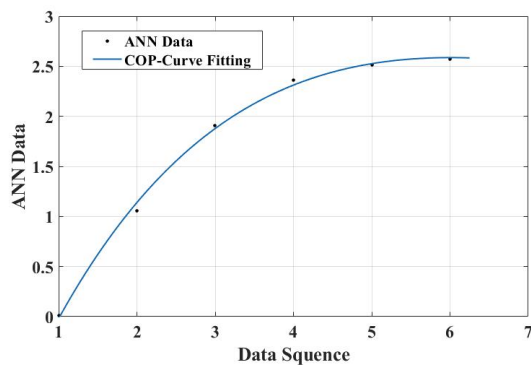


Figure 13. The best curve fit for predicted data.

CONCLUSIONS

The present research highlights the improvement efficiency and thermal stability of the TEC module driving with the PFM method. The PFM and constant dc driving methods can be applied to the module using the system at the same operation condition. Therefore, the results are accordingly comparable to each other. Although, the COP was improved the on-off control with constant dc current and the PWM methods. There are some disadvantages for them such as reducing the lasting time and considerable limitations due to high switching frequencies.

The PFM driving method was developed by optimising the input power owing to duty cycle of the rectangular wave and increased the cooling efficiency up to 102% as compared to the constant dc current driving method. Moreover, the driving system does not require an extra electronic circuitry for the electromagnetic interference due to its operating frequency.

One of the significant contribution to the module resistance is to keep it almost constant at high ΔT values above 1 °C and thermal stability of the module due to driving current. High COP value obtained by the PFM method using the heat dissipation and power consumption of the module indicates that there can be made a significant contribution to the cooling challenges and cooling technology in the field of semiconductor applications and technology. The PFM driving method can be useful for cooling and temperature stability of electronic devices by means of Peltier module.

The performance of a TEC module was investigated for optimum operating energy corresponding to surface temperatures, the temperature differentiation, the driving time and frequency. Increasing temperature differentiation is the major effect on performance, while the driving time and frequency also have a significant effect on it. The developed ANN model has a good prediction capability with acceptable accuracy. When the model was tested by untrained data, the linear correlation coefficient and RMS error were found to be 99.99% and 1.38% respectively for the COP. The analytical equation for performance as depending on prediction results has been determined by using MATLAB® Curve Fitting Toolbox™. The average correlation of the two-term exponential model was found to be 0.99 and the overall calculation error was 0.074, which are within acceptable limits for the COP. The experimental results are in good agreement with the predicted and calculated data, which are useful for manufacturers working in this field.

ACKNOWLEDGMENTS

This research is a part of the Physics Ph.D. thesis of İlhan Kahraman. The authors would like to thank Gempa Electro Mechanic and Engineering Co. for financial support and Kahramansan Technology for financial and technical support of this research.

REFERENCES

- Derebasi N., Eltez M., Guldiken F., Sever A., Kallis K., Kilic H. and Ozmutlu E.N., 2015, Performance of novel thermoelectric cooling module depending on geometrical factors, *J. Elec. Mat.* 44, 6, 1566 – 1572.
- Sekiguchi R., Liu Y. and Sano Y., 2018, Thermal equivalent circuit of Peltier device considered Seebeck effect and driving method improving cooling efficiency of the device, *Elec. & Com. in Japan*, 101, 5, 73 – 83.
- Twaha S., Zhu J., Yan Y. and Li B., 2016, A comprehensive review of thermoelectric technology: Materials, applications, modelling and performance improvement, *Ren. Sus. Energy Rev.*, 65, 698 – 726.
- Song Lv., Zuogin Q., Dengyun H., Xiaoyuan L. and Wei H., 2020, A comprehensive review of strategies and approaches for enhancing the performance of thermoelectric module, *Energies*, 13, 3142, 2 – 24.
- Derebasi N., Eltez M., Guldiken F., Sever A., Kallis K. and Kilic H., 2015, Influence of geometrical factors on performance of thermoelectric material using numerical methods, *J. Elec. Mat.* 44, 6, 2068 – 2073.
- Baubaris A., Karampasis E., Voglitsis D. and Papanikolaou N., 2017, Experimental survey on active thermoelectric cooling driven by PWM techniques, *Panhellenic Conference on Electronics and Telecommunications PACET*.
- Guclu T. and Cuce E., 2019, Thermoelectric Coolers (TECs): From Theory to Practice, *J. Electronic Materials*, 48, 1, 211 – 230.
- Laidi M. and Hanini S., 2013, Optimal solar COP prediction of a solar-assisted adsorption refrigeration system working with activated carbon/methanol as working pairs using direct and inverse artificial neural network, *Int J Ref.*, 36, 247 – 257.
- Sulaiman A. C., Amin N. A. M., Basha M. H., Majid M. S. A., Nasir N. F. M. and Zaman I., 2018, Cooling performance of thermoelectric cooling (TEC) and applications: A review, *Matec Web of Conferences*, 225, 03021, 1 – 10.
- Rowe D. M., 2006, *Thermoelectrics Handbook Macro to Nano*, CRC Taylor & Francis.
- Riffat S. B. and Ma X., 2003, Thermoelectrics: a review of present and potential applications, *Appl. Therm. Eng.*, 23, 913 – 935.
- Bar-Cohen A., Solbrekken G. L. and Yazawa K., 2005, Thermoelectric-Powered convective cooling of microprocessors, *IEEE Trans. Adv. Packag.*, 28, 2, 231 – 239.
- Graupe D., 1997, *Principles of Artificial Neural Networks*, Singapore: World Scientific.
- Qnet2000 Help Manual.
- MATLAB®, Curve Fitting Toolbox™ User's Guide, R2018b.



İlhan Kahraman graduated from the Physics Department of Dumlupınar University, Kütahya. in 2010. Later, he received his M. Sc. degree in Physics from Bursa Uludag University, Bursa in 2014. His main research areas are the solid state lasers and thermoelectric cooling. He has also had a comprehensive industrial experience on the laser systems, who was working on this field more than 5 years. He is studying the Ph. D. degree on the field of thermoelectric cooling and temperature stability of solid state lasers and the efficiency of thermoelectric cooler modules at Bursa Uludag University.



Naim Derebasi received the B. Sc. and M. Sc. degrees from Physics Department of the Middle East Technical University, Ankara, in 1986 and Bursa Uludag University, Bursa in 1988 respectively. Later, he received the Ph. D. in Electrical Electronic Engineering, from Cardiff University, U.K. in 1994. He also has the second Ph. D. in Physics from Bursa Uludag University. His principle research interests are in magnetic materials, domains, transformer core losses and efficiency, transducers, sensors, thermoelectric, thermoelectric materials and cooling and solar cells. He is a Professor at Physics Department, Bursa Uludag University, where he has been on the academic staff since 1987.



FINDING CONDITIONS IN REPROCESSING OF GLASS WOOL WASTE AS A HEAT INSULATOR

Saharat CHUNTHUM^{a,*}, Anchasa PRAMUANJAROENKIJ^{a,b,**}, Siriluk PHANKHOKSOONG^{a,***},
Rungsima CHOLLAKUP^{c,****} and Sadik KAKAC^{d,*****}

^a Faculty of Science and Engineering, Kasetsart University, Chalermphrakiat Sakon Nakhon Province Campus, Thailand 47000

^b International College, Kasetsart University, Bangkok, Thailand 10900

^c Kasetsart Agricultural and Agro-Industrial Product Improvement Institute, Bangkok, Thailand 10900

^d Department of Mechanical Engineering, TOBB University of Economics and Technology, Ankara, Turkey

* anchasa.p@ku.th, ORCID: 0000-0001-9288-7224

** Saharat.cha@ku.th, ORCID: 0000-0002-5356-3232

*** siriluk.pan@ku.th, ORCID: 0000-0003-3397-4592

**** aaprmc@ku.ac.th, ORCID: 0000-0002-9659-7854

***** sadikkakac@yahoo.com, ORCID: 0000-0002-7839-8034

(Geliş Tarihi: 29.03.2022, Kabul Tarihi: 03.10.2022)

Abstract: This research aimed to find the process of value adding for glass wool waste from the glass wool composite board used in the vehicle industry. The waste was reprocessed to be an insulator and to determine the suitable conditions for hot-press forming to create new materials having high thermal resistant properties. Firstly, the properties of the original board; the thermal resistances (R) and the noise absorption coefficients (NRC), were measured and were found averages of 0.9055 m²K/W and 0.3955, respectively. The reprocessing conditions were varied by 2 levels; high and low, of 5 control factors; density, thickness, pressure, temperature, and surface roughness. Three repeating processes for each condition were performed. The Design of Experiment (DoE) was the full factorials; 2⁵ experiments, by using the Analysis of Variance (ANOVA) to find main and interaction factors relating to the properties. From the ANOVA results with the α level of significance at 0.05, it was found that the main factors responding to the high values of the thermal resistance were the thickness and density. This resulted in the suitable conditions for the hot-press process of both the new smooth and rough pads with a density of 96 kg/m³ and a thickness of 25 mm. The R values of the new insulators were in between 0.88 – 0.98 m²K/W and, additionally, the high NRC values were also provided in between 0.46 – 0.49. These findings could be applied for wall designing, wall decorations and heat shields for indoor rooms and different types of buildings.

Keywords: Glass wool waste, Insulator, Reprocessing, Heat transfer, Thermal resistance

CAM YÜNÜ ATIĞININ ISIL YALITKAN OLARAK YENİDEN PROSES EDİLMESİNİN KOŞULLARININ BULUNMASI

Özet: Bu çalışma otomotiv endüstrisinde kullanılan cam yünü kompozit levhadan elde edilen cam yünü atığının değer katma sürecini bulmayı hedeflemektedir. Atık, bir yalıtkan olması ve yüksek ısı direnç özelliklerine sahip yeni malzemeler oluşturmak için kullanılan sıcak pres şekillendirme için uygun koşulların belirlenmesi amacıyla tekrar işlenmiştir. İlk olarak orijinal tahtanın özellikleri; ısı direnç (R) ve gürültü emilim katsayıları (NRC) ölçülmüş ve sırasıyla ortalama 0,9055 m²K/W ve 0,3955 olarak bulunmuştur. Tekrar işleme koşulları, yoğunluk, kalınlık, basınç, sıcaklık ve yüzey pürüzlülüğü olmak üzere 5 adet kontrol faktörüne ve yüksek ve alçak olmak üzere 2 adet seviyeye göre değişmektedir. Her koşul için üç tekrarlı işlem gerçekleştirilmiştir. Tasarım analizi, 2⁵ deneyden oluşarak, tam faktöriyeldir ve özelliklere ilişkin ana ve etkileşim faktörlerini bulmak için Varyans Analizi (ANOVA) kullanılmıştır. α anlamlılık düzeyi 0,05 olan sonuçlardan, ısı direncin yüksek değerlerine sebebiyet veren ana faktörlerin kalınlık ve yoğunluk olduğu bulunmuştur. Bunun sonucunda hem yeni pürüzlü hem de pürüzsüz pedler için sıcak pres işlemi uygun koşullarının 25 mm kalınlık ve 96 kg/m³ yoğunluk olduğu açığa çıkmıştır. Yeni yalıtkanların R değerleri 0,88 – 0,98 m²K/W arasında olmaktadır ve ayrıca yüksek NRC değerleri de 0,46 – 0,49 arasında olacak şekilde verilmiştir. Bu bulgular, iç mekanlarda ve farklı bina tiplerinde duvar tasarımı, duvar dekorasyonları ve ısı kalkanları için kullanılabilir.

Anahtar Kelimeler: Cam yünü atığı, Yalıtkan, Tekrar işleme, Isı transferi, Isıl direnç

NOMENCLATURE

Symbols

R	thermal resistance (m^2 W/m)
k	thermal conductivity [W/m·K]
NRC	Noise Reduction Coefficient
SAC	Sound Absorption Coefficient
S	Standard deviation
$R-sq$	Explained variation / total variation

Greek Symbols

μ	overall mean
τ	The effect of factor A (surface)
β	The effect of factor B (density)
γ	The effect of factor C (temperature)
σ	The effect of factor D (thickness)
α	The effect of factor E (pressure)
ε	Random error of the experimental
ρ	density [kg/m^3]

INTRODUCTION

Climate changes have affected all countries in the world. Thailand climates fluctuate as risen atmospheric temperatures continuously. The growing amounts of energy consumption and carbon dioxide emission are main keys causing greenhouse effect and heat waves. There are many campaigns promoting energy conservation in every section such as industrial and residential sections. Green and recycle materials are recommended and investigated to be manufactured in the industrial level. These materials are considered as safe products from environmental-friendly processes which use low energy consumption in their production lines and reduce operating cost of the manufacturers. Glass wool is one of many insulators used in construction and vehicles because of its low thermal conductivity; 0.032 W/m K. Glass wool is used to pad on vehicle bodies to reduce conductive heat transfer rates from ambient into vehicle compartments helping refrigerating systems to maintain the compartment conditions. Moreover, glass wool can absorb sound and reduce noise from outside into the compartments. The International Agency for Research on Cancer, World Health Organization (WHO) certified that glass wool does not harm human health. If a glass wool fraction goes into the human respiratory system, the person will sneeze and get rid of the fraction due to its cylindrical structure is big and its diameter is approximately 7 microns. Since glass wool is commonly used in construction and vehicle industries, a great amount of glass wool waste is disposed by burning and burying in landfills each year. The Department of Industrial Works, Ministry of Industry, Thailand, encourage manufacturers to recycle and reuse waste in many forms and purposes as 3Rs (Reduce Reuse Recycle). This campaign has reduced glass wool waste but this waste; more than one million tons, has potentials to be reprocessed and utilized.

The glass wool waste weights more than 20 tons. Every month, the manufacturers spent certain amount of budget to get rid of it properly. Glass wool can be formed in blanket and board both bare and covered surfaces with layers such as aluminum foil. The glass wool made according to ASTM standard and Thai Industrial standard codes can be used as insulators and acoustic in offices, dwellings, and buildings. The glass wool qualifications are 1) thermal insulation with a low thermal conductivity of 0.032 W/m K, a good thermal resistance, 2) acoustic insulation, 3) non-flammable, 4) easy installation, 5) compressive strength, 6) condensation control, 7) long life performance, and safe to use approved by WHO.

Yodkaew et al. (2007) developed acoustic ceiling by using rice shell. The developed ceilings were examined to find their Noise Reduction Coefficients (NRCs) and their NRCs were compared with those of gypsum, acoustic, and glass wool boards. Their results showed that the developed ceiling from the rice shell-to-glue ratio at 5:1 had better NRC than those of the gypsum and acoustic boards. Choowonglert and Thakphanont (2015) developed acoustic boards from paper waste from offices. The waste was shredded by paper shredders before it was reprocessed by a hot pressing process. The reprocessed boards had thicknesses of 10, 15 and 25 mm. Noise absorption properties showed the board potentials to be developed into the commercial acoustic material which was made from the office-paper waste, environment-friendly, and nicely adding values to the waste.

Pakhunworakit et al. (2006) investigated thermal conductivity values of insulators made from agricultural waste; corn cob and cassava tree, having different density values. The best insulator was the cassava-tree insulator having the density of 200 kg/m^3 , the thickness of 10 mm, the lowest thermal conductivity was found at 0.059 W/m K. Homaswin et al. (2007) developed building acoustic insulators made from coconut-shell fiber with the size of 0.5 m in height and width. The fiber insulator covered with the 2-inch latex layer provided the NRC close to that of the glass wool board and this NRC was better than those of the gypsum and acoustic boards. Narakaew and Narakaew (2015) developed activated carbon made from corn cob and boards made from hay, and the corn-cob activated carbon. The smell and noise absorptive performances were experimentally investigated by using the developed boards as walls of a one cubic meter room. The noise absorptive performance was higher than those of the walls made from acoustic foam and glass wool.

Zhao et al. (2018) presented lifecycle assessment of typical glass wool production in China, this work was aimed to reduce unnecessary energy in the glass wool production. The commercial software named eBalance which was developed by Integrated Knowledge for our Environment (IKE) was used to investigate Primary Energy Demand (PED), Global Warming Potential

(GWP), Acidification Potential (AP), Photochemical Oxide Formation Potential (POFP) and Refractive Index (RI). The lifecycle assessment analysis found that the glass wool waste mostly affected environment on energy in manufacturing processes. The GWP was 49% while the AP, POFP and RI were 50%, 25% and 39%, respectively. This research claimed that the energy conservation measures played an important role on reducing environmental impacts caused by the glass wool waste.

Jeon et al. (2017) experimentally studied effects of humidity on glass wool by measuring thermal conductivity of the glass wool specimens after they exposed to humidity. Results indicated that the non-coating glass wool or the glass wool without anti-moisture agent could absorb water about 4% - 8% of its weight and the thermal conductivity was increased 4 times higher. The coated glass wool or the glass wool covered with anti-moisture agent by Fluoroalkylsiloxane (SH-AF) technique provided the thermal conductivity at 0.0329 W/m K. Therefore, the anti-moisture agent reduced the thermal conductivity of the coated glass wool, approximately at 0.0344 W/m K.

Wajima and Matsuka (2019) presented a decomposing process for glass wool waste by using the sodium hydroxide pyrolysis. This research was aimed to reduce the waste having glass wool fibers and resin as the main components. This method was introduced as a new recycle process to reduce the waste by changing chemical components of the waste in 400 - 500 Celsius anaerobic conditions and using sodium hydroxide as a chemical catalyst. From the results, the most decomposition of the resin-glass wool waste could be found when 3 grams of the sodium hydroxide was used, the decomposition was 20% of the original weight.

Since the world focuses on the sustainable development goals, this research aimed to promote inclusive sustainable industrialization and fostering innovation and to take action to combat climate change by recycling and reprocessing the glass wool waste, as well as to ensure sustainable consumption and production patterns by producing the new insulator for building in cities and human settlements inclusive, safe, resilient and sustainable. This work paid particular attention to find reprocessing conditions to recycle the glass wool waste from the vehicle industries, to investigate properties of the reprocessed insulators and to compare the properties with the original properties of the glass wool board and the commercial one. The recreating conditions; thermal resistances (Rs) and Noise Reduction Coefficients (NRCs) were investigated and reported in this paper. The results of this research could provide necessary information for insulator manufacturers to reprocess the glass wool waste and to produce the new insulator from the waste. The recreated insulator as a composite board could be used in the construction, furniture or design industries as user demands.

METHODOLOGY

The glass wool waste was collected from a vehicle assembly factory, it was reprocessed under 5 control parameters; density, thickness, pressure, temperature, and surface roughness. Three repeating processes for each condition were performed. All reprocessed specimens were tested to find thermal conduction (k) and thermal resistance (R) followed the procedure of ASTM C518 by using sample sizes of 17.5 cm width, 17.5 cm length, and 5 cm height. Then, Sound Absorption Coefficient (SAC) and Noise Reduction Coefficient (NRC) were evaluated followed the procedure of ISO 10534-2 by using 10 cm and 3 cm diameter specimens for low and high frequency tests, respectively. In this work, the factorial design of 5 control parameters at high (+1) and low (-1) levels as shown on Table 1 was applied by using Analysis of Variance or ANOVA to reduce possible errors.

Table 1. Research factors

Control factors	Factors	Factor levels	
		Low (-)	High (+)
Surface	A	Smooth	Rough
Density (kg/m ³)	B	64	96
Temperature (°C)	C	160	190
Thickness (mm)	D	15	25
Pressure (bar)	E	10	15

The Factorial Experimental Design of the Two Power Five (2⁵) was used to collect experimental data and analyze statistical results. The ANOVA significance level of the experiments was specified as $\alpha = 0.05$ from 32 conditions and 3 repeating experiments to find responses of thermal conductivity and Noise Reduction Coefficient. The total of 96 experimental units were gathered as shown on Table 2. Steps of experimental analysis consisted of two main steps.

Firstly, the linear statistical model of the two power five full factorial was defined as following (Ayuttaya, 2007);

$$\begin{aligned}
 y_{ijklmn} = & \mu + \tau_i + \beta_j + \gamma_k + \delta_l + \alpha_m \\
 & + (\tau\beta)_{ij} + (\tau\gamma)_{ik} + (\tau\delta)_{il} + (\tau\alpha)_{im} \\
 & + (\beta\gamma)_{jk} + (\beta\delta)_{jl} + (\beta\alpha)_{jm} \\
 & + (\gamma\delta)_{kl} + (\gamma\alpha)_{km} + (\delta\alpha)_{lm} \\
 & + (\tau\beta\gamma)_{ijk} + (\tau\beta\delta)_{ijl} + (\tau\beta\alpha)_{ijm} \\
 & + (\tau\gamma\delta)_{ikl} + (\tau\gamma\alpha)_{ikm} + (\tau\delta\alpha)_{ilm} \\
 & + (\beta\gamma\delta)_{jkl} + (\beta\gamma\alpha)_{jkm} + (\beta\delta\alpha)_{jlm} \\
 & + (\gamma\delta\alpha)_{klm} + (\tau\beta\gamma\delta)_{ijkl} + (\tau\beta\gamma\alpha)_{ijkm} \\
 & + (\tau\beta\gamma\delta\alpha)_{ijklm} + \varepsilon_{ijklmn}
 \end{aligned} \tag{1}$$

where subscripts; i, j, k, l, and m, are the effects of the low and high factors (Table 1) which can be 1 and 2, respectively. Secondly, Analysis of Variance was performed by using a commercial computer software, the trademark name was MINITAB.

EXPERIMENTAL PROCEDURES

Glass wool waste from the car-roof-insulation process in the vehicle factory was taken in a form of a composite board. The insulator reprocessing steps started with taking polyester cloth covering the waste out. Polyester must be separated because it can affect environment. The waste was, then, put into a plastic granulator to make glass wool scraps. The scraps were weighted to meet the investigating density values and arranged on the designed molds; two surface types and thicknesses. Two steel plates were sandwiched on the mold surfaces before the molds were put in the hot-press machine to form the reprocessed insulators such that heat from the machine did not come into direct contact with the scraps. The machine operating conditions; temperature and compression values, were set according to the experimental designs, all experimental design factors are shown on Table 1. Since the sample roughness is one of the interesting parameters, the definition of the sample roughness should be given. The reprocessed samples with two surface types; smooth and rough, are shown on Figure 1. The rough surface mold was prepared separately from the smooth surface mold.

Table 2. Experimental conditions

Conditions	A	B	C	D	E
1	Smooth	64	160	15	10
2	Smooth	64	160	15	15
3	Smooth	64	160	25	10
4	Smooth	64	160	25	15
5	Smooth	96	160	15	10
6	Smooth	96	160	15	15
7	Smooth	96	160	25	10
8	Smooth	96	160	25	15
9	Smooth	64	190	15	10
10	Smooth	64	190	15	15
11	Smooth	64	190	25	10
12	Smooth	64	190	25	15
13	Smooth	96	190	15	10
14	Smooth	96	190	15	15
15	Smooth	96	190	25	10
16	Smooth	96	190	25	15
17	Rough	64	160	15	10
18	Rough	64	160	15	15
19	Rough	64	160	25	10
20	Rough	64	160	25	15
21	Rough	96	160	15	10
22	Rough	96	160	15	15
23	Rough	96	160	25	10
24	Rough	96	160	25	15
25	Rough	64	190	15	10
26	Rough	64	190	15	15
27	Rough	64	190	25	10
28	Rough	64	190	25	15
29	Rough	96	190	15	10
30	Rough	96	190	15	15
31	Rough	96	190	25	10
32	Rough	96	190	25	15

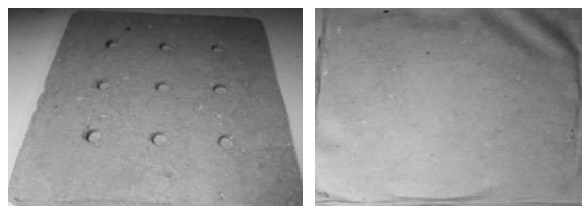


Figure 1. Reprocessed boards with two surface roughness; a rough surface (left) and a smooth surface (right)

RESULTS AND DISCUSSIONS

The insulator used in door assembly processes of vehicle industries combined of glass wool and non-woven polyester. The glass wool properties are shown in Table 3. From the information, the non-woven polyester must be separated because it can affect environment. The non-woven polyester was separated from the rest of the insulator waste. Three waste samples were investigated to find their properties at 20 and 50 Celsius as shown on Table 4, the average thermal conductivity (k) and thermal resistance (R) were 0.0166 W/mK and 0.9055 m²K/W, respectively. The samples were also tested to find Sound Absorption Coefficient (SAC) in 4 frequency levels; 250, 500, 1000, and 2000 Hz. Noise Reduction Coefficient (NRC); the average value of 4 SACs at 23 Celsius and 50%RH, was calculated. All SACs are presented on Table 5 and the NRC was 0.3955 or approximately 0.4. The sound absorption materials or acoustic materials commonly have NRCs at 0.4 or higher. These properties can be referred as the raw material properties of the reprocessed insulator. Before the waste was reprocessed, the waste flammability test was performed by using UL95 technique (Underwriters Laboratories 95 of USA) with 5 random samples at 24 Celsius and 53 %RH. The flammability test results are shown on Table 6, no sample was burned up to the holding clamp and no cotton indicator ignited was found.

Table 3. Properties of the glass wool insulator

Information	Details
Component	Glass wool 85 – 95% Cured binder 5 – 15%
Appearance	The material is yellow that can be flexible
Smell	None
Soluable	Insoluable
Be stable and fast reaction	Stable
Information about the danger	Direct skin contact may cause irritation.

Table 4. Thermal conductivity (k) and thermal resistance (R) results of the samples

Sample Types	Thick-ness (m)	Test Temp (°C)	Test Temp (°C)	k-value s (W/m K)	R-values (m ² K/m)
Composited board (0.321±0.005 kg)	0.0156±0.0050	20	50	0.0166 ± 0.005	0.9384
Composited board (0.321±0.005 kg)	0.0138±0.0005	20	50	0.0141 ± 0.005	0.9769
Composited board (0.321±0.005 kg)	0.0138±0.0005	20	50	0.0190 ± 0.005	0.8012

Table 5. Sound Absorption Coefficient (SAC) and Noise Reduction Coefficient (NRC) results of the samples

Type	Sound Absorption Coefficient (%) and NRC					
	250 Hz	500 Hz	1000 Hz	2000 Hz	Ave.	NRC
Composited board	7.02 %	29.3%	58.9 %	62.8 %	39.5 %	0.3955

Analysis of Variance for Thermal Conductivity (k) and Thermal Resistance (R)

All thermal conductivity (k) and thermal resistance (R) results of 96 reprocessed samples were analyzed statistically by using the data analysis, statistical and process improvement tools; Minitab as the trademark, Analysis of Variance or ANOVA was performed by considering only two-way interaction. ANOVA for the thermal resistance was performed. Firstly, the hypothesis test started with a test of main factors; H₀ and H₁ represented the main factors having no effect and having effects on the thermal resistances, respectively. Then, a test of interaction factors was carried on; H₀ and H₁ represented the interaction factors having no effect and having effects on the thermal resistances, respectively. All ANOVA results for the thermal resistance are exhibited on Table 7. Statistical testers; F-Value or F₀ > F_{0.05}, (1,64) was higher than 4.08 or P-Value was less than the significance level (α) of 0.05. The H₀ was rejected and the H₁ was accepted, the main and interaction factors had effects on the thermal conductivity of the reprocessed samples at the significance level (α) of 0.05 as following;

- 1) The interaction factors; B*D or density (kg/m³) and thickness (mm), and
- 2) The main factor; E or compression pressure (bar).

Table 6. The results of the horizontal flame spread test of the samples

No.	Thick-ness (mm)	T ₁ (s)	T ₂ (s)	T ₃ (s)	Sample Burn Up to Holding Clamp	Cotton indicator ignited
1	12.61	0	0	0	No	No
2	11.02	0	0	1	No	No
3	9.75	0	0	1	No	No
4	9.76	0	0	0	No	No
5	11.50	0	0	0	No	No

* T₁ T₂ and T₃ are the flame spread seconds of the three samples, respectively.

Table 7. Analysis of Variance (ANOVA) results in the thermal resistance investigation

Source	df	SS	MS	F-value (F ₀)	p-value	Note ^d
A	1	0.00428	0.00428	0.86	0.357	
B	1	0.00767	0.00767	1.54	0.219	
C	1	0.01018	0.01018	2.04	0.158	
D	1	1.38055	1.38055	276.96	0.000	Sig.
E	1	0.02217	0.02217	4.45	0.039	Sig.
A*B	1	0.00119	0.00119	0.24	0.626	
A*C	1	0.00529	0.00529	1.06	0.306	
A*D	1	0.00304	0.00304	0.61	0.437	
A*E	1	0.00098	0.00098	0.20	0.658	
B*C	1	0.00056	0.00056	0.11	0.737	
B*D	1	0.02622	0.02622	5.26	0.025	Sig.
B*E	1	0.00067	0.000677	0.14	0.714	
C*D	1	0.00192	0.001921	0.39	0.537	
C*E	1	0.00000	0.000002	0.00	0.986	
D*E	1	0.00546	0.005469	1.10	0.299	
Error	64	0.31901	0.319018			
Total	95	1.90151				

S = 0.0706021 R-Sq = 83.22% R-Sq(adj) = 75.10%
Sig. = Significant

Secondly, Model Adequacy Checking was rendered to investigate suitability and accuracy of the information; error patterns followed the fundamental of $\epsilon_{ij} \sim N(0, \sigma^2)$ by using residual values. This analysis confirmed the accuracy and dependability of the information as shown on Figure 2. From the normal probability plot on Figure 2, the residual distribution was linear. The fitted value of each factor level distributed randomly and ordinarily around the center line, the residual distribution was not a megaphone pattern, this distribution implied that the data had the stability of their deviation and the data was

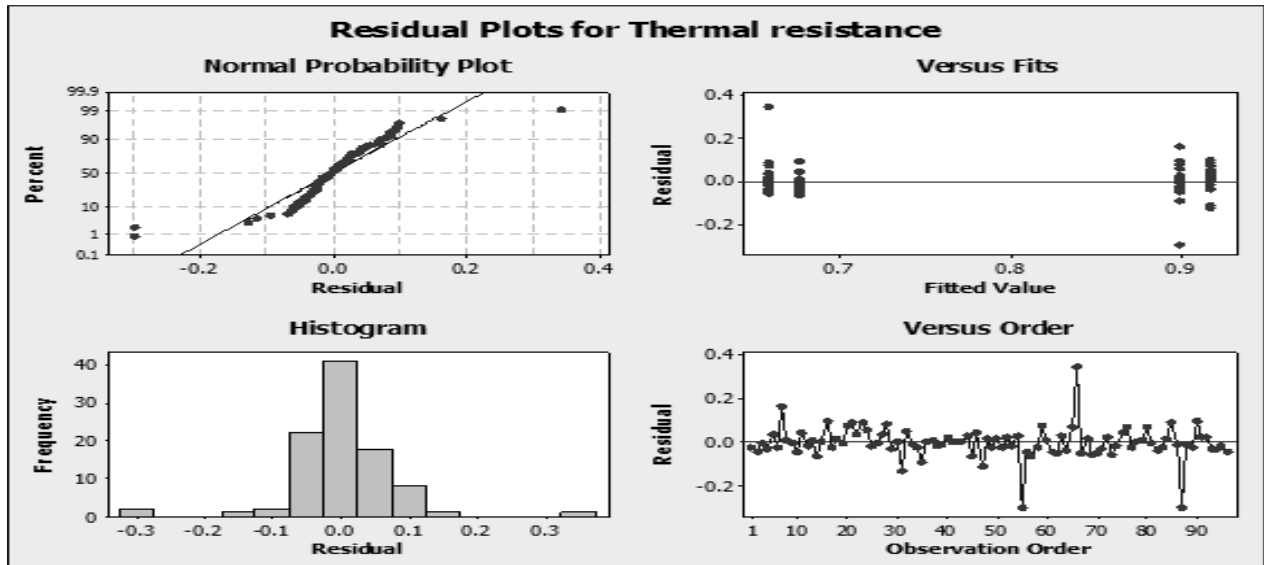


Figure 2. Residual plots in the thermal resistance investigation independent. The residual distribution was not in any trends and patterns, the data were independent and not related to their collecting sequence.

Thirdly, the analysis of the interaction and main factors was performed to find the suitable factor level. From Table 7, the interaction factors; B*D, and the main factor; E, had effects on the thermal resistances. The effect of the interaction factors; B*D, on the thermal resistance (R) was considered primarily as displayed on Figure 3. The high thermal resistance was encountered when the interaction factors; B*D or density was at 96 kg/m³ and thickness was at 25 mm. The high thermal resistance was met when the main factor; E or compression pressure was at 15 bar as shown on Figure 4. Therefore, the suitable factors responding to the thermal resistance and the hot pressed process were as following; the high level (+) of the factor; B or the density at 96 kg/m³, the high level (+) of the factor; D or the thickness at 25 mm, and the high level (+) of the factor; E or the compression pressure at 15 bar. as shown on Figure 4. Therefore, the suitable factors responding to the thermal resistance and the hot pressed process were as following; the high level (+) of the factor; B or the density at 96 kg/m³, the high level (+) of the factor; D or the thickness at 25 mm, and the high level (+) of the factor; E or the compression pressure at 15 bar. These factors could be used as the conditions of the reprocessing process and the highest average thermal resistance was obtained from the 16th condition on Table 8 as 0.98028 K/W.

Table 8. Conditions providing the high thermal resistances of the reprocessed insulators

Conditions	Thermal Resistances			Average
	Numbers of Replicate			
	1	2	3	
8	0.89854	0.94529	0.98804	0.94396
16	1.0172	0.93574	0.9879	0.98028
24	1.0028	0.92499	0.94249	0.95676
32	0.96683	0.88084	0.87746	0.90838

Analysis of Variance for Sound Absorption Coefficient (SAC) and Noise Reduction Coefficient (NRC)

Next, all Sound Absorption Coefficient (SAC) and Noise Reduction Coefficient (NRC) results of 96 reprocessed samples were analyzed statistically by using the same tools, ANOVA. Firstly, the hypothesis test started with a test of main factors; H 0 and H 1 represented the main factors having no effect and having effects on the NRCs, respectively. Then, a test of interaction factors was carried on; H 0 and H 1 represented the interaction factors having no effect and having effects on the NRCs, respectively. All ANOVA results for the Noise Reduction Coefficients (NRCs) are indicated on Table 9. Statistical testers; F-Value or $F_0 > F_{0.05, (1,64)}$ was higher than 4.08 or P-Value was less than the significance level (α) of 0.05. The H 0 was rejected and the H 1 was accepted, the main and interaction factors had effects on the thermal conductivity of the reprocessed samples at the significance level (α) of 0.05 as following; 1) The main factor; B or density (kg/m³), and 2) The main factor; D or thickness (mm).

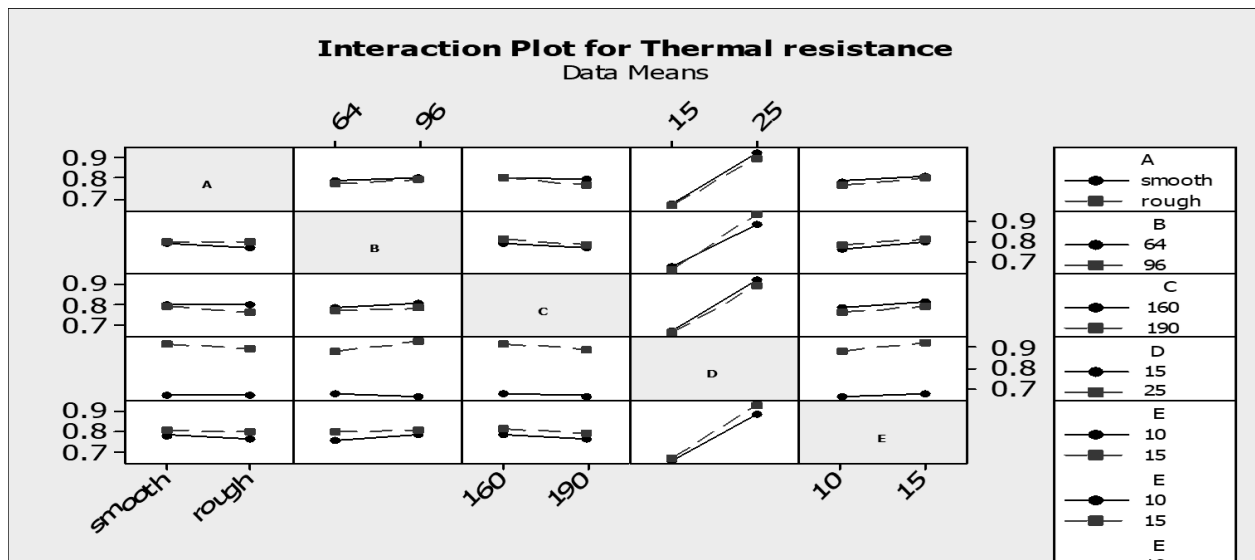


Figure 3. Interaction plots in the thermal resistance investigation

Then, Model Adequacy Checking was rendered to investigate suitability and accuracy of the information; error patterns followed the fundamental of $e_{ij} \sim N(0, \sigma^2)$ by using residual values. This analysis confirmed the accuracy and dependability of the information as shown on Figure 4. From the normal probability plot on Figure 5, the residual distribution was linear. The fitted value of each factor level distributed randomly and ordinarily around the center line, the residual distribution was not a megaphone pattern, this distribution implied that the data had the stability of their deviation and the data was independent. The residual distribution was not in any trends and patterns, the data were independent and not related to their collecting sequence.

Table 9. Analysis of Variance (ANOVA) results in the the Noise Reduction Coefficient (NRC) investigation

Source	df	SS	MS	F-value (F0)	p-value	Not ed
A	1	0.00045	0.0045	1.05	0.315	
B	1	0.00477	0.00477	11.14	0.003	Sig.
C	1	0.000125	0.000125	0.29	0.593	
D	1	0.089860	0.089860	209.81	0.000	Sig.
E	1	0.000503	0.000503	1.18	0.288	
Error	64	0.011136	0.000428			
Total	95	0.106844				

S = 0.0206953 R-Sq = 89.58% R-Sq(adj) = 87.57%
Sig. = Significant

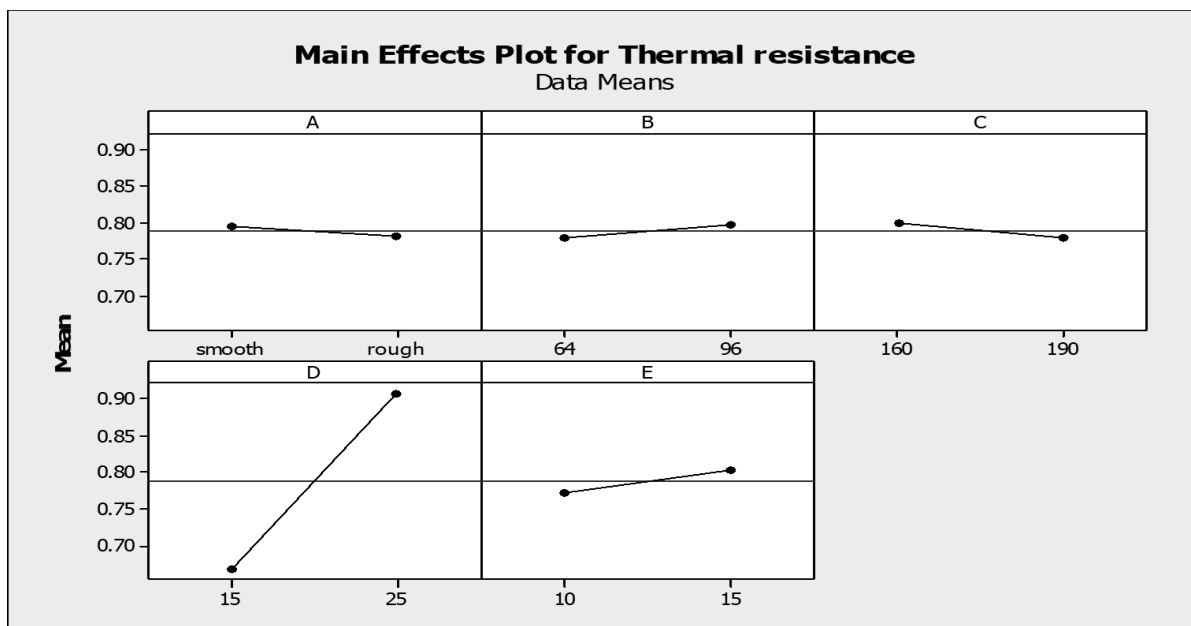


Figure 4. Main effect plots in the thermal resistance investigation

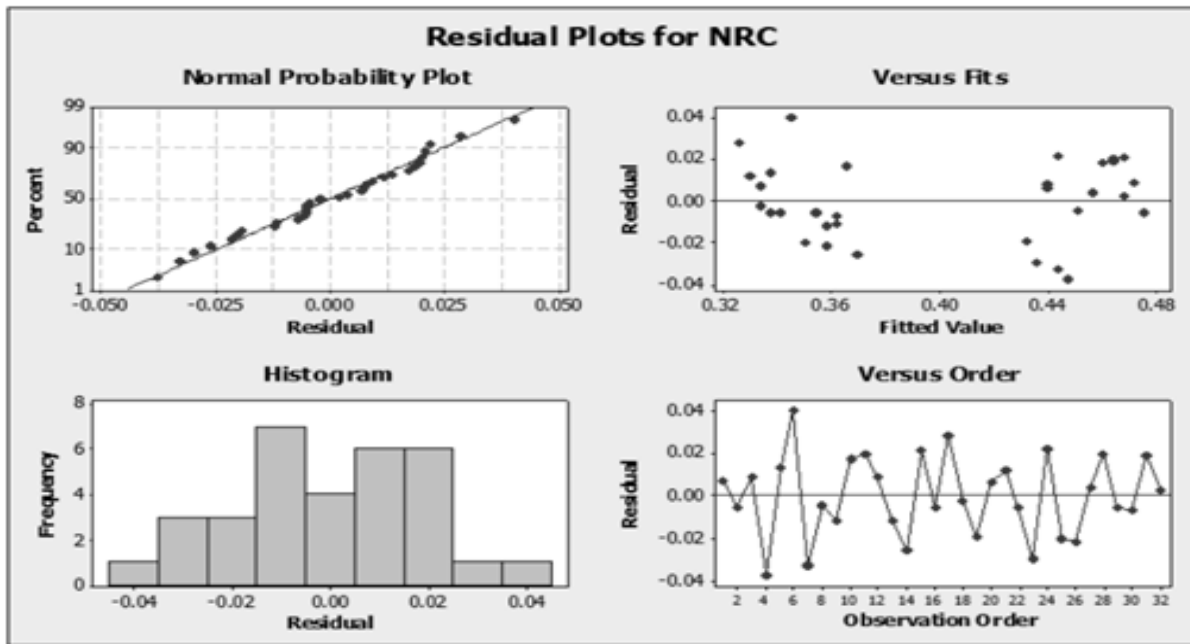


Figure 5. Residual plots in the Noise Reduction Coefficient (NRC) investigation

Finally, the analysis of the main factors was performed to find the suitable factor level. From Table 9, the main factors; B and D, had effects on the NRCs. The effect of the main factors; B and D, on the NRCs was considered primarily as displayed on Figure 6. The highest NRC (good noise reduction) was indicated when the main factors; B or density was at 96 kg/m³ and D or thickness was at 25 mm. Therefore, the suitable factors responding to the NRC and the hot press process were as following; the high level (+) of the factor; B or the density at 96 kg/m³ and the high level (+) of the factor; D or the thickness at 25 mm. These factors could be used as the conditions of the reprocessing process and the highest average NRC was obtained from the 15th condition on Table 10 as 0.48881. Materials having NRCs above 0.4 can be considered as highly absorptive materials or acoustic, for an example, NRC values of materials used in offices and dwellings are in the range

of 0.4 to 0.6 (Cowan, 1994). The acoustic property of the reprocessed sample related to the density and the thickness of the sample. Both surface roughness did not affect the NRCs notably, their NRCs were close, the average NRC of the rough surface sample. The Sound Absorption smooth surface sample was a little bit higher than that of the rough surface sample. The Sound Absorption Coefficient or SAC varied in proportion to frequency levels; 125, 250, 500, 1,000, 2,000 and 4,000 Hz, respectively. NRC is the average of the SAC. Therefore, better acoustic materials have higher SACs as presented on Figures 7 and 8.

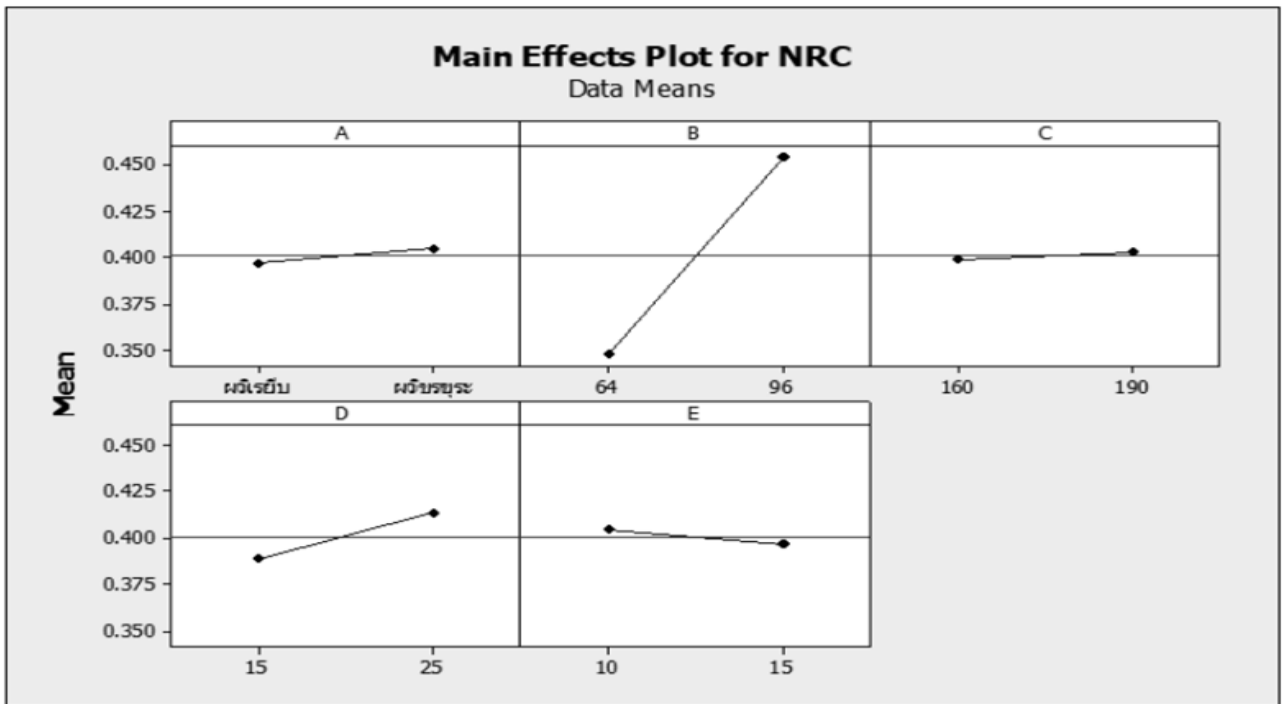
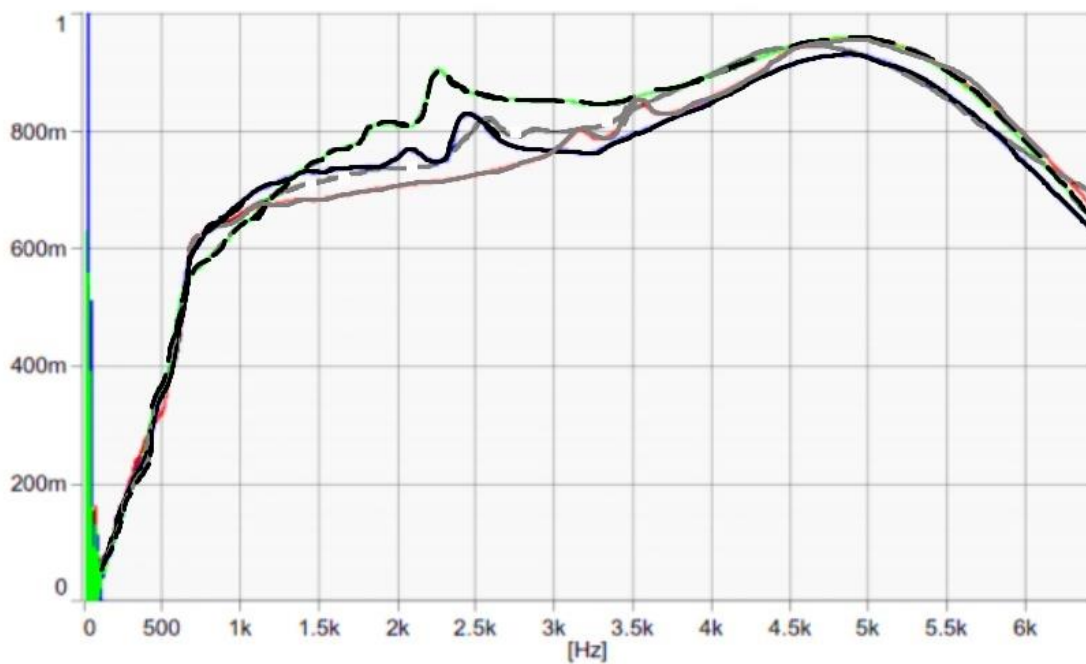


Figure 6. Main effect plots in the Noise Reduction Coefficient (NRC) investigation

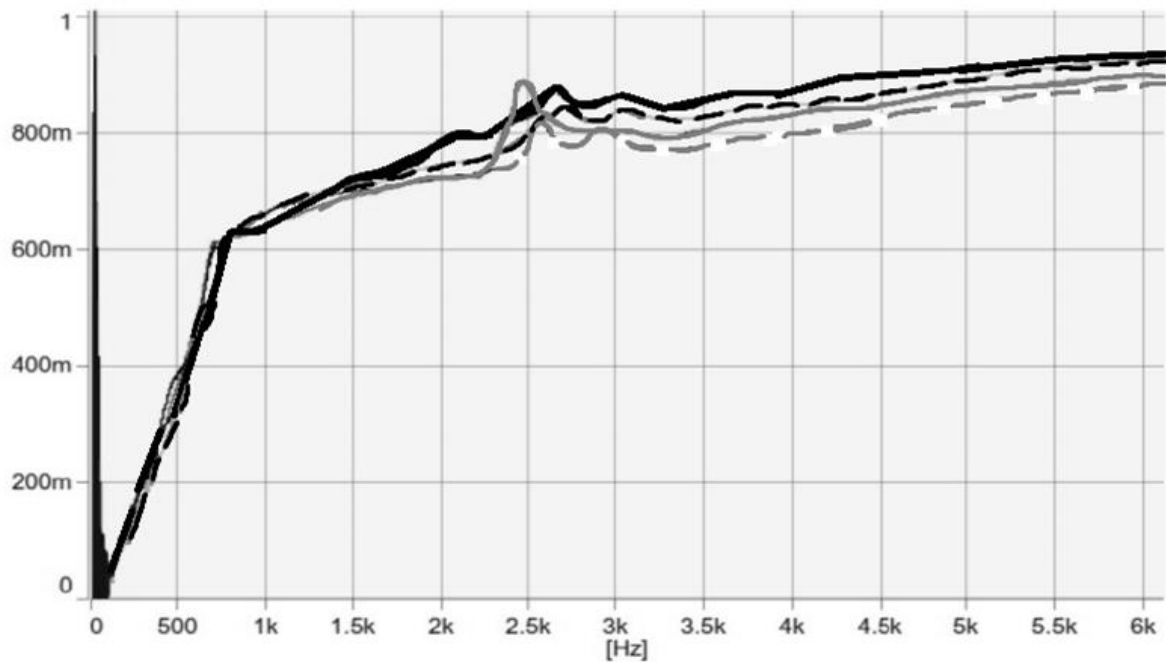
Sound absorption coefficient (SAC)



Remark: Conditions; (black solid line) 96 g, 25 mm, 10 MPa, 160°C and smooth surface, (grey solid line) 96 g, 25 mm, 10 MPa, 160°C and rough surface, (black dash line) 96 g, 25 mm, 10 MPa, 190°C and smooth surface, (grey dash line) 96 g, 25 mm, 10 MPa, 190°C and rough surface.

Figure 7. Sound Absorption Coefficient (SAC) plots of the samples prepared at 10 MPa

Sound absorption coefficient (SAC)



Remark: Conditions; (black solid line) 96 g, 25 mm, 15 MPa, 160°C and smooth surface, (grey solid line) 96 g, 25 mm, 15 MPa, 160°C and rough surface, (black dash line) 96 g, 25 mm, 15 MPa, 190°C and smooth surface, (grey dash line) 96 g, 25 mm, 15 MPa, 190°C and rough surface.

Figure 8. Sound Absorption Coefficient (SAC) plots of the samples prepared at 15 MPa

The Cost Analysis and Product Comparison

Glass wool market survey was carried on to analyze and specify market feasibility of the reprocessed glass-wool board by using marketing mix or 4Ps; product, price, place and promotion. The product is an analysis and formulating strategy related to products or services. The price analyzes and determines the pricing strategy of the product from the customer's point of view, including comparisons with competitors. The place analyzes and defines shipping strategy, by adhering to the principles of efficiency, accuracy, safety and speed. The promotion is an analysis and formulating strategy that will boost the sales of the product. The information of the reprocessed glass wool board or the product is detailed on Table 11. The NRCs of different materials are compared on Table 12. The reprocessed board price was the same or a little lower than market prices. Since the reprocessed board was made from glass wool waste from vehicle industries, the reprocessed board properties were lower than the properties of the original glass wool boards. But the thermal resistance and NRC properties of the reprocessed board were well accepted. Board manufacturer interviews were conducted and expenses of the glass wool waste transportation and disposal had to be taken into the cost analysis, the cost tended to be lower than new glass wool boards in Thai markets. The certain cost could not be specified because this research was in the pilot plant stage.

Product distribution places could be divided into 2 ways; 1) the indirect-way in 2 levels (from manufacturers to wholesalers, retailers and customers, respectively, and 2)

the direct-way from manufacturers to customers (customers may include absorptive manufacture industries and acoustic users). Since the reprocessed board can be considered as a waste-to-recycle product, promotional guidelines may emphasize acoustic users, green and recycle product users. This board can be raw materials for other acoustic composite boards. The reprocessed-board manufacturers may seek for commercial partners such as small acoustic businesses to develop the board quality and their own products or startup businesses. The startup businesses can make the reprocessed board widely known faster. Middleman promotions may play a role because they are professional, they know markets and customers trust their new product offers. If the reprocessed board is used as the raw material in the insulator and acoustic industries, the manufacturers fully develop their products by increasing the reprocessed board qualities and properties to meet their product standards and goals. The thermal resistances of three different boards were compared as shown on Table 13. These three boards were not covered with any layers. The first board was the reprocessed board from this work, the second was the board waste or the reprocessing raw material and the last board was the commercial insulation board. The lowest density was provided by the new commercial one while the reprocessing one provided the higher thermal resistance; 20.69% higher. As compared on the table, the reprocessed board could provide the competitive thermal resistance.

Table 10. Conditions providing the high Sound Absorption Coefficients of the reprocessed insulators

Coddition	Factors					Noise Reduction Coefficient
	A	B	C	D	E	
7	Smooth	96	160	25	10	0.48331
8	Smooth	96	160	25	15	0.48071
15	Smooth	96	190	25	15	0.48881
16	Smooth	96	190	25	15	0.47035
23	Rough	96	160	25	15	0.46025
24	Rough	96	160	25	15	0.48424
31	Rough	96	190	25	10	0.47905
32	Rough	96	190	25	15	0.47035

Table 11. Prices of the sound absorbing materials in Thai market

Product Name	Size (MxM)	NRC	Price
acoustic wall panels CYLENCE ZofTone	0.60 × 0.60 0.60 × 1.20	0.69 – 0.98	240 – 440 Bath per Sheet
acoustic ceiling CYLENCE Wondary	0.60 × 0.60	0.70	655 – 754 Bath per m ³
acoustic decorative wall CYLENCE Zandera	0.60 × 0.60 0.60 × 1.20	0.75	645 – 1715 Bath per Sheet
Reprocessed insulator (from Glass wool waste)	0.175 × 0.175	0.46 – 0.49	N/A*

* No selling price for a prototype product

Table 12. Sound Absorption Coefficients of General Building Materials (Owens Corning, 2004)

Materials	Frequency (Hz)					NRC
	250	500	1000	2000	4000	
Brick	0.03	0.03	0.04	0.05	0.07	0.05
Carpet	0.05	0.10	0.20	0.30	0.40	0.15
Concrete Block	0.44	0.31	0.29	0.29	0.25	0.35
Fabrics	0.04	0.11	0.17	0.24	0.35	0.15
Glass	0.03	0.02	0.02	0.03	0.02	0.05
Gypsum Board	0.08	0.05	0.03	0.03	0.03	0.05
Hardwood	0.22	0.07	0.04	0.03	0.07	0.10
Reprocessed insulator (from Glass wool waste)	0.15	0.35	0.63	0.80	0.48	0.48

Table 13. Thermal resistance values of three samples; the reprocessed board (1), the board waste (2) and the commercial insulation board (3)

Numbers	Thickness	Density	R (m ² W/m)
1	25	96	0.9879
2	37	64	0.0630
3	25	48	0.7810

Since the pressure, density and thickness of the reprocessed board were the interaction factors playing important roles on the board thermal resistance and

Noise Reduction Coefficient (NRC) while both board surfaces; smooth and rough, were not significant, the thermal resistance and NRC correlations were proposed according to the significant factors as following;

$$R = 0.158 + (0.00359 \text{ Density}) + (0.0368 \text{ Thickness}) - (0.00267 \text{ Pressure}) + (0.00022 \text{ Density} \times \text{Thickness}) \quad (2)$$

$$NRC = 0.3258 + (0.000563 \text{ Density}) + (0.00855 \text{ Thickness}) + (0.00150 \text{ Pressure}) + (0.000137 \text{ Density} \times \text{Thickness}) \quad (3)$$

The correlations are applicable for the range of the reprocessed-insulator density, thickness and compression pressure from 64 to 96 kg/m³, from 15 to 25 mm and from 10 to 15 bar, respectively. These correlations can help the manufacturers and users to predict the thermal resistances and Noise Reduction Coefficients of the recycled insulators in the forms of the significant factors. The manufacturers and users can also select these properties according to their desired thermal resistance and Noise Reduction Coefficient values.

CONCLUSION

Vehicle industries have to set budget to transport and dispose insulator waste from vehicle assembly processes. Glass wool is about 85% to 95% of the insulator waste; the main component of the insulator waste. This component, glass wool waste, was focused in this research as a raw material for the reprocessed insulator. A target insulator must provide thermal conductivity less than 0.031 W/m K and Noise Reduction Coefficient (NRC) more than 0.4. Analysis of Variance (ANOVA) was applied to find factors which responded to thermal resistances (R) and NRCs of the reprocessed specimens. Two levels of five factors were analyzed by ANOVA full factorial method. Five factors combined of reprocessing temperatures and pressures, density, thickness, and surface roughness values of reprocessed insulators. The total of 96 final reprocessed specimens were evaluated for their thermal resistances and NRCs. The analysis showed that density and thickness played an important role to the thermal resistance and NRC, the highest thermal resistance was 0.98028 m² K/W and the highest NRC was 0.48881. The R and NRC satisfied with the insulator properties. These factors were investigated from the reprocessing process in 0.2 m width and 0.2 m length molds. Results of this current research are applicable and useful in fabricating the reprocessed waste boards which can be used in building works. The reprocessed boards provide the same NRC as that of an open cell foam board. Moreover, the reprocessed boards could absorb noise better than concrete, wood and glass. The reprocessed boards are good insulators made from waste. However, the glass-wool-waste insulator have to be developed for better

NRC and thermal resistance properties. The insulator manufacturers that aim to reduce glass wool waste and desire to add values to the waste can take advantages from the research results. The reprocessed insulator can be considered as the better product for the better life quality in the sustainable society of our world.

ACKNOWLEDGEMENTS

This research was supported in part by the Graduate Program Scholarship from The Graduate School, Kasetsart University. This research was also financially supported by the Office of the Ministry of Higher Education, Science, Research and Innovation; and the Thailand Science Research and Innovation through the Kasetsart University Reinventing University Program 2021, as well as the research funding supported by Faculty of Science and Engineering, Kasetsart University, Chalermphrakiat Sakon Nakhon Province Campus.

REFERENCES

- Ayuttaya P., 2007, *Design and Analysis of Experiments*, TOP Publishing Company, Bangkok, Thailand.
- Choowonglert M. and Takkanon P., 2015, Sound Absorbing Sheets from Used Paper in the Office, *Proc. of 53th Kasetsart University Annual Conference*, Bangkok, 625-631.
- Cowan J., 1994, *Handbook of Environmental Acoustics*, Van Nostrand Reinhold, New York, USA.
- Homaswin K., Sangsupata S. and Intrachooto S., 2007, Para-Rubber and Coconut Fiber Integrated Acoustic Panels, *Proc. of 45th Kasetsart University Annual Conference*, Bangkok, 235-244.
- Jeon C., Lee J., Chung H., Kim J. and Park J., 2017, A Study on Insulation Characteristics of Glass Wool and Mineral Wool Coated with a Polysiloxane Agent, *Advance in Meterials Science and Engineering*, 2017(3938965), 1-6.
- Narakaew P. and Narakaew S., 2015, *The Efficiency of the Wall for Noise and Smell Adsorptions from Rice Straw Blended with Corncob Based Activated Carbon*, Research Report, Lampang Rajabhat University, Lampang, Thailand.
- Owens Corning™, 2004, *Noise Control Design Guide*, United Artists Corporate, Ohio, USA.
- Pakunworakij T., Puthipiroj P., Oonjittichai W. and Tisavipat P., 2006, Thermal Resistance Efficiency of Building Insulation Material from Agricultural Waste, *Journal of Architectural/Planning Research and Studies*, 4, 3-13.
- Wajima T. and Matsuka S., 2019, A New Recycling Process of Waste Glass Wool Using Pyrolysis with Sodium Hydroxide, *International Journal of Chemical Engineering and Applications*, 10(3), 75-79.
- Yodkaew R., Sangsupata S. and Intrachooto S., 2007, Sound Absorption of an Interior Ceiling Material from Chaff, *Proc. of 44th Kasetsart University Annual Conference*, Bangkok, 217-225.
- Zhao C., Liu Y., Ren S. and Zhang Y., 2018, Life Cycle Assessment of Typical Glass Wool Production in China, *Materials Science Forum*, 913, 998-1003.



HİMMETOĞLU VE SEYİTÖMER BİTÜMLÜ ŞEYLLERİ İLE PLASTİK ŞEHİR ATIKLARININ KABARCIKLI AKIŞKAN YATAKLI REAKTÖRDE GAZLAŞTIRILMASI

Duygu UYSAL*, Hazal ÖZTAN**, Ahmed Abdullah GAFUR*** ve Özkan Murat DOĞAN****

Gazi Üniversitesi, Mühendislik Fakültesi, Kimya Mühendisliği Bölümü, 06570 Maltepe, Ankara

* duysal@gazi.edu.tr, ORCID:0000-0002-8963-6026

** hazaloztan@gazi.edu.tr, ORCID: 0000-0003-1456-7238

*** ahmet0516@yahoo.com

**** mdogan@gazi.edu.tr, ORCID: 0000-0003-3801-3141

(Geliş Tarihi: 09.03.2022, Kabul Tarihi: 07.10.2022)

Özet: Artan plastik kullanımı ve kullanılan plastiklerin bir süre sonra atık olarak birikmesi günümüzün başlıca sorunlarından. Atık plastiklerin yeniden değerlendirilmesi için termokimyasal dönüşüm prosesleri oldukça verimlidir. Atık plastiklerin tek başına ve çeşitli yerli kömürler ile birlikte gazlaştırılması sayesinde yakıt olarak kullanıma uygun CO, CH₄ ve bir enerji taşıyıcısı olan H₂ içeren sentez gazı üretimi mümkündür. Bu amaçla yapılan çalışmada, Himmetoğlu ve Seyitömer bitümlü şeylleri ile plastik atık karışımı (%56 polietilen, %28 polipropilen ve %16 polistiren) gazlaştırılmıştır. Deneysel çalışmalar, 4 cm iç çapında ve 110 cm boyundaki kuvars camdan imal edilen laboratuvar ölçekli akışkan yataklı sistemde gerçekleştirilmiş olup akışkanlaştırıcı gaz olarak hava ve gazlaştırıcı akışkan olarak da su buharı kullanılmıştır. Sıcaklığın (750°C, 800°C, 850°C), su buharı akış hızının (5-10-15 g/dak) ve beslemedeki plastik oranının (%40 ve %70) sentez gazındaki H₂ ve CH₄ konsantrasyonuna etkileri incelenmiştir. 5-10 g/dak akış hızındaki su buharı kullanımı Himmetoğlu bitümlü şeylinin ve karışımlarının gazlaştırılması için uygundur. Seyitömer bitümlü şeyli ve karışımlarının gazlaştırılmasında ise 10-15 g/dak olacak şekilde daha yüksek akış hızlarının uygun olduğu görülmüştür. Himmetoğlu ve Seyitömer bitümlü şeyllere %40 ve %70 oranında plastik atık karıştırıldığında üretilen sentez gazındaki H₂ konsantrasyonu azalırken CH₄ konsantrasyonu artmıştır. Çalışma sonucunda, en yüksek H₂ konsantrasyonu %21,33 (750°C - 10 g/dak- %60 Himmetoğlu bitümlü şeyli ve %40 plastik beslemesi) ve en yüksek CH₄ konsantrasyonu ise %74,71 (850°C - 10 g/dak- %30 Himmetoğlu bitümlü şeyli-%70 plastik atık) olarak elde edilmiştir. Üretilmesi planlanan sentez gazının kullanım alanına göre sıcaklık, su buharı akış hızı ve besleme karışım oranı değiştirilerek uygun çalışma koşulları belirlenebilir.

Anahtar Kelimeler: Bitümlü şeyl, Plastik atık, Akışkan yatak, Gazlaştıma, Hidrojen

GASIFICATION OF HIMMETOĞLU AND SEYITOMER OIL SHALES WITH PLASTIC CITY WASTES IN A BUBBLING FLUIDIZED BED REACTOR

Abstract: Increasing use of plastics and accumulation of used plastics as waste after a while are the main problems of today. Thermochemical conversion processes are highly efficient for recycling waste plastics. With the gasification of waste plastics alone and with various local coals, it is possible to produce syngas containing H₂, as an energy carrier, with CO and CH₄ suitable for use as fuel. In this study, Himmetoğlu and Seyitömer bituminous shales and plastic waste mixture (56% polyethylene, 28% polypropylene, and 16% polystyrene) were gasified. Experimental studies were carried out in a laboratory-scale fluidized bed system made of quartz glass with an inner diameter of 4 cm and a length of 110 cm, and the air was used as a fluidizing gas and water vapor was used as a gasifier agent. The effects of temperature (750 °C, 800 °C, 850 °C), water vapor flow rate (5-10-15 g / min), and plastic in the feed (40% and 70%) on the concentration of H₂ and CH₄ in the syngas were investigated. When the gasification results were examined, the use of steam with a flow rate of 5-10 g/min is suitable for the gasification of Himmetoğlu bituminous shale and its

mixtures. In the gasification of Seyitömer bituminous shale and mixtures, it was determined that higher flow rates of 10-15 g min should be preferred. When 40% and 70% plastic waste was mixed into Himmetoğlu and Seyitömer bituminous shales, the concentration of H₂ in the syngas decreased while the concentration of CH₄ increased. As a result of the study, the highest H₂ concentration was obtained as 21.33% (750 °C - 10 g / min- 60% Himmetoğlu bituminous shale - 40% plastic waste) and the highest CH₄ concentration was obtained as 74.71% (850°C- 10 g / min- 30% Himmetoğlu bituminous shale- 70% plastic waste). Suitable operating conditions can be determined by changing temperature, steam flow rate, and feed mixture ratio according to the usage area of the syngas planned to be produced.

Keywords: Oil shale, Plastic waste, Fluidized bed, Gasification, Hydrogen

SEMBOLLER

HM	Himmetoğlu bitümlü şisti
SYT	Seyitömer bitümlü şisti
U	Boş kolon hızı [m/s]
U _{mf}	Minimum akışkanlaşma hızı [m/s]

GİRİŞ

Küresel enerji tüketimi, artan insan nüfusu ve gelişen endüstriden dolayı hızla artmaktadır. Enerji tüketiminin olduğu başlıca alanlar endüstri, ulaşım ve konut içeriklidir. Uluslararası Enerji Ajansı (IEA) 2021 verilerine göre sektör bazlı enerji tüketimi endüstride 2339,3 Mtoe, ulaşımda 2890,9 Mtoe ve konutta 2109,2 Mtoe olmuştur (IEA, 2021). Kaynak bazlı enerji tüketiminde ise ilk üç sırada kömür, petrol ve doğal gaz olmak üzere fosil yakıtların yer aldığı bildirilmiştir. Giderek artan enerji ihtiyacını karşılamada fosil yakıtların kullanımı rezervlerin planlanandan daha hızlı tükenmesine yol açmış ve sera gazı olarak bilinen CO₂ emisyonlarının endişe verici düzeylere gelmesinde birinci sırada rol oynamıştır. Türkiye Kömür İşletmeleri'nin (TKİ) 2019 yılı Kömür Sektör Raporu'na göre dünya fosil yakıt kaynaklarından kömür 119 yıl, petrol 47 yıl ve doğal gaz 60 yıllık bir rezerve sahiptir (TKİ, 2019).

Enerji üretimindeki fosil yakıt rezervi ve emisyon sorunlarının yanı sıra hızlı endüstriyel üretim ve tüketim sonucu çeşitli atık sınıfındaki malzemelerin doğada birikimi de sürdürülebilir yeşil ekonominin başlıca bir sorunu hâline gelmiştir (Adami ve Schiavon, 2021; Lopez vd, 2018; Aguilar- Hernandez vd, 2019). Atık sınıfındaki malzemelerden en önemlisi günümüzde atık plastiklerdir. Plastikler modern yaşamın en temel destek malzemesi hâline gelmiş durumdadır. Düşük üretim maliyetine, çok geniş kullanım alanına ve farklı özelliklere sahip olmaları diğer malzemelerin yerini almalarını sağlamıştır (Wong vd, 2015). Plastik malzemelerin üretiminin ve tüketiminin hızla artmasına bağlı olarak günümüzde geri dönüşüm için çok fazla çaba sarf edilmesi gerektiği de açıktır. Doğada uzun süre bozunmamaları sebebiyle büyük bir çevre problemi

haline gelmiş durumdadırlar (Lopez vd, 2018). Lopez vd. 2018'nin çalışmasında belirtildiği üzere 2015 yılında dünyada 322 milyon ton plastik üretimi gerçekleşmiştir ancak 275 milyon ton plastiğin ise karasal alanda kontrolsüz şekilde yayılmış atık olarak kaldığı belirtilmiştir (Jambeck vd, 2015). Atık plastikler büyük bir çevre sorunu yaratmalarına karşın aslında karbon içerikli malzemeler olmaları nedeniyle ciddi bir karbon kaynağının da kaybı olarak görülmelidir.

Küresel enerji krizleri ve artan insan nüfusu, yerli enerji kaynaklarına sahip olunamaması, fosil yakıt rezervlerinin azalan ömürleri, geleneksel enerji üretim sistemlerinin emisyon sorunları ve buna bağlı olarak küresel ısınma, artan atık ve bunların depolama sorunları gibi günümüzün en temel sorunları araştırmaları daha sürdürülebilir, daha temiz ve daha çevre dostu enerji kaynağı arayışına yöneltmiştir. Önemli bir enerji taşıyıcısı olması nedeniyle günümüzde H₂ gazı yeşil ekonominin büyük bir parçası hâline gelmiş durumdadır (Dinçer ve Zamfirescu, 2014). Pek çok enerji kaynağından üretilebilir olma, kullanıldığında sera gazı emisyonu yapmaması, sıvı ya da gaz olarak depolanabilmesi, sıkıştırıldığında pillere kıyasla daha fazla enerji yoğunluğuna sahip olması gibi birçok olumlu özelliği yakıt olarak kullanılabilmesinin önünü açan özellikler olmuştur (Australian Hydrogen Council, 2021).

H₂ gazı, pek çok kaynaktan çeşitli prosesler yardımı ile üretilebilmektedir (Dinçer ve Zamfirescu, 2014). Bu proseslerden günümüzde endüstriyel olarak hali hazırda uygulanabilir olanı gazlaştırma prosesleridir (Cocco vd, 2014; Geldart, 1986; Kunii ve Levenspiel, 1991; Grace, 2020). Temelde kömür gazlaştırması ile sentez gazı üretimi yapılmakta ve daha sonrasında sentez gazı bileşeni olan H₂, PSA sistemlerinde saflaştırılarak yakıt hücrelerinde kullanıma sunulmaktadır (Du vd, 2021). Saf H₂ eldesinin yanında sentez gazının hammadde olarak kullanımı da metanol, sentetik doğal gaz, dimetil eter ve amonyak gibi değerli kimyasalların üretilmesinde önemli bir uygulamadır (Kovac vd, 2021; Chaudhari vd, 2001; Labochyov vd, 1998; Hamelinck vd, 2004; Canbaz ve

Gür, 2020). Plastik atıkların yeniden değerlendirilmesinde içerdikleri yüksek kalorifik değerden dolayı yakma prosesleri akla gelen ilk dönüşüm süreci olsa da plastik atıkların yakılması yerine değerli kimyasallara dönüştürülmesi için gazlaştırma prosesleri ön plandadır (Moya vd, 2017; Benim ve Kuppa, 2016). Özellikle plastik atıkların en iyi değerlendirme yollarından biri kömür ile birlikte gazlaştırılmasıdır (Straka ve Bicakova, 2014). Birlikte gazlaştırma işlemi hem atık yönetimine hem de fosil yakıt tüketiminin bir miktar da olsa önüne geçilmesine yardımcı olmaktadır (Emami-Taba vd, 2013). Gazlaştırma teknolojisi özellikle akışkan yataklı sistemlerde yüksek dönüşüm verimi ile düşük karbon içeriğine sahip atıkların bile kolayca dönüştürülebilmesine olanak verdiğinden atık plastiklerin yanı sıra düşük kalitedeki kömürlerin de verimli kullanımına son derece uygundur (Basu, 2006; Basu, 2010; Emami-Taba vd, 2012; Ramos vd, 2018; Pinto vd, 2009; NETL, 2021)

Ülkemiz yüksek kalitedeki kömürlerden çok genç kömürler olan linyit ve bitümlü şeyller açısından daha zengin bir yapıya sahiptir (TKİ, 2010). Bitümlü şeyller, kerojen adı verilen organik madde içeren sedimanter kayalardır ve kömüre benzer yapıdadırlar. İstıldıklarında petrol ve gaz üretebildikleri için önemli bir fosil yakıt kaynağı olarak görülmektedirler (Öztürk, 2020). Ülkemizde Kütahya/Seyitömer ve Bolu/Himmetoğlu sahaları önemli bitümlü şeyll sahalarımızdır. Himmetoğlu bitümlü şeyli (HM) üst ısıl değeri 4992 kcal/kg ve Seyitömer bitümlü şeyli (SYT) üst ısıl değeri ise 847 kcal/kg olup kül içerikleri yüksek kaynaklardır (Toraman ve Uçurum, 2009).

Bu çalışma kapsamında, plastik şehir atıklarını yerli fosil kaynaklar olan Himmetoğlu (HM) ve Seyitömer (SYT) bitümü şeylleri ile birlikte akışkan yatakta gazlaştırarak hidrojen zengin sentez gazı üretimi amaçlanmıştır. Deneysel çalışmalar, laboratuvar ölçekli akışkan yataklı gazlaştırma sisteminde gerçekleştirilmiştir. Sıcaklığın, su buharı akış hızının ve besleme karışımındaki plastik oranının sentez gazı bileşimine etkileri araştırılmıştır. Sentez gazı bileşimindeki H₂, CO, CO₂ ve CH₄ konsantrasyonları incelenmiştir. H₂ ve CH₄ üretimi için gerekli optimum işletme koşulları ve birlikte gazlaşma davranışı çalışma sonucunda belirlenmiştir. Belirlenen amaç doğrultusunda, yerli kaynakların ve verimli gazlaştırma sistemlerinin kullanımı ile atıkların katma değer ürünlere dönüştürülmesi teşvik edilmiştir.

MATERYAL VE METOT

Yapılan çalışmada, Himmetoğlu bitümlü şeyli, Seyitömer bitümlü şeyli ve plastik şehir atığı (%56 polietilen- %28 polipropilen-%16 polistiren) kullanılmıştır. Bitümlü şeyllere ait kaba ve elementel analiz sonuçları Tablo 1 ve 2'de verilmiştir.

Tablo 1. Bitümlü şeyllere ait kaba analiz sonuçları

%	Himmetoğlu bitümlü şeyli	Seyitömer bitümlü şeyli
Nem	6,65	4,64
Kül	14,68	42,20
Uçucu madde	59,81	49,93
Sabit karbon	18,86	3,23

Tablo 2. Bitümlü şeyllere ait elementel analiz sonuçları

%	Himmetoğlu bitümlü şeyli	Seyitömer bitümlü şeyli
C	61,35	43,47
H	7,06	6,58
N	1,44	1,08
O	12,91	15,62
S	4,44	3,57
Kül	12,80	29,68

Akışkan Yataklı Gazlaştırma Sistemi

Gazlaştırma deneyleri laboratuvar ölçekli akışkan yataklı sistemde (7) gerçekleştirilmiştir (Şekil 1). Yatak kuvars camdan imal edilmiş olup yatak iç çapı 4 cm ve boyu 110 cm uzunluğundadır. Gazlaştırıcı akışkan olarak su buharı beslemesi, 100°C'de (1 atm) 45 kg/saat buhar besleyebilen buhar jeneratörü (4) ile yapılmıştır. Su buharı akış hızı 5-10-15 g/dak olacak şekilde bir yıkama şişesinin (5) yardımı ile ayarlanmıştır. Yıkama şişesinde yoğunlaşan buhar miktarı birim zamanda ölçülmüş, en az üç ölçüm yapılmış ve ortalaması alınarak sabit akış hızında olmak üzere plastik boru hattı (6) ile yatağa gönderilmiştir. Yatak malzemesi olarak 0,6 mm partikül çaplı silika kum tercih edilmiştir. Yatak malzemesi (silika kum) yoğunluk değeri deneysel olarak 2235 kg/m³ olarak belirlenmiştir. Yataktaki akışkanlaşma sabit 0,47 m/s hızında hava ile sağlanmıştır ($U/U_{mf} = 2$). Yatağa hava beslemesi, ortamdaki (1) havayı alıp ön ısıtıcıya ve yatağa gönderen bir kompresör (2) ile yapılmıştır. Hava, buhar jeneratöründen gelen ikinci bir hat ile ön ısıtıcıda (3) ısıtılarak yatağa beslenmiştir. Yatakta homojen gaz dağılımı sağlanması için delikli plaka kullanılmıştır.

Gazlaştırma için gerekli enerji elektrikli bir fırın (8) tarafından sağlanmış ve ısılı çift (11) ile yatak içindeki sıcaklık kontrol edilmiştir. Gazlaştırılacak hammaddeler yatağın üst kısmında yer alan bunkere (10) doldurulmuş ve bir vidalı besleyici (9) ile yatağa beslenmiştir. Yataktan çıkan gaz soğutma kolonunda (12) soğutulmuş ve soğuyan gazdan numune şişesine (13) bir miktar gaz alınmıştır.

Deneylerde sıcaklığın, su buharı akış hızının ve farklı karışım oranlarının sentez gazı bileşimine etkisi incelenmiştir. Gazlaştırma sıcaklıkları 750°C, 800°C ve 850°C olarak ve su buharı akış hızı 5, 10, 15 g/dak olacak şekilde ayarlanmıştır. Gazlaştırılacak hammaddeler farklı kütsel oranlarda %100 HM, %60 HM- %40 plastik atık, %30 HM- %70 plastik atık, %100 SYT, %60 SYT- %40 plastik atık, %30 SYT-%70 plastik atık ve %100 plastik atık (%56 polietilen, %28 polipropilen, %16 polistiren karışımı) olarak hazırlanmıştır. Her bir karışım üç farklı sıcaklıkta (akış hızı sabit tutulup) ve üç farklı akış hızında (sıcaklık sabit tutulup) gazlaştırılarak 63 adet deney gerçekleştirilmiştir.

Deneye başlarken yatağın istenen sıcaklığa gelmesi için sıcaklık kontrol cihazı çalıştırılmış ve sıcaklık ayarlanmıştır. Yatağın istenen sıcaklığa gelmesi için beklenirken buhar jeneratörü de çalıştırılarak kazan basıncının artması beklenmiştir. Basıncı artan jeneratörde bypass kolu açılarak akış sağlanmış ve yıkama şişesine gönderilen buharın (birinci hat) akış hızı ayarlanmıştır. Buhar jeneratöründen çıkan ikinci hat ön ısıtıcıya gönderilmiş ve kompresörden gelen havanın ısıtılması sağlanmıştır böylece ilk hattan gelen buhar beslemesinin yatak girişinde yoğunlaşması önlenmiştir.

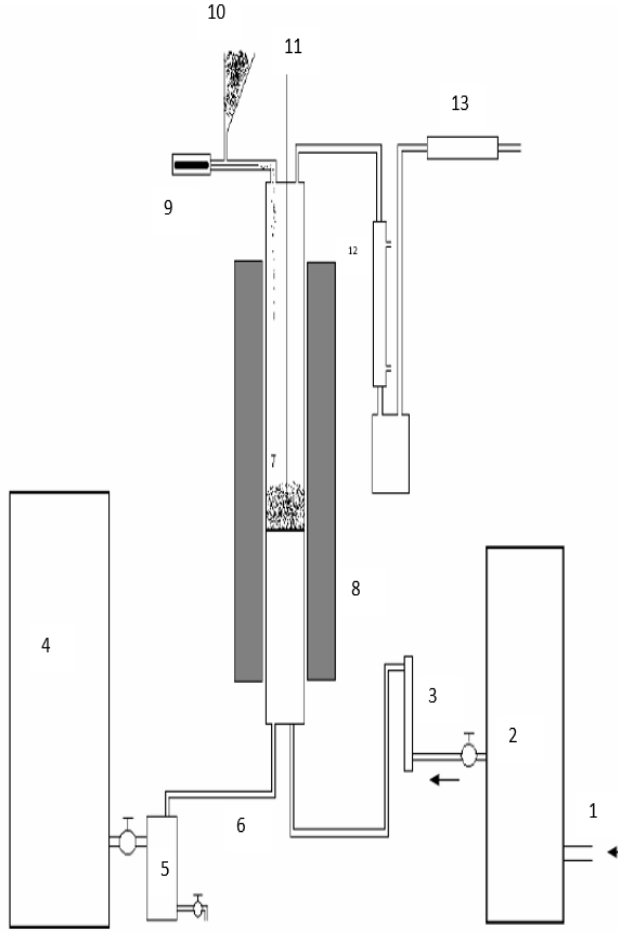
Isınan hava ve birinci hattan gelen buhar, yan yana yatağın alt bölgesinden beslenmiştir. Yatak istenen sıcaklığa geldiğinde bunkere doldurulan hammadde vidalı besleyici ile üstten beslenmiştir. Elde edilen ürün gazı, yatağın üst kısmından geçip soğutma kolonuna girerek hem soğutulmuş hem de içinde buhar mevcutsa yoğunlaştırılıp tutulmuştur. Soğutucudan geçen gaz, numune şişesine alınmıştır. Gaz analizleri SRI 310 TCD model gaz kromatografi cihazında gerçekleştirilmiştir. Numune şişesinden 0,5 ml numune şırınga ile çekilip cihaza basılmış, analiz sonuçları kaydedilmiştir. Deneyler her sıcaklık ve her akış hızı için tekrarlanmıştır.

Yatak Hidrodinamiği

Gazlaştırıcı içinde yatak sıcaklığının homojen tutulması, yatak içi karışımın çok iyi sağlanması ve gaz-katı

arasındaki hem kütle hem de ısı transferinin en iyi düzeyde sağlanması adına akışkan yataklarda yatak malzemeleri kullanılmaktadır. Yatak malzemeleri, inert ya da katalitik etkide bulunabildiği gibi tasarlanacak olan yatağın akışkanlaştırma rejimine uygun özelliklere de sahip olmalıdır. İnert yatak malzemelerinden en çok tercih edileni silika kumdur. Silika kum, yapısı gereği gazlaştırma sıcaklık aralığında (500°C-1000°C) bozunmadan yatak içinde kullanılabilir. Ayrıca, Geldart partikül sınıflandırılmasına göre B tipi yatak malzemeleri (100-1000 µm) çok iyi akışkanlaşırlar. B grubundaki yatak malzemeleri kullanıldığında kabarcıklı yataklardaki kabarcıklar son derece hareketli olup karışımın çok iyi gerçekleşmesini sağlamaktadır. Bu nedenle, B grubundaki yatak malzemelerine verilebilecek en iyi örnek kum taneleridir. Yapılan çalışmada, yatak malzemesi olarak B grubunda bulunan ve 600 µm çapa sahip silika kum tercih edilmiştir. Diğer bir yandan, kolay akışkanlaştırılabilmesi yatak içinde boş kolon hızının $U/U_{mf}=2$ olacak şekilde tasarlanmasına olanak vermektedir. Bu tasarım parametresi aynı zamanda yatak içinde kullanılacak hava debisinin minimumda tutulmasını sağlayarak gazlaştırmada reaktant olarak su buharının ön planda olmasına yardımcıdır.

Yapılan çalışmada, yatak malzemesinin akışkanlaşması için hava kullanılmış ve yatak içinde hava debisi 0.0007473 m³/s olarak sabit tutulmuştur. 5, 10 ve 15 g/dak akış hızları için yatak içindeki buhar debileri sırası ile 0,000141 m³/s, 0,000283 m³/s ve 0,000423 m³/s'dir. Su buharı/hava oranları ise sırasıyla 0,18, 0,37 ve 0,56'dır. Yatak içi boş kolon hızı $U/U_{mf}=2$ olacak şekilde buhar debisinden bağımsız olarak belirlenmiştir. Buhar debisi ile birlikte yatak içi U/U_{mf} oranları 5, 10 ve 15 g/dak buhar akış hızları için sırası ile %15, %27 ve %36 olacak şekilde artmaktadır. U/U_{mf} oranlarındaki bu artış, genel çalışma aralığı kabul edilen ve akışkanlaşma şartlarının sağlandığı uygun akışkanlaşma şartı olan $U/U_{mf}=2-3$ arasındadır. Tasarlanan akışkan yatağın statik yatak yüksekliği, 0,045 m olarak hesaplanmıştır.



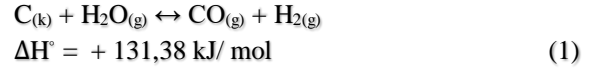
Şekil 1. Akışkan yataklı gazlaştırıcı sistemi şematik görünümü

BULGULAR VE TARTIŞMA

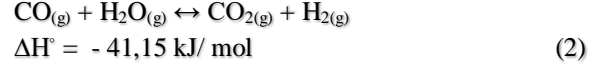
Sentez gazı bileşimi temel gazlaştırma reaksiyonlarının denge şartlarına son derece bağlıdır. Gazlaştırıcının işletme şartlarına göre üretilen sentez gazının dengedeki bileşimi değişmektedir (Basu, 2006). Temel gazlaştırma reaksiyonları Eş. 1 ve Eş. 5 arasında sunulmuştur. Karbonun tüketildiği temel reaksiyonlar su gazı Eş. (1) ve Boudouard Eş. (3) reaksiyonlarıdır. Gazlaştırmada H₂ üretimi temelde su gazı reaksiyonu Eş. (1) ile gerçekleşir. Bunun yanı sıra, su gazı yönlendirme Eş. (2) ve metanın buharla reformlanma reaksiyonu Eş. (5) da gazlaştırıcı akışkan çeşidi ve miktarına göre gerçekleşebilmektedir.

Gazlaştırmada CH₄ üretimi piroliz sırasında metanlaşma reaksiyonu Eş. (4) ile gerçekleşirken aynı zamanda gazlaştırılan malzemenin çeşidine-yapısına göre de sentez gazındaki miktarı değişiklik gösterebilir (Emami-Taba vd, 2013; Emami-Taba vd, 2012).

Su gazı reaksiyonu



Su gazı yönlendirme reaksiyonu



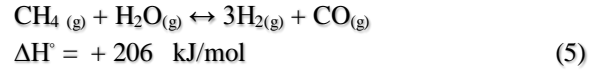
Boudouard reaksiyonu



Metanlaşma reaksiyonu



Metanın buharla reformlanma reaksiyonu

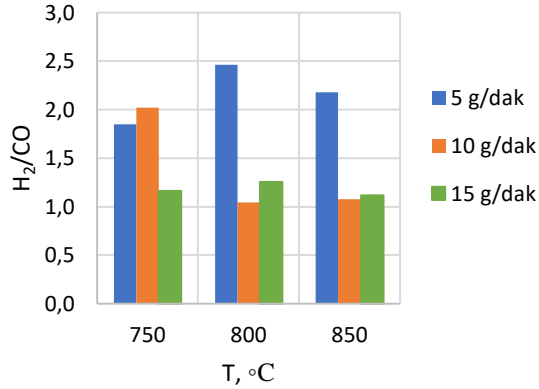


Himmetoğlu ve Seyitömer bitümlü şeylleri, plastik şehir atıkları ile birlikte akışkan yataklı bir gazlaştırıcı sistemde gazlaştırılmıştır. Çalışmada sıcaklığın, su buharı akış hızının ve beslemedeki plastik atık oranının sentez gazı bileşimine etkileri araştırılmıştır. Deneysel çalışmalarda, gazlaştırıcı işletme sıcaklıkları 750°C, 800°C ve 850°C ve işletme basıncı atmosferik basınçtır. Buhar akış hızı 5, 10 ve 15 g/dak olacak şekilde değiştirilmiştir. Bitümlü şeyller ve plastik atıklar tek başlarına gazlaştırılmış ardından birlikte gazlaştırma deneyleri gerçekleştirilmiştir. Birlikte gazlaştırma deneylerinde beslemedeki plastik atık oranı kütleye %40 ve %70 olacak şekilde ayarlanmıştır.

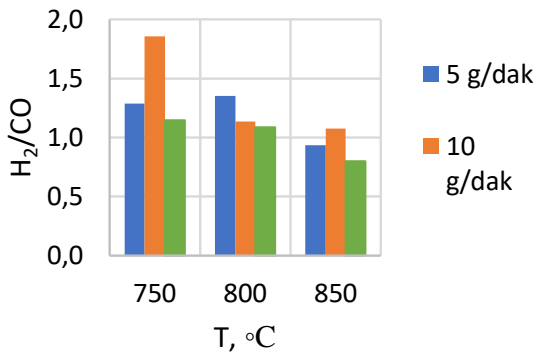
H₂ Konsantrasyonlarının Değerlendirilmesi

Himmetoğlu bitümlü şeyli ile gerçekleştirilen deneylerde elde edilen sentez gazı bileşimindeki H₂ konsantrasyonları incelenmiştir. Sentez gazının hidrojen zengin olarak değerlendirilmesi için H₂/CO oranının 2'ye yakın olması beklenmektedir (Özbayoğlu vd, 2013). Özellikle metanol üretiminde H₂/CO oranının 2 olması üretim açısından önemlidir (Ciferno and Marano, 2002; Liu vd, 2016; NETL Liquid Fuels, 2021). Himmetoğlu bitümlü şeyli 750°C'de tek başına gazlaştırıldığında 5 g/dak ve 10 g/dak su buharı akış hızındaki H₂/CO oranları sırası ile 1,9 ve 2 olarak elde edilmiştir. 5 g/dak sabit su buharı akış hızındaki deneylerde 800°C'deki H₂/CO oranı 2,5 ve 850°C'deki H₂/CO oranı ise 2,2 olarak belirlenmiştir (Şekil 2). Himmetoğlu şeyli ve plastik atıkların birlikte gazlaştırılmasına bakıldığında yine hidrojen zengin

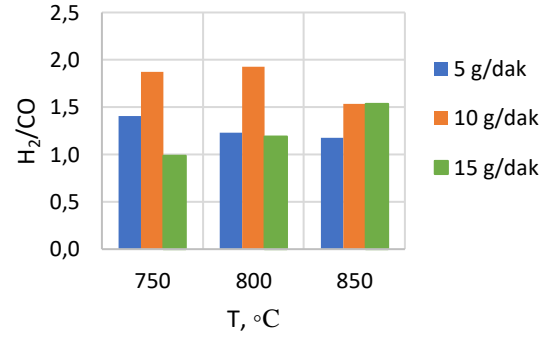
sentez gazı eldesinin mümkün olduğu görülmüştür. Her iki karışımın gazlaştırması için de H_2/CO oranı, $750^\circ C$ ve 10 g/dak su buharı akış hızı için $1,9$ olarak belirlenmiştir (Şekil 3 ve Şekil 4).



Şekil 2. %100 Himmetoğlu bitümlü şistisine ait H_2/CO oranları



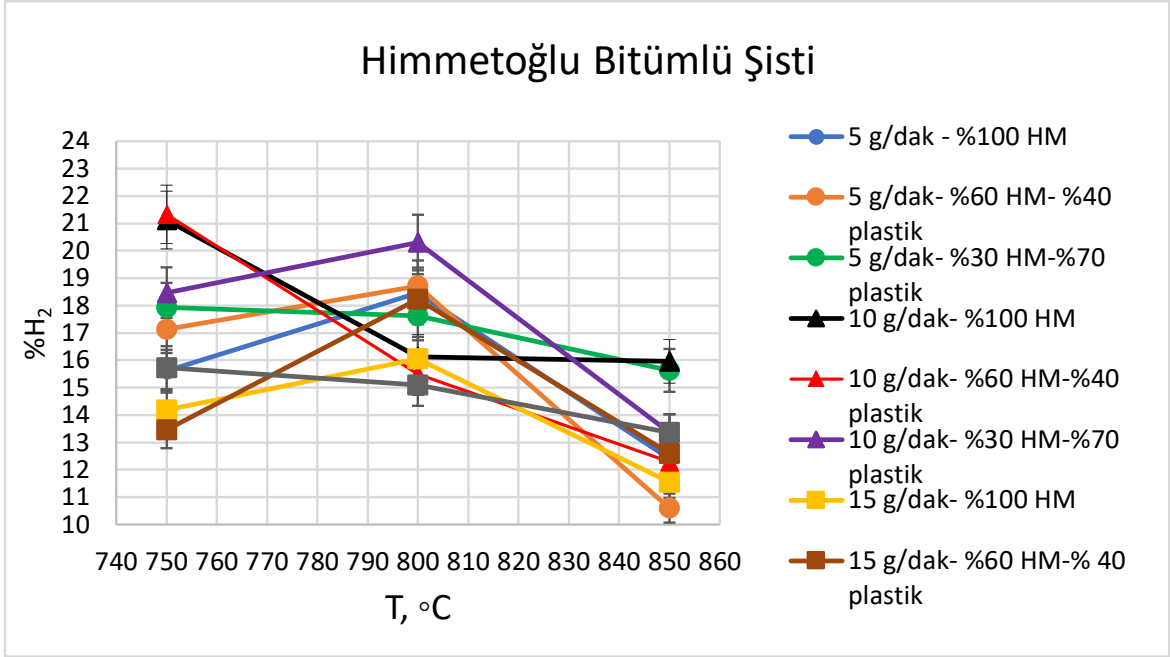
Şekil 3. %60 Himmetoğlu- %40 plastik karışımına ait H_2/CO oranları



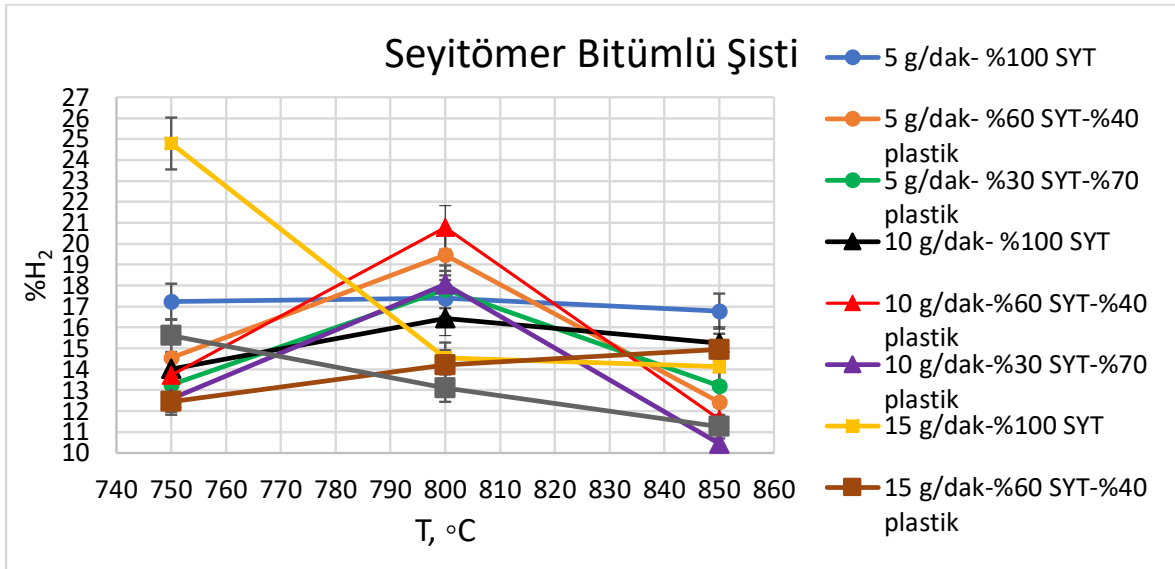
Şekil 4. %30 Himmetoğlu- %70 plastik karışımına ait H_2/CO oranları

$800^\circ C$ 'de 10 g/dak akış hızında %30 Himmetoğlu bitümlü şisti-%70 plastik karışımının gazlaştırılmasında da H_2/CO oranı $1,9$ olarak elde edilmiştir. Ancak, işletme maliyetleri düşünüldüğünde olabildiğince düşük gazlaştırma sıcaklıkları tercih edilmektedir. H_2 üretimi için düşük gazlaştırma sıcaklıklarının daha uygun olduğu yapılan çalışmalarda da vurgulanmıştır (Uysal vd, 2013; Vural vd, 2014; Hammad vd, 2016).

H_2 üretiminde su gazı reaksiyonu aktif rol alırken gazlaştırıcıda su buharı miktarı artırılarak su gazı yönlendirme reaksiyonu sayesinde H_2 konsantrasyonu daha da artırılabilir. Böylece sentez gazındaki CO gazı da değerlendirilmiş olmaktadır. Literatürdeki çalışmalara bakıldığında, gazlaştırıcı akışkan su buharı olduğunda ve beslemede fazla miktarda bulunduğu su gazı yönlendirme reaksiyonunun gerçekleştiği ve H_2 üretimine destek olduğu belirtilmiştir (Kryca vd, 2018; Li vd, 2014; Zhang vd, 2014; Uysal vd, 2013). Himmetoğlu bitümlü şeyli ile yapılan deneylerde hidrojen zengin sentez gazı eldesinde su gazı yönlendirme reaksiyonunun etkili olduğu ve sahip olduğu sabit karbon oranından dolayı gazlaştırma prosesi ile H_2 üretiminde değerlendirilebileceği belirlenmiştir. Buna göre, en yüksek H_2 konsantrasyonu, %60 Himmetoğlu- %40 plastik atık karışımı için $750^\circ C$ 'de ve 10 g/dak su buharı akış hızında %21,33 olarak belirlenmiştir (Şekil 5)



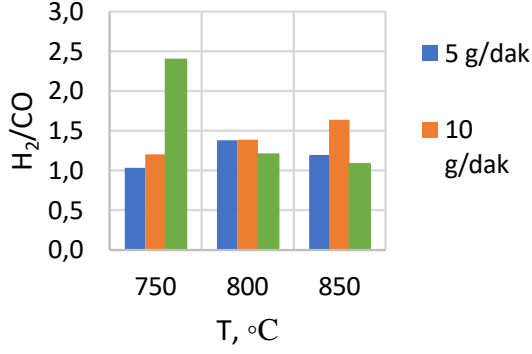
Şekil 5. Himmetoğlu bitümlü şeylinin gazlaştırılmasında elde edilen tüm H₂ konsantrasyonları (%5 hata barı ile)



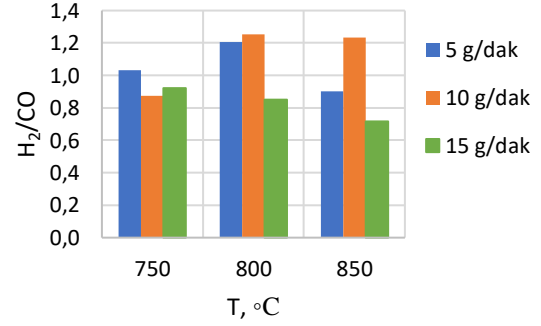
Şekil 6. Seyitömer bitümlü şistin gazlaştırılmasında elde edilen tüm H₂ konsantrasyonları (%5 hata barı ile)

Seyitömer bitümlü şeylinin sabit karbon miktarı Himmetoğlu bitümlü şeylinin sabit karbon miktarından daha düşük olduğundan sentez gazındaki H₂ konsantrasyonları da daha düşüktür (Şekil 6). 750°C'de %100 Seyitömer bitümlü şeyli gazlaştırıldığında H₂ miktarının artması için daha yüksek su buharı akış hızına (15 g/dak) ihtiyaç duyulmuştur (Şekil 7). Seyitömer bitümlü şeyli ve plastik atıkların gazlaştırma sonuçlarına bakıldığında, hidrojen zengin sentez gazı üretimi için %60 Seyitömer bitümlü şeyli-%40 plastik karışımının 800°C'de 10 g/dak ve 15 g/dak sabit su buharı akış hızlarında gazlaştırılması uygundur. Bu şartlarda elde edilen sentez gazındaki H₂ konsantrasyonları sırasıyla %20,78 ve %14,20 olarak belirlenmiştir. H₂/CO oranları

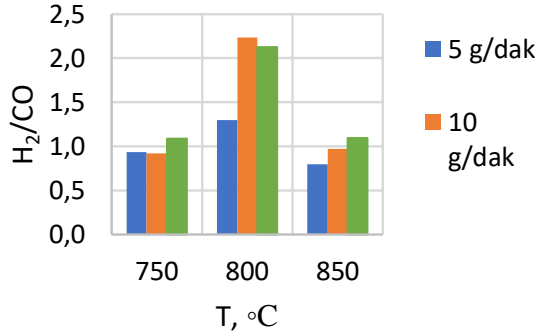
ise sırasıyla 2,2 ve 2,1'dir (Şekil 8). %30 Seyitömer bitümlü şeyli-%70 plastik atık karışımının H₂/CO oranlarına bakıldığında hidrojen zengin sentez gazı için bu karışım oranının uygun olmadığı görülmüştür (Şekil 9).



Şekil 7. %100 Seyitömer bitümlü şeyline ait H₂/CO oranları



Şekil 9. %30 Seyitömer- %70 plastik karışımına ait H₂/CO oranları



Şekil 8. %60 Seyitömer- %40 plastik karışımına ait H₂/CO oranları

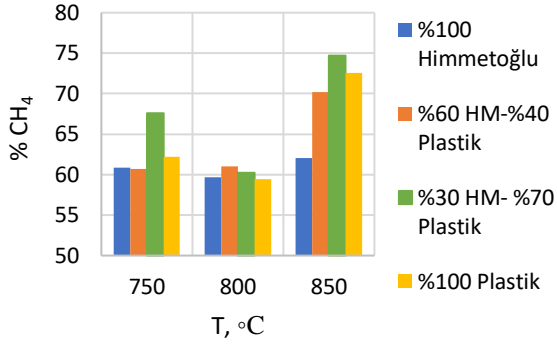
CH₄ Konsantrasyonlarının Değerlendirilmesi

Himmetoğlu şeyli ve plastik atık karışımlarındaki plastik oranı arttıkça üretilen sentez gazındaki CH₄ konsantrasyonu da artmıştır. CH₄ konsantrasyonundaki bu davranış literatür çalışmaları ile uyum göstermektedir (Pinto vd, 2009). Birlikte gazlaştırma çalışmalarında elde edilen sentez gazındaki CH₄ konsantrasyonunun karışımdaki plastik miktarı ve yapısı ile doğrudan ilişkili olduğu belirtilmiştir (Arena vd,2014). Gazlaştırma sırasında plastik malzemelerdeki C-H bağları diğer besleme malzemesinden gelen C-H atomları ile daha çok CH₄ oluşturma eğilimi göstermektedir (Lopez vd, 2018). CH₄ konsantrasyonunu artıran bir diğer önemli etmen de gazlaştırıcıda hava bulunmasıdır. Gazlaştırma çalışmalarında su buharı kullanımı sentez gazındaki H₂ konsantrasyonunu desteklerken hava kullanımı ise H₂ üretimini sınırlayarak CH₄, çeşitli hidrokarbonlar ve yanma ürünlerinin oluşumuna yol açmaktadır (Xiao vd, 2007; Leung and Wang, 2003). Bu nedenle, su buharı/hava oranının üretilecek sentez gazı üzerindeki etkisi önemlidir (Straka ve Bucko, 2009).

Yapılan çalışmada, özellikle 800°C'de H₂ ve CH₄ konsantrasyonlarının dengedeki davranışı gözlenmiştir. Su gazı reaksiyonu ile H₂ üretimi 750°C'de varlığını gösterirken sıcaklığın artışı ile Boudouard reaksiyonu beslemedeki karbonun daha çok CO üretimi için kullanımına neden olmaktadır (Öztan vd, 2020; Mastral vd, 2003). Gazlaştırıcıda su buharı miktarı da hava ile sınırlandırıldığında su gazı yönlendirme reaksiyonu ile H₂ üretimi desteklenemez ve genellikle konsantrasyonda düşüş gözlenmektedir. Ayrıca, metanlaşma reaksiyonu ile kısa da olsa piroliz aşamalarında oluşan CH₄ ise su buharı yetersizliği sebebiyle metanın reformlanma reaksiyonunda harcanamamaktadır (Wie vd, 2012; Upadhyay vd, 2020; Khzouz ve Gkanas, 2018). Gazlaştırma reaksiyonlarının dengedeki davranışlarının bilinmesi ve üretilmesi planlanan ürün için en uygun koşulların belirlenmesi önemlidir.

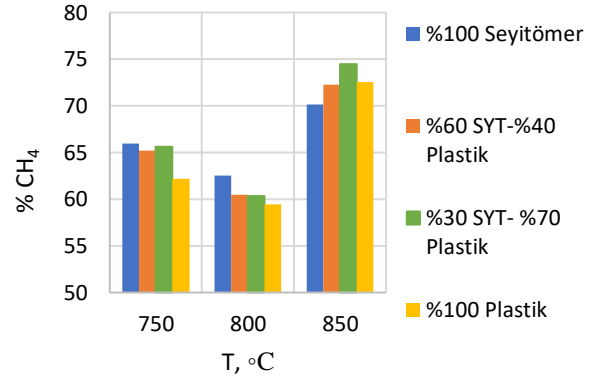
Şekil 10 incelendiğinde sentez gazındaki CH₄ konsantrasyonu beslemeye plastik atık ekledikçe artış göstermiştir. Elde edilen sentez gazı motorlarda değerlendirilmek istenirse CH₄ konsantrasyonunun yüksek olması beklenir. Bu nedenle, Himmetoğlu bitümlü şeyli ve plastik atık karışımı kullanılırsa

850°C'de (10 g/dak sabit su buharı akış hızında) %30 Himmetoğlu bitümlü şeyli-%70 plastik atık karışımının gazlaştırılması uygundur ve bu koşullar altında yapılan deney sonucunda, sentez gazındaki CH₄ konsantrasyonunun maksimum değerinde (%74,71) olduğu görülmüştür.



Şekil 10. Himmetoğlu bitümlü şeyline plastik atık eklenmesi sonucu elde edilen CH₄ konsantrasyonları

Seyitömer bitümlü şeyline plastik şehir atığı karıştırıldığında sentez gazındaki CH₄ konsantrasyonları artmıştır. %30 Seyitömer bitümlü şeyli-%70 plastik karışımı (10 g/dak sabit su buharı akış hızında) 850°C'de gazlaştırıldığında sentez gazındaki maksimum CH₄ konsantrasyonu %74,47 olarak belirlenmiştir (Şekil 11). Plastik oranının artması sonucu sentez gazında CH₄ konsantrasyonunda artış gözlenmesi literatür sonuçları ile uyumlu bulunmuştur. Pinto vd. yaptıkları çalışmada Puertollano ve Colombian kömürleri ile polietileni ve çeşitli biyokütleleri birlikte gazlaştırmıştır. Çalışma sonucunda en yüksek CH₄ konsantrasyonları, her iki kömür çeşidi ile polietilen birlikte gazlaştırıldığında ve polietilen miktarı arttığında elde edilmiştir (Pinto vd, 2009). Benzer şekilde, Win vd., plastik atıkların gazlaştırılmasında atıkların yapısal bozunma reaksiyonları sonucu CH₄ üretimine yakınlık olduğu belirtilmiştir (Win vd, 2019).



Şekil 11. Seyitömer bitümlü şeyline plastik atık eklenmesi sonucu elde edilen CH₄ konsantrasyonları

Su buharı/Hava Oranı Etkisinin Değerlendirilmesi

Deney sonuçları incelendiğinde, su buharı/hava oranı arttıkça (buhar akış hızı artırıldığı için yatak içindeki oran) hem HM hem SYT için elde edilen sentez gazı içeriğindeki H₂ konsantrasyonları ya da H₂/CO oranları için belirli bir davranış elde edilmemiştir. Özellikle, %100 HM ve %100 SYT gazlaştırma sonuçlarına bakıldığında su buharı/hava oranı artsa da H₂ konsantrasyonunu etkileyen iki önemli parametre gazlaştırma sıcaklığı ve bitümlü şeylin sabit karbon miktarıdır. Şekil 7 incelendiğinde, %100 SYT'nin 750°C'de gazlaştırılmasında yüksek su buharı akış hızına ihtiyaç duyulmuştur. Su buharı akış hızındaki artış H₂/CO oranını artırsa da bu etki 800°C ve 850°C'lerde gözlenmemiştir. Burada etkili olan parametre yakıtın düşük sabit karbon içeriğidir. Çünkü, sıcaklık ve su buharı akış hızı artsa bile H₂/CO oranları istenen değer altında kalmıştır. Aynı şekilde Şekil 8 incelendiğinde, su buharı akış hızı H₂ konsantrasyonunu artırsa da sıcaklık etkisi ön plandadır. Şekil 9'da ise su buharı/hava oranı ve sıcaklık artmasına rağmen yakıt karışımının bileşimi H₂/CO oranlarını ilk sırada etkileyerek istenen değer altında kalmasına neden olmuştur. Su buharı/hava oranının sentez gazı konsantrasyonuna etkisinin sıcaklık ve yakıt bileşimi sabit tutularak incelenmesi önerilmektedir.

Su buharı/hava oranının sentez gazı bileşimindeki etkisi CH₄ üretimi için daha sınırlayıcı bir faktör olabilir. Çünkü, sentez gazındaki CH₄ konsantrasyonu bir önceki bölümde de belirtildiği gibi gazlaştırıcı akışkanın içinde hava olması ya da tamamen hava ile gazlaştırma işlemlerinde denge reaksiyonlarına bağlı olarak artış gösterebilmektedir. Sentez gazı içeriğindeki CH₄ ve H₂

konsantrasyonlarının dengedeki davranışı su buharı/hava oranının optimizasyonu ile belirlenebilir. Sentez gazından CH₄ üretimi amaçlandığında sabit sıcaklık, sabit buhar akış hızı ve sabit yakıt karışımı bileşiminde beslenen hava debisinin CH₄ konsantrasyonuna etkisi incelenebilir.

SONUÇLAR

Seyitömer ve Himmetoğlu bitümlü şeyllere plastik şehir atığı karıştırılarak laboratuvar ölçekli akışkan yataklı bir sistemde gazlaştırma deneyleri gerçekleştirilmiştir. Sıcaklığın, su buharı akış hızının ve beslemedeki plastik oranının sentez gazı bileşimine etkileri incelenmiştir. Yapılan çalışma sonucunda hidrojen zengin sentez gazı üretimi amaçlandığında Himmetoğlu bitümlü şeylinin Seyitömer bitümlü şeyline tercih edilebileceği belirlenmiştir. Her iki bitümlü şeyl beslemesi için de plastik atık oranı arttıkça sentez gazındaki CH₄ konsantrasyonu artmıştır. Maksimum CH₄ konsantrasyonu eldesi için hem Himmetoğlu bitümlü şeyli hem de Seyitömer bitümlü şeyli tercih edilebilir. Sentez gazı bileşiminin sıcaklığa, su buharı akış hızına ve plastik oranına son derece bağlı olduğu görülmüştür. Bu nedenle, sentez gazının hangi alanda kullanılacağı belirlenerek işletme şartlarının optimize edilmesi gerektiği sonucuna varılmıştır. Ayrıca, ülkemiz için önemli bir fosil yakıt kaynağı olması açısından bitümlü şeyllerin gazlaştırma gibi verimli sistemlerde değerlendirilmesi yerli kaynakların kullanımını teşvik edecek niteliktedir.

Yapılan çalışma, Himmetoğlu ve Seyitömer bitümlü şeyllerinin sabit karbon içeriklerinin gazlaştırmada değerlendirmek üzere uygun olup olmadığını belirlemek amacıyla ile laboratuvar ölçekli akışkan yataklı gazlaştırıcıda gerçekleştirilmiştir. Büyük ölçekli sistemlere geçildiğinde reaktör boyutları, besleme noktası ve akış dinamikleri vb. gibi parametrelerin HM ve SYT bitümlü şeyllerinden elde edilecek sentez gazı konsantrasyonlarına etkisi gerekli yatak tasarımı hesapları yapılarak gerçekleştirilmelidir. Besleme noktasının uygun konumlandırılması ile yakıt-buhar etkileşiminin maksimum düzeye çıkarılması ve dolayısıyla karbon dönüşümünün maksimum derecede elde edilebilmesi yapılacak çalışmalar ile mümkün olacaktır. Aynı şekilde, farklı akışkanlaşma rejimlerinde çalıştırılan akışkan yatakların kullanımı ile yine gaz-katı etkileşimlerinin incelenmesi önerilmektedir. Yatak özelliklerinin sentez gazı üzerindeki etkilerinin araştırılması akışkan yatakların gazlaştırmada etkin rol oynaması için öncülüdür.

TEŞEKKÜR

Bu çalışma, Gazi Üniversitesi Bilimsel Araştırma Projeleri Birimi tarafından desteklenen 06/2007-26 nolu proje kapsamında yapılmıştır. Ayrıca yazarlar, çalışmalar sırasında desteğini esirgemeyen çok kıymetli Prof. Dr. Bekir Zühtü UYSAL'a teşekkürlerini sunmaktadır.

REFERANSLAR

Adami L. and Schiavon M., 2021, From circular economy to circular ecology: a review on the solution of environmental problems through circular waste management approaches, *Sustainability*, 13(2), 1-2.

Aguilar-Hernandez G.A., Sigüenza-Sanchez,C.P., Donati F., Merciai S., Schmidt J., Rodrigues J., F., D. Tukker A., 2019, The circularity gap of nations: A multiregional analysis of waste generation, recovery, and stock depletion in 2011. *Resour. Conserv. Recycl.*, 151.

Arena U. and Gregorio F. D., 2014, Energy Generation by Air Gasification of Two Industrial Plastic Wastes in a Pilot Scale Fluidized Bed Reactor, *Energy*, 68, 735-743.

Basu P., 2006, *Combustion and gasification in fluidized bed.*, Halifax- Nova Scotia: Taylor and Francis Group, (1. Basım), 59-101.

Basu P., 2010, *Gasification theory and modeling of gasifiers* . New York: Elsevier, (1. Basım), 125-191.

Benim A., C. ve Kuppa K., 2016, Modeling of Entrained-flow coal gasification by an equilibrium Eulerian-Eulerian two-phase flow formulation, *Isı Bilim. Tek. Derg.*, 36(2), 93-102.

Canbaz E., D. ve Gür M. (2020). Prediction of underground coal gasification performance of Turkish lignite reserves using stoichiometric equilibrium model, *Isı Bilim. Tek. Derg.*, 40(2), 195-200.

Chaudhari S., T., Bej S., K., Bakhshi N., N., Dalai A., K., 2001, Steam gasification of biomass-derived char for the production of carbon monoxide-rich synthesis gas, *Energy Fuel*, 15, 736-742.

Ciferno J., P. and Marano J., J., 2002, Benchmarking biomass gasification Technologies for fuels, chemicals and hydrogen production, U.S. Department of Energy-National Energy Technology Laboratory, 14.

- Cocco R., Karri S., B., R., and Knowlton T., 2014, Introduction to fluidization. *Chem Eng Prog*, 110(11), 21-29.
- Dinçer İ. ve Zamfirescu C., 2014, Advanced Power Generation Systems, *Elsevier*, (1st ed.), USA, 134-141.
- Du Z., Liu C., Zhai J., Gou X., Xiong Y., Su W. and He G., 2021, A review of hydrogen purification technologies for fuel cell vehicles, *Catalysts*, 2-17.
- Emami Taba L., Irfan M. F., Wan Daud W. A. M., and Chakrabarti M. H., 2012, The effect of temperature on various parameters in coal, biomass and CO-gasification: A review. *Renew. Sust. Energ. Rev.*, 16(8), 5584-5596.
- Emami-Taba L., Irfan M. F., Wan Daud W. M. A., and Chakrabarti M. H., 2013, Fuel blending effects on the co-gasification of coal and biomass - A review. *Biomass Bioenerg.*, 57, 249-263.
- Geldart D., 1986, *Gas Fluidization Technology*, Great Britain: Wiley-Interscience Publication, (1st ed.), 1-153.
- Grace J. R., 2020, Introduction, History, and Applications. In *Essentials of Fluidization Technology*, 1-9.
- Hamelinck C., N., Faaij A., P., C., den Uil, and Boerrigter, H., 2004, Production of FT transportation fuels from biomass; technical options, process analysis and optimization, and development potential, *Energy*, 29(11), 1743-1771.
- Hammad A. E. A., Nadirov E., Uysal D., Doğan Ö. M. ve Uysal, B. Z., 2016, Pirinadan Su Buharı Gazlaştırmasıyla Sentez Gazı Üretimi, 12. *Ulusal Kimya Mühendisliği Kongresi*, İzmir.
- İnternet, 2021, International Energy Agency (IEA), *Total final consumption by source*, <https://www.iea.org/data-and-statistics>.
- İnternet, 2019, Türkiye Kömür İşletmeleri (TKİ), *Temiz Kömür Teknolojileri*, <http://www.tki.gov.tr/bilgi/komur/komurteknolojileri/235>.
- İnternet, 2021, Australian Hydrogen Council, *About Hydrogen*, <https://h2council.com.au/about-hydrogen>.
- İnternet, National Energy Tehnology Laboratory (NETL), *Fluidized Bed Gasifiers*, <https://www.netl.doe.gov/research/coal/energy-systems/gasification/gasifipedia/fluidizedbed>.
- İnternet, National Energy Technology Laboratory (NETL), *Syngas conversion to methanol*, <https://www.netl.doe.gov/research/coal/energysystems/gasification/gasifipedia/methanol>.
- Jambeck J. R., Geyer R., Wilco, C., Siegler T.R., Perryman M., Andrady A., Narayan R., and Law, K.L., 2015, Plastic waste inputs from land into the ocean, *Science*, 347, 768-71.
- Khzouz M. and Gkanas E. I., 2018, Experimental and Numerical Study of Low Temperature Methane Steam Reforming for Hydrogen Production, *Catalysts*, 8, 1-20.
- Kovac A., Paranos M. and Marcius D., 2021, Hydrogen in energy transition: A review, *Int. J. Hydrog. Energy*, 46, 10016- 10035.
- Kryca J., Priscak J., Lojewka J., Kuba M. and Hofbauer H., 2018, Apparent Kinetics of The Water-gas-shift Reaction in Biomass Gasification Using Ash-layered Olivine as Catalyst, *Chem. Eng. J.*, 346, 113-119.
- Kunii D. and Levenspiel O., 1991, *Fluidization Engineering*. Buterworth- Heinemann Series in Chemical Engineering (1st ed.), ABD.
- Leung D. Y. C. and Wang C. L., 2003, Fluidized-bed Gasification of Waste Tire Powders. *Fuel Process. Technol.*, 84, 175-96.
- Li B., Wei L., Yang H., Wang X., and Chen H., 2014, The Enhancing Mechanism of Calcium Oxide on Water Gas Shift Reaction for Hydrogen Production, *Energy*, 68, 248-254.
- Liu Z., Peng W., Motahari-Nezhad M., Shahraki S. and Beheshti M., 2016, Circulating fluidized bed gasification of biomass for flexible end-use of syngas: a micro and nano scale study for production of bio-methanol, *J. Clean. Prod.*, 129:249-255.
- Lobachyov K., V., Richter H., J., 1998, An advanced integrated biomass gasification and molten fuel cell power system, *Eng. Convers. Manag.*, 39(16-18), 1931-1943.
- Lopez G., Artetxe M., Amutio M., Alvarez J. Bilbao J. and Olazar M., 2018, Recent Advances in the Gasification of Waste Plastics- A Critical Overview, *Ren. Sust. Energ Rev.*, 82,576-596.

- Mastral F. J., Esperanza E., Berruenco C., Juste M., and Ceamanos J., 2003, Fluidized Bed Thermal Degradation Products of HDPE in an Inert Atmosphere and in Air-nitrogen Mixtures. *J. Anal. Appl. Pyrolysis*, 70, 1-17.
- Moya D., Aldas C., Jaramillo D., Jativa E. and Kaparaju P., 2017, Waste-to-Energy Technologies: an opportunity of energy recovery from manucipal solid waste using Quito-Ecuador as case study, *Procedia Eng.*, 134, 327-336.
- Özbayoğlu A. M., Kasnakoğlu C., Güngör A., Brykoğlu A., ve Uysal, B. Z., 2013, Sentez Gazı Elde Etmek için Kontrol Edilebilir Reaktör Parametrelerine Bağlı Geliştirilen İki Aşamalı Bir Su Gazı Yönlendirme Reaktörü Modeli, *J. Fac. Eng. Archit. Gaz.*, 28(2), 339-351.
- Öztan H., Uysal Zıraman D., Doğan Ö. M. and Uysal B. Z., 2020, Production of Hydrogen-Rich Syngas in a Fluidized Bed, *10th Int. 100% Renewable Energy Conference*, İstanbul, 133-142.
- Öztürk S., 2020, The effects of CO₂, H₂O, and N₂ dilutions on pollutants of shale gas combustion, *Isı Bilim. Teknik. Derg.*, 40(1), 15-25.
- Pinto F., André R. N., Franco C., Lopes H., Gulyurtlu I., and Cabrita I., 2009, Co-gasification of coal and wastes in a pilot-scale installation 1: Effect of catalysts in syngas treatment to achieve tar abatement. *Fuel*, 88(12), 2392–2402.
- Ramos A., Monteiro E., Silva V., and Rouboa A., 2018, Co-gasification and recent developments on waste-to-energy conversion: A review. *Ren. Sust. Energ. Rev.*, 81, 380–398.
- Straka P. and Bucko Z., 2009, Co-gasification of a Lignite/Waste-Tyre Mixture in a Moving Bed. *Fuel Proces. Technol.*, 90, 1202-6.
- Toraman Ö., Y. ve Uçurum M., 2009, Alternatif fosil enerji kaynağı: bitümlü şeyl, TÜBAV Bilim Dergisi, 2(1), 37-46. Türkiye Kömür İşletmeleri Kurumu (TKİ), 2010, Kömür sektör raporu (linyit), *Türkiye Kömür İşletmeleri Kurumu*, Ankara, 1-12.
- Upadhyay D. S., Panchal K. R., Skhiya A. K. and Patel R. N., 2020, Air-steam Gasification of Lignite in a Fixed Bed Gasifier: Influence of Steam to Lignite Ratio on Performance of Downdraft Gasifier, *Energy*, 211, 118187.
- Uysal D., Doğan Ö., M., ve Uysal B., Z., 2013, Soma Linyitinin Su Buharı Gazlaştırmasıyla Sentez Gazı Üretimi, *ULIBTK'13 19. Isı Bilimi ve Tekniği Kongresi*, Samsun.
- Vural E. S., Uysal B. Z., ve Doğan Ö. M., 2014, Soma-Eynez Linyitinden Su Buharı Gazlaştırmasıyla Hidrojen İçeriği Yüksek Sentez Gazı Üretimi, *11. Ulusal Kimya Mühendisliği Kongresi*, Eskişehir.
- Wie J., Zhong W., Jin B., Shao Y. and Liu H., 2012, Simulation on Gasification of Forestry Residues in Fluidized Beds by Eulerian- Lagrangian Approach. *Bioresour. Technol.*, 121, 36-46.
- Win M. M., Asari M., Hayakawa R., Hosada H., Yano J. and Sakai S., 2019, Characteristics of Gas from the Fluidized Bed Gasification of Refuse Paper and Plastic Fuel (RPF) and Wood Biomass, *Waste Manage.*, 87, 178.
- Wong S.L., Ngadi N., Abdullah TAT and Inuwa I. M., 2015, Current State and Future Prospects of Plastic Wastes as Source of Fuel: a review, *Ren. Sust. Energ. Rev.*, 50, 1167-80.
- Xiao R., Jin ., Zhou H., Zhong Z. and Zhang M., 2007, Air Gasificaion of Polypropylene Plastic Waste in Fluidized Bed Gasifier. *Energ. Convers. Manag.*, 48,778-86.
- Zhang Y., Gong X., Zhang B., Liu W. and Xu,M., 2014, Potassium Catalytic Hydrogen Production in Sorption Enhanced Gasification of Biomass With Steam, *Int. J. Hydrog. Energ.*, 39, 4234-42.



ANALYSIS OF HEAT TRANSFER ENHANCEMENT IN TUBES WITH CAPSULE DIMPLED SURFACES AND Al_2O_3 -WATER NANOFLUID

Ekin ÖZGİRGIN YAPICI*, Mahmoud Awni A. Haj İBRAHİM** and Haşmet TÜRKÖĞLÜ***

Çankaya University, Department of Mechanical Engineering, Etimesgut, Ankara

*ekinozgirgin@ankaya.edu.tr, ORCID: 0000-0002-7550-5949

**mahmoud.awni96@gmail.com, ORCID: 0000-0002-7932-9583

***hasmet@ankaya.edu.tr, ORCID: 0000-0002-1941-986X

(Geliş Tarihi: 09.08.2022, Kabul Tarihi: 24.10.2022)

Abstract: This study aims to numerically investigate and evaluate the enhancement of heat transfer by new capsule dimples on tube surfaces for flow of water and Al_2O_3 -water nanofluid with different concentrations, under uniform surface heat flux. The originality of this work lies in combining two passive heat transfer enhancement methods such as geometrical improvements and nanofluids together. Capsule dimples with different depths were considered. Al_2O_3 -water nanofluid was modeled as a single-phase flow based on the mixture properties. The effects of dimple depth and nanoparticle concentrations on Nusselt number, friction factor and performance evaluation criteria (PEC) were studied. Numerical computations were performed using ANSYS Fluent commercial software for 2000-14000 Reynolds number range. It was found that when laminar, transient and fully developed turbulent flow cases are considered, increase in the dimple depth increases the Nusselt number and friction factor for both pure water and Al_2O_3 -water nanofluids cases. Also, the friction factor increases as dimple depth increases. Results show that increase in PEC is more pronounced in the laminar region than in the transition region, it starts to decrease for turbulent flows. For nanofluid, PEC values are considerably higher than pure water cases. The variation of PEC for capsule dimpled tubes are dependent on flow regimes and dimple depths. Increasing the nano particle volume concentration and dimple depth in laminar flows increase the PEC significantly.

Keywords: Heat transfer enhancement, nanofluid, capsule dimples, computational analysis

BORU YÜZEYİNDEKİ KAPSÜL TİPİ KABARTMANIN VE Al_2O_3 -SU NANOAKIŞKANIN ISI TRANSFERİNE ETKİSİNİN SAYISAL ANALİZİ

Özet: Bu çalışmanın amacı, duvar yüzeyinden düzenli ısı akışı uygulanan boru içi akışlarda geometrik modifikasyon yapılarak elde edilecek ısı transferi iyileştirmesinin numerik olarak incelenmesidir. Geometrik modifikasyon olarak kapsül tipi kabartmalar kullanılmış, akışkan olarak ise su ve Al_2O_3 -su nano-akışkan kullanılmıştır. Isı transferi iyileştirmesi için hem geometrik modifikasyon yapılmış olması hem de bununla birlikte farklı yüzdelerde nano-akışkan kullanılmış olması çalışmayı benzerlerinden farklı bir noktaya taşıyabilmektedir. Kapsül tipi kabartmalar borunun iç yüzeyine farklı derinliklerde uygulanmıştır. Al_2O_3 -su nano-akışkan 1%, 2% ve 3% konsantrasyonlarında tek fazlı akış olarak modellenmiş ve uygulanmıştır. Kabartmaların derinliğinin ve nano-akışkanın farklı konsantrasyonlarda uygulamalarının Nusselt sayısı, Sürtünme katsayısı ve Performans Değerlendirme Kriteri (PEC) üzerindeki etkileri çalışılmıştır. Sayısal analizler ANSYS Fluent kullanılarak 2000-14000 Reynolds Sayısı aralığında gerçekleştirilmiştir. Sonuçlar incelendiğinde, tüm akışkanlar için, laminer akış, geçiş akışı ve tamamen gelişmiş türbülanslı akış durumunda kabartma derinliği arttıkça Nusselt Sayısı ve aynı zamanda da sürtünme katsayısının arttığı görülmüştür. Laminer rejimde PEC daki artış etkisi türbülans rejimine göre oldukça fazladır. Performans Değerlendirme Kriterinin değişimi akış rejimine ve kabartma derinliğine oldukça bağlıdır. Genel olarak, laminer akışta nano-akışkan konsantrasyonu ve kabartma derinliği arttıkça Performans Değerlendirme Kriterinin önemli ölçüde arttığı görülmüştür.

Anahtar Kelimeler: Isı transferi iyileştirmesi, nano-akışkan, kapsül tipi kabartma, sayısal analiz

INTRODUCTION

Heat transfer in tubes is a field of interest for many researchers due to its usability and accessibility in many engineering applications, such as heat exchangers, which

are widely used in refrigeration, air conditioning, space heating, power generation, chemical processing for cooling or heating purposes, district heating systems,

renewable energy systems, geothermal water distribution systems, solar collectors, etc.

In the variety of these applications, main challenge is to increase the heat transfer performance of the systems per unit area or volume regarding the limits of sizing to achieve this goal. This challenge offers an opportunity for improvement to develop methods to make heat transfer equipment more compact and achieve a high heat transfer rate using less pumping power to minimize the energy and material costs. For this, the most effective parameter is the heat transfer coefficients on the hot and cold fluid sides, and the heat transfer coefficient can be increased by one or more active or passive methods.

Methods that improve heat transfer by giving additional energy are called active methods such as surface vibration and flow vibration, electrostatic fields, and mechanical aids. Methods that improve heat transfer rate without additional energy requirement are called the passive method which include surface geometrical modifications to increase the heat transfer surface area or using additives in the working fluid, such as nanoparticles. Passive methods are more advantageous than active methods since they do not require external energy and are easier to apply. In the scope of this study, two passive methods have been employed for heat transfer enhancement.

Most common passive methods of geometrical modifications found in the literature include louvered strips (Eiamsa-Ard et al., 2008), twisted tapes (Tabatabaie et al., 2014), helical screw inserts (Pathipakka et al., 2010), wire coil insert (Chandrasekar et al., 2013) and dimples on the tube surface Li et al. (2015). These are used to increase the turbulent flow characteristics through the tube and thus enhance the heat transfer coefficient. One of the most applicable and advantageous passive methods is using three-dimensional dimples along the heat transfer surface. The main reason of heat transfer enhancement along the dimple surface is that thermal boundary layer formation is disturbed and hence, Nusselt number and heat transfer coefficient increases. (Cheraghi et al., 2019)

While increasing the heat transfer coefficient, geometrical modifications may also cause increase in the friction which is generally not desired. As result of increase in the friction, the pressure drop and necessary pump/compressor work increases. Thus the proper design and application of geometrical modifications, including the dimples, is crucial. For this reason, a dimensionless performance evaluation criterion (PEC) is used to assess the thermal-hydraulic performance of heat transfer enhancement techniques. (Li et al., 2016).

Flow regime is found to have a significant effect on the heat transfer performance. Enhancement of heat transfer

using dimpled tubes has been studied for different Reynolds numbers in the literature.

Cheraghi et al., (2020) conducted a numerical study on a new configuration of deep dimpled tube under constant heat flux to evaluate the effects of dimple pitch, dimple diameter and dimple depth on the heat transfer and flow field for considering Reynolds numbers of 500, 1,000 and 2,000. The study showed that decreasing the distance between dimples while increasing the dimple depth and diameter would result increase in the Nusselt number and friction factor. A sudden growth in the friction factor is observed due to the formation of vortexes behind each dimple, causing a larger pressure drop than that of plain tubes. According to the performance evaluation criteria, the higher enhancement for the deep dimpled tubes can be achieved by increasing the dimple diameter, pitch and Reynolds number and reducing the dimple depth.

On the transitional ($2000 < Re < 4000$) and the moderate ($4000 < Re < 10000$) ranges of Reynolds numbers, (Vicente et al., 2002) experimentally studied flow and heat transfer in helically dimpled tubes by using water and ethylene glycol and ten different configurations of tubes with various depths and pitches of dimples. The results showed that as the depth of dimples increased, the heat transfer performance of the tube improved.

On higher Reynolds numbers, (turbulent flow $Re > 10000$), (Kumar et al., 2017) experimentally and numerically investigated the effects of dimples on the heat transfer and hydrodynamics performance of dimpled tubes for Reynolds numbers between 4,000 and 28,000 and using air as the working fluid. The study showed that the highest Reynolds numbers yielded the highest Nu and lowest friction factor as expected. On the other hand, increasing the stream and span-wise direction to a certain extent would positively affect heat transfer enhancement, and both thermal and hydraulic performance would increase if the stream and span-wise directions decrease. The author revealed that the optimum thermal and hydraulic performance is reached when stream and span-wise direction had the value of 15 times the dimple diameter.

Shape, size, depth, and pitch of the dimples are important properties that affect heat transfer performance in such flows. Ming et al. (2016) numerically studied the effects of geometrical parameters on heat transfer and pressure loss inside a dimpled tube. The results showed that the reduction in the pitch of dimples and increase in the depth contributed to the heat transfer enhancement. However, these variations increased the pressure loss.

Wang et al. (2010) experimentally investigated the heat transfer enhancement and friction factor of different shape dimpled tubes. Experimental data showed that tubes with ellipsoidal dimples simultaneously had higher Nusselt number and lower friction factor than the tubes with spherical dimples. Also, ellipsoidal dimples

roughness accelerated the transition to critical Reynolds number down to less than 1000.

Chen et al. (2001) experimentally studied six different dimpled tubes with different dimple parameters, ratio of depth to tube diameter, depth to pitch ratio and number of dimples on the tube surface. The Reynolds numbers taken in this experiment had ranged from 7,500 to 52,000. It was found that the enhancement in heat transfer reached 137% compared to standard plain tubes and the performance criteria showed values from 0.93 to 1.16 in which the dimpled tube with values above unity were considered to succeed in the performance enhancement.

Another important heat transfer enhancement method employs nanoparticles suspended in water solutions, called nanofluids to improve the thermo-physical properties of the working fluid. Combining this technique with surface alterations makes further enhancement of heat transfer characteristics. Nanofluids have proven to affect heat transfer positively, and the use of nanofluids in many research applications has been of interest to researchers, especially in the heat transfer and fluid dynamics communities due to advantages in improving heat transfer rate.

Because metals have higher thermal conductivity than nonmetals, metallic or metal oxide nanofluids have been chosen for heat transfer fluid. Xuan and Li (2000) achieved a remarkable heat transfer enhancement of 39% using 2% volume fraction of Cu nanoparticles dispersed in water. Briclot et al. (2020) have also accomplished a 40% increment in Nusselt number using Al_2O_3 water nanofluid with a volume fraction of 6.8% in their study intended for liquid cooling of electronic components. (Firoozi et al. 2020)

Khedkar et al. (2014) experimentally investigated the effect of different nanoparticle concentrations of a TiO_2 -water base nanofluid on the heat transfer performance in a concentric tube heat exchanger; hence the use of nanofluid was for cooling purposes in which the inner tube was for the nanofluid, and the outer tube was for water as a hot fluid. The coolant working range of this experiment had Reynolds numbers ranging from 300 to 4,000. They investigated the effects of different nanoparticle concentrations (2% and 3%), and showed that increasing the Reynolds number resulted in a significant increase in heat transfer performance compared to pure water as a cooling fluid.

Ho et al. (2018) performed experimental investigations on a tube with circular cross-sections under constant heat flux for laminar flow with Reynolds numbers ranging from 120 to 2,000 using an Al_2O_3 -water nanofluid as a working fluid. To evaluate the effects of the nanofluid subjected to variable operating temperatures on heat transfer characteristic and pressure differences, an additional numerical study was conducted. The results proved that using Al_2O_3 nanoparticles in a water based

nanofluid for forced heat transfer applications would minimize the temperature difference between the mean fluid temperature and wall temperature that results a better heat transfer characteristic but increases the pressure drop.

In this study, heat transfer enhancement by new capsule dimpled tube surfaces is numerically investigated with pure water and Al_2O_3 -water nanofluid for different geometrical properties of dimpled tubes and different concentrations of nanoparticles. Heat transfer enhancement regarding Nusselt number and heat transfer coefficient, and pressure drop regarding friction factor changes are investigated, and performance evaluation criteria is calculated and compared for different cases.

METHODOLOGY

In the present study, flow of pure water and Al_2O_3 -water nanofluid in a dimpled tube with a constant surface heat flux was considered. Methodology followed is based on the mathematical modelling and numerical solution of the governing equations. ANSYS Fluent was used for the numerical simulations. Then, from the numerically obtained temperature and flow fields, the heat transfer coefficient and friction factor were calculated. Different cases were simulated and compared to evaluate the effects of the dimple geometrical parameters, Reynolds number and nano particle concentration on heat transfer coefficient and PEC.

Problem Geometry and Mathematical Formulation

The geometry of the flow domain considered in the study is shown in Fig. 1. As seen in the figure, heat transfer surface has capsule dimples, and the flow domain is extended with an undimpled inlet section. The tube cross section is circular. Fluid is flowing through the tube. A constant heat flux is applied through the outer surface.

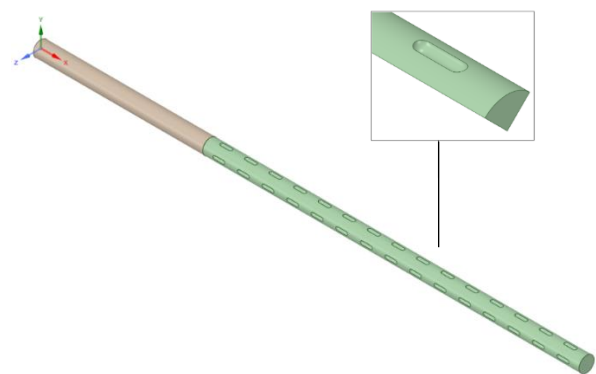


Figure 1. Capsule dimpled tube with undimpled entrance section and a periodic quarter sector used for the analysis.

As shown in Fig. 1, the tube consists of 200 mm undimpled entrance length and 440 mm dimpled region. The tube diameter is 18 mm and kept constant for all the simulations.

A sketch of the geometry of dimples is shown in Fig. 2. As seen in this figure, a dimple is characterized by depth (h), length (d), pitch (P) and length from center to center (w). In the present study, dimple depth is varied as all other dimple parameters are kept constant.

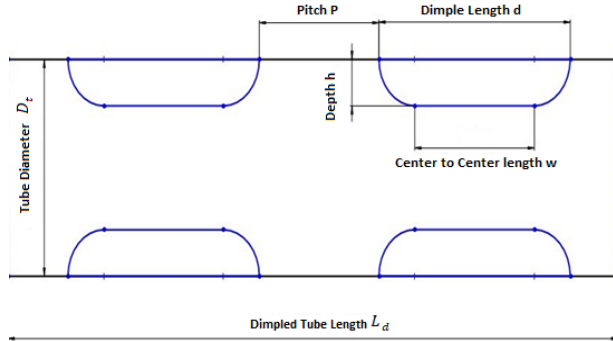


Figure 2 Schematics view of the dimple geometry and important dimple parameters.

Governing Equations

To derive the governing equations for the current physical problem, the equations of conservation of mass, Newton's Second Law, and the Law of Conservation of Energy should be formulated. For the derivation of the governing equations the following assumptions were made: Flow is three-dimensional, steady, viscous, incompressible, turbulent, body forces are negligible, working fluid properties are constant, and the fluid is Newtonian.

In addition, it is assumed that the nano particle distribution in the flow field is uniform, nanoparticles and the base fluid are in thermal equilibrium, and the velocities of the nanoparticles and base fluid are equal. The physical properties of the nanoparticle-water mixture are calculated using the correlations in the literature as given below.

Based on the above assumptions, Reynolds averaged governing equations can be written as below:

Continuity equation:

$$\frac{\partial \bar{u}}{\partial x} + \frac{\partial \bar{v}}{\partial y} + \frac{\partial \bar{w}}{\partial z} = 0 \quad (1)$$

Where \bar{u} , \bar{v} and \bar{w} are the time-averaged velocity components in the x , y and z directions, respectively

Momentum equations:

x -direction:

$$\rho_{nf} \left(\bar{u} \frac{\partial \bar{u}}{\partial x} + \bar{v} \frac{\partial \bar{u}}{\partial y} + \bar{w} \frac{\partial \bar{u}}{\partial z} \right) = -\frac{\partial p}{\partial x} + \mu_{nf} \left(\frac{\partial^2 \bar{u}}{\partial x^2} + \frac{\partial^2 \bar{u}}{\partial y^2} + \frac{\partial^2 \bar{u}}{\partial z^2} \right) - \left(\frac{\partial \bar{u}'^2}{\partial x} + \frac{\partial \bar{u}'v'}{\partial y} + \frac{\partial \bar{u}'w'}{\partial z} \right) \quad (2)$$

y -direction:

$$\rho_{nf} \left(\bar{u} \frac{\partial \bar{v}}{\partial x} + \bar{v} \frac{\partial \bar{v}}{\partial y} + \bar{w} \frac{\partial \bar{v}}{\partial z} \right) = -\frac{\partial p}{\partial y} + \mu_{nf} \left(\frac{\partial^2 \bar{v}}{\partial x^2} + \frac{\partial^2 \bar{v}}{\partial y^2} + \frac{\partial^2 \bar{v}}{\partial z^2} \right) - \left(\frac{\partial \bar{v}'u'}{\partial x} + \frac{\partial \bar{v}'^2}{\partial y} + \frac{\partial \bar{v}'w'}{\partial z} \right) \quad (3)$$

z -direction:

$$\rho_{nf} \left(\bar{u} \frac{\partial \bar{w}}{\partial x} + \bar{v} \frac{\partial \bar{w}}{\partial y} + \bar{w} \frac{\partial \bar{w}}{\partial z} \right) = -\frac{\partial p}{\partial z} + \mu_{nf} \left(\frac{\partial^2 \bar{w}}{\partial x^2} + \frac{\partial^2 \bar{w}}{\partial y^2} + \frac{\partial^2 \bar{w}}{\partial z^2} \right) - \left(\frac{\partial \bar{w}'u'}{\partial x} + \frac{\partial \bar{w}'v'}{\partial y} + \frac{\partial \bar{w}'^2}{\partial z} \right) \quad (4)$$

In these equations, p , ρ_{nf} and μ_{nf} denote the pressure, effective density (mixture density) and effective viscosity (mixture viscosity) of the nanofluid, respectively.

Energy equation:

$$\text{div}(\rho_{nf} \bar{V} C_{p,nf} \bar{T}) = \text{div}(k_{nf} \text{grad}(\bar{T})) - \rho_{nf} \bar{T}' C_{p,nf} \bar{V}' \quad (5)$$

where, T is the temperature, k_{nf} is the effective thermal conductivity (mixture conductivity) and $C_{p,nf}$ is the effective specific heat (mixture specific heat) of the nanofluid.

Boundary conditions

Considering the physics of the problem described above, the boundary conditions can be expressed as follows:

- The velocity at the inlet is only in axial direction and uniform.
- Inlet temperature is uniform and constant (293 K).
- Uniform heat flux is applied along the surface of the tube (10,000 W/m²).
- The exit gage pressure is zero.

Further explanations regarding boundary conditions are found in the following parts.

Properties of nanofluid

The properties of the nanofluid are calculated using the equations proposed by different researchers in the literature.

Calculation of nanofluid density is carried out using the correlation proposed by Cho and Pak (1998) as below:

$$\rho_{nf} = (1-\varphi)\rho_{bf} + \varphi\rho_{np} \quad (6)$$

where φ , is volume concentration of the nano particles, the subscripts bf and np refer to base fluid and nanoparticles, respectively.

The effective specific heat of the nanofluid ($C_{p,nf}$) can be calculated based on the expression proposed by Xuan and Roetzel (2000):

$$(C_p)_{nf} = \frac{(1-\varphi)(\rho C_p)_{bf} + \varphi(\rho C_p)_{np}}{\rho_{nf}} \quad (7)$$

The Maxwell's model (1954) is used for evaluation of the thermal conductivity as shown below:

$$k_{nf} = \frac{k_{np} + 2k_{bf} - 2\varphi(k_{bf} - k_{np})}{k_{np} + 2k_{bf} + \varphi(k_{bf} - k_{np})} k_{bf} \quad (8)$$

where k_{np} , k_{bf} and φ are the thermal conductivity of nanoparticles, thermal conductivity of the fluid and the volume concentration, respectively.

For the calculation of the effective viscosity, expression developed by Pak and Cho (1998) is used.

$$\mu_{nf} = \mu_{bf} (1 + 39.11\varphi_{np} + 533.9\varphi_{np}^2) \quad (9)$$

Important Flow Parameters

Reynolds number is one of the important parameters used to characterize fluid flows. For the problem under consideration, Reynolds number is defined in terms of mixture properties as:

$$Re = \frac{\rho_{nf} U D_h}{\mu_{nf}} \quad (10)$$

where ρ_{nf} is the nanofluid density, U the average velocity, D_h the hydrodynamic diameter (for circular tube D_h being the same as the tube diameter) and μ_{nf} is the dynamic viscosity of the nanofluid.

Nusselt number quantifies the convection heat transfer relative to conduction heat transfer within a fluid layer (Cengel, 2014). The average Nusselt number is defined as

$$Nu = \frac{h D_h}{k_{nf}} \quad (11)$$

where h , k_{nf} and D_h are the average heat transfer coefficient, thermal conductivity of nanofluid and hydraulic diameter of the tube, respectively.

The average friction factor for the plain tube and capsule dimpled tube are calculated using the Darcy equation as (Cengel, 2014):

$$f = \frac{2 D_h \Delta p}{\rho_{nf} L U^2} \quad (12)$$

To ensure that the flow is hydrodynamically fully developed before entering the dimpled tube, it is important to have the necessary entrance length. To meet this requirement, the tube is extended by a plain section at inlet end as seen in Fig. 1.

Heat Transfer Enhancement and Performance Evaluation Criteria

Contribution of the dimples to the heat transfer rate is determined by comparing the Nusselt number with the Nusselt number for non-dimpled plain cases. For the estimation of the enhancement, heat transfer enhancement ratio (ER), which is the ratio of the Nusselt number in an enhanced case (dimpled tube) to the Nusselt number in the plain tube case (plain tube) (Kukulka et al., 2013), i.e.

$$ER = \frac{Nu_d}{Nu_p} \quad (13)$$

Since the geometrical modification at the heat transfer surface may cause an increase in the pressure drop (friction coefficient), a performance criterion combining the Nusselt number and friction coefficient (pressure drop) is defined. This criterion is known as Performance evaluation criteria (PEC), and different expression are proposed. PEC is the ratio of heat transfer enhancement to the hydraulic losses. Expression used for PEC proposed by Gee and Webb (1980) is given as:

$$PEC = \frac{Nu_d}{Nu_p} \left(\frac{f_d}{f_p} \right)^{\frac{1}{3}} \quad (14)$$

In this study the performance evaluation criterion (PEC) is used to estimate the performance of the different cases considered.

Turbulence Equations

In the current study, laminar, transient, and turbulent flows were considered. Literature review shows that for low Reynolds number flows (one considered in this study) the realizable k- ϵ model yields better predictions in near wall flows in comparison to other turbulence models (Alshehri et al., 2020). Hence, the realizable k- ϵ turbulence model was chosen for the numerical simulations.

For turbulent kinetic energy k , the transport equation is;

$$\frac{\partial(\rho k u_i)}{\partial x_i} = \frac{\partial}{\partial x_i} \left[\left(\mu + \frac{\mu_t}{\sigma_k} \right) \frac{\partial k}{\partial x_i} \right] + G_k - \rho \epsilon - Y_M \quad (15)$$

Where G_k , Y_M and σ_k represent the generation of turbulent kinetic energy due to the mean velocity gradient, the contribution of fluctuating dilatation in compressible turbulence to overall dissipation rate and a turbulent Prandtl number for k , respectively.

In addition, the transport equation for the turbulent kinetic energy dissipation rate (ϵ), is written as:

$$\frac{\partial(\rho \epsilon u_i)}{\partial x_i} = \frac{\partial}{\partial x_i} \left[\left(\mu + \frac{\mu_t}{\sigma_\epsilon} \right) \frac{\partial \epsilon}{\partial x_i} \right] + \rho C_1 S \epsilon - \rho C_2 \frac{\epsilon^2}{k + \sqrt{v \epsilon}} \quad (16)$$

where;

$$C_1 = \max \left[0.43, \frac{\eta}{\eta + 5} \right], \eta = \frac{k}{\epsilon} \sqrt{2S_{ij}S_{ij}} \quad (17)$$

The constants are: $C_2 = 1.9$, $\sigma_k = 1.0$ and $\sigma_\epsilon = 1.2$.

The eddy viscosity μ_t is calculated as

$$\mu_t = \rho C_\eta \frac{k^2}{\epsilon} \quad (18)$$

C_η is calculated as

$$C_\eta = \frac{1}{A_0 + A_s \frac{kU^*}{\epsilon}} \quad (19)$$

where

$$U^* = \sqrt{S_{ij}S_{ij} + \tilde{\Omega}_{ij}\tilde{\Omega}_{ij}}, A_0 = 4.04, A_s = \frac{\sqrt{6} \cos \phi}{2} \quad (20)$$

$$\phi = 3 \cos^{-1} \sqrt{6W} \text{ and } W = \frac{S_{ij}S_{ik}S_{ki}}{\tilde{S}^3} \quad (21)$$

and

$$\tilde{S} = \sqrt{S_{ij}S_{ij}}, \quad \tilde{\Omega}_{ij} = 0.5 \left(\frac{\partial u_j}{\partial x_i} + \frac{\partial u_i}{\partial x_j} \right) \quad (22)$$

NUMERICAL SOLUTION

ANSYS Fluent software is utilized to solve the nonlinear governing equations presented in the previous part for the described physical problem of steady, incompressible, turbulent flow and heat transfer in a capsule dimpled tube with water and nanofluid as the working fluids.

The pressure and velocity coupling the Semi-Implicit Method for Pressure Linked Equations (SIMPLE) algorithm is used. Momentum and energy equations are discretized by the second order upwind scheme. For the convergence criteria, the residuals for all the variables are set to 10^{-6} .

Mesh Generation and Mesh Independence Study

To ensure the reliability and compatibility of the numerical results, a good computational mesh should be generated. As seen in Fig. 3, a quarter sector of the pipe enclosing one row of the dimples was considered as the computational field. Due to the 3-dimensional capsule geometry, a 3-dimensional mesh is formed. (For the simulations in plain pipes a 2-D mesh system is used.) To resolve the sublayer regions developed near the tube wall, a fine mesh structure usually with $y^+ \cong 1$ is implemented. The tetrahedral mesh structure was used, and it was produced using ANSYS meshing tool.



Figure 3. Mesh structure of capsule dimpled tube.

To verify the validity of the simulation results and keeping the computational costs as low as possible, a mesh independence study was conducted. For the mesh independence study, case with Reynolds numbers 14,000 is considered and computations were repeated with different mesh sizes. To determine the optimum mesh size, Nusselt numbers obtained with different mesh sizes for different dimple depths were compared. The average Nusselt numbers calculated from the numerical results with different meshes are shown in Fig. 4 and Fig. 5 for plain and dimpled tubes, respectively.

Analysis of Fig. 4 shows that a mesh 700,000 with nodes yields mesh independent results for plain pipe flows considered. Also, from Fig. 5 conclude that a mesh of 3.0 million nodes is good for mesh independent results for different dimple depths considered. Hence, for all the plain tube simulations and dimpled tube cases, mesh size of 700,000 and 3.0 million was used, respectively.

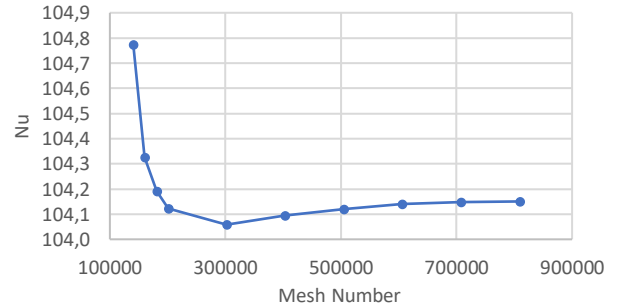


Figure 4. Variation of Nusselt number obtained with mesh number for the plain tube.

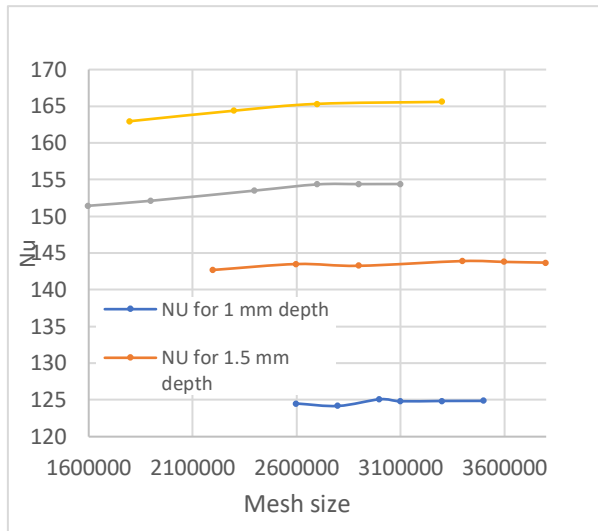


Figure 5. Variation of Nusselt numbers obtained with mesh sizes for dimple depths of 1.0, 1.5, 2.0 and 2.5 mm.

Comparison of Turbulence Models

To assess the suitability of the turbulence model used, a sequential study was conducted for flows with different Reynolds numbers using different turbulence models (realizable k-ε, standard k-ε with enhanced wall treatment for the near wall flow and the SST k-ω). The Nusselt numbers and friction factors are obtained with different models and compared with the Petukhov correlation given below (Cengel, 2014):

$$Nu = \frac{\left(\frac{f}{8}\right)(Re-1000)Pr}{1+12.7\left(\frac{f}{8}\right)^{0.5}\frac{2}{(Pr^3-1)}} \quad (23)$$

This correlation is valid for the ranges of $3,000 < Re < 5 \times 10^6$ and $0.5 \leq Pr \leq 2,000$.

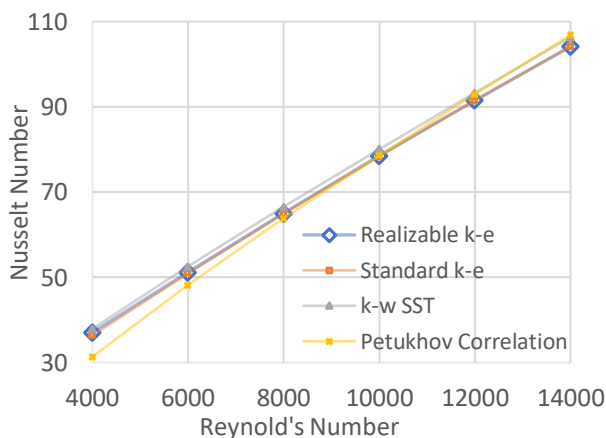


Figure 6. Comparison of Nusselt Numbers obtained using different turbulence models with the Petukhov correlation

As seen in Fig. 6, Nusselt numbers for the realizable k-ε model has a better approach than the other models for all Reynolds numbers being considered. Based on that, the realizable k-ε turbulence model is selected.

Validation of Numerical Results

To validate the numerical method and computer program used in the present study, a verification study was carried out considering the flow of water in the plain and dimpled tubes separately.

Numerical computations were performed for flows with different Reynolds numbers. The Nusselt numbers calculated from the numerical results and Nusselt numbers calculated from Petukhov correlation were calculated and compared in Fig. 7. As seen in Fig. 7, the results show a good agreement. For the case of a fully developed laminar flow, Nusselt number was calculated as 4.29, which is excepted when compared with the literature (Cengel, 2014).

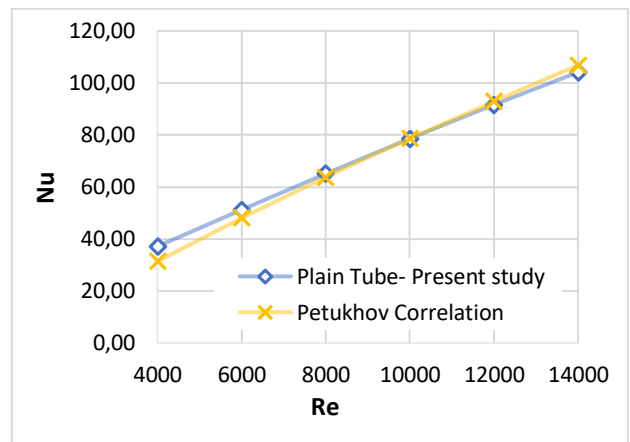


Figure 7. Comparison of numerically calculated Nusselt numbers with Petukhov correlation in plain tube.

The friction factor calculated from the numerical results in the plain tube also shows good agreement with the Petukhov correlation given below, with an average value of 0.03 and the errors fall within the acceptable range.

$$f = (0.790 \ln Re - 1.64)^{-2} \quad (24)$$

Validity range of this expression is $3000 < Re < 5 \times 10^6$.

To demonstrate the validity of the numerical results in the dimpled tubes, a verification study was carried out based on the study by Sabir et al. (2020) in ellipsoidal dimpled tube. The tube used in the study has a diameter of 17.3 mm, dimple diameter and depth are 3.9 mm and 1.17 mm, respectively with a pitch of 10 mm. A constant heat flux of $10,000 \text{ W/m}^2$ was applied.

The Nusselt numbers are compared in Fig 8. Maximum difference in the Nusselt numbers is calculated about 10%. The average friction factor is calculated as 0.06 and compared with the results given by Sabir et al. (2020) a 15% difference is observed. These differences are considered in the acceptable ranges.

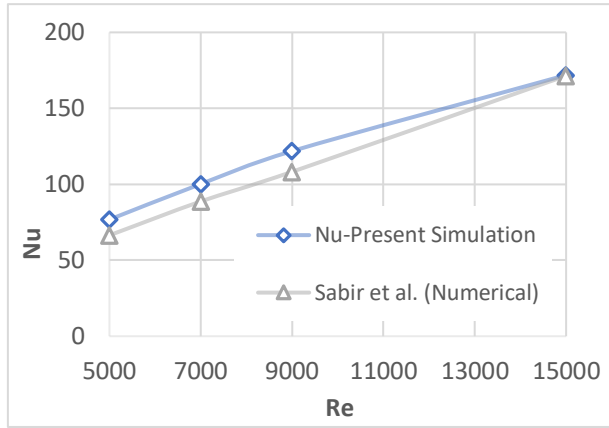


Figure 8. Comparison of numerically calculated Nusselt numbers with study of Sabir et al. (2020) for dimpled tubes.

RESULTS AND DISCUSSIONS

The objective of the study is to investigate the heat transfer enhancement for a tube flow using dimpled tube surface and nanofluid. For this purpose, numerical simulations were performed in plain and dimpled tubes. To investigate the effects of dimple depth on the heat transfer rate, the computations were performed with dimple depths of 1, 1.5, 2 and 2.5 mm for pure water flow and nanofluid flow with nanoparticle volumetric concentrations of 1%, 2% and 3%. The values of geometrical parameters of the tube and dimples are given in Table 1. The computations were performed for Reynolds numbers 2,000, 4,000, 6,000, 8,000, 10,000, 12,000 and 14,000.

Table 1. Values of tube and of dimple geometric parameters.

Tube Diameter D_t	18 mm
Length of dimpled section L_d	440 mm
Dimple length d	12/13/14/15 mm
Pitch P	15 mm
Dimple Depth h	1/1.5/2/2.5 mm
Center to center length w	10 mm
Entrance Length	12,000 mm (Laminar) 200 mm (Turbulent)

As the nanofluid, water- Al_2O_3 mixture is used. Thermophysical properties of the Al_2O_3 -water nanofluid are calculated using the expressions given in Section 2 and given in the Table 2 for different volume concentrations (Minea, 2017).

Table 2. Thermophysical properties of Al_2O_3 -water nanofluid for different nanoparticle volume concentrations

Volume Concentration (%)	ρ (kg/m^3)	μ (Pa.s)	c_p (J/kgK)	k (W/mK)
1	1,026.2	0.001444	4,048.8	0.63
2	1,056	0.001996	3,924.2	0.649
3	1,085.7	0.002654	3,806.3	0.667

The simulations were performed first for plain tube cases using pure water and nanofluid as working fluid. Then for dimpled tubes again for pure water and nanofluid as working fluid. The effects of Reynolds number, dimple depth and nanoparticle volumetric concentration on Nusselt number and friction factor are calculated. To characterize the heat transfer enhancement, the performance evaluation criteria (PEC) is also calculated for all the cases considered. The results are presented as graphs and analyzed below.

Effects of Capsule Dimples

Fully developed flow enters the dimpled tubes. Due to the dimples on the surface, considerable changes take place in the velocity and temperature fields, especially near the tube wall. Velocity increases and drops form because of the change in the flow cross sectional area due to the dimples.

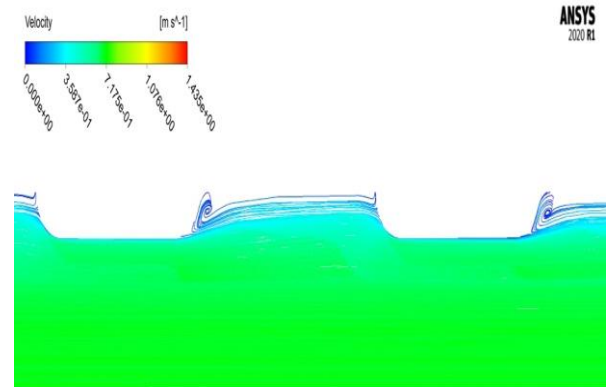


Figure 9. Velocity contours at a section of dimpled pipe for the flow of pure water flow with $Re=10000$ and dimple depth of 2 mm.

For the flow of pure water with $Re=10000$ and dimple depth of 2 mm, velocity contours for the dimples at the middle of the pipe on z direction along the flow are given in Fig. 9. As seen in Fig. 9, over the dimples, boundary layer thickness decreases while some recirculation forms between the dimples at downstream face of the dimples.

From the temperature field calculated, the average heat transfer coefficients and then average Nusselt numbers were calculated for the flow of pure water at different Reynolds numbers in tubes with different dimple heights. These Nusselt number results are shown in Fig. 10.

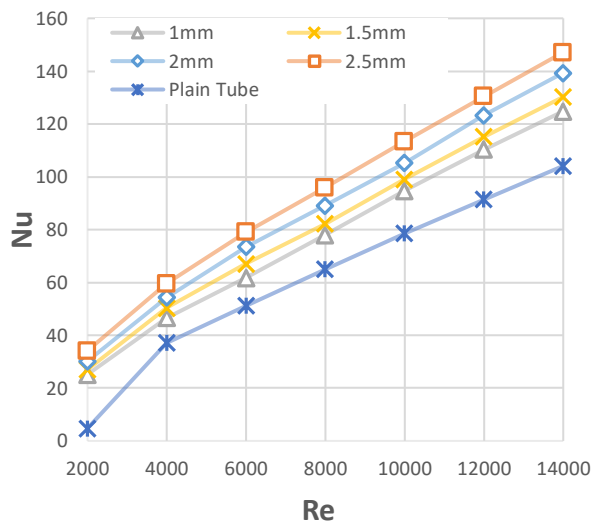


Figure 10. Variation of Nusselt number with Reynolds numbers at different dimple depths for pure water flows.

One can observe from Fig. 10 that both with increasing Reynolds number and the dimple depth, the Nusselt number increases. It is also seen in this figure that the increase in Nusselt number is more pronounced as flow regime changes from laminar regime ($Re = 2000$) to turbulent regime ($Re=4000$). This behavior is seen in both plain and dimpled tubes. In this transition region, it is seen that the rate of increase of the Nusselt number is higher in plain pipe flows than that of dimpled pipes. The reason for this phenomenon is that, for low Reynolds number flows, the presence of dimples in a tube surface affects the flow domain by generating vortices which disturb the flow and allow the flow to reach a turbulent state even at lower Reynolds numbers where the flow is considered to be laminar in a plain tube. (Suresh et al., 2011). In the fully turbulent flows, the increase in the Nusselt numbers is almost linear for both plain and dimpled pipes. Increasing the dimple depth also increases the tube surface area accordingly and in contrast, allow the convective heat transfer to occur far more efficiently, thereby increasing the Nusselt number (Firoozi, 2020).

In Fig. 11, variations of friction factor with Reynolds number in dimpled pipes with different dimple depths and plain pipe for pure water flow are given. In this figure it is clearly seen that dimples cause an increase in the friction factor compared to the plain tube as expected. In the transition region, as in the Nusselt number variation, the variation of the friction factor in plain pipe is also high compared to the dimpled tube flows. For the laminar flows, increase in the friction factor is much higher with increasing dimple depth.

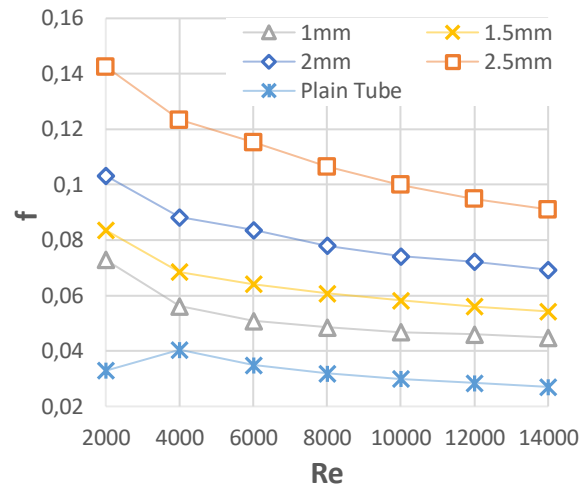


Figure 11. Variation of friction factor with Reynolds numbers at different dimple depths for water.

The performance evaluation criteria (PEC) which is an important tool to study the heat transfer and pressure drop within the capsule dimpled tubes calculated and plotted in Fig. 12. With the aid of PEC, performance of the dimpled tube can be evaluated considering both Nusselt number and friction factor effects.

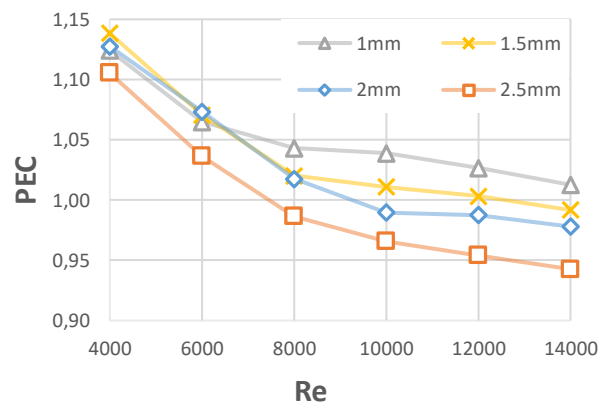


Figure 12. Variation of PEC with Reynolds numbers for different dimple depths for water.

As can be seen in Fig. 12, PEC values are decreasing with Reynolds number and dimple depth. For the transitional flow, ($Re=4000-6000$) 1.5 mm depth yields the best performance. However, as Re increases and flow becomes more and more turbulent, the dimples with 1 mm depth give better performance. It can be seen that, increasing dimple depth increases the performance till an optimum depth value. After that, especially in the turbulent region, PEC starts to drop. So when 2 mm dimple depth is used in the tubes, for the lower Reynolds Number flows (laminar and transition) it gives better performance, but when flow velocity increases and turbulence dominates, the friction factor does not fall, on the contrary it increases because of the dimples and performance decreases. When the graphic is further examined, it can be seen that, 2.5 mm dimple depth has the worst characteristics since the friction factor

increases dramatically and flow becomes blocked due to decreased flow area for high dimple depths.

The effects of nanofluid

To investigate the effects of nanofluid on heat transfer enhancement, the simulations were performed for flows of Al_2O_3 -water nanofluid with volumetric nanoparticle concentrations of 1%, 2% and 3% for different dimple depths (1.0, 1.5, 2.0 and 2.5 mm) and different Reynolds numbers. Again, from the simulated temperature, velocity, and pressure fields, Nusselt numbers, friction factors and performance evaluation criterion were calculated. For Nusselt number variation, it is noted that, increasing capsule depth increases Nusselt number more than the water flow in capsule dimpled pipes. In Fig. 13, PEC variation for 1% nanofluid is given as an example. Trends for all concentrations are similar.

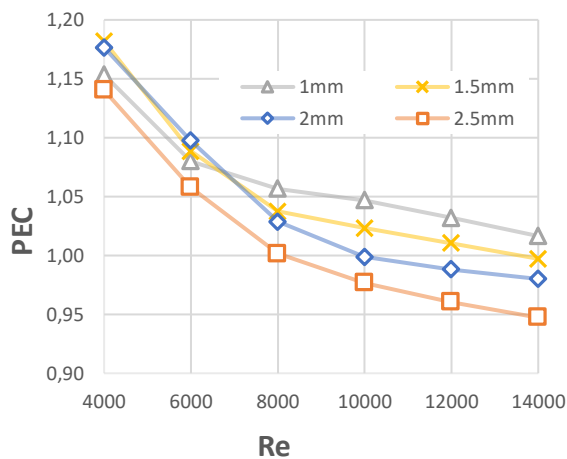


Figure 13. Variation of (PEC) with Reynolds numbers for different dimpled depths for Al_2O_3 -water nanofluid with 1% concentration.

The variations of PEC with dimple depths at different Reynolds number and nano particle concentrations are shown in Fig. 14. As seen in these figures, at all lower Reynolds numbers ($Re < 8000$) considered, PEC increases with increasing nano particle concentration. However, as Reynolds number increases, the effects of nano particles diminish.

In low Reynolds number flows, the presence of dimples affects the flow field by generating vortices which disturb the flow and allow the flow to reach a turbulent state even at lower Reynolds numbers where the flow is considered to be laminar in a plain tube. Hence, in the laminar region PEC increases with both increasing dimple depth and nanofluid concentration. This can be seen in Figure 14. PEC values for the laminar region are very high compared to transitional and turbulent flows.

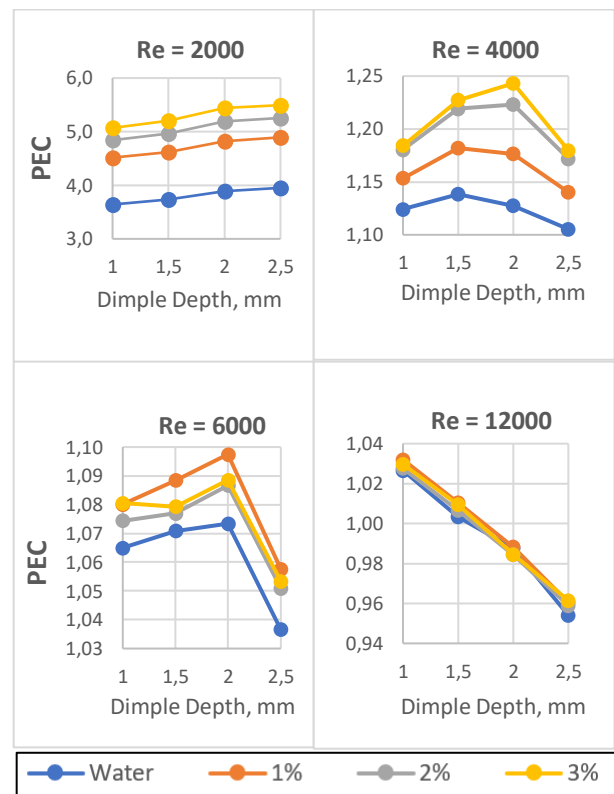


Figure 14. Effect of increasing dimple depth on PEC for different Reynolds Numbers for different nanofluid concentrations.

For the transition region, increase in volume concentration of nanofluid increases the PEC. On the other hand, as dimple depth increases, especially beyond 1.5 mm, it causes a reduction in performance for all cases. It should also be noted that with the increasing dimple depth, the blockage effects of the dimples increase which can cause and increase in friction coefficient. This may be because of the unpredictable flow phenomena that relates to the transition region.

On the early formation of turbulent flow around $Re=6000$, an increasing pattern in the PEC and a sudden drop can be seen around the 2 mm depth of dimple depth. In this region, 1 % in nanoparticle concentration of nanofluids shows best performance among all cases.

For a higher Re, (12000 for instance) The dimple depth adversely affects the performance since the friction factors are very high. The PECs drop dramatically with increasing depths. Moreover, the best performance is found for 1% nanofluid and a tube with a dimple depth of 1 mm.

CONCLUSION

A numerical investigation was carried out to investigate the heat transfer, pressure drop characteristics and performance evaluation criteria (PEC) for newly

proposed capsule dimpled tubes with pure water and Al₂O₃-water nanofluid as the working fluids. The study was performed for fully developed laminar, transition and turbulent flow conditions with uniform heat flux through the tube surface. The simulations were performed using ANSYS Fluent. For capsule dimpled tubes, three-dimensional; and for plain tubes, 2-D simulations were performed for steady state flow conditions.

Effects of Reynolds number, dimple depth, nano particle volumetric concentration on Nusselt number, friction factor and PEC were analyzed. The dimple depths varying between 1 and 2.5 mm, Reynolds numbers ranging between 2000-14000, nano particle concentration varying between 1% and 3% are considered in the numerical simulations.

The findings of the study can be summarized as following:

- For water as the heat transfer fluid, the Nusselt number increases with increasing dimple depths at all Reynolds numbers considered. Unfortunately, the friction factor also increases with increasing dimple depth. Hence, as PEC shows a significant increase in the laminar region, it starts to decrease gradually in the transition and then in the turbulent regions.
- For Al₂O₃-Water nanofluid as the heat transfer fluid, the trend of variation of Nusselt number, friction factor and PEC with Reynolds number is similar to those of pure water. Furthermore, for each dimple depth considered, as the nanoparticle concentration increases, Nusselt number and the friction factor increases significantly compared to plain tube.
- For small Re (laminar flow), higher depths of dimples seem to have a better performance due to the increase in Nusselt number for dimpled tube compared to plain tube.
- In high Reynolds numbers, the nanoparticle concentration has less effect on increasing PEC, since deeper dimples causes the friction factor to increase very much.
- A blockage phenomenon is observed when dimple depths become deeper. This acts as barrier against fluid flow, which in turn results in an increase in the friction factor and a decrease in PEC. This also depends on the Reynolds Number.

When considering PEC, the best performance among the cases studied are found as follows:

- For laminar region, 2.5 mm dimple depth and 3% nanoparticle concentration.
- For transition region, 2 mm dimple depth and 3% nanoparticle concentration.
- For early turbulence region (Re=6,000), 2 mm dimple depth and 1% nanoparticle concentration.
- For turbulence region (Re≥8,000), 1 mm dimple depth and 1% nanoparticle concentration.

REFERENCES

- Alshehri, F., Goraniya, J., and Combrinck, M. L., 2020, Numerical investigation of heat transfer enhancement of a water/ethylene glycol mixture with Al₂O₃-TiO₂ nanoparticles. *Applied Mathematics and Computation*, 369, 124836.
- Batchelor, G. K., 1977, The effect of Brownian motion on the bulk stress in a suspension of spherical particles. *Journal of fluid mechanics*, 83(1), 97-117.
- Briclot, A., Henry, J. F., Popa, C., Nguyen, C. T. and Fohanno, S., 2020, Experimental investigation of the heat and fluid flow of an Al₂O₃-water nanofluid in the laminar-turbulent transition region. *International Journal of Thermal Sciences*, 158, 106546.
- Cengel, Y., 2014, *Heat and mass transfer: fundamentals and applications*. McGraw-Hill Higher Education.
- Chandrasekar, M., Suresh, S. and Bose, A. C., 2010, Experimental studies on heat transfer and friction factor characteristics of Al₂O₃/water nanofluid in a circular pipe under laminar flow with wire coil inserts. *Experimental Thermal and Fluid Science*, 34 (2), 122-130.
- Cheraghi, M. H., Ameri, M. and Shahabadi, M., 2020, Numerical study on the heat transfer enhancement and pressure drop inside deep dimpled tubes. *International Journal of Heat and Mass Transfer*, 147, 118845.
- Chen, J., Müller-Steinhagen, H. and Duffy, G. G., 2001, Heat transfer enhancement in dimpled tubes. *Applied thermal engineering*, 21 (5), 535-547.
- Corcione, M., 2011, Empirical correlating equations for predicting the effective thermal conductivity and dynamic viscosity of nanofluids. *Energy Conversion and Management*, 52 (1), 789-793.
- Eiamsa-Ard, S. and Promvonge, P., 2007, Heat transfer characteristics in a tube fitted with helical screw-tape with/without core-rod inserts. *International Communications in Heat and Mass Transfer*, 34 (2), 176-185.
- Firoozi, A., Majidi, S. and Ameri, M., 2020, A numerical assessment on heat transfer and flow characteristics of nanofluid in tubes enhanced with a variety of dimple configurations. *Thermal Science and Engineering Progress*, 19, 100578.
- Gee, D. L. and Webb, R. L., 1980, Forced convection heat transfer in helically rib-roughened tubes. *International Journal of Heat and Mass Transfer*, 23 (8), 1127-1136.

- Ho, C. J., Chang, C. Y., Yan, W. M. and Amani, P., 2018, A combined numerical and experimental study on the forced convection of Al₂O₃-water nanofluid in a circular tube. *International Journal of Heat and Mass Transfer*, 120, 66-75.
- Khedkar, R. S., Sonawane, S. S. and Wasewar, K. L., 2014, Heat transfer study on concentric tube heat exchanger using TiO₂-water based nanofluid. *International communications in Heat and Mass transfer*, 57, 163-169.
- Kukulka, D. J. and Smith, R., 2013, Thermal-hydraulic performance of Vipertex 1EHT enhanced heat transfer tubes. *Applied Thermal Engineering*, 61 (1), 60-66.
- Kumar, A., Maithani, R. and Suri, A. R. S., 2017, Numerical and experimental investigation of enhancement of heat transfer in dimpled rib heat exchanger tube. *Heat and Mass Transfer*, 53 (12), 3501-3516.
- Liu, B. Y. and Agarwal, J. K., 1974, Experimental observation of aerosol deposition in turbulent flow. *Journal of Aerosol Science*, 5 (2), 145-155.
- Minea, A. A., 2017, Hybrid nanofluids based on Al₂O₃, TiO₂ and SiO₂: numerical evaluation of different approaches. *International Journal of Heat and Mass Transfer*, 104, 852-860.
- Ming Li, Tariq S., Khana Ebrahim, Al-HajriaZahid and H. Ayubb, 2016, Single phase heat transfer and pressure drop analysis of a dimpled enhanced tube, *Applied Thermal Engineering*, 101, 2016, 38-46.
- Maxwell, J. C., 1954, *Electricity and magnetism* (Vol. 2). New York: Dover.
- Pak, B. C. and Cho, Y. I., 1998, Hydrodynamic and heat transfer study of dispersed fluids with submicron metallic oxide particles. *Experimental Heat Transfer an International Journal*, 11 (2), 151-170.
- Pathipakka, G. and Sivashanmugam, P., 2010, Heat transfer behavior of nanofluids in a uniformly heated circular tube fitted with helical inserts in laminar flow. *Superlattices and Microstructures*, 47 (2), 349-360.
- Sabir, R., Khan, M. M., Sheikh, N. A., Ahad, I. U. and Brabazon, D., 2020, Assessment of thermo-hydraulic performance of inward dimpled tubes with variation in angular orientations. *Applied Thermal Engineering*, 170, 115040.
- Suresh, S., Chandrasekar, M. and Sekhar, S. C., 2011, Experimental studies on heat transfer and friction factor characteristics of CuO/water nanofluid under turbulent flow in a helically dimpled tube. *Experimental Thermal and Fluid Science*, 35(3), 542-549.
- Tabatabaeikia, S., Mohammed, H. A., Nik-Ghazali, N. and Shahizare, B., 2014, Heat transfer enhancement by using different types of inserts. *Advances in Mechanical Engineering*, 6, 250354.
- Vicente, P. G., García, A. and Viedma, A., 2002, Heat transfer and pressure drop for low Reynolds turbulent flow in helically dimpled tubes. *International journal of heat and mass transfer*, 45 (3), 543-553.
- Wang, Y., He, Y. L., Lei, Y. G. and Zhang, J., 2010, Heat transfer and hydrodynamics analysis of a novel dimpled tube. *Experimental thermal and fluid science*, 34 (8), 1273-1281.
- Xuan, Y. and Roetzel, W., 2000, Conceptions for heat transfer correlation of nanofluids. *International Journal of heat and Mass transfer*, 43 (19), 3701-3707.
- Yimin X. and Qiang L., 2000, Heat transfer enhancement of nanofluids, *International Journal of Heat and Fluid Flow*, 21, 58-64.

ISI BİLİMİ VE TEKNİĞİ DERGİSİ İÇİN MAKALE HAZIRLAMA ESASLARI

Isı Bilimi ve Tekniği Dergisi'nde, ısı bilimi alanındaki özgün teorik ve deneysel çalışmaların sonuçlarının sunulduğu makaleler ve yeterli sayıda makaleyi tarayarak hazırlanmış olan literatür özeti makaleler yayınlanmaktadır. Makaleler, Türkçe veya İngilizce olarak kabul edilmektedir. Makaleler ilk sunumda serbest formatta hazırlanabilir. Ancak yayın için kabul edilmiş olan makaleler dergimizin basım formatına tam uygun olarak yazarlar tarafından hazırlanmalıdır. Aşağıda, ilk sunuş ve basıma hazır formatta makale hazırlamak için uyulması gereken esaslar detaylı olarak açıklanmıştır.

İLK SUNUŞ FORMATI

İlk sunuşta, makale A4 boyutundaki kağıda tek sütun düzeninde, 1.5 satır aralıklı ve sayfa kenarlarından 25'er mm boşluk bırakılarak yazılmalıdır. Yazı boyutu 11 punto olmalı ve **Times New Roman** karakter kullanılmalıdır. Şekiller, tablolar ve fotoğraflar makale içinde **olmaları gereken yerlere** yerleştirilmelidir. Makale, elektronik olarak editörün e-posta adresine gönderilmelidir.

BASIMA HAZIR MAKALE FORMATI

Hakem değerlendirmelerinden sonra, yayın için kabul edilmiş olan makaleler, dergimizin basım formatına tam uygun olarak yazarlar tarafından hazırlanmalıdır. Makaleler yazarların hazırladığı haliyle basıldığı için, yazarların makalelerini basım için hazır formatta hazırlarken burada belirtilen esasları titizlikle takip etmeleri çok önemlidir. Aşağıda, basıma hazır formatta makale hazırlamak için uyulması gereken esaslar detaylı olarak açıklanmıştır.

Genel Esaslar

Makaleler genel olarak şu başlıklar altında düzenlenmelidir: Makale başlığı (title), yazar(lar)ın ad(lar)ı, yazar(lar)ın adres(ler)i, özet (abstract), anahtar kelimeler (keywords), semboller, giriş, materyal ve metod, araştırma sonuçları, tartışma ve sonuçlar, teşekkür, kaynaklar, yazarların fotoğrafları ve kısa özgeçmişleri ve ekler. Yazılar bilgisayarda tek satır aralıklı olarak, 10 punto Times New Roman karakteri kullanılarak Microsoft Office Word ile iki sütun düzeninde yazılmalıdır. Sayfalar, üst kenardan 25 mm, sol kenardan 23 mm, sağ ve alt kenarlardan 20 mm boşluk bırakılarak düzenlenmelidir. İki sütun arasındaki boşluk 7 mm olmalıdır. Paragraf başları, sütunun sol kenarına yaslanmalı ve paragraflar arasında bir satır boşluk olmalıdır.

Birinci seviye başlıklar büyük harflerle kalın olarak, ikinci seviye başlıklar bold ve kelimelerin ilk harfleri büyük harf olarak ve üçüncü seviye başlıklar sadece ilk harfi büyük olarak yazılır. Bütün başlıklar sütunun sol kenarı ile aynı hizadan başlamalıdır ve takip eden paragrafla başlık arasında bir satır boşluk olmalıdır. Şekiller, tablolar, fotoğraflar v.b. metin içinde ilk atıf

yapılan yerden hemen sonra uygun şekilde yerleştirilmelidir. İlk ana bölüm başlığı, Özetten (Abstract'tan) sonra iki satır boşluk bırakılarak birinci sütuna yazılır.

Başlık, Yazarların Adresi, Özet, Abstract ve Anahtar Kelimeler

Yazılar Türkçe veya İngilizce olarak hazırlanabilir. Her iki durumda da makale özeti, başlığı ve anahtar kelimeler her iki dilde de yazılmalıdır. Eğer makale Türkçe olarak kaleme alınmışsa, Türkçe başlık ve özet önce, İngilizce başlık ve Özet (Abstract) sonra yazılır. Eğer makale İngilizce olarak kaleme alınmışsa önce İngilizce başlık ve özet (abstract) sonra Türkçe başlık ve özet yazılır. Başlık, sayfanın üst kenarından 50 mm aşağıdan başlar ve kalın olarak 12 punto büyüklüğünde, büyük harflerle bütün sayfayı ortalayacak şekilde yazılır. Yazar(lar)ın adı, adresi ve elektronik posta adresi başlıktan sonra bir satır boşluk bırakılarak yazılmalıdır. Yazarların adı küçük, soyadı büyük harflerle yazılmalı ve bold olmalıdır. Yazarların adresinden sonra üç satır boşluk bırakılarak, Özet ve Abstract 10 punto büyüklüğünde bütün sayfa genişliğinde yazılır. Özet ve Abstracttan sonra anahtar kelimeler (Keywords) yazılır.

Birimler

Yazılarda SI birim sistemi kullanılmalıdır.

Denklemler

Denklemler, 10 punto karakter boyutu ile bir sütuna (8 cm) sığacak şekilde düzenlenmelidir. Veriliş sırasına göre yazı alanının sağ kenarına yaslanacak şekilde parantez içinde numaralanmalıdır. Metin içinde, denklemlere '**Eş. (numara)**' şeklinde atıfta bulunulmalıdır.

Şekiller

Şekiller 8 cm (bir sütun) veya 16 cm (iki sütun) genişliğinde olmalıdır ve makale içerisinde olmaları gereken yerlere bilgisayar ortamında sütunu (veya bütün sayfa genişliğini) ortalayacak şekilde yerleştirilmelidir. Şekil numaraları (sıra ile) ve isimleri şekil **altına, 9 punto büyüklüğünde** yazılmalıdır.

Tablolar

Tablolar 8 cm (bir sütun) veya 16 cm (iki sütun) genişliğinde olmalıdır. Makale içerisinde olmaları gereken yerlere bilgisayar ortamında sütunu (veya bütün sayfa genişliğini) ortalayacak şekilde yerleştirilmelidir. Tablo numaraları (sıra ile) ve isimleri tablo **üstüne, 9 punto büyüklüğünde** yazılmalıdır.

Fotograflar

Fotograflar, siyah/beyaz ve 8 cm (bir sütun) veya 16 cm (iki sütun) genişliğinde olmalıdır. Fotograflar digitize edilerek, makale içinde bulunmaları gereken yerlere bilgisayar ortamında sütunu (veya bütün sayfa genişliğini) ortalayacak şekilde yerleştirilmelidir ve şekil gibi numaralandırılmalı ve adlandırılmalıdır.

Yazar(lar)ın Fotoğraf ve Kısa Özgeçmişleri

Yazarların fotoğrafları digitize edilerek, makalenin en sonuna özgeçmişleri ile birlikte uygun bir şekilde yerleştirilmelidir.

SEMBOLLER

Makale içinde kullanılan bütün semboller alfabetik sırada Özetten sonra liste halinde tek sütun düzeninde yazılmalıdır. Boyutlu büyüklükler birimleri ile birlikte ve boyutsuz sayılar (Re, Nu, vb.) tanımları ile birlikte verilmelidir.

KAYNAKLAR

Kaynaklar metin sonunda, ilk yazarın soyadına göre alfabetik sırada listelenmelidir. Kaynaklara, yazı içinde, yazar(lar)ın soyad(lar)ı ve yayın yılı belirtilerek atıfta

bulunulmalıdır. Bir ve iki yazarlı kaynaklara, her iki yazarın soyadları ve yayın yılı belirtilerek (Bejan, 1988; Türkoğlu ve Farouk, 1993), ikiden çok yazarlı kaynaklara ise birinci yazarın soyadı ve "vd." eki ve yayın yılı ile atıfta bulunulmalıdır (Ataer vd, 1995). Aşağıda makale, kitap ve bildirilerin kaynaklar listesine yazım formatı için örnekler verilmiştir.

Ataer Ö. E., Ileri A. and Göğüş, Y. A., 1995, Transient Behaviour of Finned-Tube Cross-Flow Heat Exchangers, *Int. J. Refrigeration*, 18, 153-160.

Bejan A., 1998, *Advanced Engineering Thermodynamics* (First Ed.), Wiley, New York.

Türkoğlu H. and Farouk B., 1993, Modeling of Interfacial Transport Processes in a Direct-Contact Condenser for Metal Recovery, *Proc. of 73rd Steel Making Conference*, Detroit, 571-578.

Türkoğlu H., 1990, *Transport Processes in Gas-Injected Liquid Baths*, Ph.D. Thesis, Drexel University, Philadelphia, PA, USA.

İnternet, 2004, Türkiye İstatistik Kurumu, *Atıksu İstatistikleri*, <http://www.tuik.gov.tr/HaberBulteni>.

DIĞER HUSUSLAR

Hakem değerlendirmesinden sonra kabul edilen makaleler, yukarıda açıklandığı şekilde dizilerek basıma hazırlandıktan sonra, bir elektronik kopyası editöre gönderilmelidir. Makalenin basıma hazır kopyası ile birlikte, "Telif Hakkı Devri Formu" da doldurularak gönderilmelidir. Telif Hakkı Devri Formu'na ve bu yazım klavuzuna www.tibt.org.tr adresinden ulaşılabilir.



TÜRK ISI BİLİMİ VE TEKNİĞİ DERNEĞİ
ÜYELİK BAŞVURU FORMU

FOTOĞRAFINIZ

A. Adınız Soyadınız :
Ünvanınız :
Doğum yeri : : Doğum tarihi: / / 19 T.C. Kimlik No:
İş Adresiniz :
Ev adresiniz :
Telefonunuz : İş Ev Cep
E-posta :

B. *Derneğe Asil üye Fahri üye olmak istiyorum.

1. Sizi tanıyan dernek üyesi (Üyelik için) :

2. Mezun olduğunuz
Yüksek Okullar Yıl Branşınız Ünvanınız

3. İlgilendiğiniz konular :

2015 yılı aidatı olarak toplam 25 YTL (Yirmibeş Milyon TL) derneğin

İş Bankası Maltepe Şubesi Hesap No: 42120867567
IBAN: TR08 0006 4000 0014 2120 8675 67

hesabına yatırılmıştır.

Tarih :

İmza :

* Asil üye olmak için beş yıllık deneyim gereklidir.
Fahri üyelik için yüksekokul mezunu olma şartı yoktur.

Türk Isı Bilimi ve Tekniđi Derneđi
Gazi Üniversitesi
Mühendislik Fakültesi
Makina Mühendisliđi Bölümü
06570 Maltepe/ ANKARA

İÇİNDEKİLER / CONTENTS

Analysis and assessment of daily and seasonal photovoltaic heat island effect on Sekbandemirli rural region by local weather data records	157
<i>Yerel meteorolojik veri kayıtları ile Sekbandemirli kırsal bölgesinde günlük ve mevsimsel fotovoltaik ısı adasının incelenmesi ve değerlendirilmesi</i> Emre DEMİREZEN, Talat ÖZDEN and Bülent G. AKINOĞLU	
Nationwide mapping of optimum wall insulation thicknesses: A stochastic approach	169
<i>Optimum duvar yalıtımı kalınlıklarının ülke çapında haritalanması: Stokastik yaklaşım</i> Semih CAGLAYAN, Beliz OZORHON and Levent KURNAZ	
Theoretical and experimental investigation of V-Corrugated solar air heater for space heating	203
<i>V-Kat levhalı güneş enerjili hava ısıtıcının ortam ısıtması için teorik ve deneysel incelemesi</i> Murat ÖZDENEFE and Khaled ALTEER	
Physics informed neural networks for two dimensional incompressible thermal convection problems	221
<i>Sıkıştırılmaz ısıl taşınım problemlerinin fizikle öğrenen yapay sinir ağları ile çözümü</i> Atakan AYGUN and Ali KARAKUS	
Cooling performance of thermoelectric cooler modules: Experimental and numerical methods	233
<i>Termoelektrik soğutma modüllerinin soğutma performansı: Deneysel ve sayısal yöntemler</i> İlhan KAHRAMAN and Naim DEREBAŞI	
Finding conditions in reprocessing of glass wool waste as a heat insulator	245
<i>Camyünü atığının ısı yalıtkan olarak yeniden proses edilmesinin koşullarının bulunması</i> Saharat CHUNTHUM, Anchasa PRAMUANJAROENKIJ, Siriluk PHANKHOKSOONG, Rungsima CHOLLAKUP and Sadık KAKAÇ	
Himmetoğlu ve Seyitömer bitümlü şeylleri ile plastik şehir atıklarının kabarcıklı akışkan yataklı reaktörde gazlaştırılması	257
<i>Gasification of Himmetoğlu and Seyitömer oil shales with plastic wastes in a bubbling fluidized bed reactor</i> Duygu UYSAL, Hazal ÖZTAN, Ahmed Abdullah GAFUR ve Özkan Murat DOĞAN	
Analysis of heat transfer enhancement in tubes with capsule dimpled surfaces and Al₂O₃-water nanofluid	269
<i>Boru yüzeyindeki kapsül tipi kabartmanın ve Al₂O₃-su nanoakışkanın ısı transferine etkisinin sayısal analizi</i> Ekin ÖZGİRGİN YAPICI, Mahmoud Awni A. Haj İBRAHİM and Haşmet TÜRKOĞLU	